SEISMIC TOMOGRAPHY PROJECT

Department of Geophysics
Stanford University

Volume 2, No. 1
June 1991

SEISMIC TOMOGRAPHY PROJECT

Volume 2, No. 1

Contributors:

Luis Canales
Jerry M. Harris
Caroline Lambert
Spyros Lazaratos
Nathalie Lucet
Gary Mavko
Reinaldo Michelena
Richard Nolen-Hoeksema
Masazumi Onishi
Youli Quan
Jamie Rector
Nicholas Smalley
Mark Van Schaack

June, 1991

TABLE OF CONTENTS

PAPER A

HIGH RESOLUTION IMAGING WITH CROSSWELL REFLECTION DATA

Spyros K. Lazaratos, James W. Rector, Jerry M. Harris, and Mark Van Schaack
Seismic Tomography Project

ABSTRACT

Crosswell data are definitely complicated. They contain a rich variety of wave modes producing a wavefield of intimidating complexity. This is probably the reason why traveltime tomography is by far the most popular type of processing applied to such data. Yet, other parts of the wavefield may be much more appropriate for achieving the coverage and high resolution necessary for accurate reservoir characterization.

In this study we enhanced the crosswell reflected wavefield through appropriate processing and used it for imaging a region between wells. Although our data were contaminated by strong, aliased tube waves, we were able to get a good tie at the well and resolution approaching that of the wireline logs. This leads us to believe that, with some improvements on the hardware and data acquisition, reflection crosswell imaging could become an extremely useful tool for reservoir characterization.

INTRODUCTION

In most crosswell studies, especially in those applied to real crosswell data, the direct arrival traveltimes have been used to invert for seismic velocities in the region between wells. Direct arrival traveltimes are definitely a robust observation that should be used whenever available. Still they represent a small fraction of the total information contained in the data. Although processing the full waveform is complicated, good quality reflection data present the potential for very high resolution imaging of reservoirs without the large data volumes necessary for high resolution crosswell traveltime tomography. This has been pointed out by several authors and a few real data studies have been published along these lines (Baker and Harris, 1984; Iverson, 1988; Beydoun et al., 1988; Abdalla et al., 1990).

This paper presents the results of reflection processing applied to crosswell data in the frequency range of a few kHz for a well spacing of around 330 ft. A series of preprocessing operations were employed to enhance and separate upgoing and downgoing P to P primary reflections, which were used to produce depth images of a region between wells. The imaging algorithm we used is similar to the VSP-CDP method (Wyatt and Wyatt, 1984), with particular attention paid to the accurate positioning of wide angle reflections.

The result of the processing was compared to synthetic seismograms generated from well logs. This comparison provided additional evidence that resolutions of the order of a few ft can be achieved for this range of frequencies. Our main limitation was the presence of strong aliased tube wave noise, which limited our ability to get high quality images away from the well. Nevertheless, the tie at the well was exceptionally good.

The results shown here were produced from a single common receiver gather (133 traces). The good quality of the tie, given the aliased noise limitations, suggests that high resolution images of reservoirs might be produced with a small amount of data, which could be collected and processed in a short time.

DESCRIPTION OF THE DATA SET

The crosswell data were collected at BP's test site located southwest of San Antonio near Devine, Texas. The site and data acquisition technique for a different data set collected at the same site were described by Harris (1988). Two cased boreholes —Wilson 2 and Wilson 4—were used. Each borehole is about 3000 ft deep and their nominal separation is 330 ft. A sketch of the geology and the sonic logs for Wilson 2 and Wilson 4 are shown in Figure 1. Notice the similarity between the two logs, indicating lateral homogeneity.

The cylindrical piezoelectric bender transducer described by Balogh et al. (1988) was used as both a downhole seismic source and a receiver. The radiated wavelet was a short (approximately 1 ms) broadband waveform with a fundamental frequency of 2 kHz. Seismic waves with a frequency content ranging from about 200 Hz to 4000 Hz were recorded, although the received bandwidth varied depending on lithology.

The results presented in this paper were produced from just one common receiver gather. The receiver was positioned at a depth of 2355 ft. The sources were positioned over a range of depths from 2140 ft down to 2800 ft at a depth spacing of 5 ft.

DATA ANALYSIS AND PREPROCESSING

The common receiver gather that we used is shown in Figure 2. We can see a clean direct compressional arrival and a reflection at about 2540 ft. The rest of the data are dominated by strong tube waves. The goal of the preprocessing was to extract and enhance the primary upgoing and downgoing P-wave reflection arrivals using a combination of wavefield separation techniques, adaptive noise cancellation, and wavelet-shaping deconvolution.

The particular wavefield separation process used had limited success in rejecting the strong tube wave arrivals. The 5-ft vertical sampling interval in the source well created a Nyquist frequency of approximately 475 Hz. As the data contained frequencies from about 200 to 4000 Hz, much of the band contained aliased tube waves.

Additionally, the vertical sampling interval aliased shear and shear-converted waves at frequencies above 2000 Hz. For this reason, as well as lower signal-to-noise

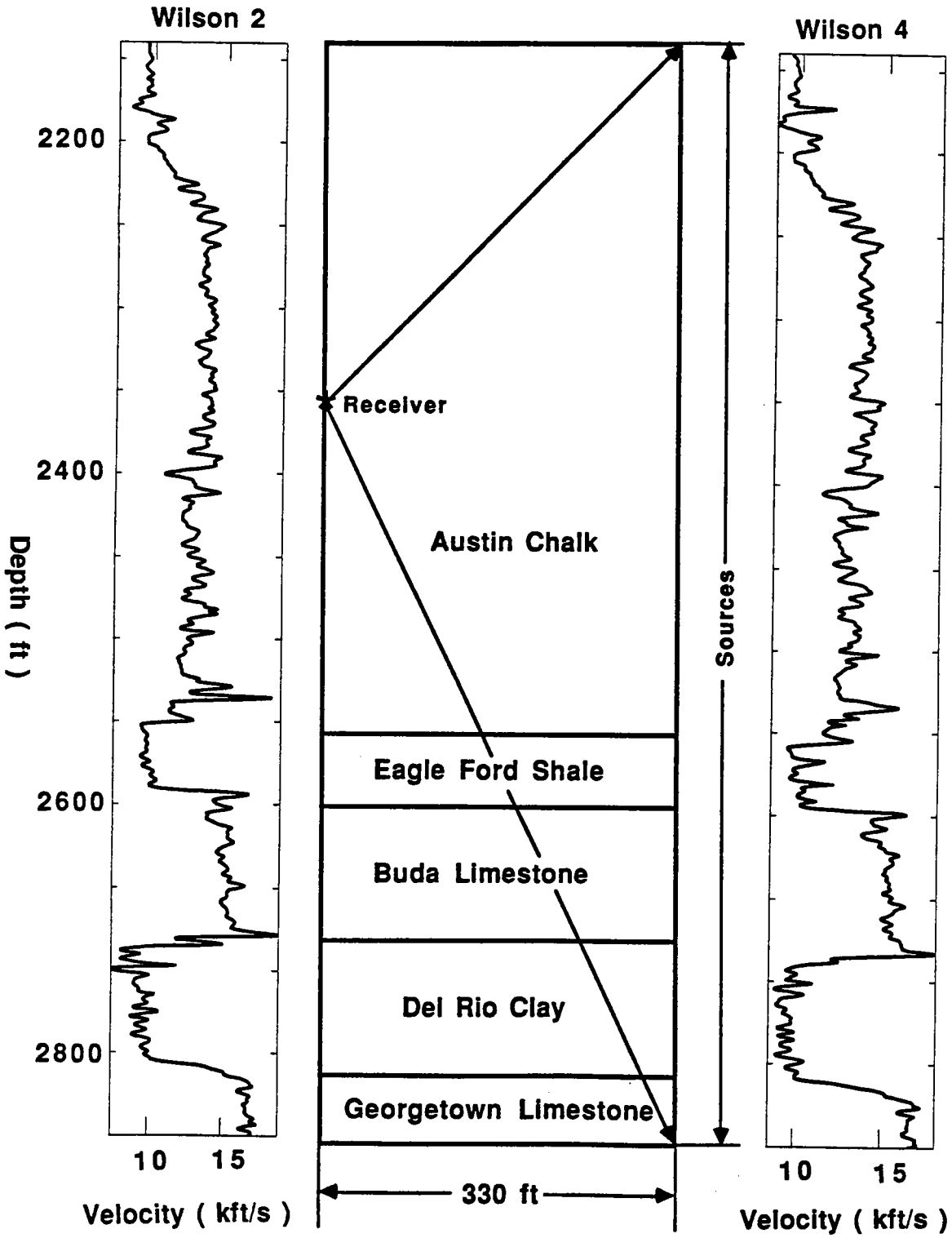

Figure 1: Sketch of geology and data acquisition geometry.

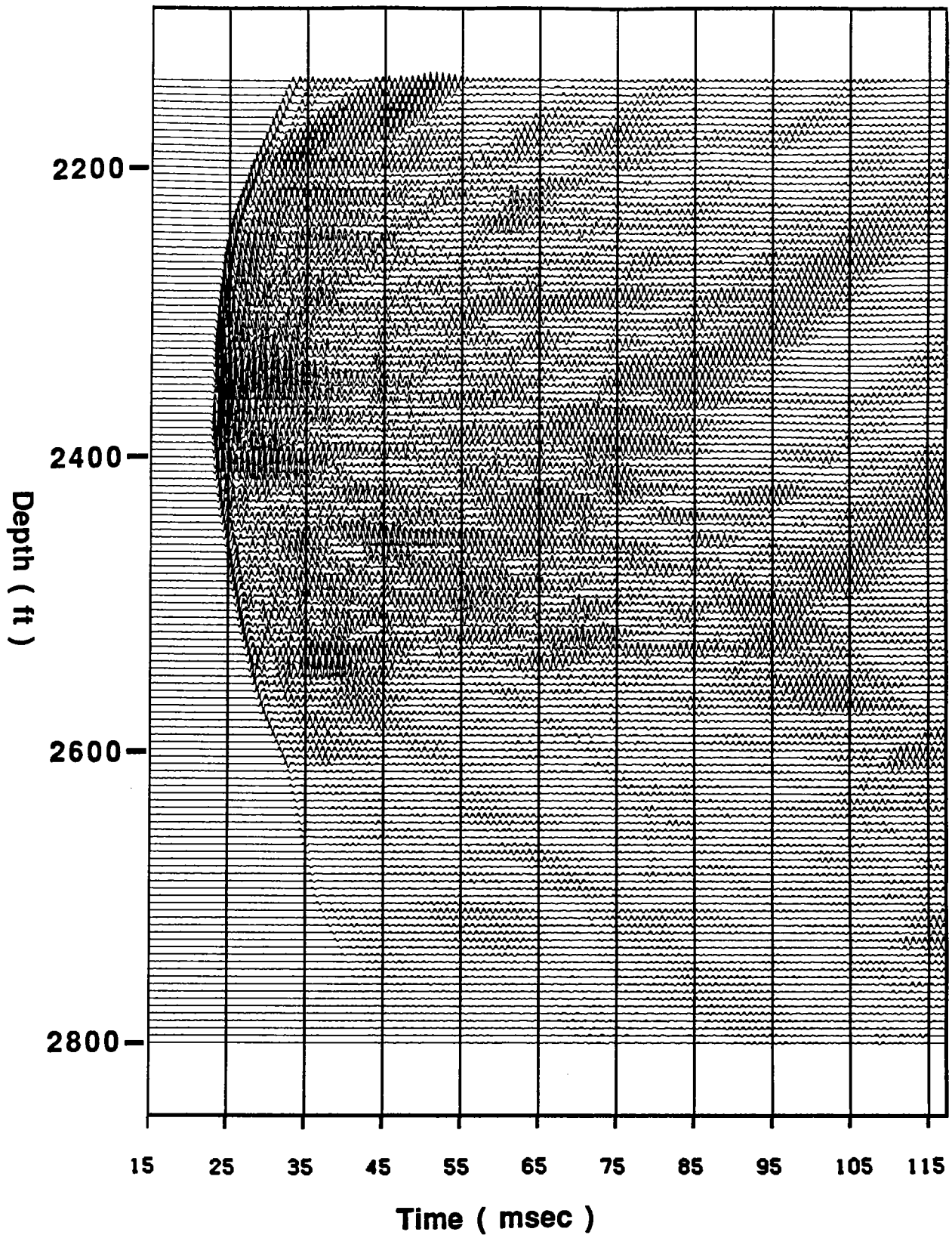

Figure 2: Raw data.

ratios at the higher frequencies, the extracted P-wave reflection wavefield was frequency bandpassed from 200 to 2000 Hz.

As an alternative to spatial filtering we used a time-domain filter that attenuates narrowband signals, such as the tube waves shown in Figure 2. Such a filter was described by Widrow (1976). This type of filter can also be formulated as a prediction error Wiener filter (Peacock and Treitel, 1969). Figure 3 shows the wavefield in Figure 2 after application of the prediction error narrowband signal filter. To preserve relative phase between traces, the autocorrelation used to derive the filter was obtained as a mix of several adjacent trace autocorrelations.

A number of new arrivals are apparent in Figure 3. The tube wave arrivals can be seen to intersect the P-wave first break from discrete depths rather than from a wide zone as the data in Figure 2 would suggest. These intersection depths appear to correlate with major reflectors, indicating that these tube waves are converted to compressional body waves at interfaces along the source well. Shear wave arrivals can also be seen. The direct shear wave is the hyperbolic event that can be seen at shallow depths between about 50 and 70 ms. This hyperbolic event has an apparent apex at the receiver depth (2355 ft). It can also be seen at the deeper source depths as well. There is a shadow zone for the shear wave in the area exactly opposite the receiver, which, we believe, is due to the shear wave radiation pattern of the piezoelectric bender—source and receiver—transducers. Theory (White, 1983) predicts a shear wave distribution sharply peaked at an angle of 45 degrees that falls off rapidly away from that angle. The theoretical P-wave radiation pattern is less sharply peaked, having a maximum at an angle of 90 degrees to the vertical and dropping to a minimum of about 1/3 the maximum in the direction of the borehole axis. The radiation pattern effect for the P wave can be observed in the data by looking at the amplitude ratio of the direct P wave to tube wave arrivals generated at smaller offsets. This ratio decreases much more rapidly with increasing offset than simple transmission effects would predict.

The shear wave arrivals can be seen much more clearly in Figure 4, which was produced by the following processing steps:

- Attenuation of the P-wave direct arrival via conventional VSP wavefield separation (Hardage, 1985) using a 21-trace mean filter
- F-K pie-slice filtering to attenuate higher apparent velocity P-wave converted arrivals and P-wave reflections as well as evanescent energy
- Zero-phase bandpass filtering from 200 to 900 Hz

In Figure 4 first note that there are residual tube wave arrivals, particularly at the deepest source depths. These residuals are the result of the tube wave aliasing. The shear wave direct arrival, which was described above, can now be seen very clearly. Its behavior is consistent with that of the direct compressional arrival: the changes in slope associated with major interfaces can be seen very clearly. Several other modes can also be identified: S to S reflections, P to S reflections, P to S conversions, and S to P conversions. Residual P to P reflections are also present. We did not attempt multiple-mode imaging in this study, although Figure 4 shows evidence that this may

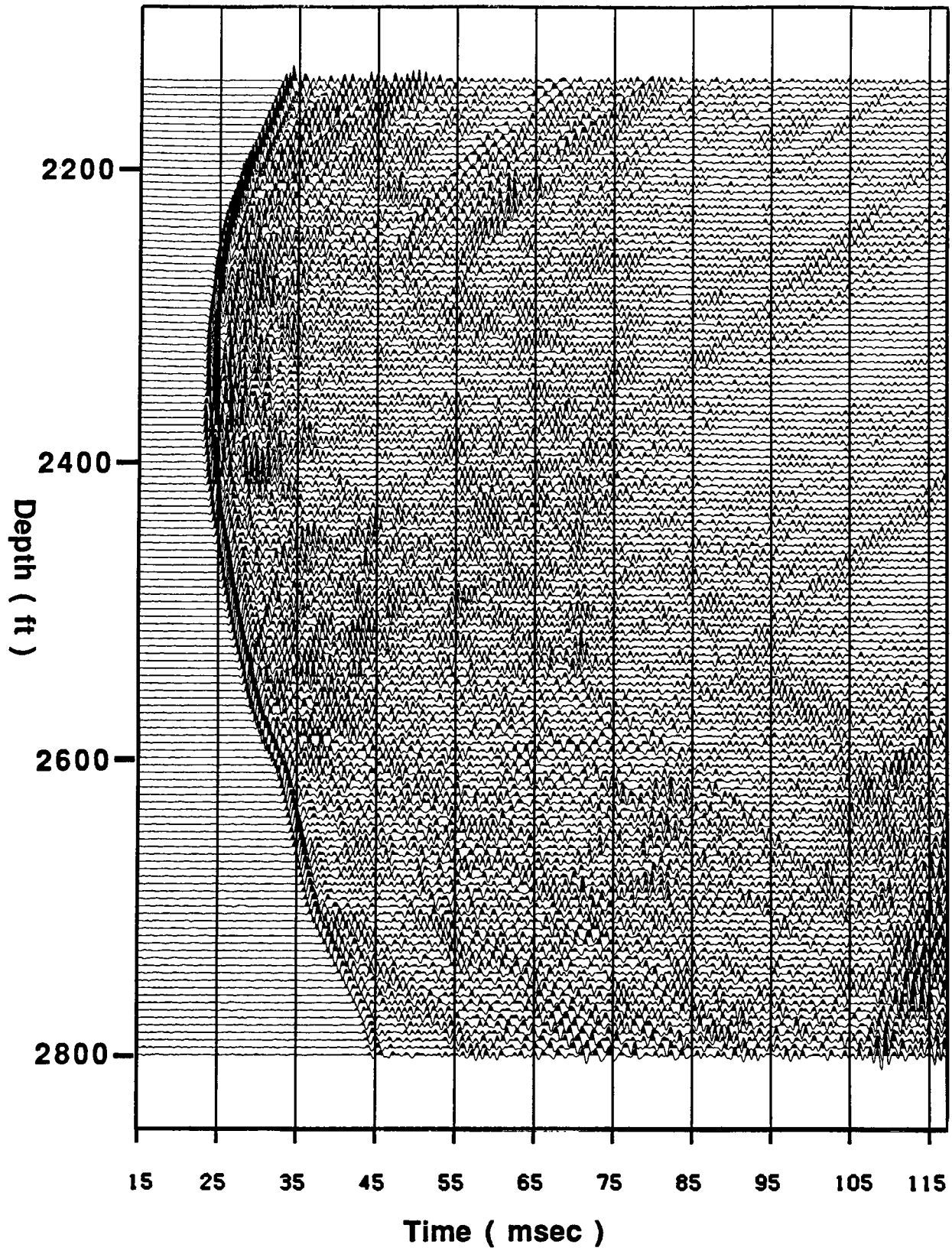

Figure 3: Data after narrowband signal attenuation.

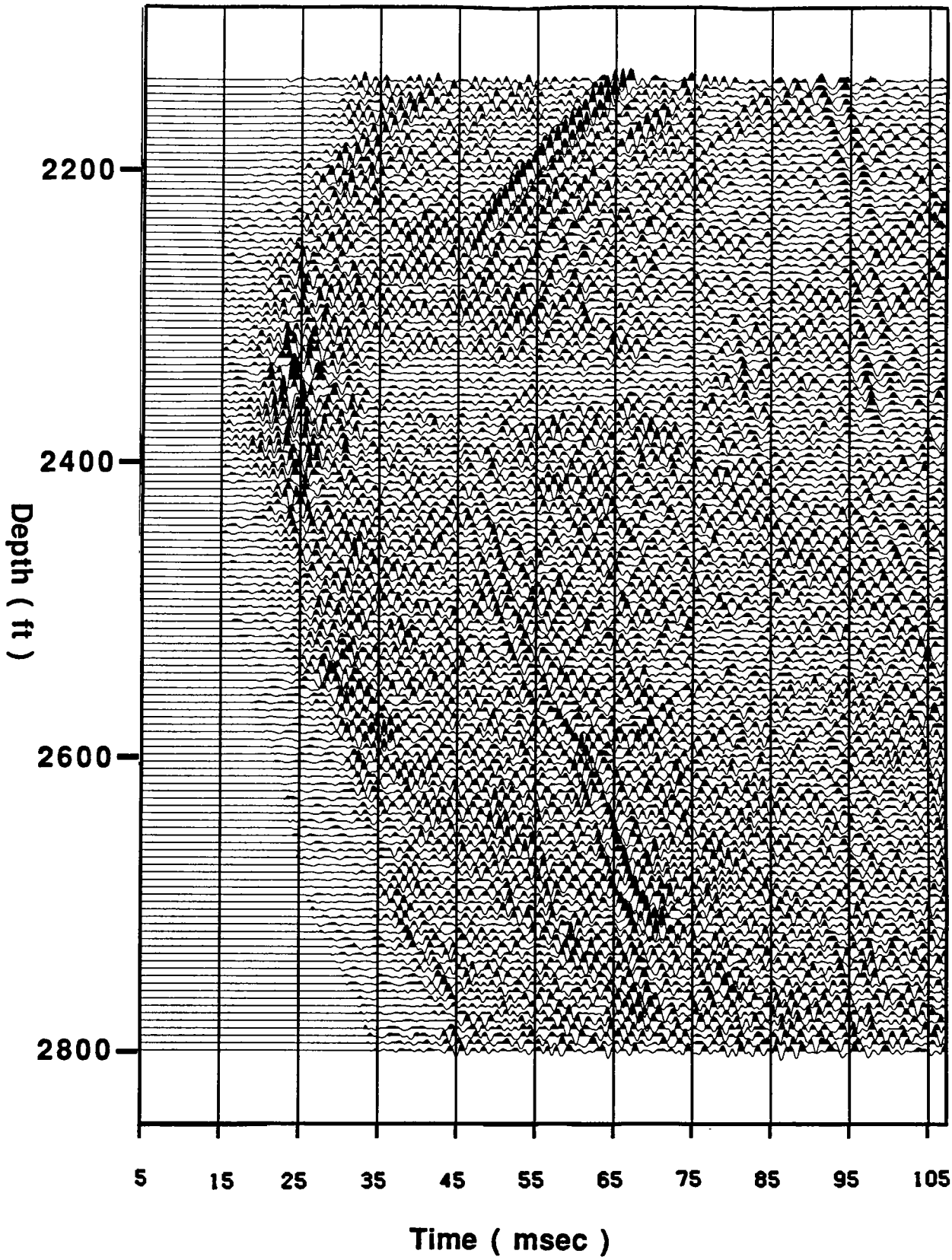

Figure 4: Enhanced shear arrivals.

be feasible, especially for data that are not aliased. Since, over some range of radiation angles, we can detect shear arrivals with the piezoelectric bender bar source and receiver, it may not be necessary to have a wall-locked source and three-component geophone receivers to produce elastic images of the subsurface.

For these data we observed that the P waves seem to be wider frequency band than the shear waves. This might be due to a combination of lower Q and longer traveltimes for shear waves.

The P to P reflected wavefield can be obtained from the total wavefield with a processing sequence similar to that used for extracting the shear wave arrivals. Instead of designing an F-K filter to reject P-wave reflections, an F-K filter that enhances these reflections is used. In Figure 5 we show the enhanced upgoing wavefield. A close-up is shown in Figure 6. A close-up of downgoing reflections due to interfaces above the receiver is shown in Figure 7.

As part of the preprocessing we also applied wavelet shaping deconvolution to remove the effects of the source wavelet, receiver related reverberations, and some of the internal multiples. Some receiver related reverberations can be clearly seen in Figure 4. They are the arrivals following the main shear arrival with almost exactly the same moveout. Similar reverberations for the P wave can be observed in Figure 3.

THE IMAGING PROCEDURE

In order to produce a depth section from our data we first need to define a velocity model. Correct imaging at depth always requires an accurate velocity model but in the case of crosswell data the need for accuracy is even more significant, since we are dealing with wide-angle reflections. The incidence angle for the major reflection that we see in the data at a depth of about 2540 ft is 57 degrees close to the source well. Small traveltime errors can easily misposition the reflectors at depth or produce artificial dips. Mispositioning and dipping are particularly noticeable at the high frequencies we are working with.

The velocity model that we used for imaging is shown in Figure 8. It was defined by matching the direct arrival traveltimes in a layer-stripping fashion and further refined to provide the correct dips for reflectors (a comparison of the two well logs shows that the reflectors in this area are essentially horizontal) and tie with the logs. On the same figure we show the fit between the picked traveltimes and the ones predicted by the model.

The imaging algorithm that we used is a variation of the VSP-CDP mapping algorithm (Wyatt and Wyatt, 1984). We were very careful to make sure that the algorithm is accurate for wide-angle reflections. Conventional VSP-CDP algorithms often have problems in dealing with them. The algorithm handles horizontal reflectors in layered velocity backgrounds. It was appropriate for the particular data set, since the area we were trying to image is laterally homogeneous as discussed before.

The first step in the algorithm is to generate, by ray tracing, trajectories connecting the possible reflection points for horizontal reflectors at different depths. Such trajectories, calculated for the velocity model in Figure 8, are shown in Figure 9. Every trajectory corresponds to a source (since here we are dealing with a common

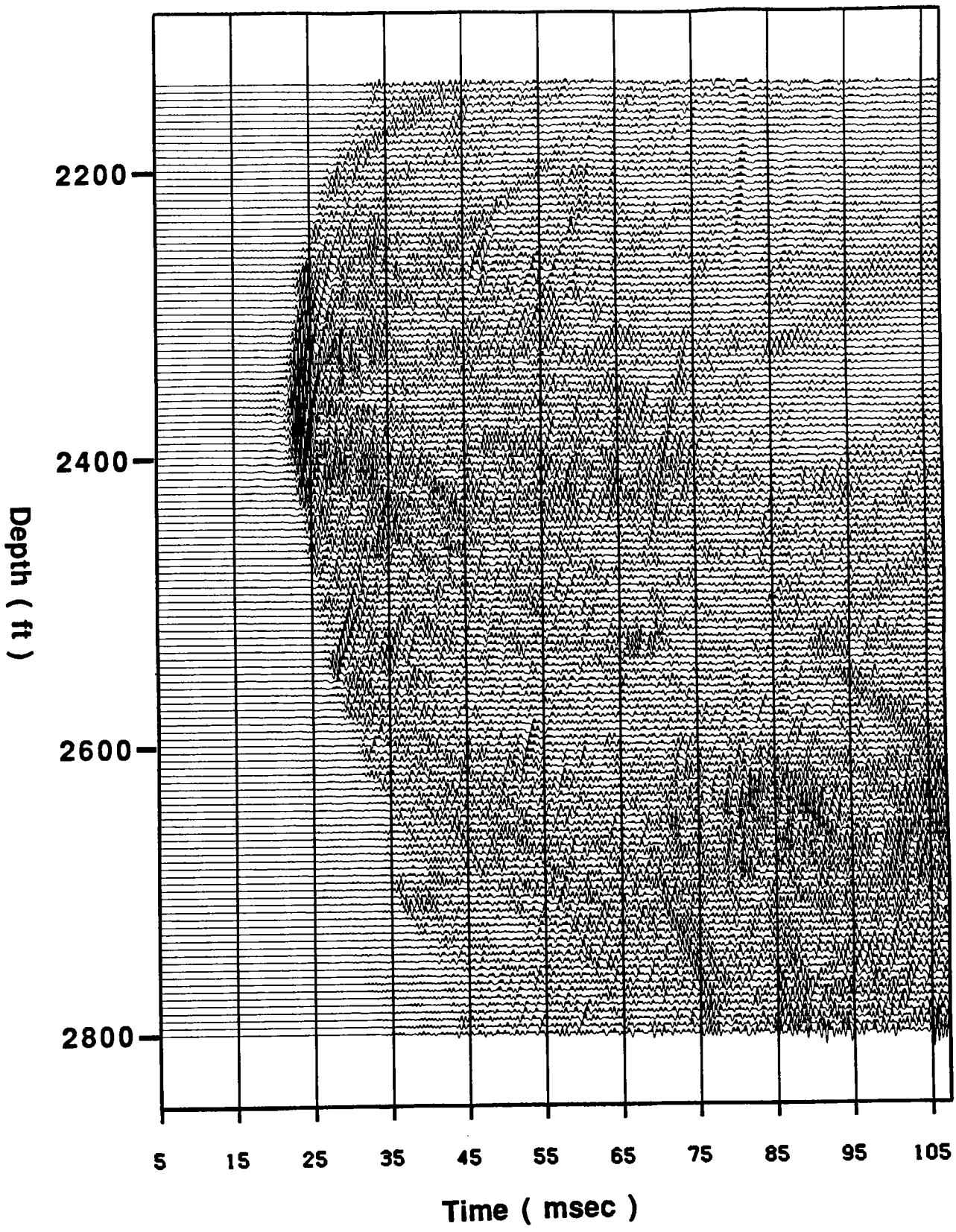

Figure 5: Enhanced upgoing wavefield.

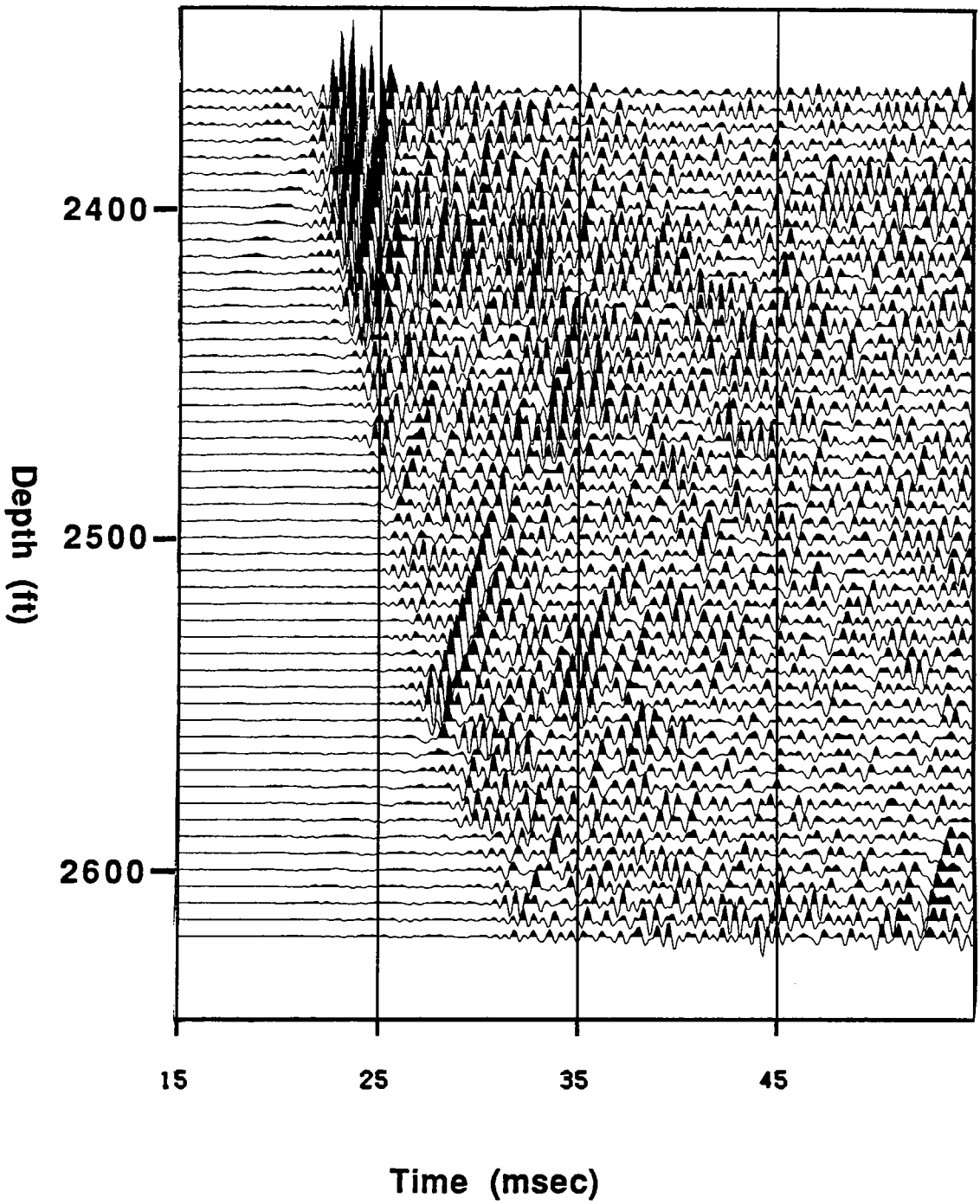

Figure 6: Upgoing wavefield. A close-up showing a number of upgoing reflections (before deconvolution).

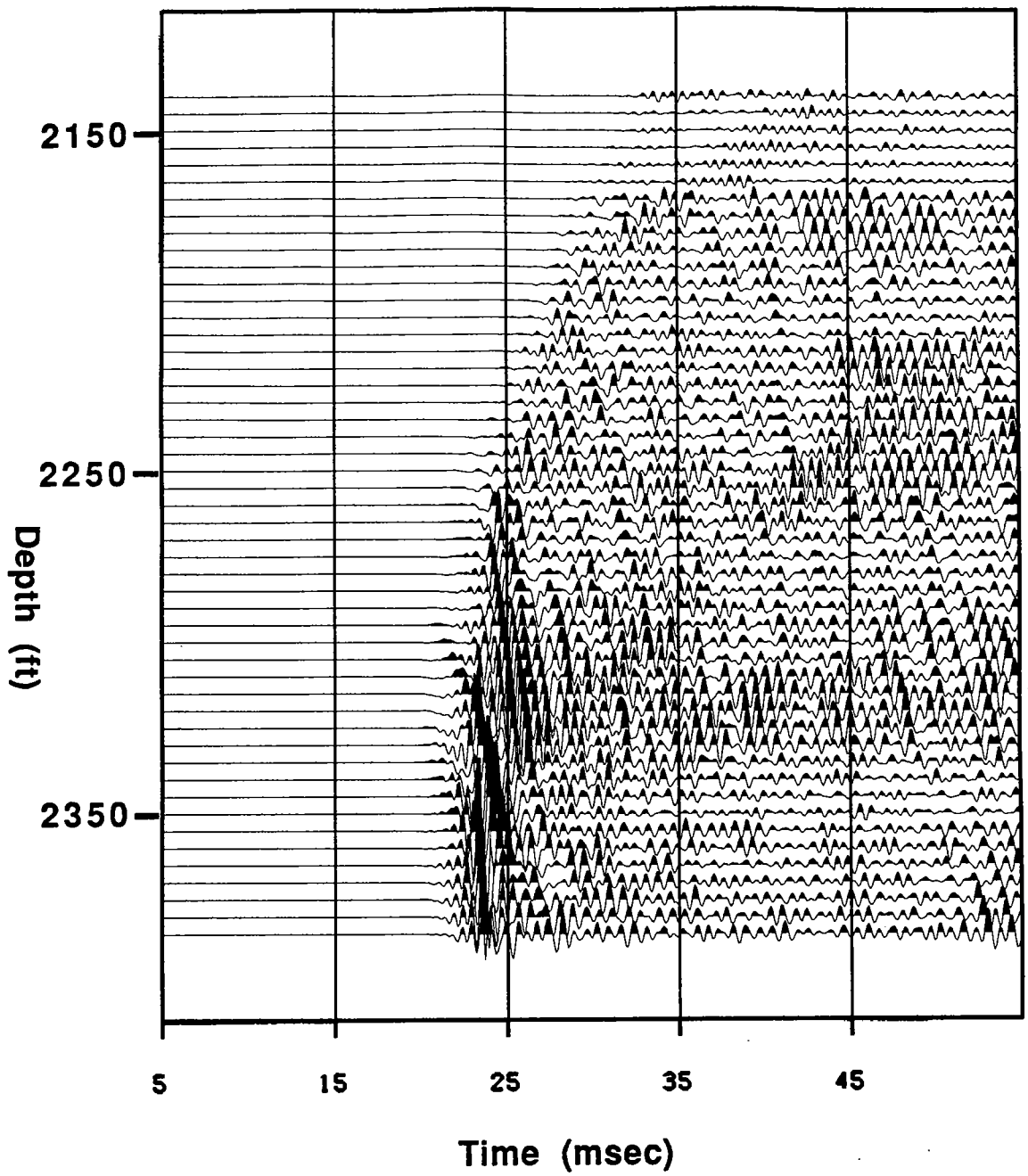

Figure 7: Downgoing wavefield. A close-up showing a number of downgoing reflections.

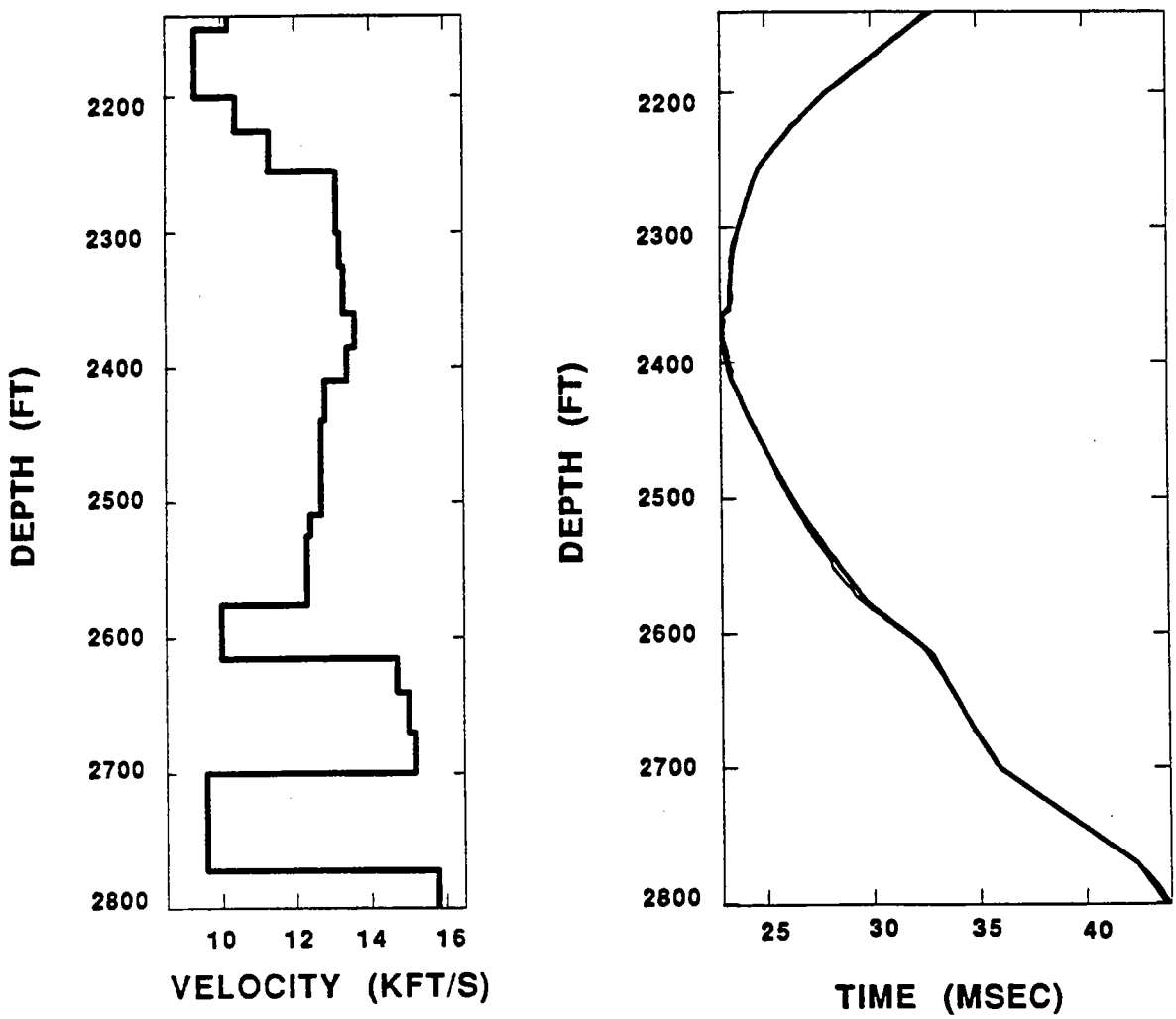

Figure 8: Left: Velocity model. Right: Fit between picked (thin line) and calculated (thick line) traveltimes.

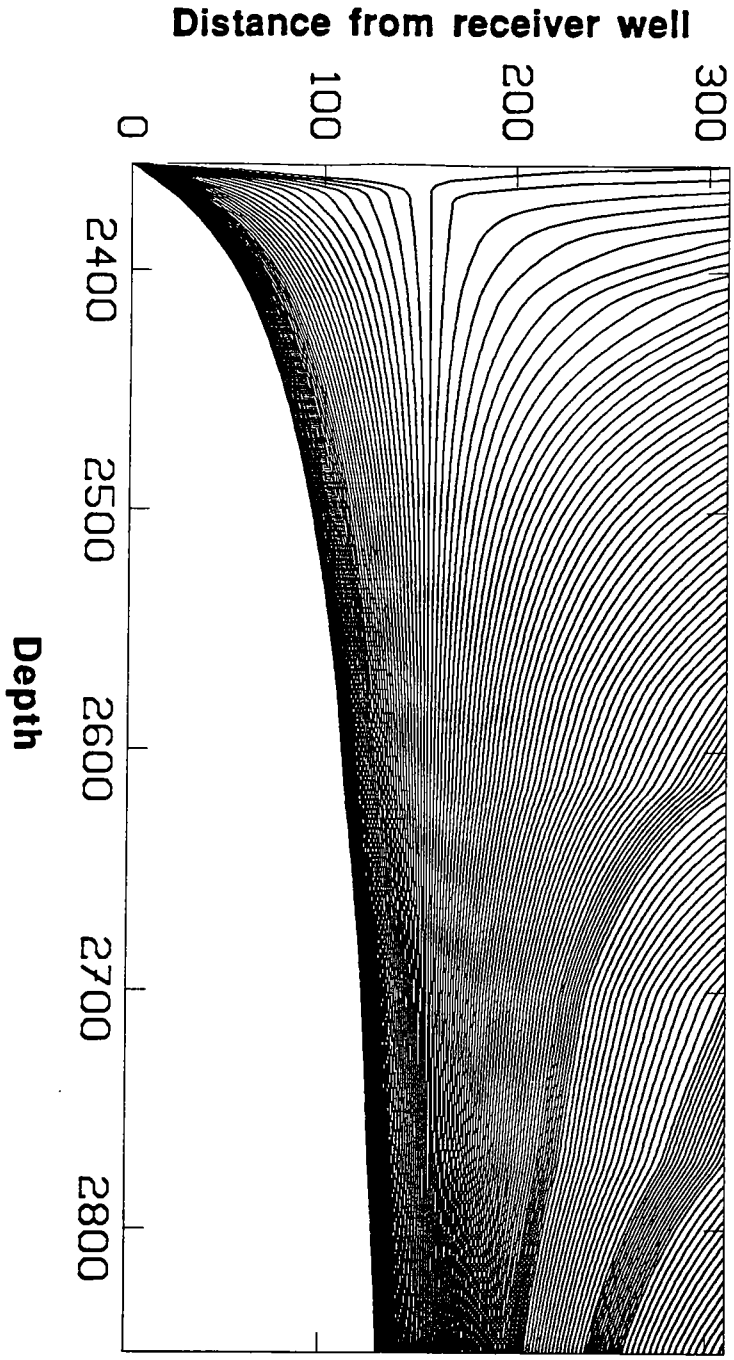

Figure 9: Reflection point trajectories.

receiver gather). The traveltimes corresponding to the reflections at different depths are also calculated.

Essentially every trajectory shown in Figure 9 corresponds to a trace. Conceptually the algorithm consists of spreading each trace on the corresponding trajectory, converting in this way the data into a depth image.

Our actual implementation is different. Based on the calculated trajectories in Figure 9, we generate maps attributing to each point in the image the following quantities:

- Depth of the source from which a specular reflection for a horizontal reflector passing through this point will be recorded
- Traveltime of the reflection event
- Ray parameter for the reflection event
- Moveout of the event in the data

Figure 10 shows contour plots of these four maps for the velocity model in Figure 8. The source depth map contains the same information as the trajectories in Figure 9 (the difference being that now the information is mapped on a regular 2-D grid). Therefore, its contours should be identical to the trajectories. Notice the similarity between the calculated trajectories and contours demonstrating the quality of the program.

Once these maps are calculated, the imaging is performed by assigning to each point in the image a data value corresponding to the source depth and time given from the maps. Since the data are discrete, an interpolation step is necessary. The moveout map is used at this stage: interpolating along the moveout direction of the reflected events allows the use of simple interpolators that work well even for sparsely sampled data. The ray parameter map allows us to easily incorporate AVO effects or radiation pattern corrections. We are currently adding a geometric spreading map which could be used for geometric spreading corrections. None of the above corrections was applied in this particular study.

To get good continuity of the events and preserve the wavelet character some smoothing of the maps has to be performed. This has to be done carefully though, since too much smoothing may start introducing mispositioning of the reflectors.

MAPPING VS. MIGRATION

The mapping algorithm is not a migration algorithm: migration handles correctly all dips while the mapping is accurate only for horizontal reflectors. This can be remedied if the local dip is known. Then we can similarly derive a mapping algorithm that correctly images events with the desirable dip. The main difference though is that the mapping algorithms image only a single dip at a time, while migration can handle a range of dips.

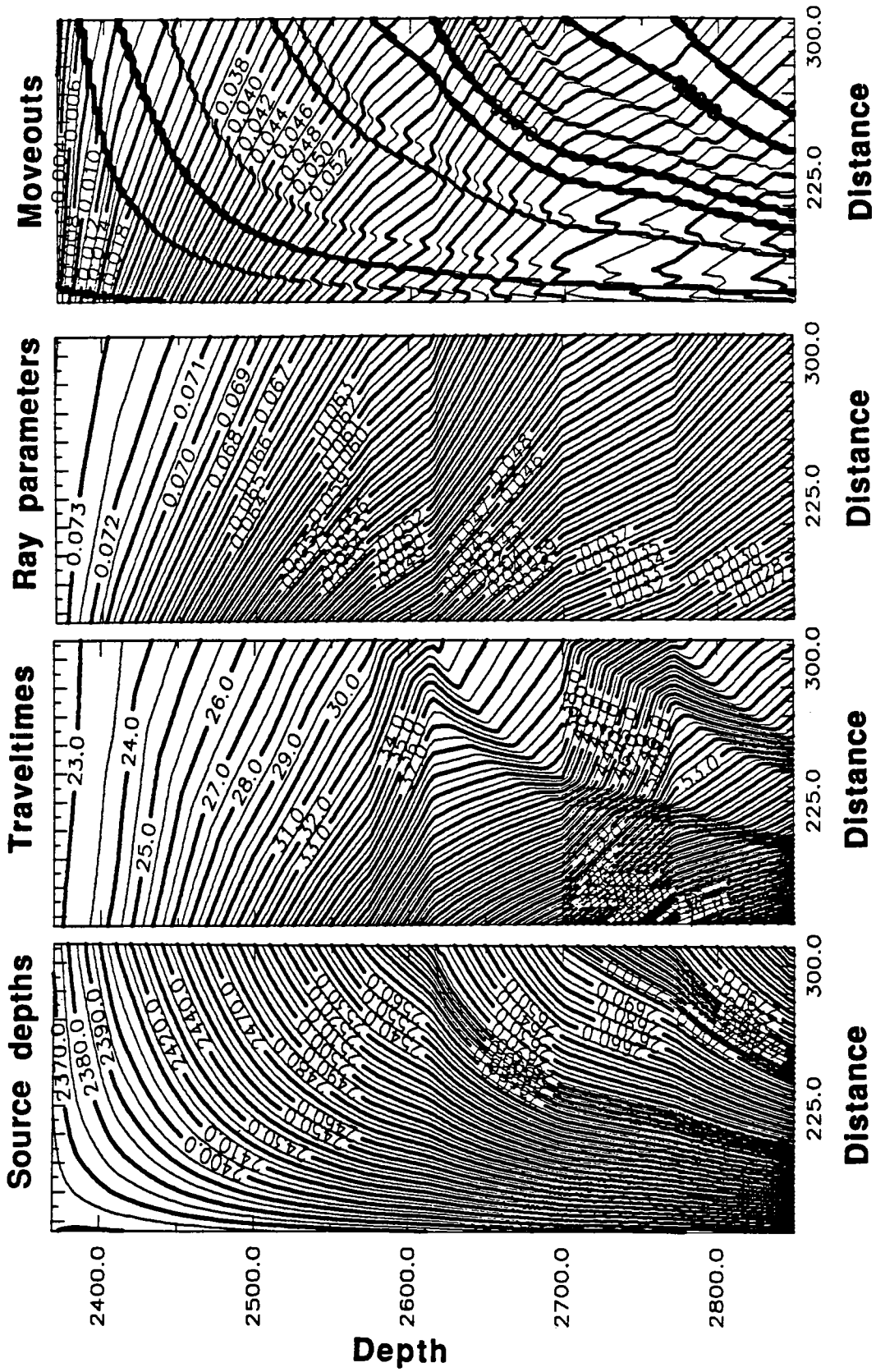

Figure 10: Maps of quantities used in the imaging algorithm.

In fact, the mapping can be considered the limit of migration as the aperture of the migration operator goes to zero. This has been our original implementation of the algorithm and it is illustrated in Figures 11 and 12. The migration algorithm that we implemented was a prestack Kirchoff migration able to handle general velocity models. In Figure 11 we show contours of traveltime maps calculated for the velocity model in Figure 8. The first two are the traveltimes from a receiver/source to all the points in the medium we want to image. The third is the sum of the first two and its contours are the familiar migration ellipses. The ellipses are distorted because the velocity model is heterogeneous. Kirchoff migration essentially consists of spreading each data point on the appropriate contour. We can spread it on the whole ellipse or on a part of it only. Using only part of the ellipse means restricting the imaging to a range of dips. In Figure 12 we give two examples of possible migration operators. The plots show partial images formed from a single trace with three band-limited spikes. The operator shown on the left plot can correctly image a 5-degree range of dips around zero dip. The operator on the right is valid for a 15-degree range of dips. As we make the aperture narrower and narrower the smiles shown in these plots tend to collapse and eventually become points on a trajectory like the ones at Figure 9.

This limited aperture migration algorithm is more general than the mapping algorithm: it can handle ranges of dips and general velocity backgrounds. Yet, the calculation of accurate traveltime maps makes this algorithm slower than the mapping and speed is a factor when we try several velocity models. A migration algorithm with the generality of Kirchoff migration but with significantly improved speed and flexibility is the Radon transform / Gaussian beam migration described by Lazaratos and Harris (1990). We will be testing this algorithm with real data over the next few months.

As a general comment, our experience has been that full aperture migration algorithms did not work well with crosswell data due to recording aperture limitations. They easily produced elliptical pseudo-reflectors (smiles). This has also been observed for VSP migrations.

On the other hand, even in the case of horizontal reflectors, imaging for a small range of dips is superior to imaging for just the dominant dip. Single-dip imaging produces a stretch along the reflectors similar to the NMO stretch. Limited aperture migration corrects for this stretch, essentially acting as a spatial deconvolution.

RESULTS - DISCUSSION

After application of the imaging algorithm to the preprocessed data a lateral mix of 30 ft (15 traces) was applied to attenuate residual aliased tube wave noise and improve the continuity of the reflectors. Inspection of the picked traveltimes shown in Figure 8 revealed that the seismic data were shifted in depth by 15 ft with respect to the well logs (observe the locations of the breaks in the traveltime curves and compare them to the depths of the major interfaces as indicated by the log). So, after imaging, a bulk shift of 15 ft was applied to the produced seismic section. In Figure 13 we show the image for the region nearest to the source well. We used both upgoing and downgoing reflections, so our image consists of two parts corresponding to reflectors

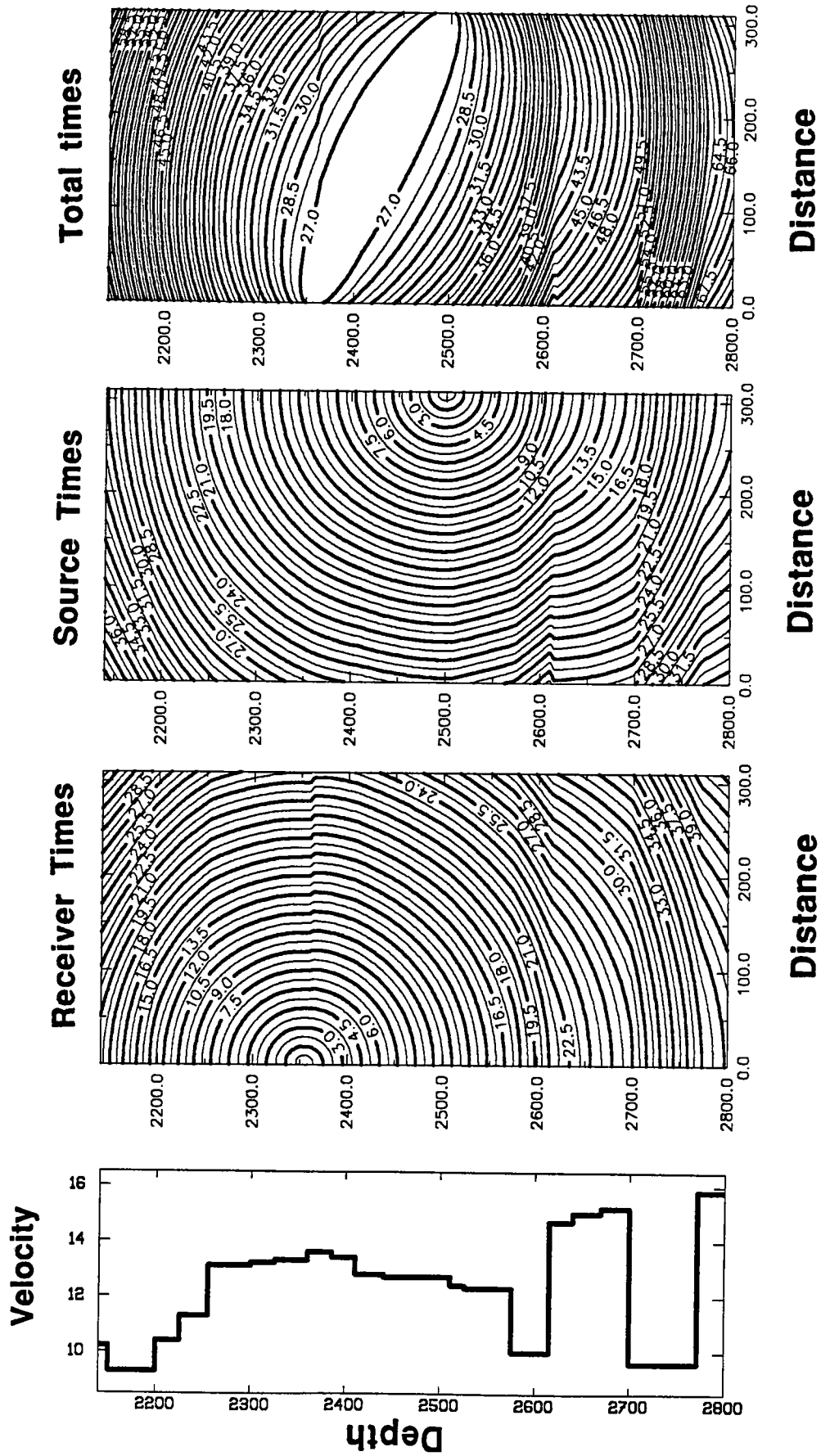

Figure 11: Example of traveltime maps used for the calculation of Kirchoff migration operators. Maps are calculated for the velocity model on the left frame.

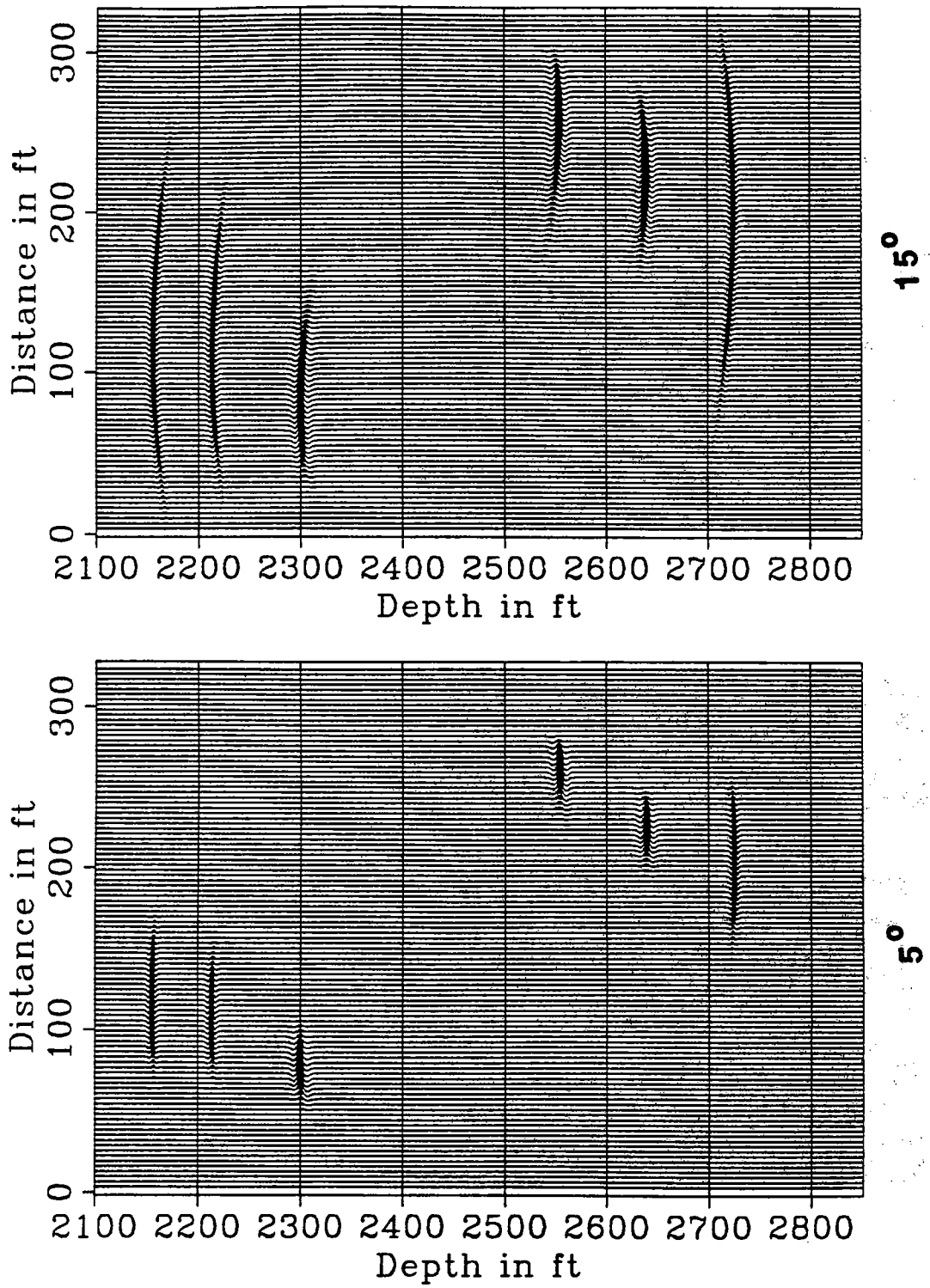

Figure 12: Limited aperture migration operators.

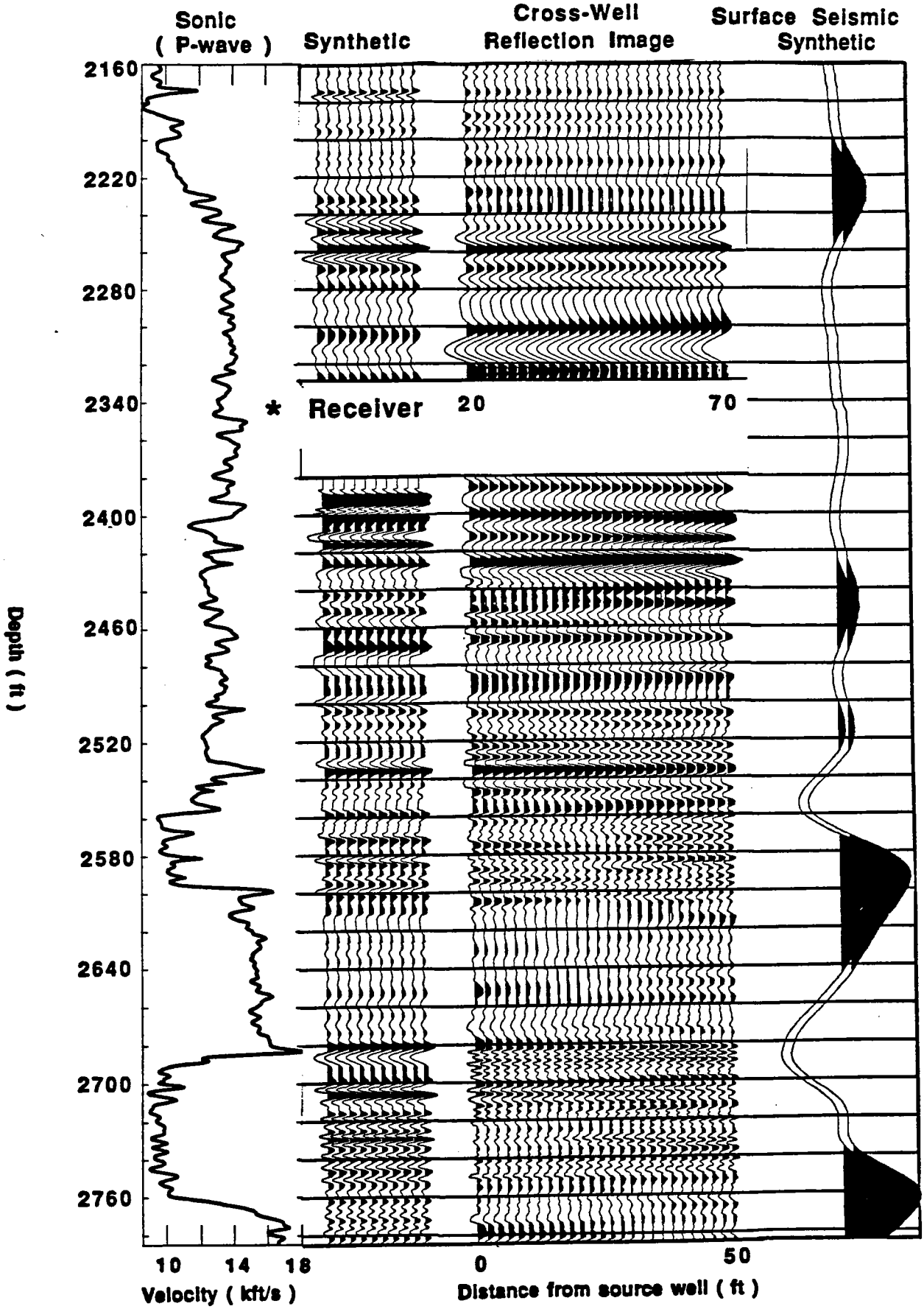

Figure 13: Result of imaging.

above (downgoing reflections) and below (upgoing reflections) the receiver. There is a small gap between these two parts of the image. This gap corresponds to the area very close to the receiver which produces extremely wide angle reflections, some of which are post-critical in nature.

A synthetic seismogram created from the sonic log at Wilson 4 is shown for comparison. The synthetic for the shallower 245 ft of the lower section (for the depth range between 2380 ft and 2625 ft) was created through the VESPA modelling software of Sierra Geophysics, to incorporate the effects of oblique incidence. Synthetic data were generated for a model built by blocking the sonic log at a very fine scale (layer thickness was of the order of 1 ft). These data contained only primary P-wave reflections. Then the data were mapped in depth using the mapping algorithm and the same velocity model that we used to map the real data. A similar lateral mix was applied and the first trace (closest to the source well) was repeated ten times for the display. The number of layers needed to appropriately block the whole interval of interest was larger than what our current version of VESPA could handle. So we calculated the synthetic for the depth range between 2625 and 2785 ft as a normal incidence synthetic seismogram. The upper part of the synthetic corresponding to the downgoing waves was also created through VESPA.

As a general observation we want to point out the amazing amount of information contained in the reflected wavefield. At the frequencies of investigation (up to 2 kHz, wavelengths down to 4.5 ft for this area) even the finer layers (2-3 ft) indicated by the well log have a detectible seismic response. This suggests that seismic data at these frequencies can provide vertical resolution similar to that of the sonic logs, that is, down to a few feet.

The tie of our image to the log is good, although certainly not perfect. We have slight mismatches in several places but we can identify the events modeled by the synthetic. In some places the tie is excellent. Look for example at the interval between 2480 and 2600 ft. The doublet at 2480 ft is perfectly matched, as well as the spike a little bit below and essentially all the events up to the strong reflector at 2540 ft. Then we get the reflection from the top of the Eagle Ford shale at 2560 ft, the response of the heterogeneities inside the shale, and the bottom of the shale at 2600 ft. Many of these features—like the distance between the two peaks of the doublet—have thicknesses of the order of 3-5 ft. Most of these features can be seen in both logs (see Figure 1), which provides evidence that they are real.

In other depth intervals the tie to the synthetic is less exact. Moving to the top we approximately get the four peaks between 2430 and 2480 ft. We also get the four reflectors between 2380 and 2430 ft, although the upper three of those are dipping (the dip is an artifact of the mapping for the area very close to the receiver). Moving below the Eagle Ford shale we get a relatively quiet zone associated with the Buda limestone and then the top of the Del Rio clay at 2680 ft. We also get the reflection inside the Del Rio at 2700 ft. It is hard to correlate the rest of the events inside the Del Rio, but at least the character of the response is similar to the one indicated by the synthetic.

The correlation for the upper part of the image (reflections above the receiver, depth interval 2160-2330 ft) is very good. Notice the sequence of reflections between

about 2230 and 2280 ft associated with the prominent peaks in the well log. Also note the responses of the doublet at 2200 ft and the peak at 2180 ft present in both the real and the synthetic. The two deeper events of the downgoing section at depths of 2300 ft and 2320 ft are post-critical reflections very close to the receiver.

Our section is still contaminated by tube wave noise, which makes interpretation away from the well ambiguous. In some places it is obvious that we have crossing events associated with coherent tube wave noise. Look, for example, at the events at 2440 ft and 2460 ft and at the bottoms of the Eagle Ford and the Del Rio that seem to be distorted by interfering noise. Subtler effects such as amplitude modulation are also apparent in many places. The distortions seem to be most significant below (for upgoing reflections) and above (for downgoing reflections) large reflection events. The Buda part is relatively quiet close to the well, as it should be (this quiet period can be seen in the data—look at Figure 5 at the appropriate depths), but starts getting noisier as we get further away.

Most of these effects are due to tube wave interference. In fact, since the reflections attenuate much faster than the tube waves as we move away from the receiver, the signal-to-noise and, consequently, the quality of our image is best close to the well and at the depths close to the receiver and degrades as we move further away. So, for these data, our ability to image farther away from the well was mainly limited by the aliased tube wave noise.

To illustrate the scale of the experiment and the detail obtained from the crosswell reflections, we included in Figure 13 a synthetic showing the image of the same area that would be obtained with zero-offset data at typical surface seismic frequencies. We used a band-limited (10-60 Hz) zero-phase wavelet.

CONCLUSION

High frequency crosswell data recorded with the piezoelectric bender transducer were found to contain a wealth of information beyond the first breaks. Several wave modes, difficult to observe and interpret on the raw data, were uncovered and partially separated with careful trace preprocessing. By carefully defining a velocity model and using appropriate imaging algorithms we were able to produce extremely high resolution (a few feet) depth sections that correlate well with the logs. We produced these images from a single common-receiver gather (133 traces). This amount of data can be collected in a relatively short period of time. Actually the amount of data used was much smaller than what is usually needed for traveltime tomography applications.

This study certainly points out that crosswell reflection imaging has the potential to evolve into an extremely useful tool for reservoir characterization, promising resolutions well beyond those that can be reached with conventional surface seismic data. Further studies in more complicated areas with non-aliased data and larger well separations are needed to firmly establish the usefulness of the approach.

ACKNOWLEDGEMENTS

The authors would like to acknowledge the support of the Gas Research Institute (GRI) and BP exploration.

REFERENCES

Abdalla, A. A., Stewart, R. R., and Henley, David, C., 1990, Traveltime inversion and reflection processing of cross-hole seismic data: paper BG2.8 presented at the 1990 Annual Meeting of SEG, San Francisco, Sept. 23-27.

Baker, L. J., and Harris, J. M., 1984, Cross-borehole seismic imaging: paper BHG2.2 presented at the 1984 Annual Meeting of SEG, Atlanta, Dec. 2-6.

Balogh, T. W., Owen, T. E., and Harris, J. M., 1988, New piezoelectric transducer for hole-to-hole seismic applications: paper DEV2.5 presented at the 1988 Annual meeting of SEG, Anaheim, Oct. 30-Nov. 3.

Beydoun, W. B., Delvaux, J., Mendes, M., Noual G., and Tarantola, A., 1988, Practical aspects of an elastic migration/inversion of crosshole data for reservoir characterization: a Paris basin example: Geophysics **54**, 1587-1595.

Hardage, B. A., 1985, Vertical seismic profiling, Part A: Principles, 2nd edition, Pergammon Press.

Harris, J. M., 1988, Cross-well seismic measurements in sedimentary rocks: paper DEV2.3 presented at the 1988 Annual meeting of SEG, Anaheim, Oct. 30-Nov. 3.

Iverson, W. P., 1988, Crosswell logging for acoustic impedance: Pet. Tech. J., 75-82.

Lazaratos, S. K., and Harris, J. M., 1990, Radon transform / Gaussian beam migration: in STP report, Volume 1.

Lazaratos, S. K., and Harris, J. M., 1990, Radon transform / Gaussian beam migration: paper SM3.8 presented at the 1990 Annual meeting of SEG, San Francisco, Sept. 23-27.

Peacock, K. L., and Treitel, S., 1969, Predictive deconvolution: theory and practice: Geophysics, **34**, 155-169.

White, J. E., 1983, Underground sound: Elsevier, New York.

Widrow, B., 1985, Adaptive signal processing: Prentice Hall.

Wyatt, K. D., and Wyatt, S. B., 1984, Determining subsurface structure using the vertical seismic profiling: *In* Toksöz, M. N., and Stewart, R. R., Eds., Vertical seismic profiling: Advanced Concepts, Geophysical Press.

PAPER B

CROSSWELL SEISMIC IMAGING IN CARBONATE ROCKS OF A WEST TEXAS 1-ACRE 5-SPOT

Richard Nolen-Hoeksema & Jerry Harris
Seismic Tomography Project

ABSTRACT

Three crosswell seismic surveys were run across the two diagonals and bottom edge of a 1-acre 5-spot in a West Texas, Permian Basin oilfield. The tomograms show the flat-lying structure of the reservoir and point to variations in reservoir quality. In the upper part of the tomograms there is a southwest to northeast increase in the slowness values, i.e., a decrease in velocities that may be attributable to waterflood effects.

OBJECTIVES

Crosswell traveltime tomography has been applied successfully to estimate seismic velocities between wells. Although much of the tomography has been used for purposes of monitoring enhanced oil recovery (EOR), the goal in this study was to image the reservoir interval to look for indications of barriers to fluid flow and to test the development of high frequency tomography in the Permian Basin environment. Specifically in West Texas, our interest was to image the reservoir interval within the Grayburg formation to look for variations in reservoir quality in otherwise flat-lying, continuous reservoir horizons.

SITE DESCRIPTION

Three crosswell surveys were conducted between four wells, each located at a corner of a 1-acre, 5-spot pattern (Figure 1; North is towards the top of the page). Survey 1 was along the 5-spot's NE-SW diagonal between Wells 57 and 55. Survey 2 was along the NW-SE diagonal between Wells 56 and 54. Survey 3 was along the 5-spot's southern edge between Wells 56 and 57. The well heads are 297.0, 298.5 and 210.6 feet apart in surveys 1, 2 and 3, respectively.

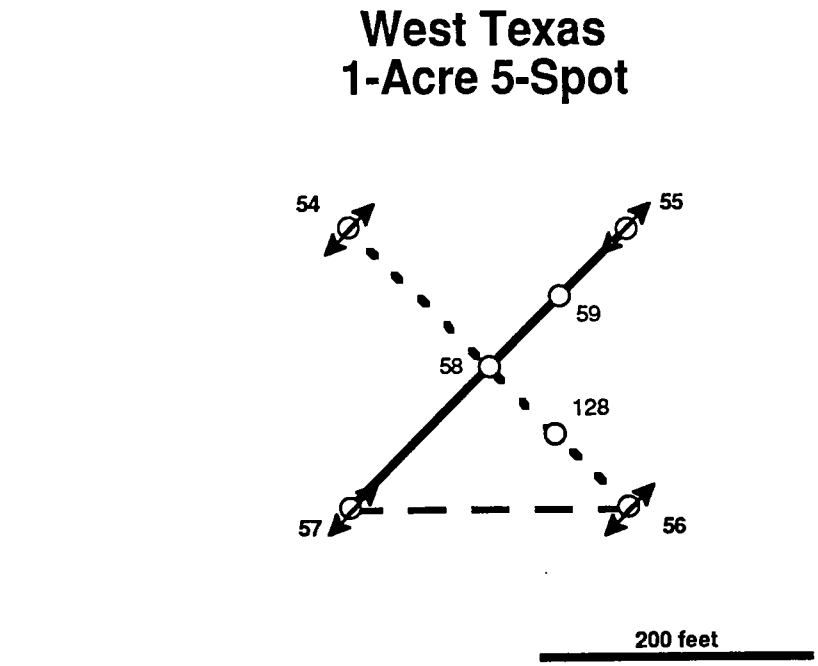

	Survey #	Source Well	Receiver Well	Well-to-Well Distance	No. of Sources	No. of Receivers
———	1	57	55	297.0 feet	70	69
- - -	2	56	54	298.5 feet	77	81
— —	3	56	57	210.6 feet	72	75

Figure 1: Three crosswell surveys were conducted between four wells, each located at a corner of a 1-acre, 5-spot pattern.

The primary targets in this study were reservoir horizons of the Permian-aged Grayburg formation. These horizons (S2, D4 and S3) are located within the payzone, which occurs between depths 4,130 and 4,250 feet, and dip roughly 3 degrees to the southeast. From logs, the dolomites (D1-D5) have typical P-wave velocities of 18,000-20,000 feet/sec and porosities around 5 percent. The sands (S1-S3) have P-wave velocities of 14,300-16,700 feet/sec and porosities of 10 percent or higher. Gas is known to exist above the payzone interval in this West Texas reservoir [Michael Stein, pers. comm., 1991].

In 1982 Amoco Production Company conducted a water-after-gas (WAG) CO_2-injection pilot project within this 1-acre 5-spot. The payzone's S2, D4 and S3 units, located from 4130 to 4250 feet, were the target for this project [Michael Stein, pers. comm., 1991]. Wells 54, 55, 56, and 57 were all used as CO_2 and water injection wells. CO_2 injection ended in March 1982. After a two-month soaking period, water injection occurred from May to July 1982. Following the pilot the wells in this 5-spot were shut in. Finally in late 1982, water injection started in a well about 420 feet to the southwest of the pilot and floodwater was driven across the 5-spot area towards a production well located about 370 feet northeast of the pilot.

DATA ACQUISITION

The field survey used a piezoelectric cylindrical bender downhole source constructed for Stanford by Southwest Research Institute. A hydrophone array built for Stanford by Century Geophysical Corporation was used as receivers. A description of the data acquisition system can be found in Paper N of this volume. The source was driven with a 250 msec upsweep from 350 to 2350 Hz. Sixteen sweeps were stacked to form the seismic trace. The data were recorded at a sample interval of 0.1 msec. Recorded data were subsequently cross-correlated to produce the seismic record. A common receiver gather taken at a depth of 4110 feet in survey 1 is shown in Figure 2.

The data were recorded with six hydrophones spaced ten feet apart. The shooting pattern fixed the hydrophones at depth and scanned the source upwards past the hydrophones through an aperture of roughly ±50 degrees. The hydrophones were moved at 5-foot or 10-foot intervals through the targeted reservoir zone from nearly 4300 feet to about 4100 feet. The source-receiver spacing was 10 feet in survey 1 and 5 feet in surveys 2 and 3.

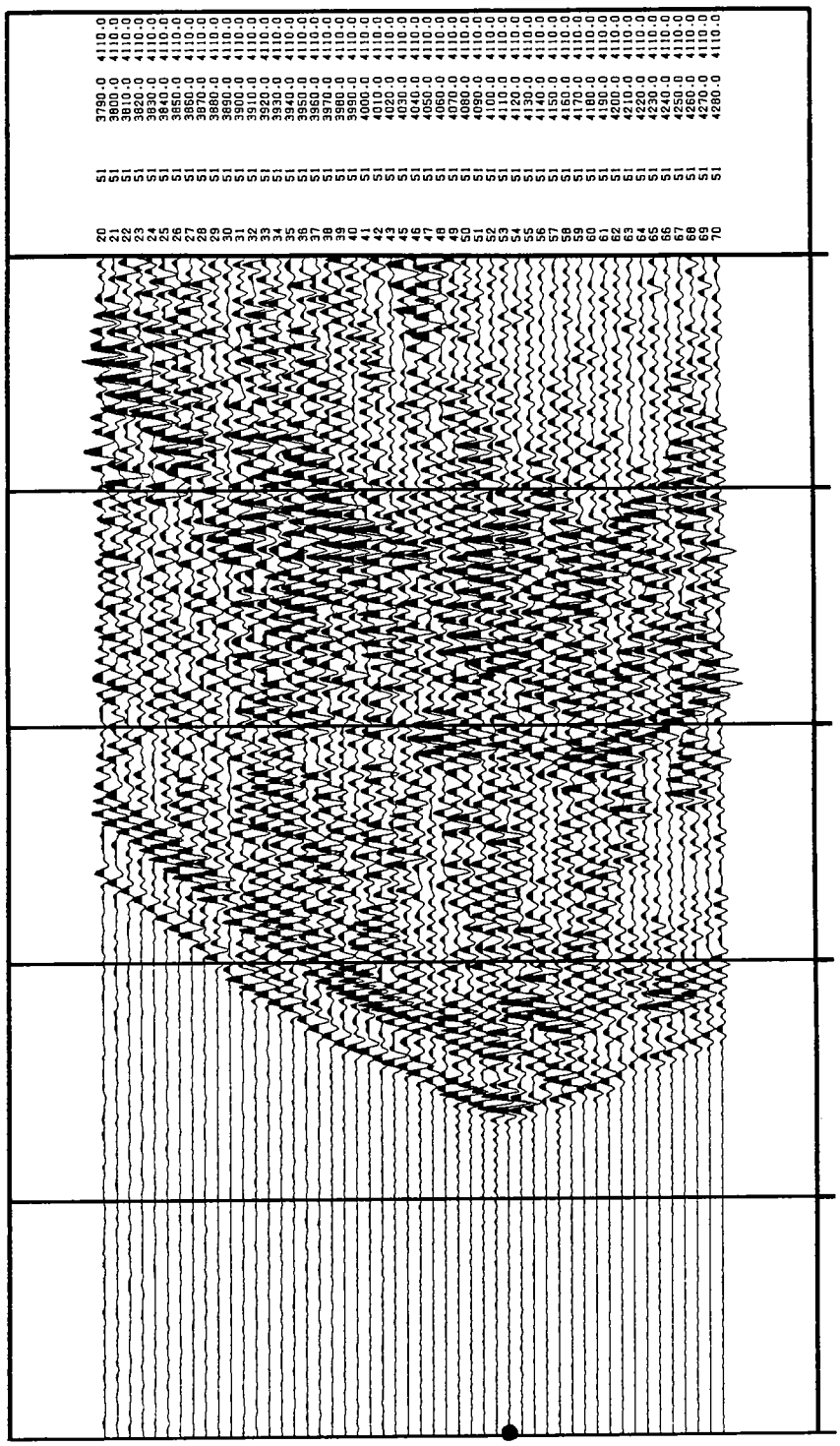

Figure 2: Common receiver gather 51 from survey 1. Receiver position is at depth 4110 feet. Each trace has been normalized to itself.

DATA PROCESSING AND INVERSION

P-wave traveltimes were picked from the cross-correlated seismic traces. Traces where reliable traveltime picks could not be obtained were ignored. Plots of the picks (which also show source-receiver coverage) are shown in Figures 3a, 3b, and 3c for surveys 1, 2, and 3, respectively.

Inversion of the traveltimes was performed using the iterative string method. This method uses two-dimensional ray tracing in an iterative backprojection scheme for matching calculated and measured traveltimes. Each data set was processed independently to produce a tomogram. The starting model for each was a smooth laterally interpolated version of the sonic logs. Twenty (20) ray trace iterations were performed on the each of the three data sets. [See Paper I for more details on string inversion processing.]

INTERPRETATION

Overall View of Tomograms

Tomograms covering depths from 3,900 to 4,300 feet are shown in Figures 4a, b and c. In each figure the receiver well is on the left and the source well is on the right. The tomograms are displayed in terms of slowness (μsec/ft); the warm colors (reds) indicate low slownesses or fast velocities and the cool colors (blues) indicate high slownesses or slow velocities. The low tomogram slownesses (high velocities) correlate with high sonic velocity, low porosity and very low permeability dolomites predicted from the well logs. The high tomogram slownesses (low velocities) correlate with lower sonic velocity, higher porosity and permeable sands. The overall flat-lying structure of the Grayburg formation is the dominant feature in the tomograms. The reservoir units are more or less continuous and are not disrupted.

Lateral Variations within Units

Lateral variations of slowness within the reservoir units may correlate with variations in reservoir quality. In West Texas reservoirs such variations in reservoir quality are caused by varying amounts of matrix material (e.g., detrital clay, fine-grained dolomite) and cement (e.g., anhydrite, dolomite). This matrix and cement occludes pore space and impedes fluid flow. Poor reservoir quality, that is, low effective porosities and permeabilities, usually occurs where there is an abundance of matrix and cements. High

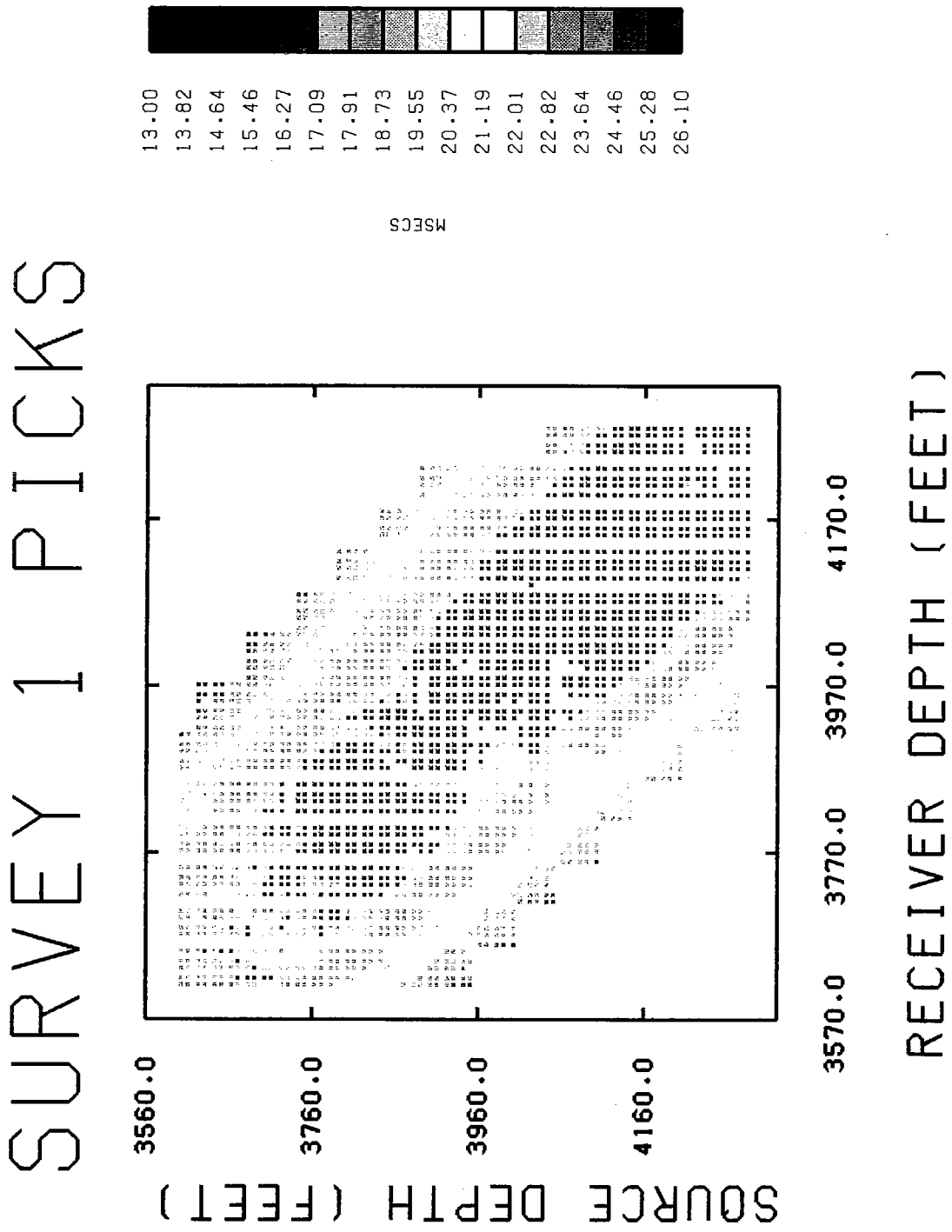

Figure 3a: Plots of picks for survey 1. The colors show the range of traveltimes (msec).

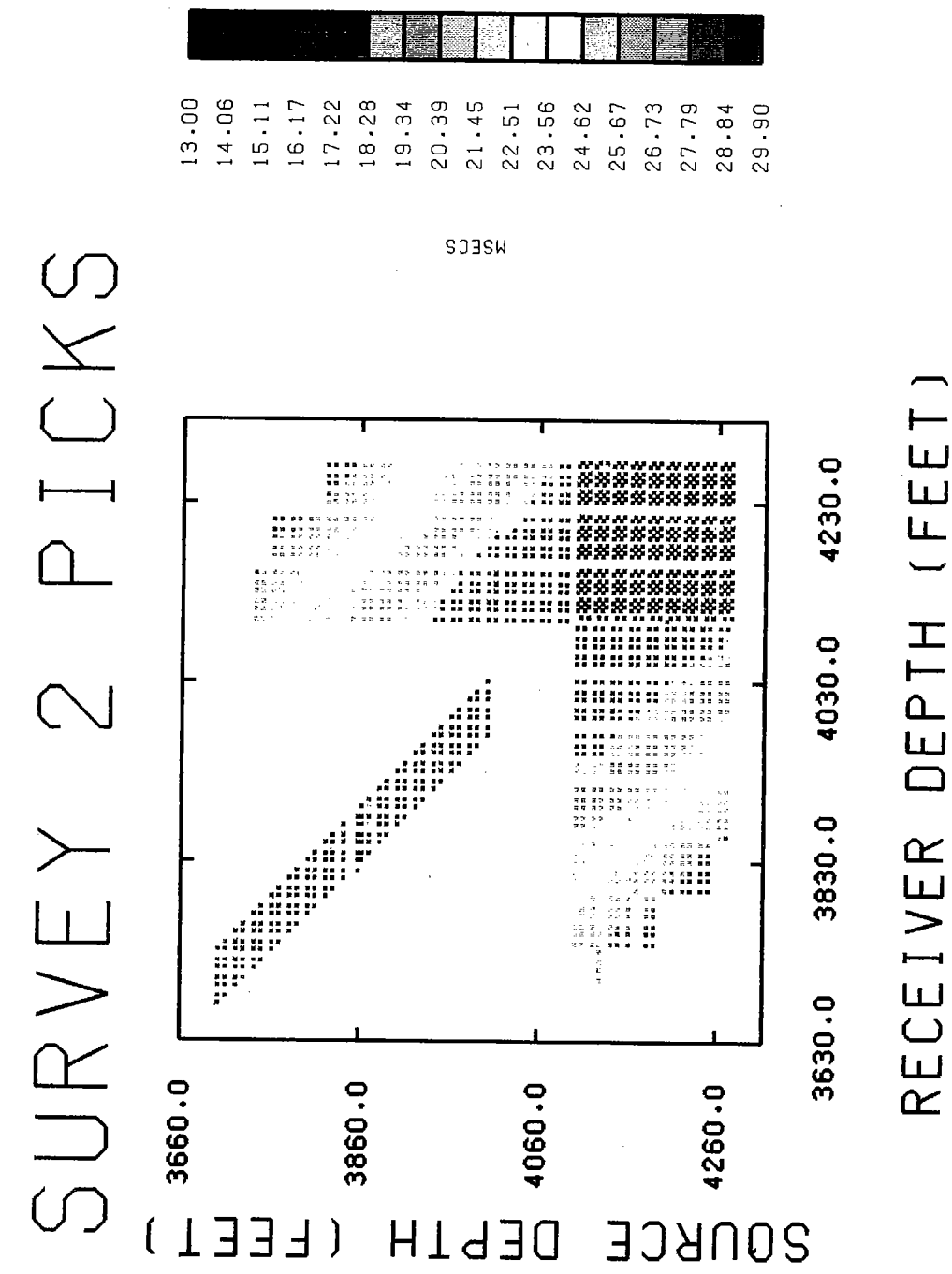

Figure 3b: Plots of picks for survey 2. The colors show the range of traveltimes (msec).

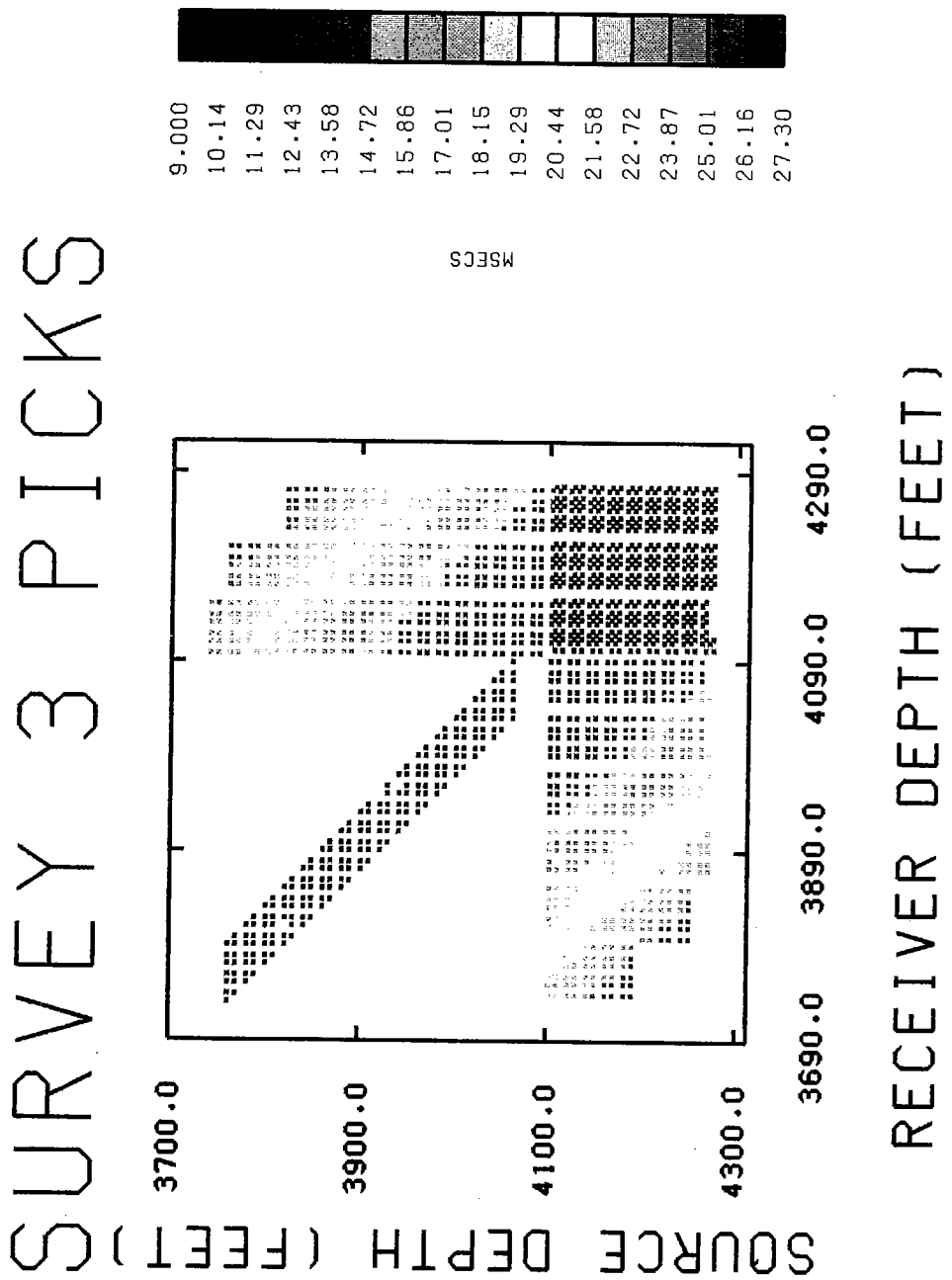

Figure 3c: Plots of picks for survey 3. The colors show the range of traveltimes (msec).

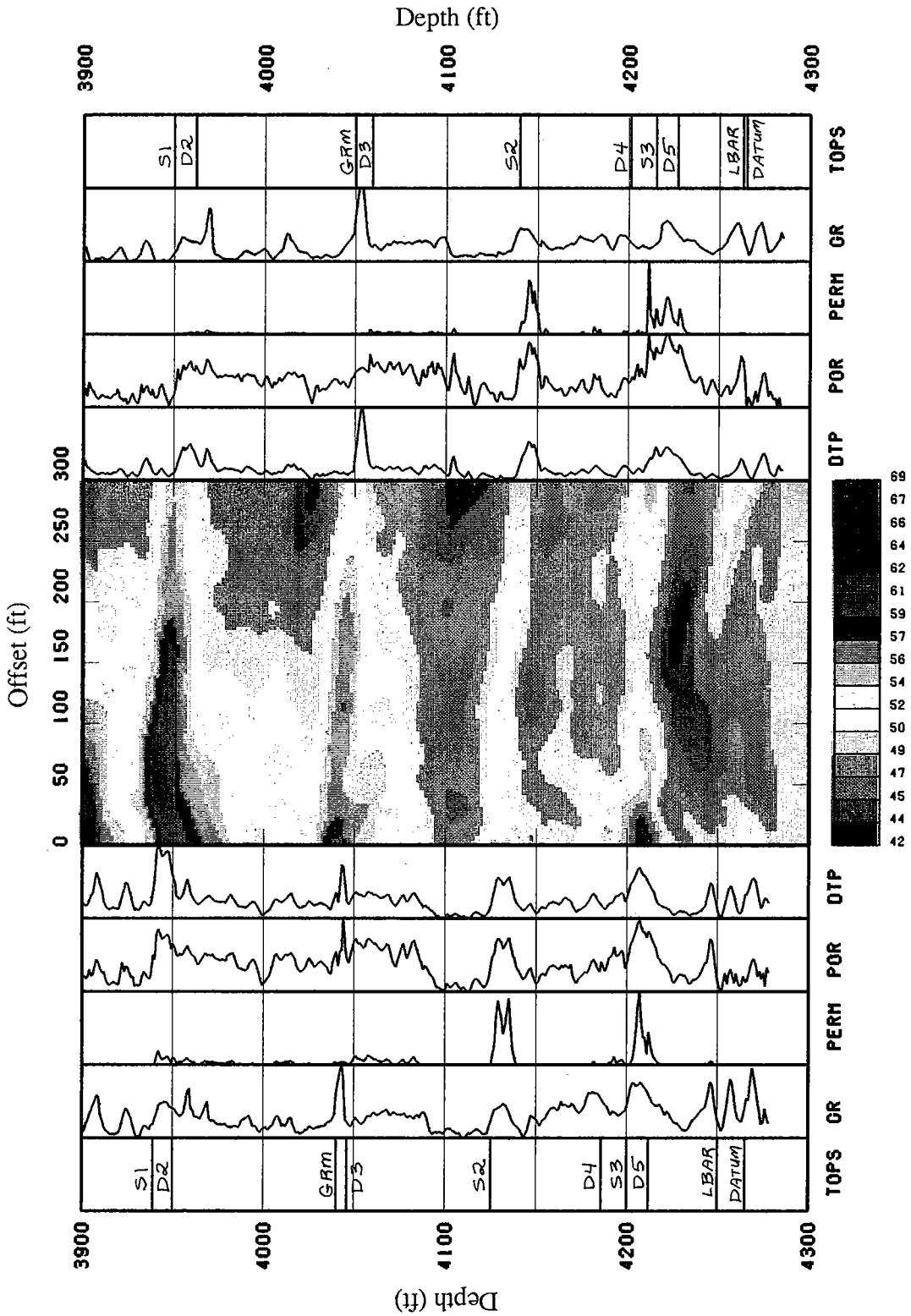

Figure 4a: Slowness tomogram for survey 1 covering depths from 3,900 to 4,300 feet. Panels on side, from outside to inside, show logs of stratigraphic tops, gamma ray, permeability, porosity, and sonic slownesses.

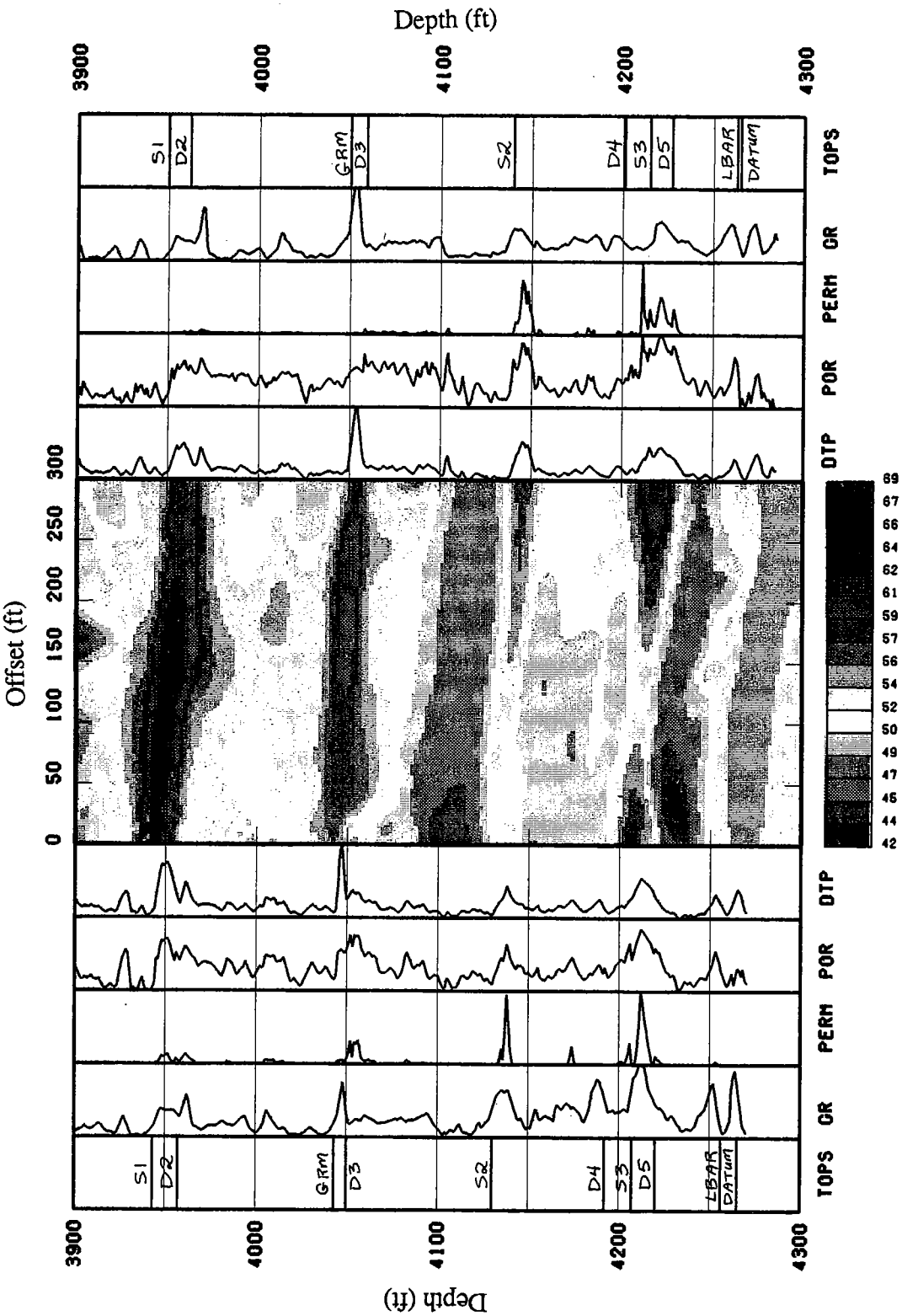

Figure 4b: Slowness tomogram for survey 2 covering depths from 3,900 to 4,300 feet.

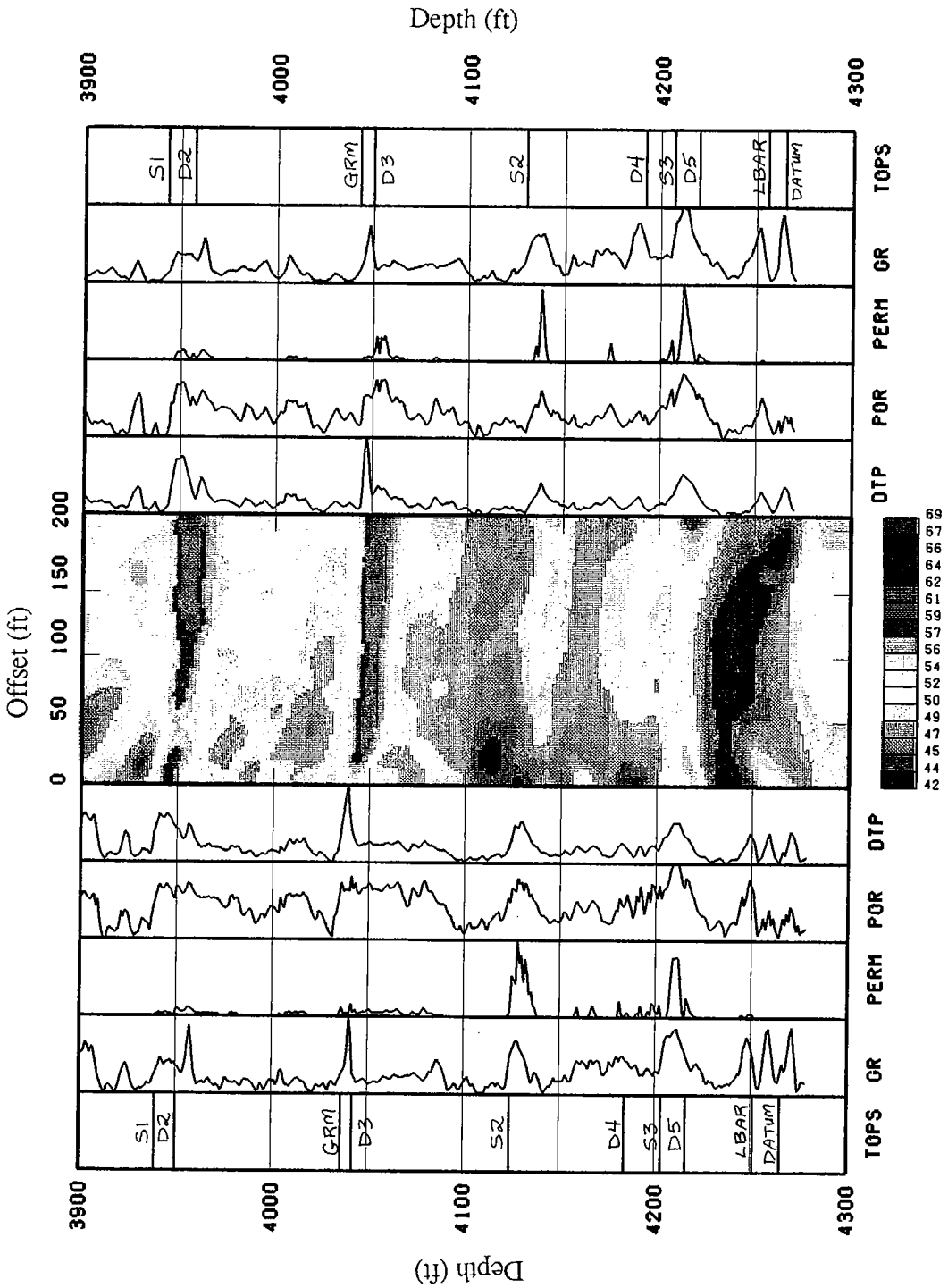

Figure 4c: Slowness tomogram for survey 3 covering depths from 3,900 to 4,300 feet.

seismic velocities would be expected in these parts of the tomograms. Conversely, good reservoir quality, that is, higher effective porosities and permeabilities, usually occurs where there is a low amount of matrix and cement. Lower seismic velocities would be expected to coincide with these zones.

Effects of Gas Above Reservoir

Another interesting feature is a SW-NE increase in slowness across the 5-spot in the upper part of the tomograms (Figure 5). Slownesses around Well 57 are lower than elsewhere in the 5-spot. Slownesses increase both to the east (Well 56) and to the north (Well 54) of Well 57. In survey 2 (Wells 56 to 54), the stratigraphic horizons in the 3,900-4,050 feet depth range have systematically higher slownesses than the lower payzone intervals. Taken all together, these observations suggest an increase in slowness from southwest to northeast in the 3,900 to 4,050 feet depth interval. This SW-NE increase in slowness may be explained by waterflooding effects on gas. This gas may occur either as residual CO_2 remaining from the WAG CO_2-injection pilot project or as a gas cap above the payzone.

Within West Texas carbonate reservoirs, it is common practice to create hydraulic fractures in wells in order to expose the wells to large surface areas of the reservoir rock—hydraulic fractures in this field align in a generally WNW-ESE direction that is consistent with in situ stress orientation measurements in this region [Zoback and Zoback, 1980; Zoback and Zoback, 1989]. Waterfloods are engineered in line-drive patterns to sweep floodwaters in the direction perpendicular to these hydraulic fractures. This flow direction is generally NNE-SSW. It is possible for these floodwaters to escape from the payzone stratigraphic units and sweep through the upper or lower bounding units.

Residual CO_2

During the pilot project, CO_2 could have escaped into the units above the payzone through leaks behind casing, natural breaks in the reservoir seal (4080-4130 ft), or hydraulic fractures induced and propagated upwards through the reservoir seal during the CO_2 and water injection phases of the pilot. The tomograms may be showing the effects of floodwater sweeping from southwest to northeast and displacing residual CO_2. Water-saturated zones would show up in the tomograms having lower slownesses (higher velocities) than gas-saturated zones. Since CO_2 is miscible with water, within the payzone itself, it is more likely than not, given time, residual CO_2 from the pilot would be dissolved in the floodwaters and swept away.

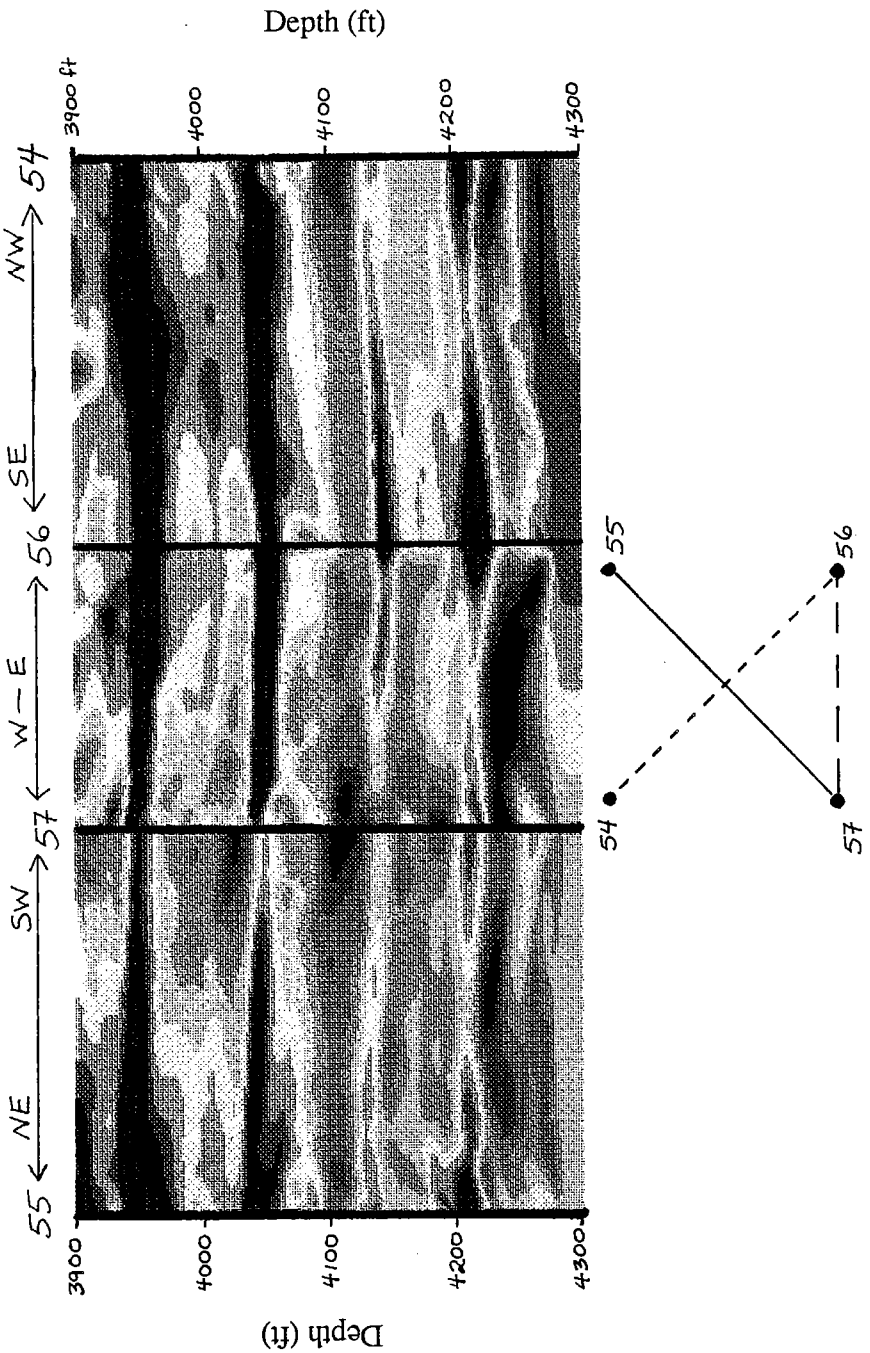

Figure 5: Slowness tomograms spliced together. Notice the SW-NE increase in slowness across the 5-spot, above 4100 feet in the tomograms. This might be explained by waterflooding effects on gas.

Gas cap above the payzone

Gas is known to exist above the payzone interval in this West Texas reservoir [Michael Stein, pers. comm., 1991]. The tomograms may be showing the effects of floodwater displacing this gas cap to the northeast. As before, water-saturated zones would show up in the tomograms having higher seismic velocities than gas-saturated zones.

FUTURE DIRECTIONS

The common receiver gather shown in Figure 2 shows several easily identified reflections. In addition, coherent S-wave arrivals are possibly visible. We see promise of extracting further information from these data.

We are planning to process these data further. Our plans are first to do reflection mapping [see Paper A in this volume], followed by reflection-constrained traveltime tomography, and finally use the results of this traveltime and reflection processing to do formation evaluation.

Although we see promise of extracting further information from these data, the vertical sampling interval (10 feet) creates spatial aliasing and difficulties with wavefield separation. In addition, the very wide-angle reflections (greater than 60°) at the top of the reservoir will create mapping complexities. Initial reflection mapping will aid us to design a more appropriate field experiment to incorporate reflection imaging with traveltime tomography at this West Texas site.

A critical need being addressed in the future is a better integration to the extensive core and log database available for the pilot site as well as an integrated interpretation using production and fluid flow data.

CONCLUSIONS

At this time, we cannot attach significance to an interpretation of lateral reservoir variations. The site has undergone significant fluid alteration due to waterflooding, WAG CO_2 injection, and continued waterflooding. A pervasive gas cap has existed in the area; so, our interpretation is complicated by the uncertain fluid dynamics of the five-spot region. We plan to map crosswell reflectors and upgrade the slowness image accordingly in order be able to give more significance and confidence to an interpretation. Further, we must work with a resident reservoir engineer in order to better understand the reservoir history and fluid distribution models acceptable for the five-spot region.

ACKNOWLEDGEMENTS

The authors are grateful to the Gas Research Institute (GRI), Amoco Production Company, Stanford University, and the Seismic Tomography Project industrial associates for their financial or in-kind support of this project.

REFERENCES

Zoback, M. L., and Zoback, M. D., 1980, State of stress in the conterminous United States: Journal of Geophysical Research, **85**, 6113-6156.

Zoback, M. L., and Zoback, M. D., 1989, Tectonic stress field of the continental United States, *in* Pakiser, L. C., and Mooney, W. D., Ed., Geophysical framework of the continental United States: Geological Society of America, Memoir 172, 523-539.

PAPER C

ANISOTROPIC TOMOGRAPHY

Reinaldo J. Michelena and Jerry M. Harris
Seismic Tomography Project

ABSTRACT

Tomographic estimation of velocities is usually performed by fitting picked traveltime data to a set of time/distance equations using a slowness function which is not dependent on angle. If the medium is assumed to be transversely isotropic with vertical symmetry axis, an elliptic form can be used to approximate the traveltime-distance relationship. When this relationship is used to fit the data, the result is two images representing the vertical and horizontal components of slowness. The inversion is a simple extension of the well known isotropic schemes and whether it is successful depends on the range of ray angles available. This is illustrated with synthetic and field-data examples.

INTRODUCTION

Depending on the degree of anisotropy of the medium and the seismic wavelengths used, the tomograms obtained from cross-well traveltime data assuming that the medium is isotropic may suffer from severe distortions. These distortions are analogous to the well known mispositions occurred in surface seismic when, in an anisotropic environment, the stacking velocity is used to control depth conversion. Eliminating these distortions is one reason to allow the model to be anisotropic in tomographic traveltime inversion. If we do that, we are not only solving an imaging problem. It is well known that anisotropy can be a useful tool for studying lithology and degree of stratification in sedimentary rocks and therefore, taking into account velocity anisotropy in tomographic traveltime inversion also helps to gain extra and useful information about the reservoir.

From surface seismic measurements, whether reflection or refraction, it is possible to obtain the horizontal component of the slowness. However, for estimating anisotropy, additional subsurface information (layer thicknesses or vertical slownesses) is required (Levin, 1978). For this reason, in recent studies where anisotropy has been quantified, either a different geometry like VSP has been used (Byun and Corrigan, 1990; White et al., 1983) or the surface seismic information has been combined with well-logs (Banik, 1984). However, based on the observation that velocity anisotropy does not affect P-wave moveout considerably, Winterstein (1986) estimated the required layer thicknesses using velocities obtained form P-wave velocity analysis and

then, from *SH*-wave velocity analysis, he was able to estimate velocity anisotropy. Dellinger (1989) concludes that because of the ill-conditioning of the problem, it is not possible to estimate with high accuracy a 2-D vector velocity field from VSP-like geometries.

From cross-well measurements, fewer attempts have been made to estimate velocity anisotropy. Karrenbach (1989) proposes a practical scheme for estimating velocity and Q in homogeneous transversely isotropic media, fitting elliptical curves to the dispersion relations. Cunha-Filho (1990) fits elliptical curves in layered models to cross-well traveltimes. Chapman and Pratt (1990) and Pratt and Chapman (1990) estimate velocity anisotropy in a general 2-D medium assuming, in contrast with the works of Karrenbach and Cunha-Filho, weak anisotropy. This allows the ray tracing to be performed in isotropic media.

The main difference between tomographic velocity estimation from surface measurements and cross-well measurements is that the former requires to know a priori the depths of the reflectors whereas the later does not. The only positions needed to estimate velocities from cross-well traveltimes are the source-receiver locations. When sources and receivers are located at depth, the cross-well configuration eliminates one non-linearity of the tomographic inversion of reflection traveltimes: unknown positions of reflectors. By eliminating this non-linearity, the estimation of other non-linear effects in the traveltimes, such as velocity anisotropy, should be simpler when cross-well traveltimes are used.

In this paper we present a tomographic technique to estimate velocity anisotropy if the medium is transversely isotropic with vertical symmetry axis. The technique presented here generalizes the idea of tomographic inversion in isotropic media (McMechan, 1983) where the model is discretized into orthogonal regions and the Jacobian is related to the intersection of the rays with all those regions. Instead of using a circular relationship between time and distance, we assume an elliptical relation. Both components of the slowness are estimated *simultaneously*, without using any additional information.

When fitting ellipses to the traveltimes we obtain: S_x and S_{znmo} (for cross-well geometries) and S_{xnmo} and S_z (for VSP-like geometries). In the previous notation, "*nmo*" highlights the slownesses poorly sampled by the corresponding recording geometry. These slownesses do not necessarily correspond to the true slownesses of the medium. However, they can be used to estimate the real slowness surface using an approximate expression derived by Muir (1990).

We study the effects of the limited view of the measurements (from cross-well geometries) in the estimation of both slowness components. We conclude that our technique is stable when used to invert 1-D (layered) models if the range of ray angles is "wide enough". In 2-D models, the estimation of lateral variations in the vertical component of the slowness is particularly difficult from cross-well geometries alone. Consequently, spatial variations in velocity anisotropy cannot be estimated at the same scale of variations in velocity.

The theory presented in the first part of the paper is illustrated with synthetic examples and applications to field data from a cross-well geometry.

FORWARD MODELING

We start by defining the equations needed to do the forward modeling step in the inversion algorithm. In an homogeneous transversely isotropic media, the traveltime between two different points separated by a distance $l = \sqrt{\Delta x^2 + \Delta z^2}$ can be expressed as

$$t = \sqrt{\Delta x^2 S_x^2 + \Delta z^2 S_z^2} \tag{1a}$$

or

$$t^2 = \Delta x^2 S_x^2 + \Delta z^2 S_z^2, \tag{1b}$$

where S_x and S_z are the horizontal and vertical slownesses respectively. Since the medium is homogeneous, the ray path is straight.

An heterogeneous medium can be approximated as a superposition of non-overlapping homogeneous regions. For this medium, the previous expression for the traveltime between two points can be easily generalized as follows:

$$\begin{aligned} t_i &= \sum_{j=1}^{N} \sqrt{\Delta x_{ij}^2 S_{x_j}^2 + \Delta z_{ij}^2 S_{z_j}^2} \qquad i = 1, ..., M, \\ &= \sum_{j=1}^{N} t_{ij} \end{aligned} \tag{2}$$

where t_{ij} is the traveltime of the i^{th} ray in the j^{th} cell and S_{x_j} and S_{z_j} are the horizontal and vertical slownesses respectively in that cell. Δx_{ij} and Δz_{ij} are the horizontal and vertical distances traveled by the i^{th} ray in each cell. If the slowness contrasts among adjacent cells are small, the ray paths can be approximated by straight lines. In equation (2), N is the total number of cells and M is the total number of traveltimes.

The slowness model can be seen as a vector $\boldsymbol{S}$ whose components contain the horizontal and vertical slownesses of each cell. This vector can be defined as follows:

$$S_i = S_{x_i} \tag{3a}$$

$$S_{i+N} = S_{z_i}. \tag{3b}$$

Then, the slowness vector $\boldsymbol{S}$ has the following form:

$$\boldsymbol{S} = (S_1, S_2, \ldots, S_N, S_{N+1}, S_{N+2}, S_{N+3}, \ldots, S_{2N})^T \tag{4}$$

where T means transpose. The first N components correspond to the horizontal slownesses of all the cells and the second N components correspond to the vertical slownesses. When the model is homogeneous, $\boldsymbol{S}$ is 2-dimensional and in general, for an heterogeneous model described by N cells, $\boldsymbol{S}$ is $2N$-dimensional. Figure 1 shows the vector $\boldsymbol{S}$ for the particular case of a layered medium.

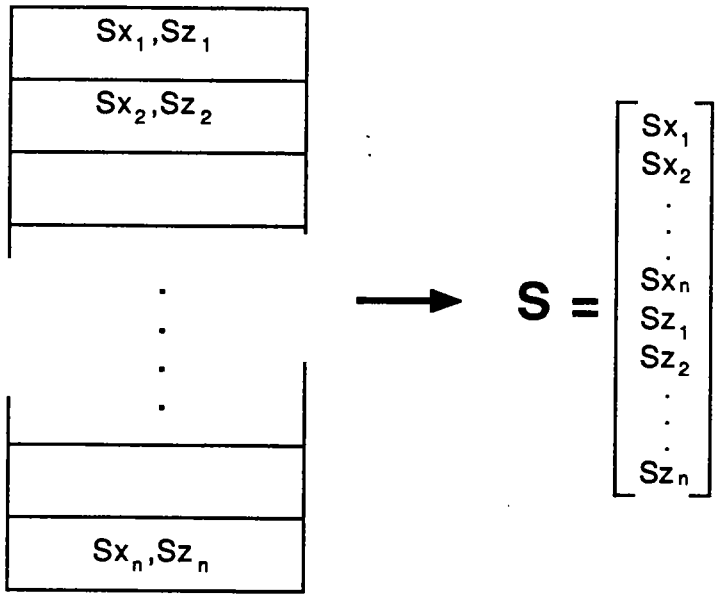

Figure 1: Slowness vector in a layered medium. (S-in-layers) [R]

Using the new variables introduced in (3), the traveltime equation (2) can be written as

$$t_i \;=\; t_i(\boldsymbol{S}) \;=\; \sum_{j=1}^{N} \sqrt{\Delta x_{ij}{}^2 S_j^2 + \Delta z_{ij}{}^2 S_{j+N}^2}. \tag{5}$$

Notice that when the medium is isotropic ($S_j = S_{j+N}$), equation (5) reduces to the familiar equation that approximates the traveltimes computed in an isotropic model described by cells (McMechan, 1983):

$$\begin{aligned} t_i \;&=\; \sum_{j=1}^{N} S_j \sqrt{\Delta x_{ij}{}^2 + \Delta z_{ij}{}^2} \\ &=\; \sum_{j=1}^{N} S_j l_{ij} \end{aligned} \tag{6}$$

where l_{ij} is the length of the i^{th} ray in the j^{th} cell.

In the next section we will see that when expression (5) is linearized, it can be used for estimating the horizontal and vertical slownesses in an heterogeneous anisotropic model given a set of traveltimes measurements from a cross-well configuration. Equation (5) can also be used for surface geometries, as long as the depths of the reflectors are known a priori.

INVERSE MODELING

As mentioned above, expression (5) will be used to estimate the $2N$-dimensional slowness vector $\boldsymbol{S}$ given the traveltimes from a cross-well experiment. However, we can investigate some of the difficulties in estimating such a vector by first studying the case of a homogeneous medium ($N = 1$)

When the model is isotropic, we usually estimate the slowness S of the homogeneous medium that best fits the traveltimes by simply averaging all the slownesses S_i obtained from the individual rays:

$$S = \frac{1}{M}\sum_{i=1}^{M} S_i = \frac{1}{M}\sum_{i=1}^{M} \frac{t_i}{l_i}, \tag{7}$$

where l_i is the source-receiver distance and M the total number of traveltimes.

When the model is anisotropic, the 2-D vector $\boldsymbol{S}$ that best fit the traveltimes can be obtained by generalizing the average (7). This generalization is, as expected, in a least-squares sense. Note that expression (1b) is linear in S_x^2 and S_z^2. Therefore, for a given set of traveltimes and source-receiver locations, it is possible to set up a least-squares problem to find the vector $\boldsymbol{S}$ of the homogeneous medium. Defining $W_x = S_x^2$ and $W_z = S_z^2$, the least-squares problem is

$$\underset{\sim}{\mathbf{M}} \begin{pmatrix} W_x \\ W_z \end{pmatrix} = \boldsymbol{d}, \tag{8}$$

where

$$\underset{\sim}{\mathbf{M}} = \begin{pmatrix} {\Delta x_1}^2 & {\Delta z_1}^2 \\ {\Delta x_2}^2 & {\Delta z_2}^2 \\ \vdots & \vdots \\ {\Delta x_M}^2 & {\Delta z_M}^2 \end{pmatrix},$$

and

$$\boldsymbol{d} = \begin{pmatrix} t_1^2 \\ t_2^2 \\ \vdots \\ t_M^2 \end{pmatrix}.$$

Equation (8) can be solved in different ways. The most popular approach is by using the normal equations, resulting

$$\begin{pmatrix} W_x \\ W_z \end{pmatrix} = (\underset{\sim}{\mathbf{M}}^T \underset{\sim}{\mathbf{M}})^{-1} \underset{\sim}{\mathbf{M}}^T \boldsymbol{d}. \tag{9}$$

However, the normal equations may have undesirable features with respect to numerical stability because the condition number of $\underset{\sim}{\mathbf{M}}^T\underset{\sim}{\mathbf{M}}$ is the square of the condition number of $\underset{\sim}{\mathbf{M}}$. If $\underset{\sim}{\mathbf{M}}$ is only moderately ill-conditioned, $\underset{\sim}{\mathbf{M}}^T\underset{\sim}{\mathbf{M}}$ is severely ill-conditioned. For this reason, methods that do not amplify the condition number

of $\underset{\sim}{\mathbf{M}}$ should be used to solve systems like (8) (for example QR factorization, Gill at al., 1990).

For estimating W_x and W_z *simultaneously* and *accurately*, $\underset{\sim}{\mathbf{M}}$ has to be well conditioned. Note that this is not the case when most of the elements of the matrix satisfy either $\Delta x_i^2 \gg \Delta z_i^2$ or $\Delta z_i^2 \gg \Delta x_i^2$. These two conditions describe cases when rays are traveling close to the horizontal or the vertical. In such cases, it is impossible to determine simultaneously both components of the vector $\boldsymbol{S}$ because of the limited view of the measurements translates immediately into severe ill-conditioning. This can be understood by trying to estimate W_x and W_z from the simple cross-well experiment shown in Figure 2, where $\Delta x^2 \gg \Delta z_i^2$. In this case

$$\underset{\sim}{\mathbf{M}} = \begin{pmatrix} \Delta x^2 & \Delta z_1^2 \\ \Delta x^2 & \Delta z_2^2 \end{pmatrix}.$$

The eigenvalues of this matrix are

$$\lambda_{\pm} = \frac{\Delta x^2 + \Delta z_2^2 \pm \sqrt{(\Delta x^2 - \Delta z_2^2)^2 + 4\Delta x^2 \Delta z_1^2}}{2}.$$

Because $\Delta x^2 \gg \Delta z_i^2$, the eigenvalues are approximately

$$\lambda_+ = \Delta x^2$$
$$\lambda_- = 0.$$

In other words, the smallest eigenvalue (zero in this case) is related to the vertical component of the slowness whereas the largest one is related to the horizontal component. On the contrary, for a VSP-like geometry largest eigenvalue is related to S_z and the smallest one is related to S_x (Dellinger, 1989). Having more rays (M) without increasing the aperture does not solve the problem. In such a case, the largest eigenvalue of the matrix ($\underset{\sim}{\mathbf{M}}^T \underset{\sim}{\mathbf{M}}$) tends to $\sum_{i=1}^{M} \Delta x_i^4$ and the smallest one tends to zero again.

The previous inversion scheme for homogeneous models can be generalized for estimating $\boldsymbol{S}$ in an heterogeneous medium. All we have to do is to solve systems of equations like (8) at each cell. In other words, the problem in the heterogeneous model is separated into many subproblems in homogeneous models. This approach might be easily implemented when the ray paths are used as basis functions for describing the slowness (Harris et al., 1990a) if, instead of averaging the slownesses of the different rays where they intersect, system of equations like (8) are solved to estimate the two components of the slowness.

Although this idea will not be exploited in the present paper, it can help us to understand *intuitively* which components of the slowness vector $\boldsymbol{S}$ are easier (or more difficult) to estimate from cross-well traveltimes measurements. In general, vertical variations in the medium are easier to estimate than horizontal variations. Vertical variations correspond to singular vectors associated with the largest singular values

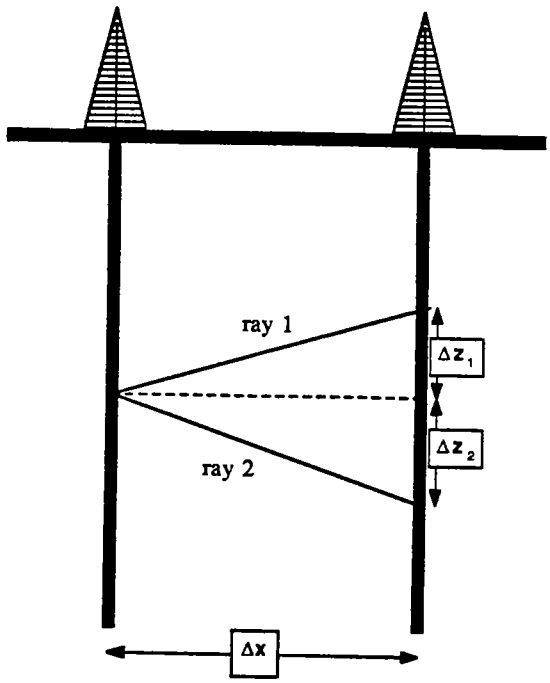

Figure 2: Cross-well experiment with two rays. (experiment) [R]

of the problem whereas lateral variations are associated to the smallest singular values (Pratt and Chapman, 1990). As explained earlier, in homogeneous models S_x is related to the larger singular value and S_z is related to the smaller one. Therefore, if the problem in a heterogeneous model is solved as many separate subproblems in homogeneous models, the largest singular values will be related to vertical variations in S_x and the smallest ones will be related to lateral variations in S_z. We will demonstrate in the field data example that estimating horizontal variations in S_z is indeed a difficult problem whereas it is always easier to estimate vertical variations in S_x.

Equation (5) can be used to estimate $\boldsymbol{S}$ for *all* the cells at the same time (rather than in a cell-by-cell basis, as explained before). This equation is obviously non-linear in S_j and S_{j+N}. One way to solve the problem is by a sequence of linearized steps. We start by approximating (5) by a first order Taylor series expansion centered in a given model $\boldsymbol{S}_o$:

$$\begin{aligned} t_i(\boldsymbol{S}) &\approx t_i(\boldsymbol{S}_o) + \nabla t_i(\boldsymbol{S}_o) \cdot (\boldsymbol{S} - \boldsymbol{S}_o) \\ &= t_i(\boldsymbol{S}_o) + \sum_{j=1}^{N} \underset{\sim}{\mathbf{J}}_{ij} (S_j - S_{0j}) \end{aligned} \tag{10}$$

where the elements of the Jacobian $\underset{\sim}{\mathbf{J}}_{ij}$ are

$$\underset{\sim}{\mathbf{J}}_{ij} = \frac{\partial t_{ij}(\boldsymbol{S}_o)}{\partial S_j} = \begin{cases} \frac{\Delta x_{ij}^2 S_{0j}}{t_{ij}} & \text{if } 1 \leq j \leq N \\ \frac{\Delta z_{ij}^2 S_{0j}}{t_{ij}} & \text{if } N+1 \leq j \leq 2N \end{cases}$$

and t_{ij} is the traveltime of the i^{th} ray in the j^{th} cell of the model $\boldsymbol{S}_o$ (equation (2)). If we assume that $t_i(\boldsymbol{S})$ represents one component of the vector of measured traveltimes, we can compute the perturbations $\Delta \boldsymbol{S}_j = (S_j - S_{oj})$ once the traveltimes in the reference model $\boldsymbol{S}_o$ has been calculated. The perturbation $\Delta \boldsymbol{S} = (\boldsymbol{S} - \boldsymbol{S}_o)$ is the solution of the following system of equations

$$\underset{\sim}{\mathbf{J}}\, \Delta \boldsymbol{S} = \Delta \boldsymbol{t} \tag{11}$$

where $\Delta \boldsymbol{t}_i = t_i(\boldsymbol{S}) - t_i(\boldsymbol{S}_o)$.

Note that the matrix $\underset{\sim}{\mathbf{J}}$ depends *explicitly* on the slowness of the reference model $\boldsymbol{S}_o$ in contrast with the isotropic case where the matrix depends only on the lengths of the rays in each pixel. In the isotropic case if the rays are straight, the estimation of the slowness becomes a linear problem because $\underset{\sim}{\mathbf{J}}$ is a constant. In the anisotropic case, however, the problem is still non-linear even if the rays are straight. Ray bending introduces another source of non-linearity.

In the examples shown later, equation (11) will be solved using the LSQR variant of the conjugate gradients algorithm (Nolet, 1987). We will show that by doing a few iterations with this method at each linearized step, the ill-conditioning of $\underset{\sim}{\mathbf{J}}$ caused by the limited view of the measurements is better handled than by solving the normal equations (in the overdetermined case).

Meaning of the Results

Isotropic tomography fits circles ($t^2 = (x^2 + z^2)S^2$) to the data. Anisotropic tomography fits ellipses ($t^2 = x^2 S_x^2 + z^2 S_z^2$). Depending on the range of ray angles available (or the geometry used) and the wave type under consideration, the estimated slownesses S_x and S_z may or may not correspond to the real slownesses of the medium.

Horizontal or near horizontal rays are typical of a cross-well geometry. These rays sample a portion of the slowness surface close to the horizontal and for this reason the estimated S_x corresponds to the real horizontal slowness. On the contrary, S_z is not sampled by cross-well geometries. The inversion gives the vertical slowness of the best fitting ellipse (S_{znmo}) which coincides with the real vertical slowness only if the wave type considered is SH. However, we can generally expect S_{znmo} to be closer than S to the real vertical slowness. This will be illustrated later with field data by comparing S, S_x and S_{znmo} with sonic logs.

Vertical or near vertical rays are typical of a VSP-like geometry. From this type of geometry we can get S_{xnmo} and S_z. These two slownesses plus S_x and S_{znmo} obtained

from cross-well geometries can be used to estimate the real slowness surface of the medium $S(\phi)$ using the following approximate expression (Muir, 1990):

$$S(\phi) = \frac{M_x^3 c^6 + M_x x^2 (2M_z + M_{znmo}) c^4 s^2 + (2M_x + M_{xnmo}) c^2 s^4 + M_z^3 s^6}{(M_x c^2 + M_z s^2)^2}$$

where

$$\begin{aligned} M_x &= S_x^{-2} \\ M_z &= S_z^{-2} \\ M_{xnmo} &= S_{xnmo}^{-2} \\ M_{znmo} &= S_{znmo}^{-2} \\ c &= cos(\phi) \\ s &= sin(\phi) \\ \phi &= \text{angle from the horizontal.} \end{aligned}$$

This expression is called the double elliptic approximation. Dellinger and Muir (1991) demonstrate that this approximation accurately fits general transversely isotropic media.

In the cross-well geometry examples that follow, the estimated vertical slowness will be referred to as S_z rather than S_{znmo}.

SYNTHETIC EXAMPLES

1-D Inversion

In this section, we will apply the previous technique to the inversion of traveltimes for a cross-well geometry. Synthetic data were generated through the 1-D isotropic model shown in Figure 3, using a geometry of 17 sources and 17 receivers equally spaced at the source and receiver well respectively. If we plot the components of the slowness vector $\boldsymbol{S}$ (equation(4)) for this model, we obtain the profile shown at the right hand side of Figure 3. Both slowness components are identical because the model is isotropic. In this example, the slowness contrast between the background and the anomalous layer is small (1%) and therefore, the propagation of the energy can be safely modeled by straight ray paths.

We can constrain the inversion by allowing only vertical variations in the model if it is know a priori that the medium is layered. Doing this we eliminate instabilities and non-uniqueness in the inversion associated with lateral variations, remaining only those associated with the vertical component of the slowness, which is not sampled propperly by the recording geometry.

The image area was divided into 100 layers of equal thickness (8 ft). The inversion process has to estimate 200 parameters from 289 traveltimes. Figure 4 shows the

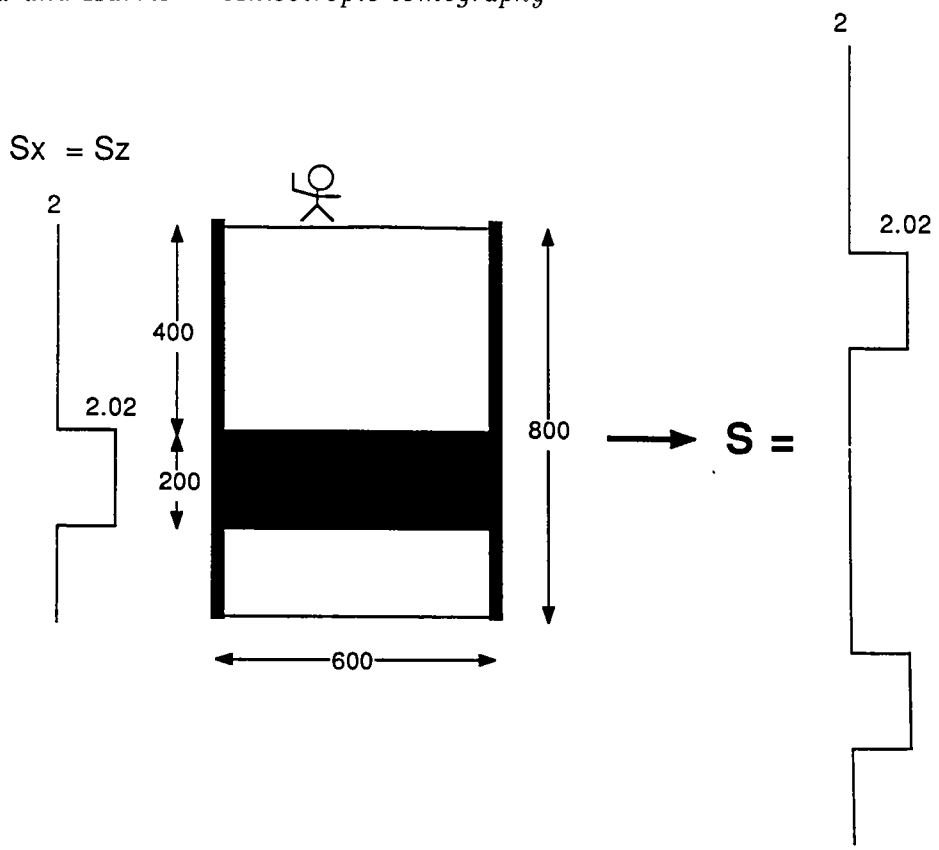

Figure 3: Synthetic isotropic model used to test the algorithm. At the right, it is shown the slowness vector S that describes this model. (syn-model) [R]

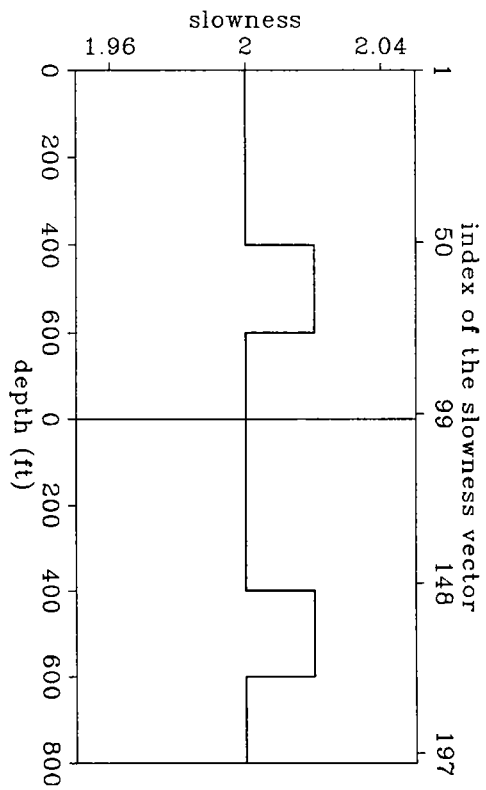

Figure 4: Result of the inversion of the synthetic data generated through the model shown in Figure 3. (1d-synthetic) [NR]

slowness vector obtained after 60 conjugate gradients (CG) iterations. There is no difference between the given S (Figure 3) and the estimated one (Figure 4). Note also that the results can be represented as a function of depth as well as a function of the index of the slowness vector. In the two next results the depth axis will be omitted.

Figure 5 shows the convergence toward the result as a function of the CG-iterations. The result shown in Figure 4 correspond in Figure 5 to 60 CG-iterations in the axis *number of iterations*. The two "hills" represent the slowness at the anomalous layer. We say that convergence has been achieved when the top and the bottom of the hills are flat. Note that the horizontal component of the slowness converges faster than the vertical component. This is because in the given model, the horizontal component of the slowness in the anomalous layer is better sampled than the vertical component: the range of ray angles (absolute values) is from 0 to 53 degrees ($53 \approx \arctan(\frac{800}{600})$) which is a typical range for cross-well experiments.

If the same geometry is used to generate synthetic data through the model shown at the top of Figure 6 (were the well to well separation has been decreased), we obtain that both components converge at the same rate. This is because the vertical component of the slowness is better sampled than before: the range of ray angles varies between 0 and 76 degrees ($76 \approx \arctan(\frac{800}{200})$).

The previous results tell us that if it is not possible to perform "enough" iterations in order to reach the flat top of both hills (Figures 5 and 6), we may wrongly conclude that the medium is anisotropic. What is really happening is that the components of the slowness vector do not converge at the same rate. Severe limited view problems as well as low signal to noise ratio are some reasons that may limit the amount of CG-iterations that can be performed before the ill-conditioning of the problem starts playing any role.

2-D Inversion

To test the performance of the algorithm in inverting data generated in a 2-D medium, we computed synthetic traveltimes through the isotropic model shown in Figure 7. The separation between contiguous sources and receivers is 10 ft and for each receiver gather, only sources located at ± 50 degrees are used. With a geometry like this, we pretend to simulate the geometry of the real data example to be analyzed later. As in the 1-D example, the slowness contrast between the anomaly and the background is small (5%), and therefore, straight rays can be used again.

The unknown model was discretized in 241 x 46 pixels (5 ft^2) and therefore, the inversion has to estimate 241 x 46 x 2 parameters from 2200 synthetic traveltimes. Figure 8 shows the results of the inversion. The slowness of the isotropic circular anomaly (1.05) is better estimated by the horizontal than by the vertical component of the slowness. Remember that this is not the case in the 1-D inversion, where both slowness components can be perfectly recovered even thought the vertical component of the slowness is not properly sampled. The extra information introduced in that

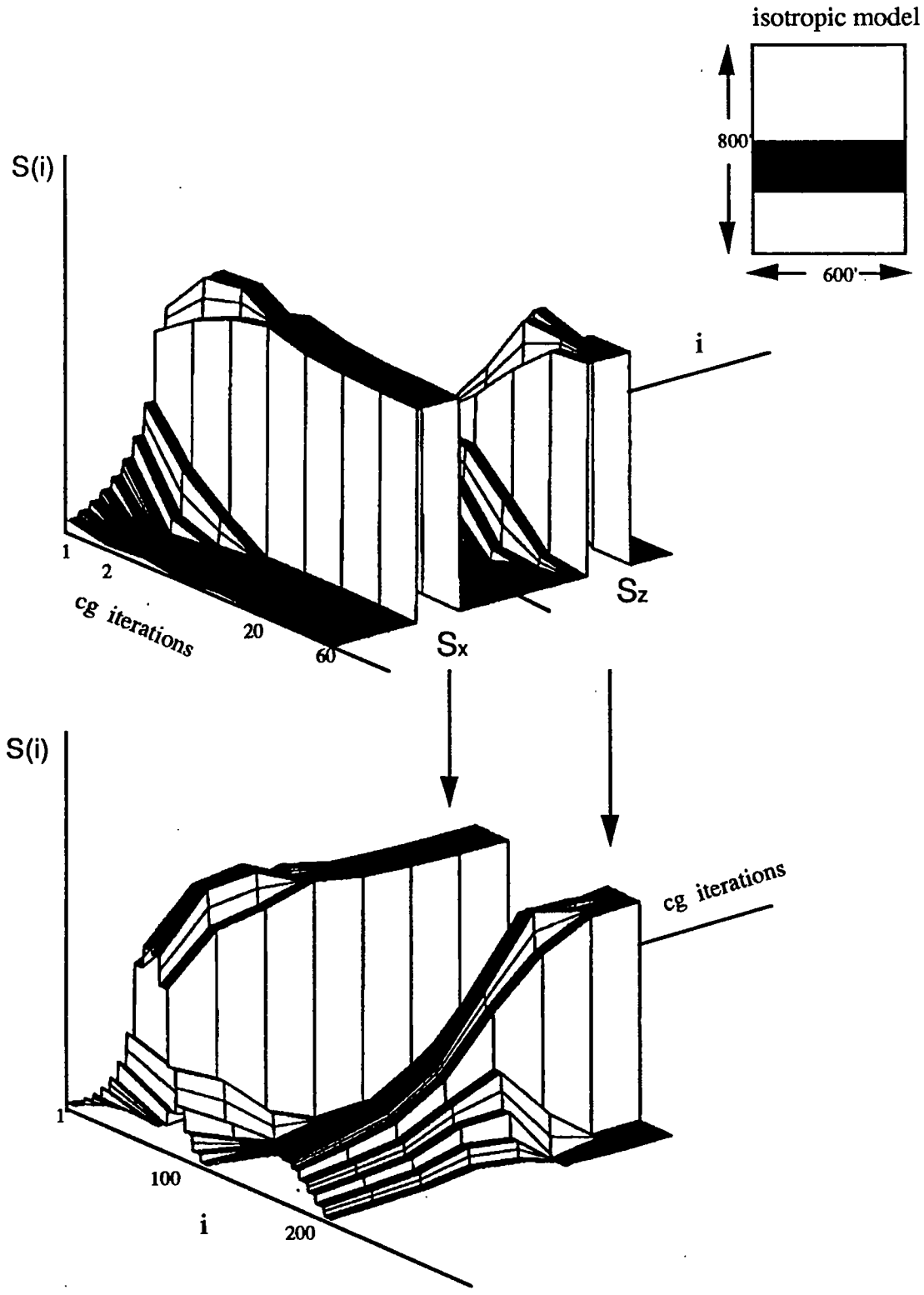

Figure 5: Variations of the slowness vector as a function of the number of conjugate gradient iterations. The original model is shown at the top. The axes "i" and "CG iterations" have been interchanged from one plot to the other. (cg-600x800) [R]

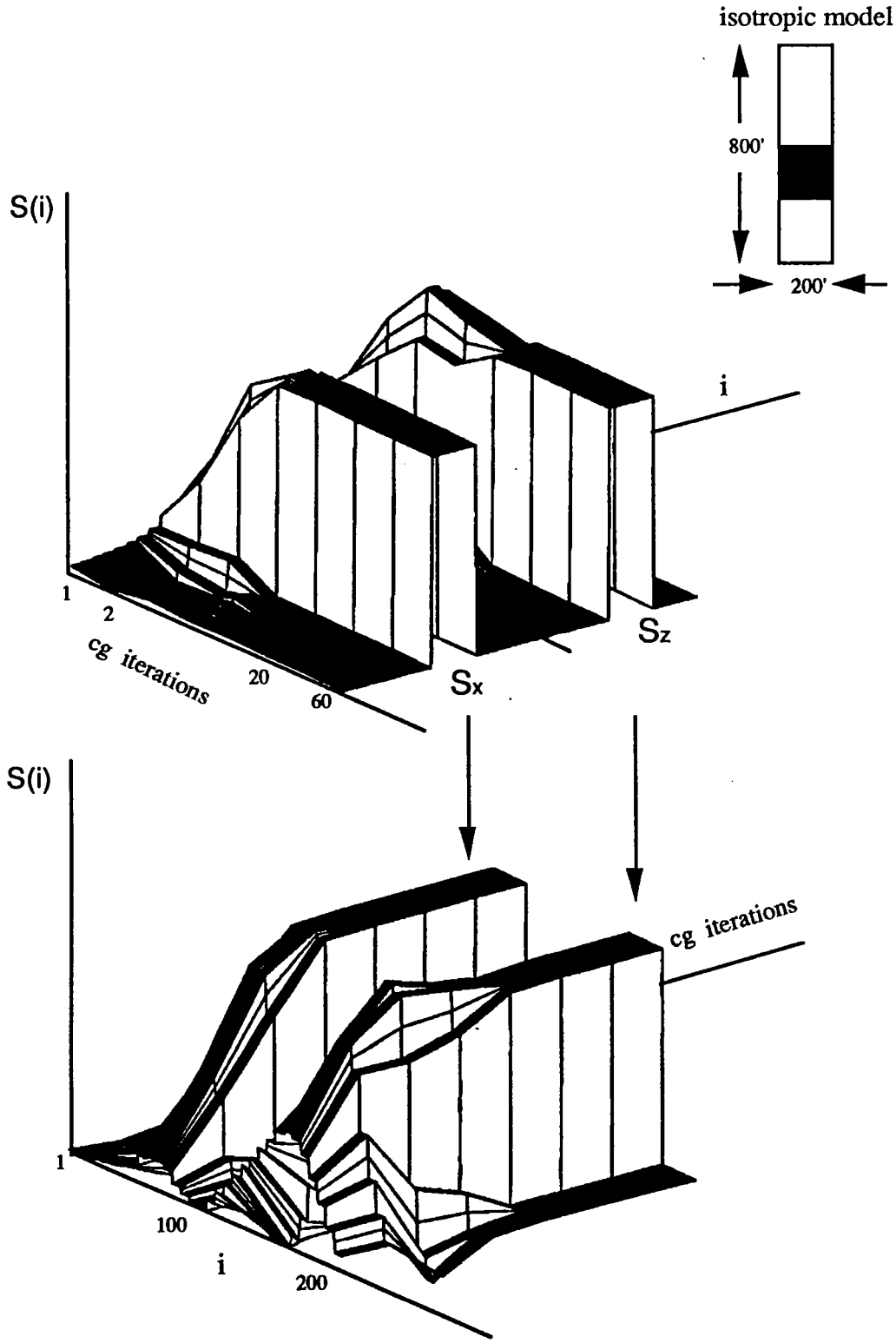

Figure 6: Variations of the slowness vector as a function of the number of conjugate gradient iterations. The only difference between the model shown at the top and the model of Figure 3 is in the horizontal dimension. The axes "*i*" and "CG iterations" have been interchanged from one plot to the other. (cg-200x800) [R]

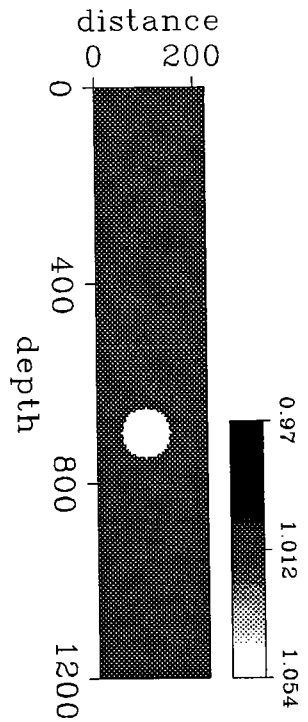

Figure 7: Isotropic slowness model. The radius of the circular anomaly is $r = 50$ and is centered at $(100, 700)$. The background slowness is 1.0 and the slowness of the disc is 1.05. (s-model-test) [NR]

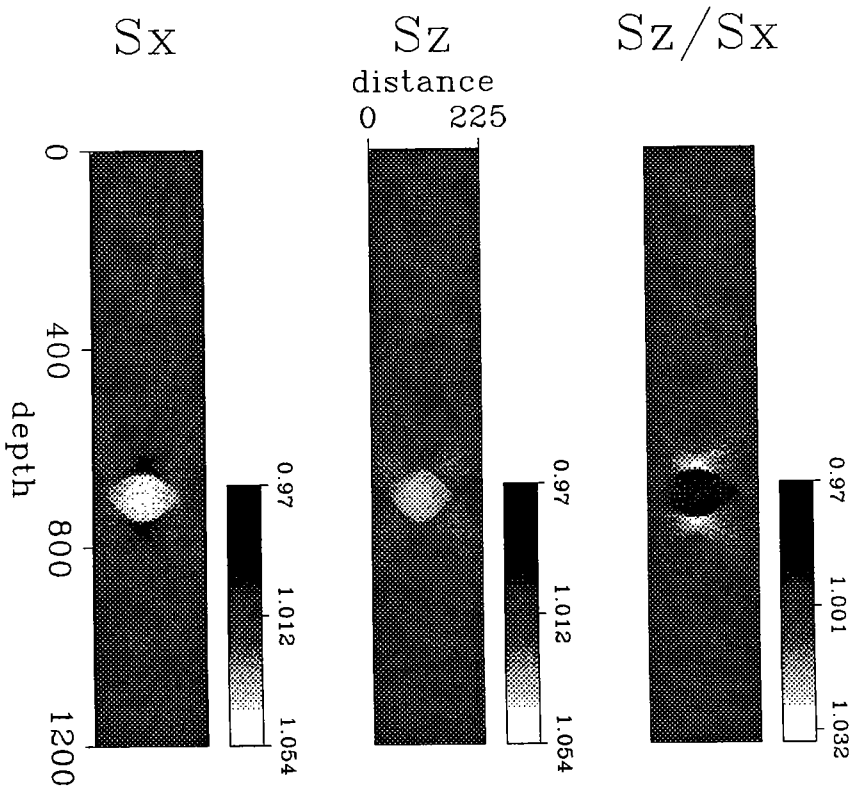

Figure 8: Reconstructed horizontal and vertical component of the slowness. The ratio of the two components is shown at the right. (sx2d-test) [NR]

problem by assuming that the model is layered compensates for the limited view of the measurements. In the 2-D inversion, where the unknown is less constrained, the better sampling of the horizontal component translates into a better recovery of that component and as a result, some artificial anisotropy is introduced by the reconstruction. In this noise-free example such an anisotropy is not greater than 3% as shown in Figure 8 by the ratio $\frac{S_z}{S_x}$. Doing more CG-iterations does not help to reduce this artificial anisotropy to zero, like in the 1-D inversion (Figures 5 and 6). In the present case the images didn't change after 120-CG iterations.

The artifacts in both slowness components are similar to the well known truncation artifacts in isotropic inversion although they are different from one component to the other. The estimated S_x is smeared along the horizontal direction whereas S_z is not. This is because the estimation of S_z is not affected by rays that travel horizontally. The different character of the artifacts for each slowness component can limit our ability to recover variations in anisotropy at the same scale of variations in velocity when data from only one geometry is used. This will be clearly observed later in the application to field data.

FIELD DATA EXAMPLE

Anisotropic tomography was performed using a field data set. This data set was acquired jointly by Amoco and Stanford University at the Gulf Coast, on shore, in Southeast Texas. The overall survey geometry is illustrated in Figure 9, and it is similar to the one used in the synthetic example of 2-D inversion. More details about the site and geometry are found in Harris et al. (1990b).

Nearly 5000 P-wave first arrival times were picked from the data. In general, we found that the traveltimes corresponding to the near horizontal rays (near offsets) were more difficult to pick than those at far offsets.

Well Deviation

In this particular geometry, the wells are not confined to a single plane. Instead, they deviate gradually form the vertical plane that contains both wells at the near surface. We have taken this effect into account following this two-steps procedure:

- Find the true 3-D distances between sources and receivers.
- Assume that one well is vertical (for example, the source well) and locate the receivers at the corresponding real distances and real depths in the other well. This is equivalent to locate the origin of the coordinates to measure the distances always at the source well.

When correcting for the well deviation in this way, true source-receiver separations are used in the inversion. The relative position of the two wells after considering the

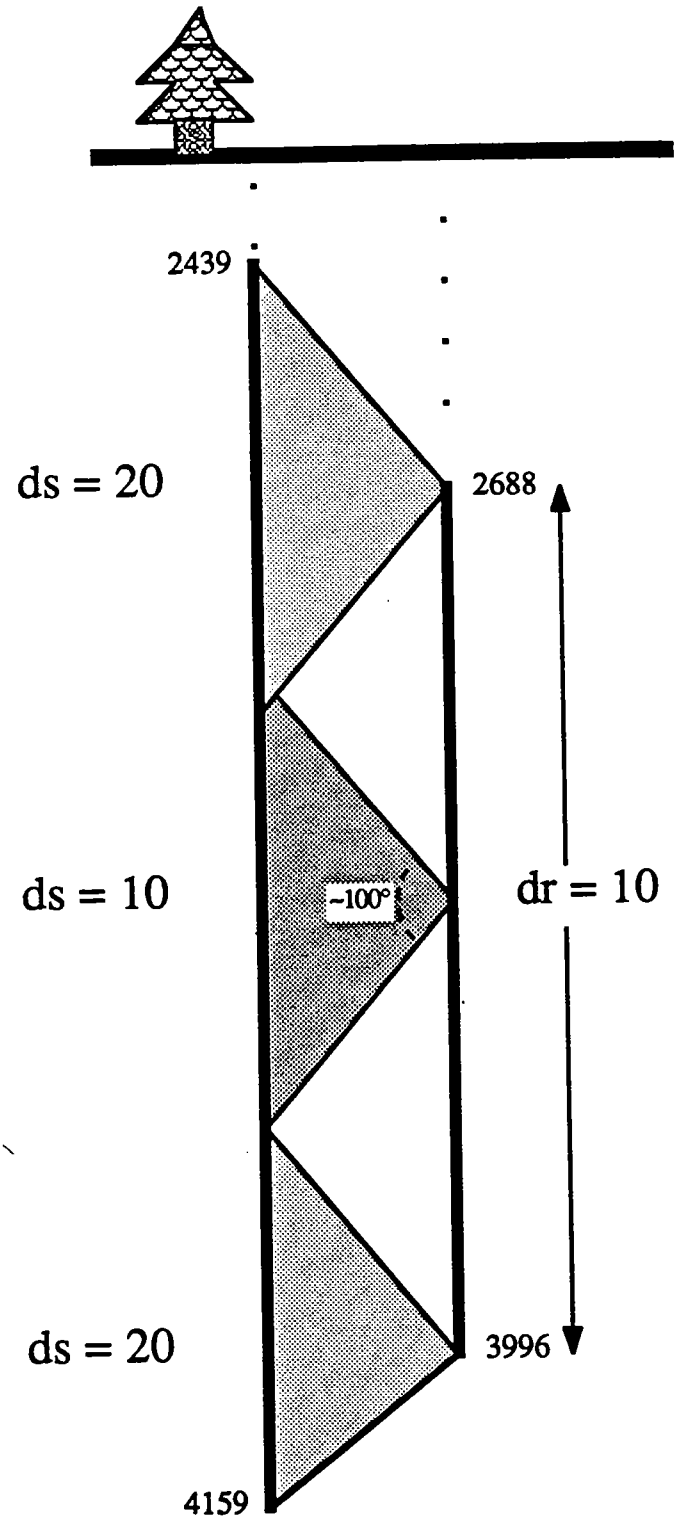

Figure 9: Overall survey geometry illustrating the shooting pattern. Receivers are spaced at $dr = 10$ ft between 2688 and 3996 ft Sources are spaced at $ds = 10$ ft interval in primary target zone and $ds = 20$ ft. above and bellow the target zone. The average separation between wells is 225 ft. (geometry) [R]

deviation is shown in Figure 10. To use the true distances, it is necessary to move the receivers positions horizontally in the deviated well. This is way the receiver positions in Figure 10 look like horizontally smeared. The selection of the vertical well used as a reference to measure the relative deviations is irrelevant if we assume that the model is 1-D. In 2-D somewhat different distorsions may occur depending on which well is chosen as a reference.

1-D Inversion

The simplest inversion that we can possibly do is assuming that the medium is homogeneous isotropic. What we obtain is the mean velocity (equation (7)), in this case $V_{iso} = 8452$ ft/sec. The next step is to assume that the model is still homogeneous but elliptically anisotropic. Using equation (8) we find that $V_x = 8586$ ft/sec and $V_z = 8079$ ft/sec. Notice that for this particular recording geometry (Figure 9), V_{iso} is closer to V_x than to V_z, which means that the "averaging" of the horizontal and vertical directions that the isotropic inversion implicitly does is not a simple arithmetic average. When the model is also heterogeneous, the same conclusion may be drawn as it will be show later.

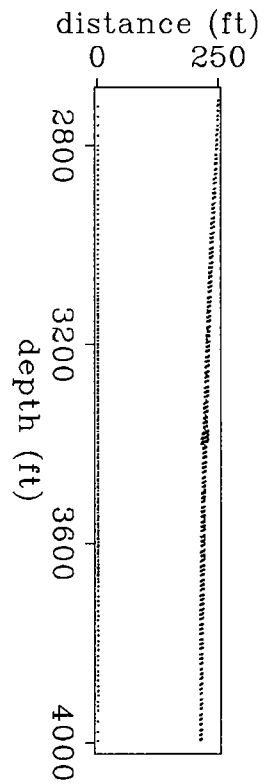

Figure 10: Positions of the source and receiver wells after considering their relative deviations. Each dot represents a source or a receiver position (left and right respectively). Note that the density of sources is larger at the middle of the surveyed area than in the extremes. (deviation) [NR]

To measure the goodness of the fit between measured and calculated traveltimes, we use the mean-absolute value of the mismatch

$$error = \frac{1}{M}\sum_{i=1}^{M}|t_{c_i} - t_{r_i}|, \tag{12}$$

where t_{r_i} and t_{c_i} are the measured and calculated traveltimes respectively and M is the total number of traveltimes.

When the estimated V_{iso} in the homogeneous model is used to compute synthetic traveltimes, $error$ = 1.04 ms. When the model is homogeneous anisotropic, $error$ = 0.94 ms.

The result of the isotropic inversion assuming a layered medium is shown in Figure 11. Only traveltimes corresponding to rays below 2705 ft and above 4000 ft were used. This depth interval was discretized in 60 horizontal layers of equal thickness (21.583 ft). Straight rays were used to compute synthetic traveltimes since small velocity variations are expected in this site (Harris et al., 1990b). Conjugate gradients iterations (40) were performed until no appreciable changes were seen neither in the model nor in the mean-absolute value of the error (equation (12)). This corresponds to reaching the flat part of the hills in Figure (5). For the model shown in Figure 11, $error$ = 0.67 ms.

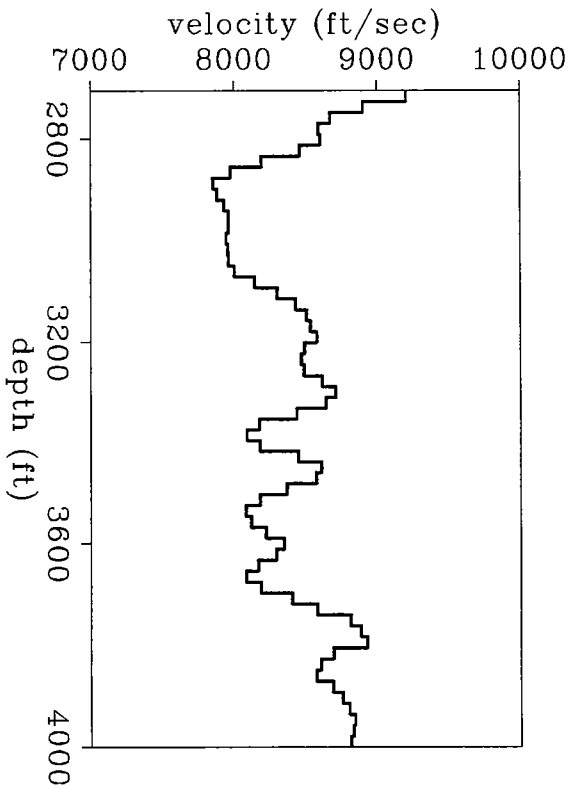

Figure 11: Result of the isotropic layered inversion. The thickness of each layer is 21.583 ft (Isos) [NR]

Now, we allow the model to be anisotropic. The result of the inversion is shown in Figure 12. For traveltimes computed through this model, *error* = 0.59 ms. The thick curve represents the horizontal velocity and the thin one represents the vertical velocity. The first thing we notice is that as expected V_x is generally larger than V_z. Figure 13 compares V_x and V_z with V_{iso}. In general, V_{iso} is closer to V_x than it is to V_z, which is consistent with the previous the results of the inversion assuming an homogeneous medium. This means that for the type of recording geometry used (ray angles between 0 and ±50 degrees) the isotropic inversion is affected primarily by the horizontal component of the velocity. Since there are fewer rays at large angles, the isotropic inversion is less constrained by them. However, rays at large angles contain independent information that might be important to improve horizontal resolution in 2-D models.

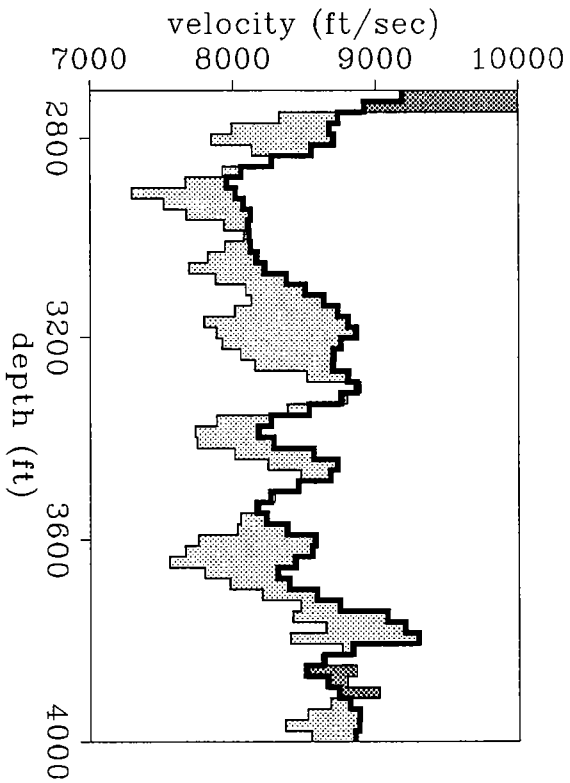

Figure 12: Result of the anisotropic layered inversion. The thickness of each layer in 21.583 ft The differences between V_x (thick line) and V_z (thin line) are represented by two colors: light gray, when $V_x > V_z$ and dark gray when $V_x < V_z$. (Anisxsz) [NR]

Sonic logs were available in this site at both wells (Figure 14). They sample the vertical velocity about the well at frequencies ($\sim$ 10 kHz) much larger than the typical frequency of the cross-well data ($\sim$ 1 kHz). To compare the information obtained from this two types of measurements (1-D tomogram and velocity logs), we did some averaging to the logs. First, we averaged each slowness log in blocks of equal thickness and equal to the layer thickness in the 1-D tomographic inversion. Secondly, the two averaged slowness logs were averaged again into a single one. The purpose of the last averaging was to simulate the horizontal averaging that the 1-D

tomographic inversion implicitly does. Figure 15 compares the average velocity log with V_{iso}, V_x and V_z. Note that V_z is not only much closer to the average velocity log (as expected) but also better correlated with it, when compared with V_{iso} and V_x.

The ratio V_x/V_z is a lithologic indicator as shown in Figure 16. In this figure, the thick line corresponds to the ratio V_x/V_z and the thin one corresponds to the average spontaneous potential (SP) log. The average SP log was obtained by blocking each log separately, taking the average of the results and removing a linear trend with depth in the final average. Notice the good correlation between large SP values (shales) and large anisotropy ratio. The same for low SP values (sands) and isotropic layers. The differences between the shape of the two curves are because 2D-variations in the true medium are averaged out in the 1-D inversion as well as in the average SP log. The 2D nature of the true medium will be seen clearly later when performing 2D inversion.

In the anisotropic inversion, we found that for this particular data set 60 layers of 21.583 ft each was a good compromise between resolution and stability. Reducing the layer thickness by half has the effect (not shown) of increasing the resolution at the expense of large variations and instabilities in the vertical component of the velocity that is not well sampled by the recording geometry. The horizontal component of

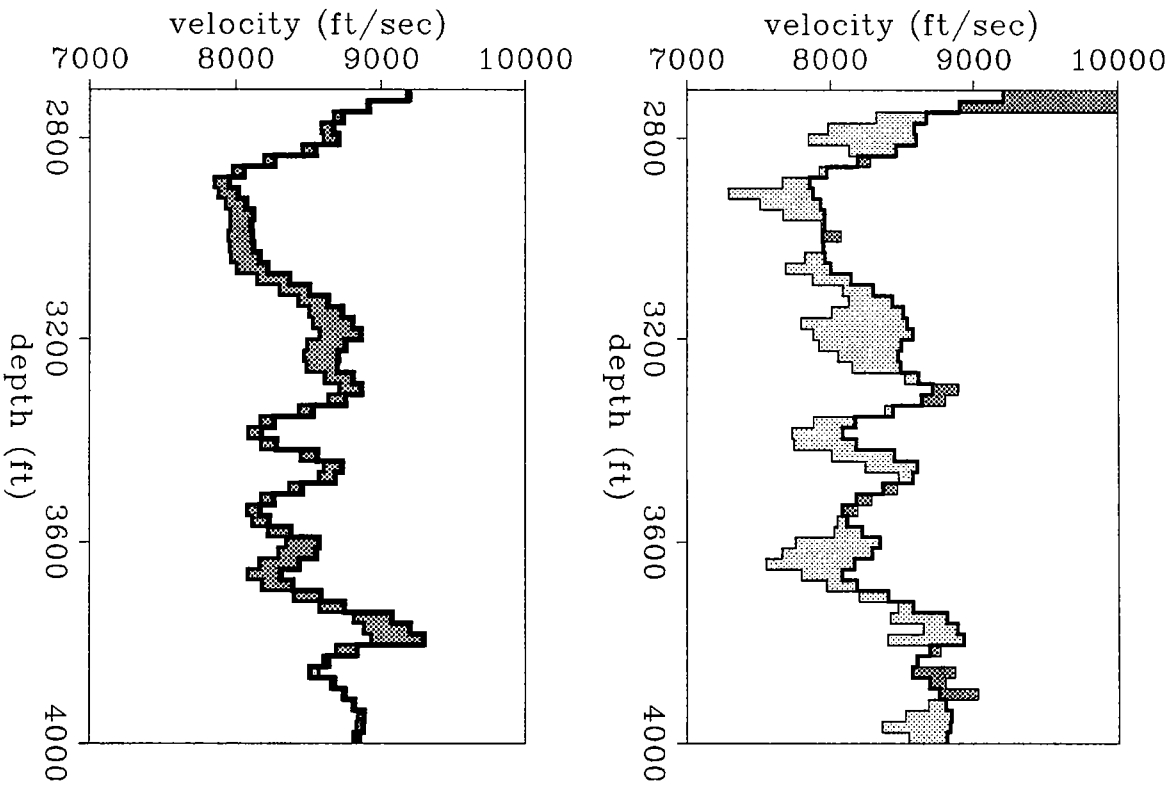

Figure 13: Comparison between isotropic and anisotropic layered inversion. Left: V_{iso} (thin line) and and V_x (thick line). Right: V_{iso} (thick line) and V_z (thin line). The differences between the isotropic and anisotropic inversion are represented by two colors: light gray when $V_{iso} > V_x$ or V_z, and dark gray when $V_{iso} < V_x$ or V_z. (IsosAnisxsz) [NR]

velocity is generally more stable than the vertical for smaller layer thicknesses. Obviously, increasing the layer thickness made the inversion more stable at the expense of less resolution.

2-D Inversion

When the problem is linear we should obtain the model that "best" fit the data in only one iteration. When the problem is non-linear one approach is to solve it as a sequence of linearized steps. We usually call these steps *external* iterations, to differentiate them from the *internal* iterations needed to solve each linear problem when using iterative techniques such as conjugate gradients. Ideally, if the problem has n unknowns, each external iteration should consists of m CG-steps (m internal iterations), where $m \leq n$ is the number of different singular values. When dealing with field data, however, we might not be able to do this because of the presence of the noise. Noise can affect the solution of each linearized problem in the following ways: (a) It might be amplified in the model by the smallest singular values recovered when m iterations are performed, (b) It might affect considerably the accuracy of the search directions and consequently, the position of the minimum associated with the solution. Therefore, we have to deal carefully with the noise.

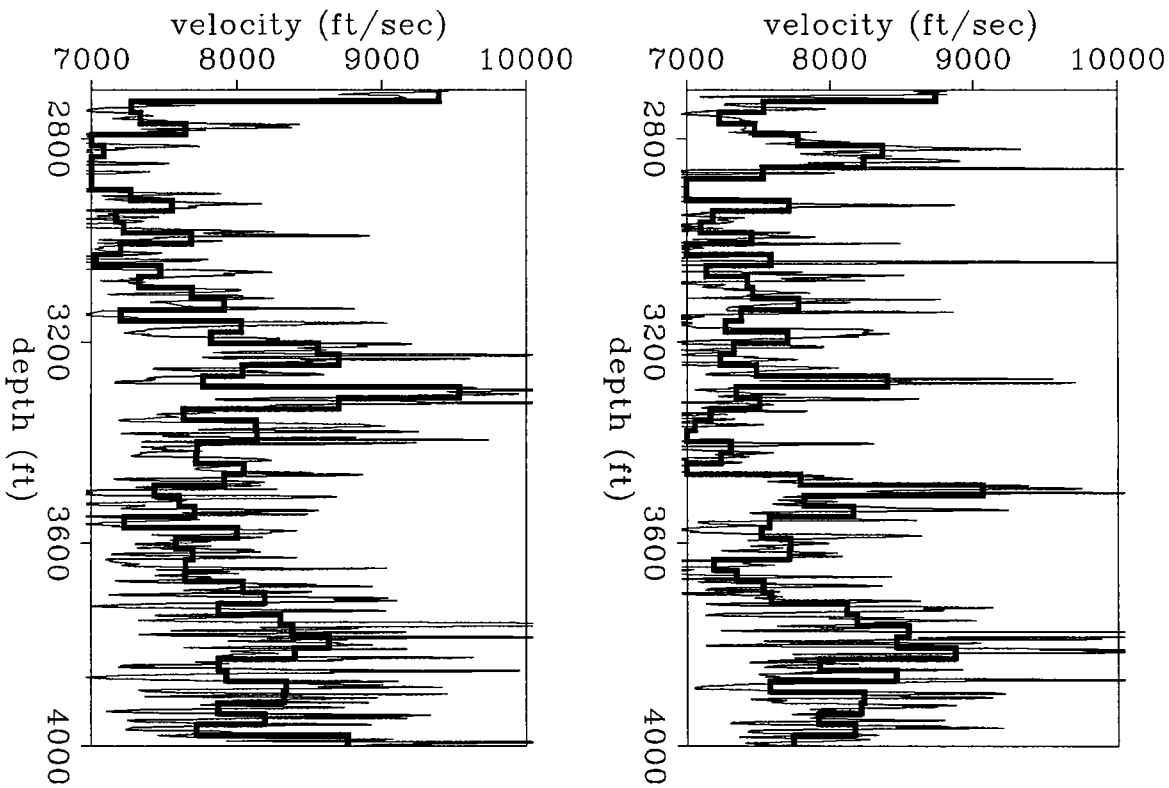

Figure 14: Sonic logs at the source and receiver well respectively. The thin line represents the original log. The thick line represents the corresponding log averaged in 60 layers of equal thickness (21.583 ft) (two-logs) [NR]

Under the straight-ray assumption, only one external iteration was needed in the 1-D inversion to find the model shown in Figure 12. By selecting the layer thickness appropriately, we were able to perform the CG-iterations required to reach convergency without being much affected by the noise: thicker layers damped the solution whereas thiner layers introduced instabilities. In 2-D, however, the situation is different. In this case we found that the results were more sensitive to noise in the data than 1-D results. This is not surprising because now we are trying to estimate horizontal variations in S_z which, as explained before, are related to the smallest singular values of the problem (that amplify the noise).

Because of the sensitiveness to the noise of the 2-D inversion, it is necessary to avoid "many" CG-iterations at each linearized step. After several tests combining in different ways external and internal iterations with mean-average smoothing of the slowness model, we adopted a conservative approach to minimize the error (12). The approach consisted of the following steps: (1) Compute traveltimes in the given model, calculate the matrix $\underset{\sim}{\mathbf{J}}$ and find the residuals. (2) Approximate the solution of the linear problem (11) by applying few (typically one or two) CG-iterations. (3) Smooth the updated slowness model. (4) Repeat all the previous steps until there is no reduction in the sum (12). When this happens, either quit or increase the number of CG-iterations by one and check if further reductions in the mismatch are obtained. If the problem is linear, the solution is not obtained in only one iteration because of the presence of the noise.

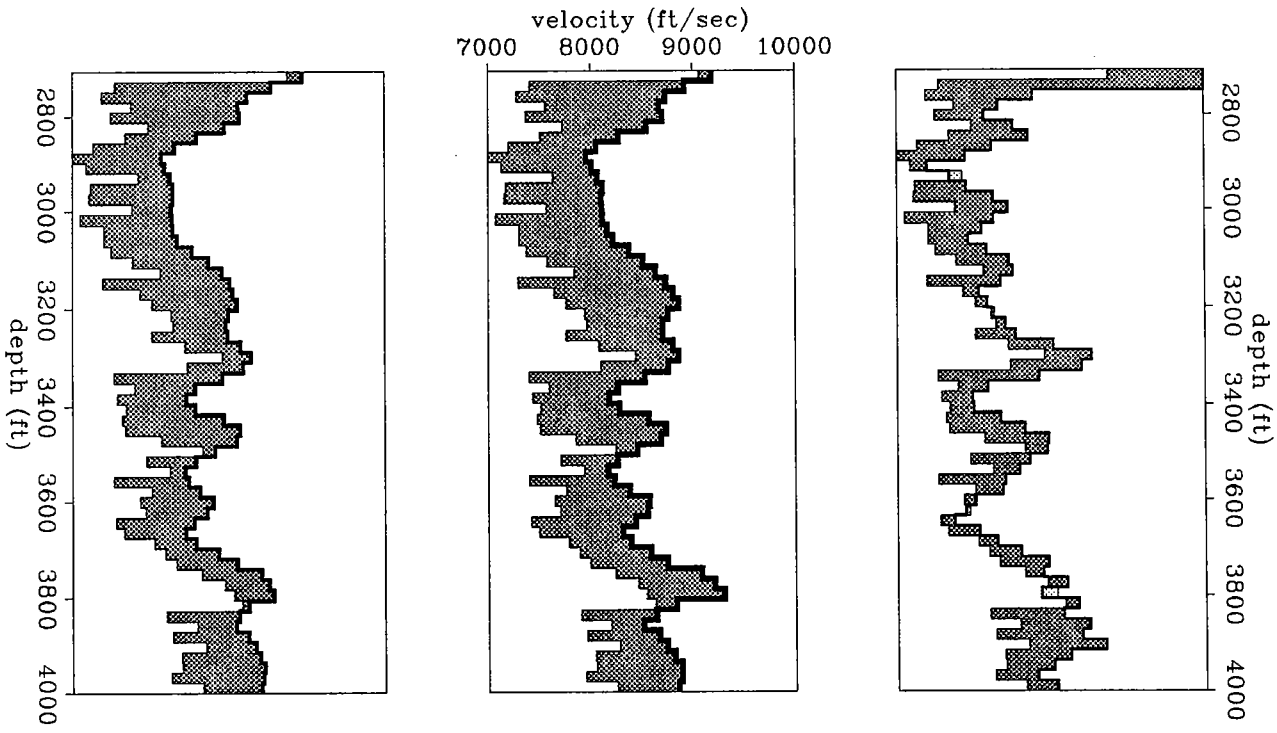

Figure 15: Average velocity log compared with V_{iso} (left), V_x (center) and V_z (right). V_z is closer and better correlated with the velocity log. (logs-vs-veloc) [NR]

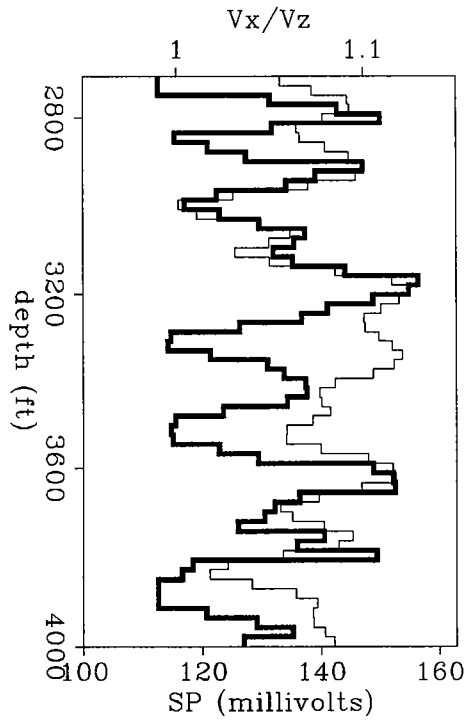

Figure 16: Anisotropy ratio V_x/V_z (thick line) compared with the SP log (thin line). (SP-Ani) [NR]

When the previous procedure was applied to estimate an isotropic model from the data, we obtained the image shown in Figure 17 (*error* = 0.54 ms). In this case, the unknown model was discretized into 131 x 26 square cells (10 ft^2 each). It is interesting to notice that adding more degrees of freedom in structure (more cells) does not improve substantially the parameter *error* obtained with 28 times less degrees of freedom in the 1-D anisotropic inversion. The model shown in Figure 17 is similar to the one obtained by Harris et al. (1990b).

The result of the anisotropic inversion is shown in Figure 18 (*error* = 0.45 ms). Notice that V_x is remarkably similar to V_{iso}, like in the 1-D inversion. The main difference between these two images is that in V_x (Figure 18) the events tend to be more horizontally smeared that in V_{iso} (Figure 17). This was expected from the synthetic example shown in Figure 8.

The events in the vertical component of the velocity tend to be smeared in the direction of the steepest rays and the spatial resolution in this component is poor when compared with V_{iso} and V_x. This is because V_z is not properly sampled by the recording geometry. In the 1-D case, as we said before, this lack of information is compensated by assuming a layered model, which allows to perform more CG-iterations without having problems with the noise. In 2-D this is not possible and therefore, the results obtained can be in a stage where V_x is close to convergency but V_z is far from that point. This in turn introduces artificial anisotropy.

Because V_x and V_z cannot be estimated at the same resolution (at least using only this type of recording geometry), it is not possible to estimate spatial variations in velocity anisotropy (the ratio V_x/V_z for example) at the same scale of the variations in velocity. Still, an image that shows variations in velocity anisotropy can be useful if it accounts only for the large scale variations that are well resolved by the inversion. Such an image is shown in Figure 18. This image is divided into four areas: highly anisotropic, moderately anisotropic, isotropic and anisotropic with $V_z > V_x$. We can see that most of the model is isotropic whereas the anisotropic areas are associated with high isotropic-velocity zones, possibly shales.

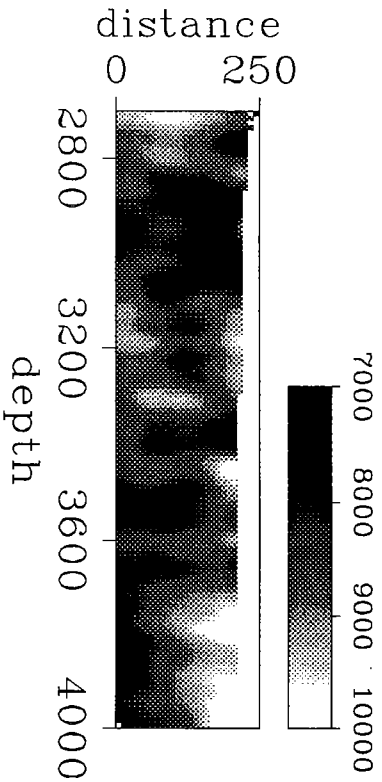

Figure 17: Isotropic 2-D inversion. The image has been divided into 131 x 26 square cells (10 ft^2 each). (s2d-iso-hast) [NR]

The mismatch estimated by equation (12) (*error*) decreases roughly 50% from the homogeneous to the 1-D inversion and about 60% from the homogeneous to the 2-D inversion. This means that for this data set, by trying to estimate lateral variations in the medium (small singular values) only a 10% reduction in the mismatch is gained with respect to estimating *only* vertical variations in the model (largest singular values).

Biases in the Inversion

The main problem considered in the previous sections was how the limited view of the measurements affect our ability to estimate velocities in different directions.

By assuming elliptic anisotropy it was necessary to estimate only two velocities: horizontal and vertical. Of course, this is too simple to describe the real complexities of the velocities in many cases but still, it is the first step beyond fitting the data with circles (isotropic tomography). We have seen that unless we constrain considerably the inversion (layered models) or we have measurements from a wide range of angles, it is difficult to estimate *accurately* and *simultaneously* S_x and S_z. Unfortunately, even if these conditions are satisfied, many other factors may affect the results.

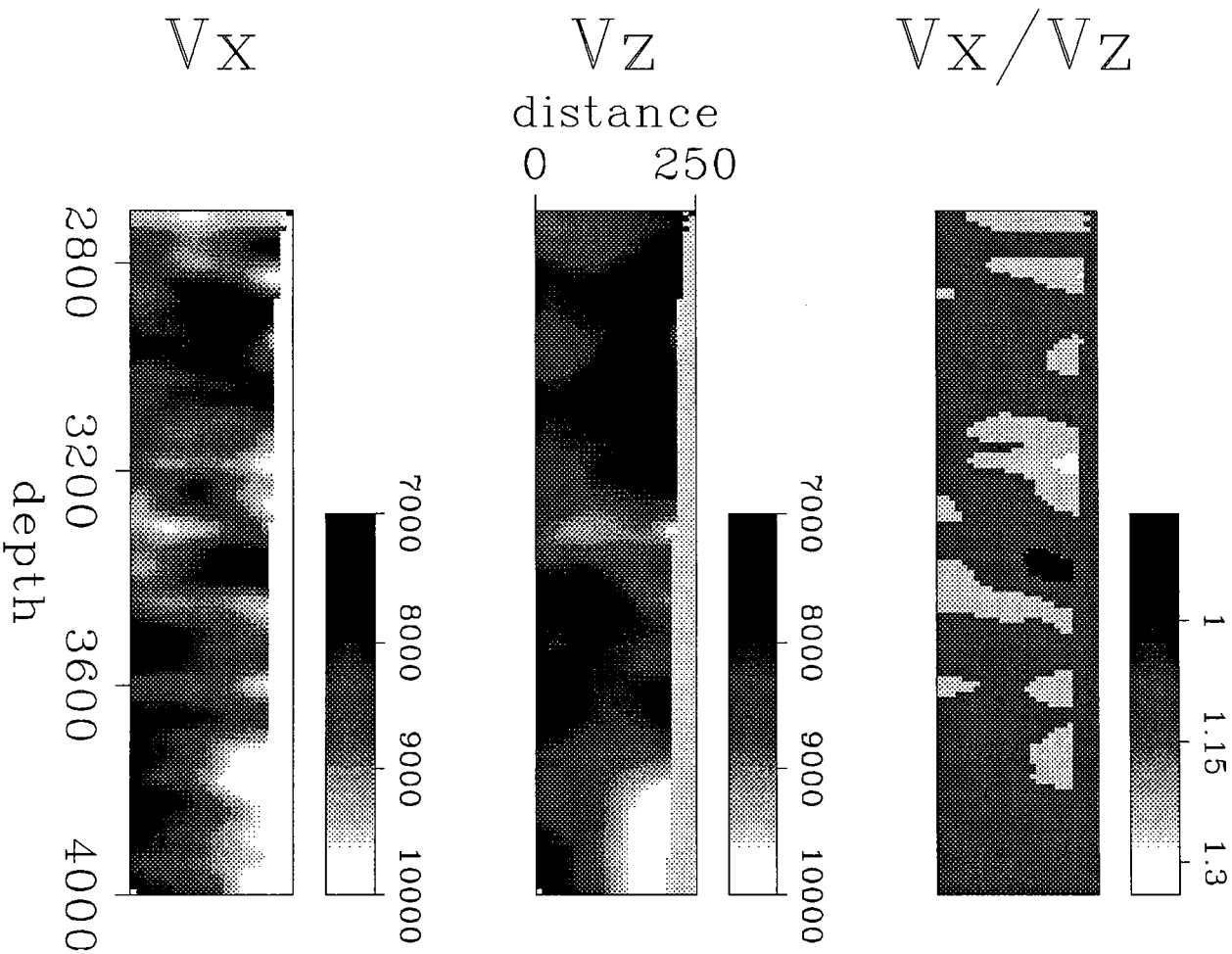

Figure 18: Anisotropic 2-D inversion. Each image has been divided into 131 x 26 square cells (10 ft^2 each). The spatial resolution of V_z is poor when compared with the spatial resolution of V_x.The ratio V_x/V_z has been separated in four areas that show percentages of anisotropy: white (ratio $>$ 1.25), light gray (1.06 $<$ ratio $\leq$ 1.25), dark gray (0.90 $<$ ratio $\leq$ 1.06) and black (ratio $\leq$ 0.9). The dark gray areas can be considered isotropic. (sx2d-hast) [NR]

Among this factors we have:

- Picking errors. These errors may increase or decrease systematically the velocities, depending on which part of the first arriving wavelet has been picked. Picking before the correct value speeds up velocities whereas picking later slows

them down. This may explain why in Figure 15 V_z is systematically 1 or 2 % faster than the sonic log.

- Well deviation. As we said before, the wells deviate in 3-D but we decided to work in 2-D. If the real 3-D variations in the medium are moderate, this is a good approximation but it may not be otherwise. When first testing our algorithm with real data the well deviation was not considered. We just substituted each well by a vertical one located at its average surface location. The results were (not shown) higher velocities (than those shown in Figure 12) where the wells were actually closer and lower velocities where the wells were actually farther apart. Considering the well deviation affected S_x more than S_z.

- Head waves vs. body waves. Although this may be considered a picking error, it affects primarily traveltimes at near offsets (small ray angles) in low velocity layers. These errors affect mainly the estimation of S_x because S_z does not use information from rays that travel at small angles. In principle, when head waves are inverted like body waves the estimated horizontal velocity turns out to be faster than the real one.

- Ray bending.

All the previous factors, when not considered appropriately, may produce artificially anisotropic results. For this reason and the ill-conditioning of the problem studied later, the estimation of small scale 2D variations in velocity anisotropy is a difficult task.

CONCLUSIONS

We have presented the basic theory and examples of an algorithm that performs anisotropic traveltime tomography. The algorithm generalizes the well known techniques of tomographic traveltime inversion by using models discretized into a set of homogeneous, elliptically-anisotropic cells, where each cell is characterized by two slownesses, one vertical and the other horizontal. Both components of the slowness can be estimated simultaneously provided that the range of ray angles is great enough. Otherwise the problem becomes ill-conditioned. As expected for cross-well geometries, the ill-conditioning is more severe in the estimation of the vertical component of the slowness. This is another reason why we should combine information from different geometries (VSP, surface-to-surface, and cross-well), since taken alone they may have limited aperture.

ACKNOWLEDGMENTS

We thank Francis Muir for many interesting discussions and important suggestions. We would like also to thank Amoco Production Company, the Gas Research

Institute and the Seismic Tomography Project at Stanford University for providing the data. The first author thanks INTEVEP, S.A. for financial support.

REFERENCES

Byun, B. S., and Corrigan, D., 1990, Seismic traveltime inversion for transverse isotropy: Geophysics, **55**, 192-200.

Chapman, C. H. and Pratt, R. G., 1990, Traveltime tomography in anisotropic media: theory: submitted to Geophys. J. Intl.

Cunha-Filho, C. A., 1990, Traveltime inversion of a cross-well data set for elliptically anisotropic media: SEP-**67**, 31-40.

Dellinger, J., 1989, Anisotropic traveltime inversion with error bars: theory: SEP-**60**, 253-260.

Dellinger, J., and Muir, 1991, The double elliptic approximation in the group and phase domains: SEP-**70**, 361-366.

Gill, P. E., Murray, W., and Wright, M. H., 1991, Numerical lineal algebra and optimization, volume 1: Addison-Wesley Publishing Company.

Harris, J. M., Lazaratos, S., and Michelena, R., J., 1990, Tomographic string inversion: STP-**1**, Paper B.

Harris, J. M., Mavko, G., Moos, D., and Nolen-Hoeksema, R., J., 1990, Cross-well tomographic imaging in Gulf Coast sediments: STP-**1**, Paper A.

Karrenbach, M., 1989, Velocity and Q in transverse isotropic media: SEP-**60**, 271-283.

Levin, F. K., The reflection, refraction, and diffraction of waves in media with elliptical velocity dependence: Geophysics, **43**, 528-537.

McMechan, G. A., 1983, Seismic tomography in boreholes: Geophys. J. Roy. Astr. Soc., **74**, 601-612.

Muir, F., 1990, A modified anisotropic system: SEP-**67**, 41-42.

Nolet, G., 1987, Seismic wave propagation and seismic tomography, *in* Nolet, G., Ed., Seismic tomography: D. Reidel Publ. Co., 1-23

Pratt, R. G., Chapman, C. H., 1990, Traveltime tomography in anisotropic media: application: submitted to Geophys. J. Intl.

White, J. E., Martineau-Nicoletis, L., and Monash, C., 1983, Measured anisotropy in Pierre shale: Geophys. Prosp., **31**, 707-725.

Winterstein, D. F., 1986, Anisotropy effects in *P*-wave and *SH*-wave stacking velocities contain information on lithology: Geophysics, **51**, 661-672.

PAPER D

ANISOTROPY FROM HEAD WAVES IN CROSSWELL DATA PART 1 : THEORY

Masazumi Onishi and Jerry M. Harris
Seismic Tomography Project

ABSTRACT

A method for using head waves observed in crosswell data to analyze anisotropic properties of sedimentary rocks was developed. Head waves are critical refractions generated at the interface of low and high velocity formations. Anisotropic properties of the low velocity formation significantly affect the velocity of the head waves because the head waves propagate obliquely through the formation. Unlike surface seismic or VSP survey, the crosswell recording geometry makes it easy to observe such head waves. This paper focuses on the theory of estimating anisotropic properties from head waves in crosswell seismic and well logs using a model of a horizontally layered transverse isotropic medium. Our theoretical study has led to a simple relationship between traveltimes of head waves observed on a wellbore and the velocity of seismic waves in the anisotropic medium. The relationship easily yields the phase velocity and the incident angle of the head waves, which are usually missing information in surface seismic or VSP survey. The information is essential to estimating anisotropic properties of sedimentary rocks.

INTRODUCTION

The model of a transverse isotropy is widely accepted for describing elastic anisotropy of sedimentary rocks. Horizontal layering of different isotropic (or anisotropic) media yields an equivalent elastically anisotropic property, if the wave length of the wave is much larger than the typical layer thickness. This type of anisotropy is called transverse isotropy. In general, elastic anisotropy can be directly associated with elastic constants of the materials. Elastic materials have twenty-one elastic constants. Usually, symmetrical properties reduce the number of independent constants. In the case of a transverse isotropy, the anisotropic behavior is governed by five independent constants (Backus,

1962). Berryman (1979) led to a relation between the phase velocity and the group velocity of seismic waves generated by a point source located in the transversely isotropic medium.

The measurement of elastic constants is usually performed in a laboratory using core samples (Tosaya, 1982; Jones and Wang, 1981). In contrast, in-situ estimation of elastic constants is rarely performed because of the limitation of resolution of in-situ measurements and the difficulties in obtaining sufficient data for determining elastic constants.

In recent years, crosswell seismic tomography has been developed in order to determine the detailed velocity structure between two wells. While surface seismic and VSP surveys observe nearly vertical velocities, this new crosswell geometry makes it possible to measure an accurate horizontal velocity. As a result, the integration of these techniques enables the detailed analysis of elastic properties of sedimentary rocks. Winterstein and Paulsson (1990) discussed anisotropic properties of a shale using both crosswell and VSP data, and determined in-situ five in-situ elastic constants according to a model of a transverse isotropy.

Head waves are critical refraction generated at the interface of fast and slow velocity formations. These waves can be easily observed in the crosswell geometry. Unlike direct body waves between two wells, the incident angle of the head waves depends only on the velocity contrasts at the interface. A large velocity contrast at the interface enhances the detection of head waves in crosswell data and makes it easy to recognize the effect of the anisotropy of a low velocity formation, regardless of the formation thickness.

In this paper, we present a method for estimating anisotropic parameters and elastic constants by combining head waves in crosswell geometry with sonic logs. The method is based on the theory of an acoustic wave propagation in a transverse isotropic medium (Thomsen, 1986). We first verify a simple relation between the apparent velocity of head waves at receiver arrays and a true phase velocity of head waves propagating through a low velocity formation. This relation leads to a practical method for deducing elastic constants and anisotropic parameters from in-situ measurements.

SEISMIC WAVE PROPAGATION

Horizontal layering of isotropic or anisotropic materials gives rise to a behavior of elastic aniostropy if the wave length of a wave is much larger than the typical thickness of each layer (Backus, 1962). This type of anisotropy is called transverse isotropy (see Figure 1). The elastic constants consists of five independent components (Thomsen, 1986). The elastic constants can be expressed in the following two-rank tensor notation:

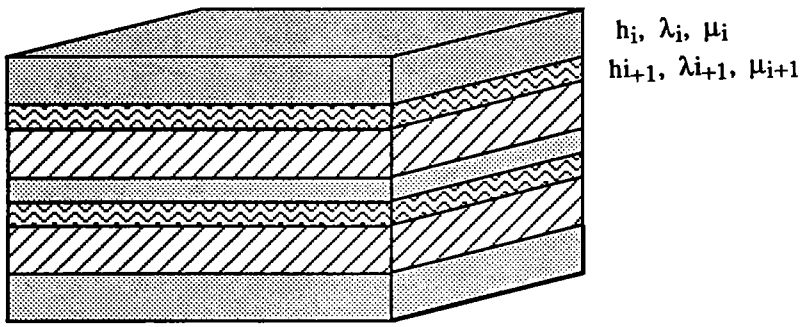

Figure 1: The equivalent model of a transverse isotropic medium. The horizontal layering of thin isotropic beds shows anisotropic property if the wave length of a seismic wave is much greater than the typical thickness of each layer.

$$C = \begin{bmatrix} C_{11} & C_{12} & C_{13} & 0 & 0 & 0 \\ C_{12} & C_{11} & C_{13} & 0 & 0 & 0 \\ C_{13} & C_{13} & C_{33} & 0 & 0 & 0 \\ 0 & 0 & 0 & C_{44} & 0 & 0 \\ 0 & 0 & 0 & 0 & C_{44} & 0 \\ 0 & 0 & 0 & 0 & 0 & C_{66} \end{bmatrix} \quad (1)$$

$$C_{12} = C_{11} - 2C_{66}.$$

Backus (1962) clarified that these five constants are deducable from the following averaging of Lamb's constant λ_i and shear modulus μ_i of each thin isotropic layer :

$$C_{11} = \frac{1}{\Sigma h_i} \Sigma \frac{4\mu_i(\lambda_i+\mu_i)h_i}{\lambda_i+2\mu_i} + \left(\frac{1}{\Sigma h_i}\Sigma \frac{h_i}{\lambda_i+2\mu_i}\right)^{-1} \left(\frac{1}{\Sigma h_i} \Sigma \frac{\lambda_i h_i}{\lambda_i+2\mu_i}\right)^2 \quad (2)$$

$$C_{33} = \left(\frac{1}{\Sigma h_i} \Sigma \frac{h_i}{\lambda_i+2\mu_i}\right)^{-1} \quad (3)$$

$$C_{13} = \left(\Sigma \frac{h_i}{\lambda_i+2\mu_i}\right)^{-1} \Sigma \frac{\lambda_i h_i}{\lambda_i+2\mu_i} \quad (4)$$

$$C_{44} = \left(\frac{1}{\Sigma h_i} \Sigma \frac{h_i}{\mu_i}\right)^{-1} \quad (5)$$

$$C_{66} = \frac{1}{\Sigma h_i} \Sigma h_i \mu_i \quad (6)$$

where h is the thickness of each layer. Hook's law provides a relation between stresses and strains. Using the above expression, the relationship is given by

$$T_i = \Sigma C_{ij} S_j \qquad (i, j = 1, 2, 3). \quad (7)$$

Ti and Sj are abbreviated expressions for components of stress and strain tensors :

$$T_1 = \sigma_{xx},\ T_2 = \sigma_{yy},\ T_3 = \sigma_{zz},\ T_4 = \sigma_{yz},\ T_5 = \sigma_{xz},\ T_6 = \sigma_{xy}$$

$$S_1 = \frac{du_x}{dx},\ S_2 = \frac{du_y}{dy},\ S_3 = \frac{du_z}{dz},$$

$$S_4 = \frac{du_z}{dy} + \frac{du_y}{dz},\ S5 = \frac{du_z}{dx} + \frac{du_x}{dz},\ S6 = \frac{du_y}{dx} + \frac{du_x}{dy}$$

On the other hand, the equations of motion are given by

$$\frac{d\sigma_{ij}}{dx_j} = \rho \frac{d^2u_i}{dt^2} \qquad (i = 1, 2, 3 \quad X_1 = x, X_2 = y, X_3 = z) \tag{8}$$

Suppose that a plane wave is propagating in X-Z plane, and the symmetry axis is Z direction. Then, the displacements vector U is expressed as

$$U = \begin{bmatrix} U_x \\ U_y \\ U_z \end{bmatrix} e^{i\{wt-k(lxX+lzZ)\}}. \tag{9}$$

where

$$l_x = \sin\theta \qquad l_z = \cos\theta \tag{10}$$

θ is an angle between the direction of the plane wave and the symmetry axis. Using Eqns. 2 and 3, the displacements U_x, U_y, U_z must satisfy the following christoffel equations :

$$k^2 \begin{bmatrix} C_{11}l_x^2+C_{44}l_z^2 & 0 & (C_{13}+C_{44})l_xl_z \\ 0 & C_{66}l_x^2+C_{44}l_z^2 & 0 \\ (C_{13}+C_{44})l_xl_z & 0 & C_{44}l_x^2+C_{33}l_z^2 \end{bmatrix} \begin{bmatrix} U_x \\ U_y \\ U_z \end{bmatrix} = \rho\omega^2 \begin{bmatrix} U_x \\ U_y \\ U_z \end{bmatrix}. \tag{11}$$

The dispersion relations are given by

$$\begin{vmatrix} C_{11}l_x^2+C_{44}l_z^2-\rho\omega^2/k^2 & 0 & (C_{13}+C_{44})l_xlz \\ 0 & C_{66}l_x^2+C_{44}l_z^2-\rho\omega^2/k^2 & 0 \\ (C_{13}+C_{44})l_xl_z & 0 & C_{44}l_x^2+C_{33}l_z^2-\rho\omega^2/k^2 \end{vmatrix} = 0 \tag{12}$$

This equation leads three seismic modes propagating in a transverse isotropic medium. The following three quadratic forms were denoted by Thomsen (1986):

$$\rho V_{SH}^2(\theta) = C_{66}\sin^2\theta+C_{44}\cos^2\theta \tag{13}$$

$$\rho V_P^2(\theta) = \frac{1}{2}[C_{33}+C_{44}+(C_{11}-C_{33})\sin^2\theta+D(\theta)] \tag{14}$$

$$\rho V_{SV}^2(\theta) = \frac{1}{2}[C_{33}+C_{44}+(C_{11}-C_{33})\sin^2\theta-D(\theta)] \tag{15}$$

$$D(\theta) = \{(C_{33}-C_{44})^2+2[2(C_{13}+C_{44})^2-(C_{33}-C_{44})(C_{11}+C_{33}-2C_{44})]\sin^2\theta + [(C_{11}+C_{33}-2C_{44})^2-4(C_{13}+C_{44})^2]\sin^4\theta\}^{1/2}.$$

These modes correspond to SH, quasi-P, and quasi-SV waves propagating in a transverse isotropic medium.

The behaviors of the seismic waves are somewhat different from those in isotropic media. First, the velocity of seismic waves depends on the direction of the incident angle (angular dispersion). This angular dispersion is directly associated with the fact that the direction of the seismic ray is not parallel to the wave normal (see Figure 2). The seismic energy propagates with a group velocity. In anisotropic media, the group velocity is different from the phase velocity which corresponds to the speed of a wave normal. Second, as for quasi-P and quasi-SV modes, the direction of displacements U_x and U_z are no longer parallel or perpendicular to the wave normal.

Berryman 1979) induced a simple relation between the phase velocity and the group velocity for seismic waves generated by a point source in a transversely isotropic medium :

$$\tan\phi = \frac{V(\theta)\sin\theta + \frac{dV}{d\theta}\cos\theta}{V(\theta)\cos\theta - \frac{dV}{d\theta}\sin\theta} \tag{16}$$

$$V_g(\phi) = \sqrt{V(\theta)^2 + \left(\frac{dV}{d\theta}\right)^2} \tag{17}$$

where $V(\theta)$ and $V_g(\phi)$ are phase and group velocities, respectively. In-situ measurements of seismic waves in a crosswell geometry is based on the group velocity and angle (see Figure 3).

Eqn. 17 shows that in the case of an angular dispersion, a group velocity is always equal to or greater than the corresponding phase velocity. If the group and phase velocities are same, then the phase angle and the group angle is also same.

It should be noted that explicit expressions of $V_P(\phi)$ and $V_{SV}(\phi)$ are very complicated. This suggests that even if we can determine the $V(\phi)$ and ϕ from observed direct waves, it is difficult to directly induce elastic constants from such results. However, as we discuss later, if we use head waves, we can directly obtain a phase velocity $V_P(\theta)$.

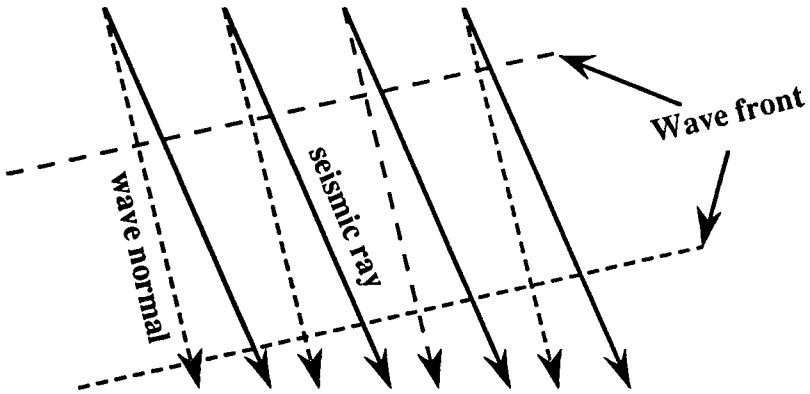

Figure 2: Difference between the wave normals and the seismic rays for incident plane waves in an anisotropic medium. The seismic rays are oblique to the wave front.

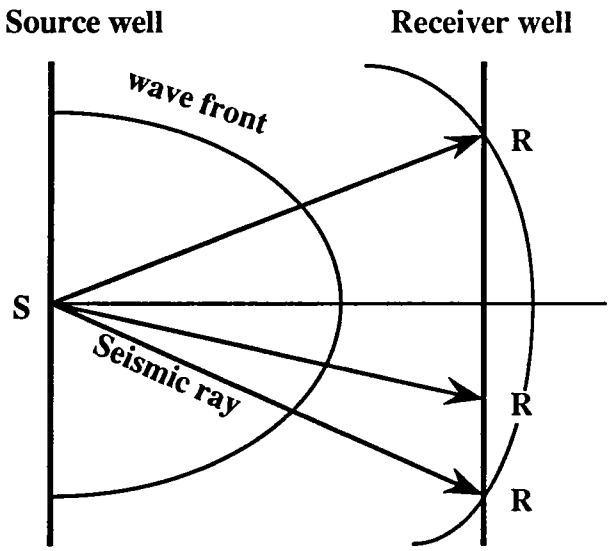

Figure 3: Detection of seismic waves in a crosswell geometry. In a homogeneous medium, the travel time is simply expressed as $T = L/Vg(\phi)$ where L is a distance between the source and the receiver.

GENERALIZED SNELL'S LAW

Seismic waves refract at the interface of two elastic media. Regardless of isotropic or anisotropic, the component of a slowness surface (reciprocal of a phase velocity) parallel to the interface has to remain constant (Henneke,1971). That is expressed as

$$\frac{K_{x1}}{\omega} = \frac{K_{x2}}{\omega} = P(\text{constant}) \tag{18}$$

where the X-axis is parallel to the interface, and K_x expresses an X-component of the wave number K (see Figure4). This is defined as the generalized Snell's law in this paper. Suppose that a symmetry axis of a transverse iostropic medium coincides with Z direction. Then, K is a function of θ, the angle between the Z-axis and the incident wave.

$$K_x = K(\theta)\sin\theta, \quad K_z = K(\theta)\cos\theta \tag{19}$$

$$V(\theta) = \frac{\omega}{K(\theta)} \tag{20}$$

The generalized Snell's law can be simply expressed as

$$\frac{\sin\theta}{V(\theta)} = P_\theta(\text{constant}). \tag{21}$$

It should be noted that the velocity used in these equation is a phase velocity. As already discussed, we can define a group velocity in anisotropic media. The expression of the Snell's law using the group velocity is also significant because in-situ measurements of seismic waves are usually based on the group angle and velocity.

Fermat's principle requires that the path of a seismic ray between two points minimize the traveltime along the pass. According to the procedure shown in Appendix A, we can obtain

$$\frac{\sin\phi}{V_g(\phi)} - \frac{dV_g}{d\phi}\frac{\cos\phi}{V(\phi)^2} = P_\phi(\text{constant}) \tag{22}$$

along the seismic ray. Using Eqn. 11 and 12, we can show that Eqn.17 is equivalent to Eqn. 16, that is $P_\theta = P_\phi$ (see Appendix B).

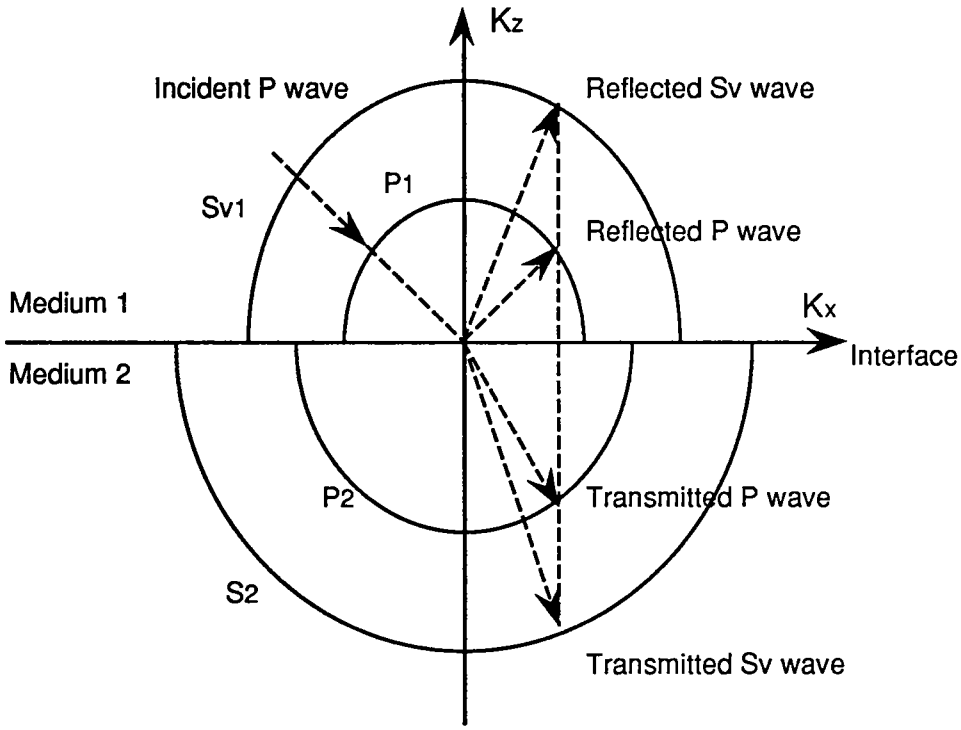

Figure 4: Slowness field in anisotropic media. An incident P wave refracts and reflects at the interface between the two media. The generalized Snell's law requires that the horizontal component of the slowness of each mode is equal to that of the incident wave.

Thus, the generalized Snell's law in anisotropic media is represented by

$$\frac{\sin\theta}{V(\theta)} = \frac{\sin\phi}{V_g(\phi)} - \frac{dV_g}{d\phi}\frac{\cos\phi}{V_g(\phi)^2} = P \text{ (constant)} \qquad (23)$$

HEAD WAVES IN CROSSWELL SURVEYS

A head wave is critical refraction at the interface of two different media. This head wave can be easily detected in the crosswell geometry. The following situations are required for the detection.

- Both an energy source and a receiver are located in a low velocity medium.
- The velocity contrast at the interface is large enough to create head waves between two wells.
- The head waves arrive at receivers earlier than direct waves because of the small amplitude of the head waves..

Figure 5 shows the concept of the detection of head waves and direct wave in the crosswell geometry.

Anisotropic property of the low velocity formation significantly affects the traveltimes of head waves observed in the crosswell geometry. The incident angle depends only on the velocity contrasts between the two media, regardless of the formation thickness. The detection of head waves itself implies a large velocity contrast at the interface.

The incident angle of a seismic ray at the critical refraction is defined as an angle such that the seismic ray becomes horizontal after the refraction. Figure 6 illustrates the ray path of head waves. The traveltime is divided into the three parts.

T_s : Traveltime between the source and the interface
T_2 : Traveltime along the interface
T_r : Traveltime between the interface and the receiver

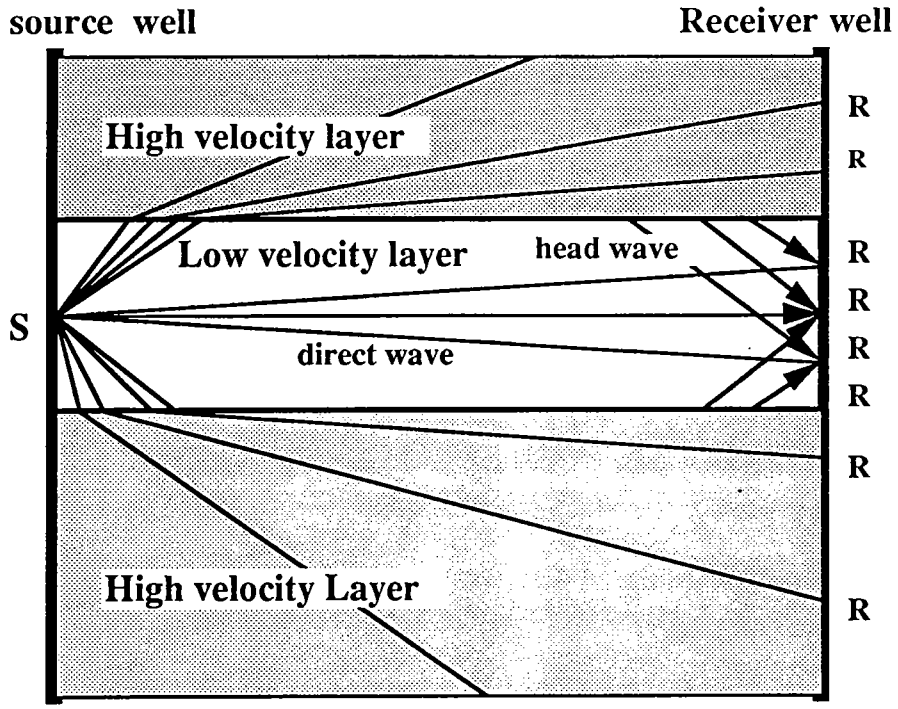

Figure 5: Observation of head waves in a crosswell survey. If both a source and a receiver are located in a low velocity layer, head waves are detectable.

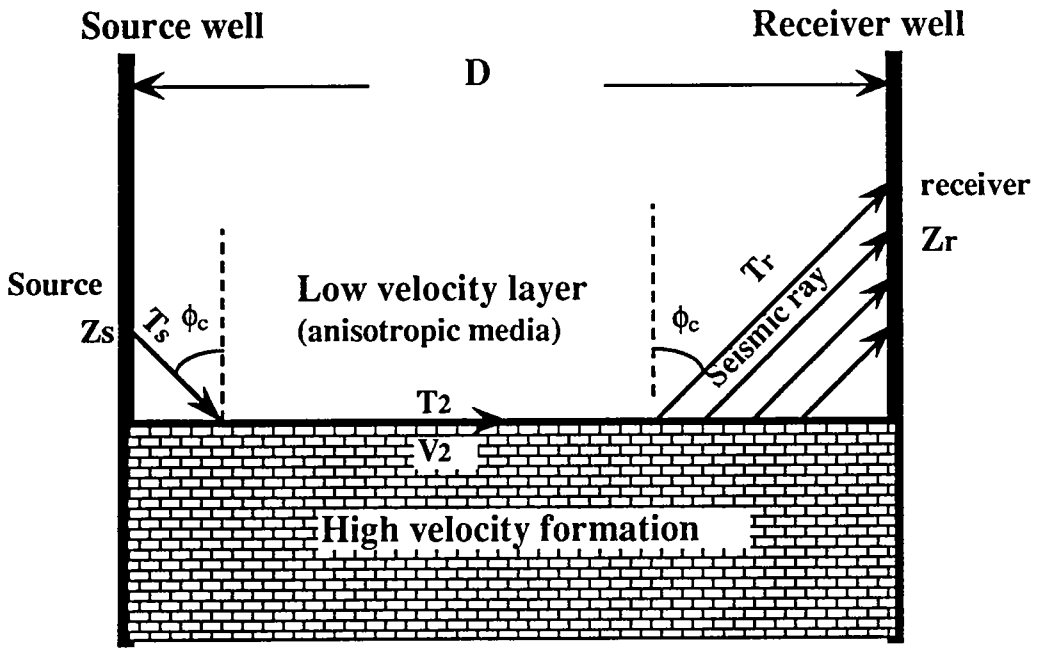

Figure 6: Seismic ray path of head waves observed in a crosswell geometry. After the critical refraction, the seismic ray propagates along the interface, turning to the low velocity formation.

T_s, T_2, and T_r are simply given by

$$T_s = \frac{\Delta Z_s}{V_g(\phi_c)\cos\phi_c} \tag{24}$$

$$T_2 = \frac{D - \tan\phi_c(\Delta Z_s + \Delta Z_r)}{V_2} \tag{25}$$

$$T_r = \frac{\Delta Z_r}{V(\phi_c)\cos\phi_c} \tag{26}$$

The total traveltime is

$$T = \frac{D}{V_2} + \left(\frac{1}{V(\phi_c)\cos\phi_c} - \frac{\tan\phi_c}{V_2}\right)(\Delta Z_s + \Delta Z_r) \tag{27}$$

where

D	:	Horizontal distance between the two well
ϕ_c	:	Incident angle (group angle) at the interface
$V_g(\phi_c)$	:	Group velocity of head waves in a low velocity formation
V_2	:	Horizontal velocity of a high velocity formation
ΔZ_s	:	Vertical offset distance of a source from the interface
ΔZ_r	:	Vertical offset distance of a receiver from the interface

V_2 is equal to the horizontal phase velocity of the high velocity formation under the assumption of transversely isotropic media with a vertical symmetry axis. The generalized Snell's law requires that the head wave satisfy the following equation :

$$\frac{\sin\phi_c}{V_g(\phi_c)} - \frac{dV_g}{d\phi c}\frac{\cos\phi_c}{V_g(\phi_c)^2} = \frac{\sin\theta_c}{V(\theta_c)} = \frac{1}{V_2} \tag{28}$$

where θ_c is the corresponding phase angle. Using equations (16), (17) and (25),

$$\frac{1}{V_g(\phi_c)\cos\phi_c} - \frac{\tan\phi_c}{V_2} = \frac{\cos\theta_c}{V(\theta_c)} \tag{29}$$

$$\cos\theta_c = \sqrt{1 - \left(\frac{V(\theta_c)}{V_2}\right)^2} \tag{30}$$

$$\frac{1}{V_g(\phi_c)\cos\phi_c} - \frac{\tan\phi_c}{V_2} = \sqrt{\frac{1}{V(\theta_c)^2} - \frac{1}{V_2^2}}. \tag{31}$$

Putting this to Eqn. 27, the traveltime is given by

$$T = \frac{D}{V_2} + \sqrt{\frac{1}{V(\theta_c)^2} - \frac{1}{V_2^2}}\,(\Delta Z_s + \Delta Z_r). \tag{32}$$

If the low velocity formation is weakly inhomogeneous in lateral, the second term of the right -hand side can be divided into two parts.

$$T = \frac{D}{V_2} + \sqrt{\frac{1}{V_s(\theta_c)^2} - \frac{1}{V_2^2}}\,\Delta Z_s + \sqrt{\frac{1}{V_r(\theta_c)^2} - \frac{1}{V_2^2}}\,\Delta Z_r \tag{33}$$

where suffixes s and r represent the source and the receiver, respectively.

Travel time T has a linear relation with ΔZ_s and ΔZ_r. This means that the head waves behave like plane waves around the receiver array in a wellbore. According to the calculations shown in Appendix B, we can show that θ_c is the angle between the interface and the wave front while ϕ_c corresponds to the angle between the seismic rays and the normal direction to the interface. In a transverse isotropic medium, the wave front is not perpendicular to the direction of the seismic rays. Figure 7 illustrates the behavior of head waves around a receiver array.

An apparent head wave velocity V_{hd} is defined as a reciprocal of the gradient of travel times along the subsequent receivers :

$$\frac{\Delta T}{\Delta Z} = \frac{1}{V_{hd}} \tag{34}$$

From Eqns. 33 and 34, V_{hd} and $V(\theta_c)$ have a simple relation :

$$\frac{1}{V_{hd}} = \sqrt{\frac{1}{V(\theta_c)^2} - \frac{1}{V_2^2}}. \tag{35}$$

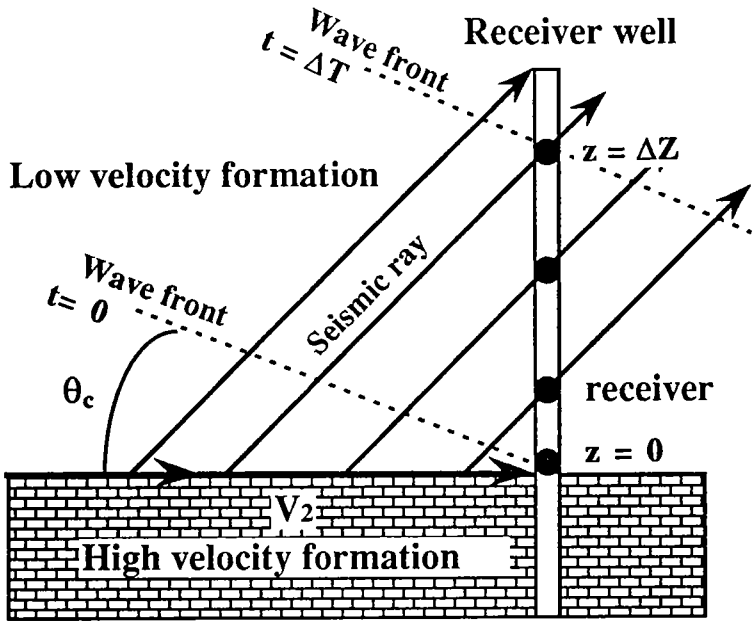

Figure 7: Behavior of head waves around receivers. θc corresponds to the angle between the wave front and the interface.

Thus, the traveltime T can be simply expressed by apparent head wave velocities observed at a source array and a receiver array :

$$T = \frac{D}{V_2} + \frac{\Delta Z_s}{V_{hds}} + \frac{\Delta Z_r}{V_{hdr}} \tag{36}$$

Analysis of Head Waves

As shown in Eqn. 36, traveltimes of head waves have a linear relation with ΔZ_s and ΔZ_r. The coefficients of ΔZ_s and ΔZ_r are reciprocals of V_{hd} around source and receiver wells. Eqn. 36 can be rewritten as

$$T = \alpha D + \beta \Delta Z_s + \gamma \Delta Z_r \tag{37}$$

where

$$\alpha = \frac{T_0}{D}, \quad \beta = \frac{1}{V_{hds}}, \quad \gamma = \frac{1}{V_{hdr}}. \tag{38}$$

All of α, β and γ have a dimension of slowness. .The least square method can easily determine the coefficients, α, β and γ from observed head waves. It should be noted that β and γ are not significantly affected by the constant bias on ΔZ_s and ΔZ_r. For the determination of these coefficients, Z_s and Z_r may be relative vertical distance from a arbitrarily fixed origin . That is

$$\Delta Z_s = Z_s - Z_0 \qquad \Delta Z_r = Z_r - Z_0 \tag{39}$$

where Z_0 is the depth of a local origin. (This is one of the advantages of the head wave analysis because the accurate depth of the interface is not required. Sometimes, it is difficult to determine the accurate location of the boundary.) In contrast, the value of α is sensitive to the bias for ΔZ_s and ΔZ_r. This suggests that we should avoid determining V_2 from α. Fortunately, V_2 can be easily derived from the direct waves propagating along the interface.

The least square method leads to the following simultaneous equation :

$$Ax = y \tag{40}$$

$$A = \begin{bmatrix} Dn & \sum_{i=1}^{n} Z_{si} & \sum_{i=1}^{n} Z_{ri} \\ D\sum_{i=1}^{n} Z_{si} & \sum_{i=1}^{n} Z_{si}^2 & \sum_{i=1}^{n} Z_{si}Z_{ri} \\ D\sum_{i=1}^{n} Z_{ri} & \sum_{i=1}^{n} Z_{si}Z_{ri} & \sum_{i=1}^{n} Z_{ri}^2 \end{bmatrix} \quad X = \begin{bmatrix} \alpha \\ \beta \\ \gamma \end{bmatrix} \quad Y = \begin{bmatrix} \sum_{i=1}^{n} T_i \\ \sum_{i=1}^{n} Z_{si}T_i \\ \sum_{i=1}^{n} Z_{ri}T_i \end{bmatrix}.$$

$V_s(\theta_c)$ and $V_r(\theta_c)$ are simply induced from the solution of the above equation:

$$V_s(\theta_c) = \frac{1}{\sqrt{\beta^2 + \frac{1}{V_2^2}}} \qquad V_r(\theta_c) = \frac{1}{\sqrt{\gamma^2 + \frac{1}{V_2^2}}}. \tag{41}$$

The generalized Snell's law gives the incident angle (critical phase angle)

$$\theta_c = \frac{V(\theta_c)}{V_2}. \tag{42}$$

Consequently, the head wave analysis allows us to simultaneously obtain $V(\theta_c)$ and θ_c.

ESTIMATION OF ELASTIC CONSTANTS

The behaviors of quasi-P and quasi-SV waves can be describe by four independent elastic constants C_{11}, C_{33}, C_{44}, and C_{13}. Except for C_{13}, each constant is directly associated with an in-situ measurement :

$$C_{11} = \rho V_h^2 \qquad C_{33} = \rho V_v^2 \qquad C_{44} = \rho V_{sv}^2 \tag{43}$$

A crosswell survey can measure the horizontal velocity V_h from a direct wave between two wells. V_v and V_{sv} are vertically propagating P and S waves, which can be provided by an acoustic logging such as a full wave sonic log. In contrast, C_{13} cannot be estimated from

the above velocities because C_{13} only affects the velocity of a obliquely propagating seismic wave.

A more convenient representation is provided in terms of the parameters s, e and δ^* for describing $V(\theta)$, the phase velocity of a quasi-P wave (Thomsen, 1986):

$$V^2(\theta) = V_v^2[\ 1 + \varepsilon\sin^2\theta + E(\theta)\ ] \tag{44}$$

$$E(\theta) = \frac{1-\sigma^2}{2}\left[\sqrt{1+\frac{4\delta^*\sin^2\theta\cos^2\theta+4(1-\sigma^2+\varepsilon)\varepsilon\sin^4\theta}{(1-\sigma^2)^2}} - 1\right] \tag{43}$$

$$\sigma = \frac{V_{sv}}{V_h} = \sqrt{\frac{C_{44}}{C_{11}}} \tag{45}$$

$$\varepsilon = \frac{1}{2}\left(\frac{V_h^2}{V_v^2}-1\right) = \frac{1}{2}\left(\frac{C_{11}}{C_{33}}-1\right). \tag{46}$$

Fortunately, σ and ε does not include the term of C_{13}. These two parameters can be easily determined by the in-situ measurements. However, δ^* does depend on C_{13} :

$$\delta^* = \frac{1}{2C_{33}^2}\left[\ 2(C_{13}+C_{44})^2 - (C_{33}-C_{44})(C_{11}+C_{33}-2C_{44})\right] \tag{47}$$

This implies that an additional oblique velocity is required for determining δ^*. Using $V(\theta_c)$, σ, and ε, we can calculate the value of δ^*:

$$\delta^* = -(1-\sigma^2+\varepsilon)\varepsilon\tan^2\theta_c + \frac{\left(\frac{V^2(\theta_c)}{V_v^2}-1-\varepsilon\sin^2\theta_c\right)\left(\frac{V^2(\theta_c)}{V_v^2}-\sigma^2-\varepsilon\sin^2\theta_c\right)}{\sin^2\theta_c\cos^2\theta_c}. \tag{47}$$

Thus, the analysis of head waves contributes directly to obtaining the value of δ^*.

Based on the model, we would like to propose a practical method for estimating δ^* and the associated C_{13}. The method consists of the following steps.

1. Determine V_{hd} from travel times of head waves.
2. Derive $V(\theta_c)$ and θ_c.
3. Estimate σ and ε from sonic logs and crosswell data.
4. Calculate δ^* and C_{13} using the above information.

CONCLUSION

Our theoretical study demonstrated that the analysis of head waves has several advantages for estimating anisotropic parameters and the associated elastic constants:

- The analysis of head waves enables the derivation of an incident angle and a velocity of a head wave in a phase domain. This makes it easy to estimate δ^* and C_{13}.
- The incident angle of head waves depends only on the velocity contrast between low and high velocity formation. The detection of head waves in the crosswell geometry itself suggests a large velocity contrast. Anisotropic property of the low velocity formation significantly affects the velocity of head waves, regardless of the formation thickness..
- The exact location of the interface that create head waves is not required because an apparent head wave velocity can be determined by the gradient of travel times along a receiver array in a wellbore

Based on the above advantages, we proposed a practical method for estimating δ^* and C_{13} by combining head waves with other in-situ measurements.

ACKNOWLEDGEMENT

We are grateful to our colleagues in the seismic Tomography Project for useful discussions and comments. The first author also thanks Japan Petroleum Exploration Co., Ltd. (JAPEX) and Japan National Oil Corporation (JNOC) for financially supporting his graduate study at Stanford University.

APPENDIX A: SNELL'S LAW IN A GROUP DOMAIN

According to the geometry illustrated in Figure A-2, the travel time between S and R can be written as

$$T = \frac{h_1}{V_{g1}(\phi_1)\cos\phi_1} + \frac{h_2}{V_{g2}(\phi_2)\cos\phi_2}. \tag{A-1}$$

The incident and refracted angles are given by

$$\tan\phi_1 = \frac{x}{h_1} \qquad \text{and} \qquad \tan\phi_2 = \frac{L-x}{h_2}. \tag{A-2}$$

Fermat's principle requires that the position of P make the traveltime minimum. That is,

$$\frac{dT}{dx} = 0. \tag{A-3}$$

Then,

$$\frac{dT}{dx} = \frac{d\phi_1}{dx}\frac{d}{d\phi_1}\left(\frac{h_1}{V_g(\phi_1)\cos\phi_1}\right) + \frac{d\phi_2}{dx}\frac{d}{d\phi_2}\left(\frac{h_2}{V_g(\phi_2)\cos\phi_2}\right). \tag{A-4}$$

From Eqn. A-2,

$$\frac{d\phi_1}{dx} = \frac{\cos^2\phi_1}{h_1} \qquad \frac{d\phi_2}{dx} = -\frac{\cos^2\phi_2}{h_2}. \tag{A-5}$$

Putting these relations into equation (53), we can derive

$$\frac{\sin\phi_1}{V_g(\phi_1)} - \frac{dV_g}{d\phi_1}\frac{\cos\phi_1}{V_g(\phi_1)^2} = \frac{\sin\phi_2}{V_g(\phi_2)} - \frac{dV_g}{d\phi_2}\frac{\cos\phi_2}{V_g(\phi_2)^2}. \tag{A-6}$$

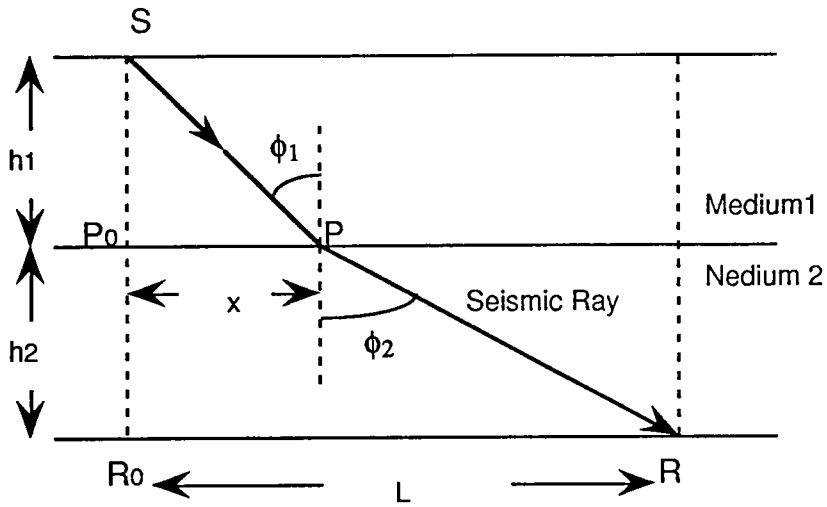

Figure A-1: Refraction of seismic rays at the interface.

APPENDIX B: WAVE FRONT OF HEAD WAVES

Let's define α, L_1, L_2 and d as illustrated in Figure B-1. α corresponds to the angle between the wave front and the interface. The angle between the seismic rays and the normal direction to the interface is given by a group angle ϕ_c. The travel time from P to O along the interface has to be equal to that from P to Q in a medium 1. This requires that

$$\frac{L_1}{V(\phi_c)\sin\phi_c} = \frac{L_1+L_2}{V_2}. \tag{B-1}$$

The relation among L_1, L_2, d, α and ϕ_c are given by

$$\frac{d}{L_1} = \cot\phi_c \qquad\qquad \frac{d}{L_2} = \tan\alpha \tag{B-2}$$

From the above two equations, we can derive

$$\cot\alpha = \frac{1}{\cos\phi_c}\left(\frac{V_2}{V(\phi_c)} - \sin\phi_c\right). \tag{B-3}$$

According to the generalized Snell's law for a critical refraction,

$$V_2 = \frac{V(\theta_c)}{\sin\theta_c}. \tag{B-4}$$

In addition, the relation between the phase and group velocities described in Eqns. 16 and 17 gives

$$\sin\phi_c = \frac{V(\theta_c)\sin\theta_c + \frac{dV}{d\theta}\cos\theta_c}{V_g(\phi_c)} \tag{B-5}$$

$$\cos\phi_c = \frac{V(\theta_c)\cos\theta_c - \frac{dV}{d\theta}\sin\theta_c}{V_g(\phi_c)}. \tag{B-6}$$

Then,

$$\frac{V_2}{V(\phi_c)} - \sin\phi_c = \frac{\cot\theta_c\left(V(\theta_c) - \frac{dV}{d\theta}\sin\theta_c\right)}{V_g(\theta_c)} = \cot\theta_c\cos\phi_c. \tag{B-7}$$

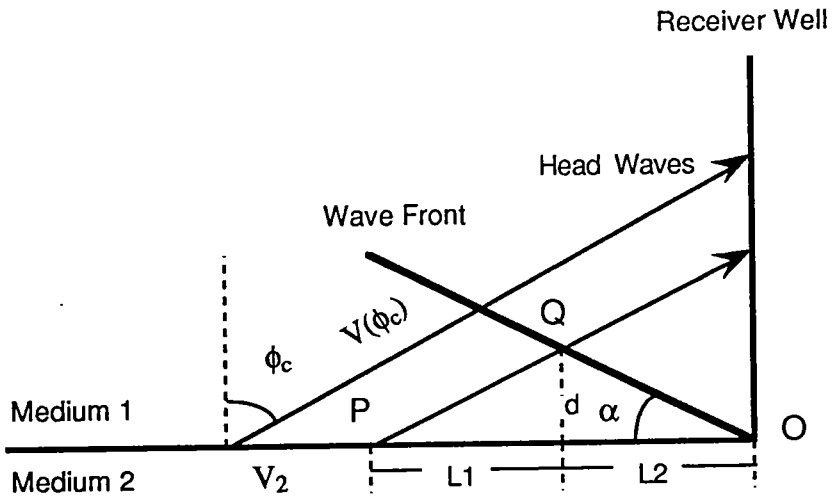

Figure B-1: Wave front of head waves around the receivers. $V(\phi_C)$ and V_2 represent the critical group velocity of head waves and the horizontal velocity in a medium 2, respectively.

Finally, we derive

$$\cot\alpha = \cot\theta_c \qquad \alpha = \theta_c. \tag{B-8}$$

This result immediately concludes that the angle between the wave front and the interface is equal to the critical phase angle.

REFERENCES

Backus, G., 1962, Long-wave elastic anisotropy produced by horizontal layering: J. Geophys. Research, **67,** 4427-4440.

Berryman, J., 1979, Long-wave elastic anisotropy in transversely isotropic media: Geophysics, **44**, 896-917.

Jones, E. A. and Wang, H.F., 1981, Ultrasonic velocities in Cretaceous shales from the Williston Basin: Geophysics, **46**, 288-297.

Henneke, E., 1971, Reflection-refraction of a stress wave at a plane boundary between anisotropic media: Acous. Soc. Am., **51**, 210-217.

Thomsen, L., 1986, Weak elastic anisotropy: Geophysics, **51**, 1954-1966.

Tosaya, C., 1982, Acoustic properties of clay-bearing rocks: Ph.D. thesis, Stanford Univ.

Winterstein, D.,and Paulsson, B., 1990, Velocity anisotropy in shale determined from crosshole seismic and vertical seismic profile data: Geophysics, **55**, 470-479.

PAPER E

ANISOTROPY FROM HEAD WAVES IN CROSSWELL DATA PART 2: CASE STUDY

Masazumi Onishi and Jerry M. Harris
Seismic Tomography Project

ABSTRACT

A method for estimating aniostropic properties of sedimentary rocks using head waves observed in crosswell data was presented in a previous paper (Onishi and Harris, Part 1, this volume). In this study, that method was applied to real crosswell data that contain easily detectable head waves generated at the interface of a low-velocity clay formation bounded by high velocity limestones. The clay formation shows strong anisotropy of about 20%. This case study confirmed the applicability of our method. The analysis of head waves significantly contribute to the verification of in-situ anisotropy and to the estimation of anisotropic parameters and elastic constants.

INTRODUCTION

In the previous paper, we presented the method for estimating anisotropic properties and elastic constants from head waves observed in crosswell data. The advantage of using head waves is that we can directly derive the phase velocity and angle for an obliquely propagating seismic wave. In addition, the angle does depend only on the velocity contrast at an interface. This implies that we can obtain a seismic velocity to recognize the effect of anisotropy, regardless of the thickness of the formation.

We clarified that the following velocities are required to in-situ determine anisotropic parameters and elastic constants of a transverse isotropic medium:

1. Horizontally propagating P wave
2. Vertically propagating P wave
3. Vertically propagating shear wave
4. Obliquely propagating quais-P wave and its angle

Direct waves between two wells allows us to derive the horizontal P wave velocity. An acoustic logging such as a full wave sonic log enables the measurements of the velocities for vertically propagating P and S waves. The head wave analysis contributes to providing the oblique velocity, which correspond to the critical phase velocity.

The method proposed in the previous paper was applied to real crosswell data. The acoustic logs have a good correlation with the lithology, and the formations are nearly horizontal between the two wells. The crosswell data contain easily detectable head waves generated at the interface of a clay formation bounded by high velocity limestones. The velocity contrast is large enough to observe head waves. Moreover, this clay formation shows a large discrepancy between the horizontal and vertical velocity. The horizontal velocity is about 20% faster than the vertical velocity. This discrepancy is considered as one evidence of the anisotropic property of the clay formation.

Based on our model of a horizontal layering transverse isotropy, anisotropic properties and elastic constants of the clay formation were estimated. The region covered by head waves can be divided into four areas around both wells. The acoustic logs data show that a seismic velocity of the clay formation slightly changes vertically and laterally. In order to consider the inhomogeneity of the clay formation, we estimated aniostropic properties independently for each area. Unfortunately, a shear wave velocity is not available from this case study. This means that we cannot mathematically determine δ^*, which is one of the anisotropic parameters introduced in the previous paper. The results, however, show δ^* is not significantly affected by the velocity of a shear wave. As for the behavior of a quasi-P wave, we can see no significant variation when we change a vertical Vp/Vs ratio from 1.7 through 2.7. This means that we can successfully estimate the behavior of a quasi-P wave without the information about a shear wave velocity. In contrast, elastic constant C_{13} is very sensitive to the velocity of a shear wave. This suggests that we cannot discuss the value of C_{13} without an accurate measurement of the shear wave velocity.

Finally, tentatively assuming that vertical Vp/Vs ratio is 2.0, we calculated δ^* and $V(\theta)$, the phase velocity of a quasi-P wave for all phase angles. We can recognize the spatial variation of δ^* and the behavior of a quasi-P wave. This fact should be carefully examined because of the limited resolution of the in-situ measurements. In order to verify it, an analysis in a laboratory is strongly recommended.

WELL DEVIATION

Figure 1 shows the location of the two wells used for this study. They are almost vertical but slightly deviated. The surface spacing is just 330 ft. Table 1 lists the deviations of both wells. Based on this table, an accurate horizontal distance at a depth of every five feet was obtained. The result is shown in Figure 2. The range of the horizontal distance at each depth is 329.5 through 337.1 feet, and the maximum deflection is within 3% of the surface spacing.

ACOUSTIC LOGGING

Figure 3 shows the sonic logs for both wells and the associated lithology. The sonic logs have a good correlation with the lithology. Each formation is nearly horizontal The anisotropic properties of the Del Rio clay formation, which exists from around 2700 ft through 2800 ft in depth, was analyzed in this case study.

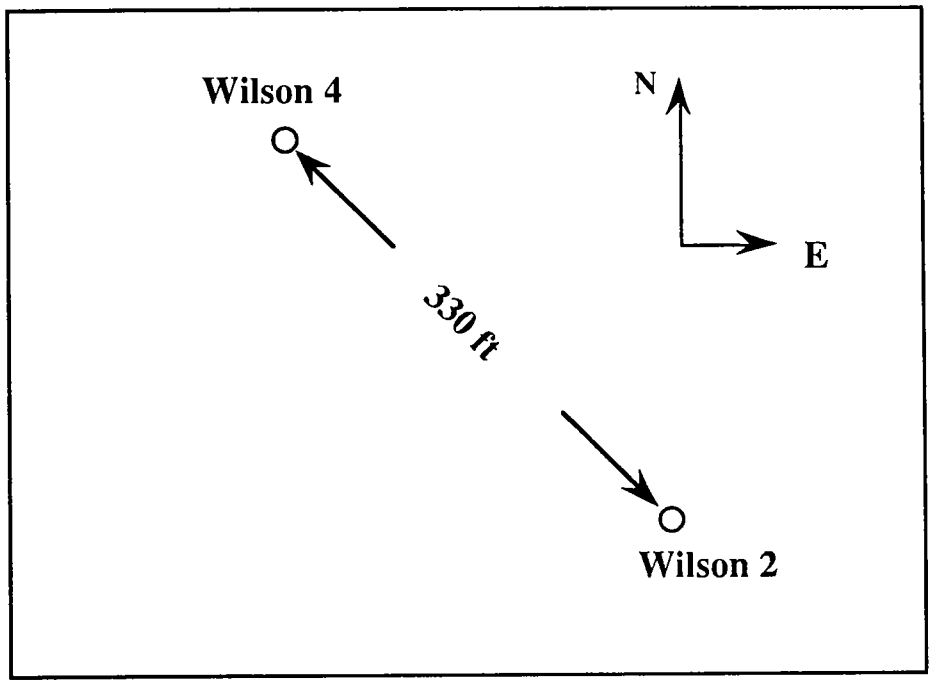

Figure 1: The location of Wilson 2 and Wilson 4 wells used in this study. The well spacing is just 330 feet. Wilson 4 is located 45 degrees north-westward of Wislon 2.

Wilson 2

Depth (feet)	North (feet)	East (feet)
0.0	0.0	0.0
500.0	2.2	-0.7
900.0	2.8	1.8
1100.0	4.2	2.7
1350.0	6.8	3.2
1400.0	7.2	4.7
1500.0	9.8	5.5
1600.0	12.6	6.6
1700.0	14.6	7.5
1800.0	16.7	8.6
1900.0	17.9	9.8
2050.0	19.0	11.8
2200.0	21.9	12.6
2350.0	24.6	13.9
2500.0	27.2	14.8
2650.0	30.6	15.4
2800.0	34.0	16.3
3000.0	39.1	16.4

Wilson 4

Depth (feet)	North (feet)	East (feet)
0.0	0.0	0.0
450.0	2.2	0.0
650.0	4.2	1.9
800.0	6.3	3.2
950.0	8.3	4.2
1100.0	10.3	3.7
1250.0	12.4	3.8
1350.0	14.0	4.0
1450.0	16.2	3.5
1550.0	18.5	3.2
1850.0	20.3	3.3
2250.0	19.1	2.8
2500.0	20.5	2.5
2850.0	23.0	0.1
3000.0	23.8	-0.7

Table 1: Well deviation of Wilson 2 and Wilson 4 wells from their surface location.

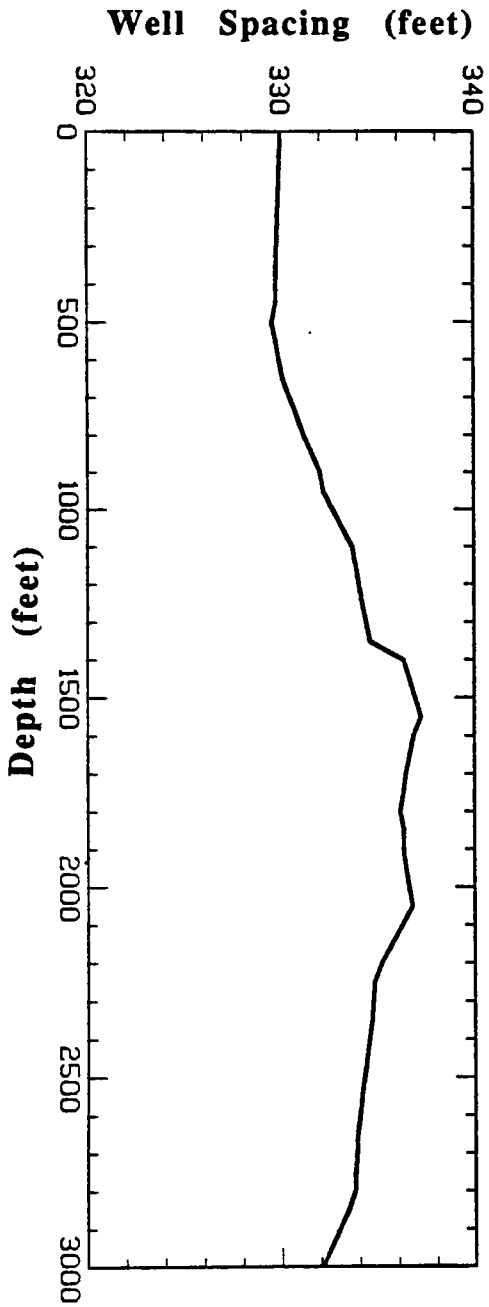

Figure 2: Horizontal distance between Wilson 2 and Wilson 4 calculated from the deviation file.

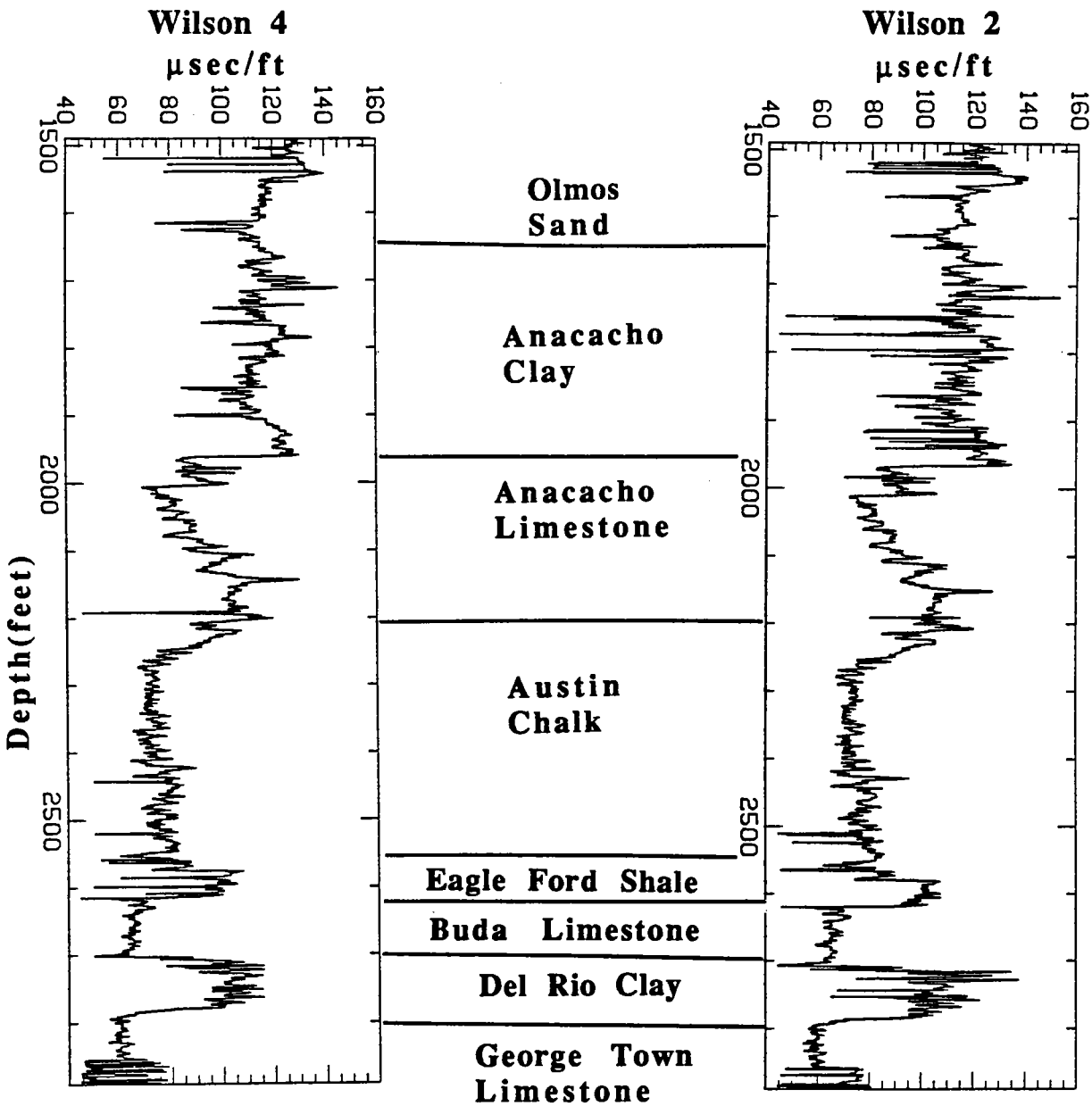

Figure 3: Acoustic Logging and lithology for Wilson 2 and Wilson 4.

CROSSWELL SURVEY

The crosswell seismic survey was performed between the two wells. The main parameters for the field acquisition are as follows (Harris, 1988).

- Energy source : Piezoelectric type(impulsive)
- Receiver : Hydrophone
- Sampling rate : 100μsec
- Pre-filter : 400 - 4000 Hz
- Notch-filter : 2, 3, 4 and 5 KHz

This crosswell survey basically measured the following two types of gathers:

- **Zero vertical offset gather**
  A source and a receiver remains at the same vertical level, and move along the wellbore. The concept is shown in Figure 4.
- **Common receiver gather**
  A receiver is fixed at a certain level. A source sequentially moves around the level of the receiver. The concept is shown in Figure 5..

The acquired zero vertical offset gather is displayed in Figure 6. As well as the acoustic logging, the first breaks reflects the lithology very well. This measurement was used for estimating horizontal velocity of P wave. Because the well spacing is only 330 ft, the seismic rays observed in the zero vertical offset gather were nearly horizontal. Therefore, traveltimes of the first breaks allow us to calculate averaged P-Wave velocity between the two wells.

Figure 7 compares the derived horizontal velocity with the vertical velocity converted from transit times of the acoustic logging. It clearly indicates a large discrepancy in the clay formation. The horizontal velocity is about 20% faster than the vertical velocity. This discrepancy anticipates strong anisotropy.

The clay formation generates clearly detectable head waves both from the upper boundary and the lower boundary because the surrounding limestones. As shown in Figure 8, such head waves were obtained as first breaks of the zero vertical offset survey when the source and the receiver were located in the clay formation. The same phenomenon is observable in common receiver gathers(see Figure 9).

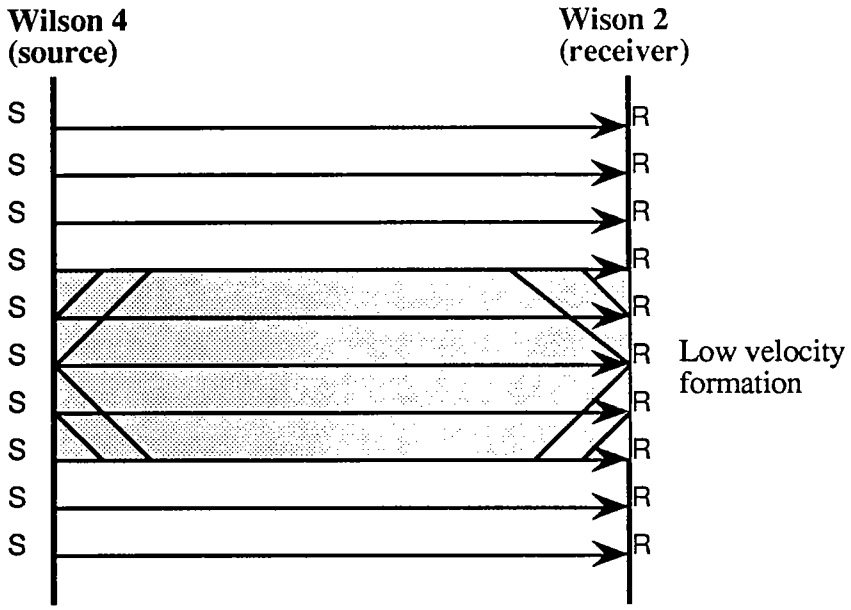

Figure 4: The concept of a zero vertical offset gather. The level of the source is equal to that of the receiver for each record.

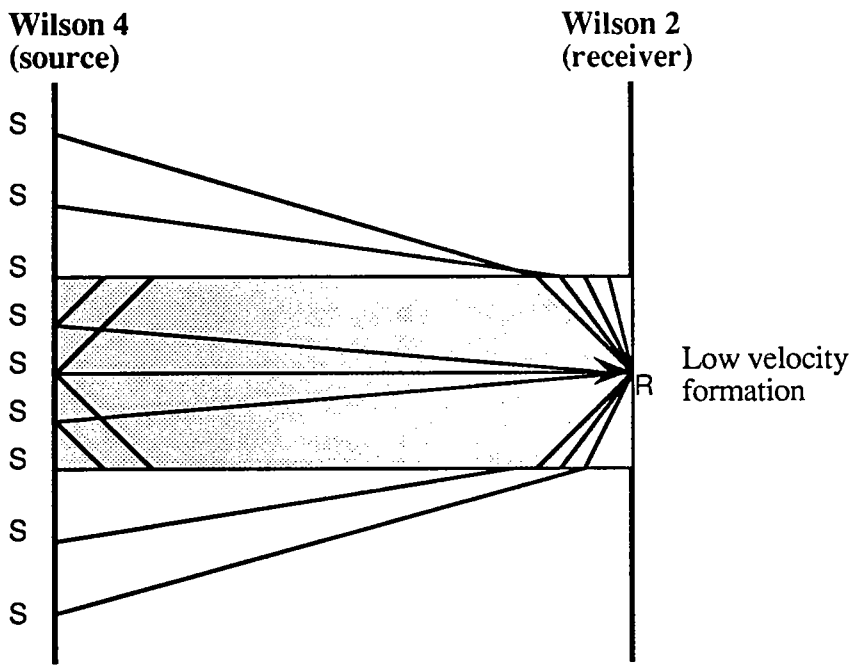

Figure 5: The concept of a common receiver gather. As well as the common zero offset gather.

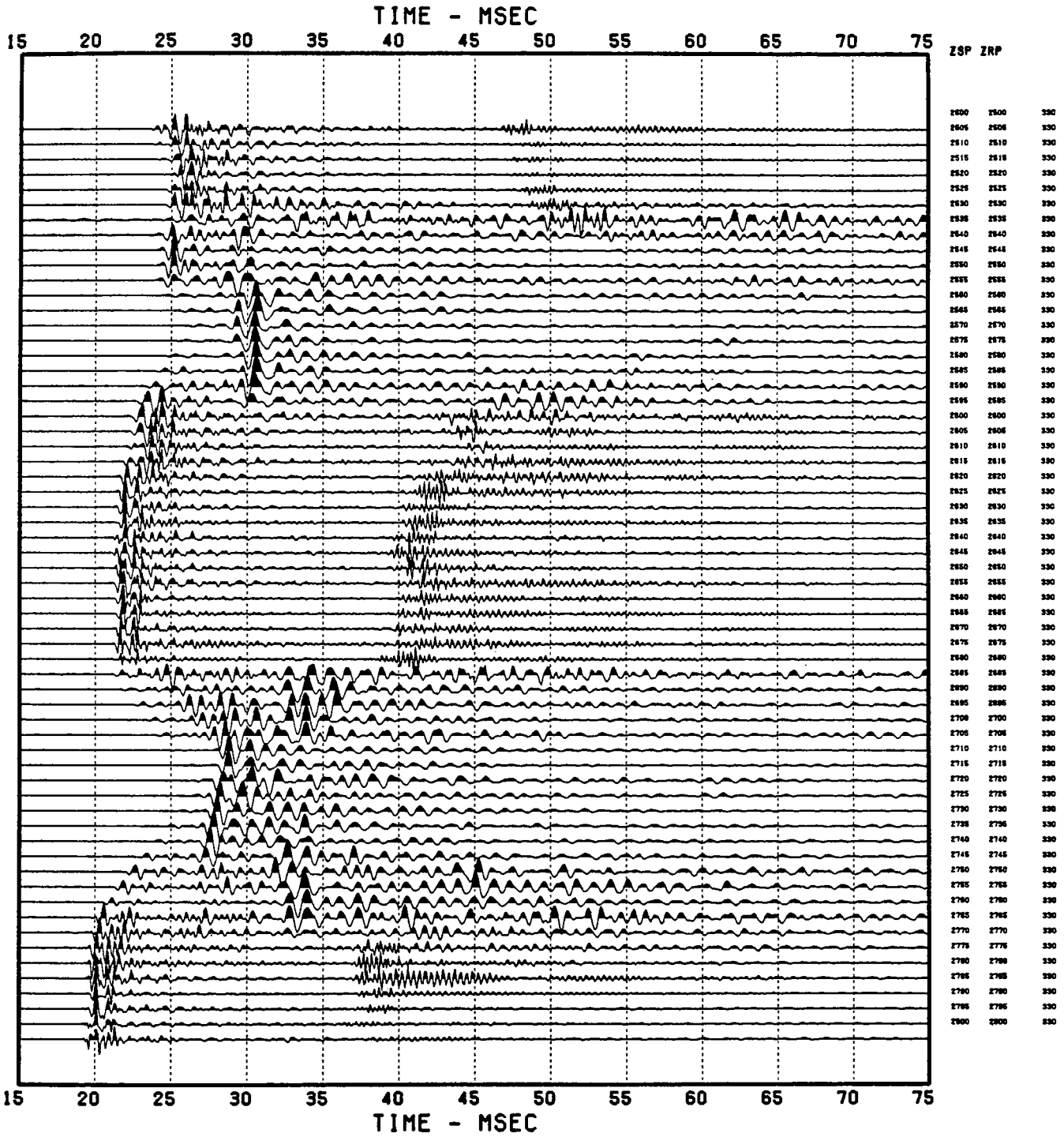

Figure 6: The zero vertical offset gather obtained between the two wells.

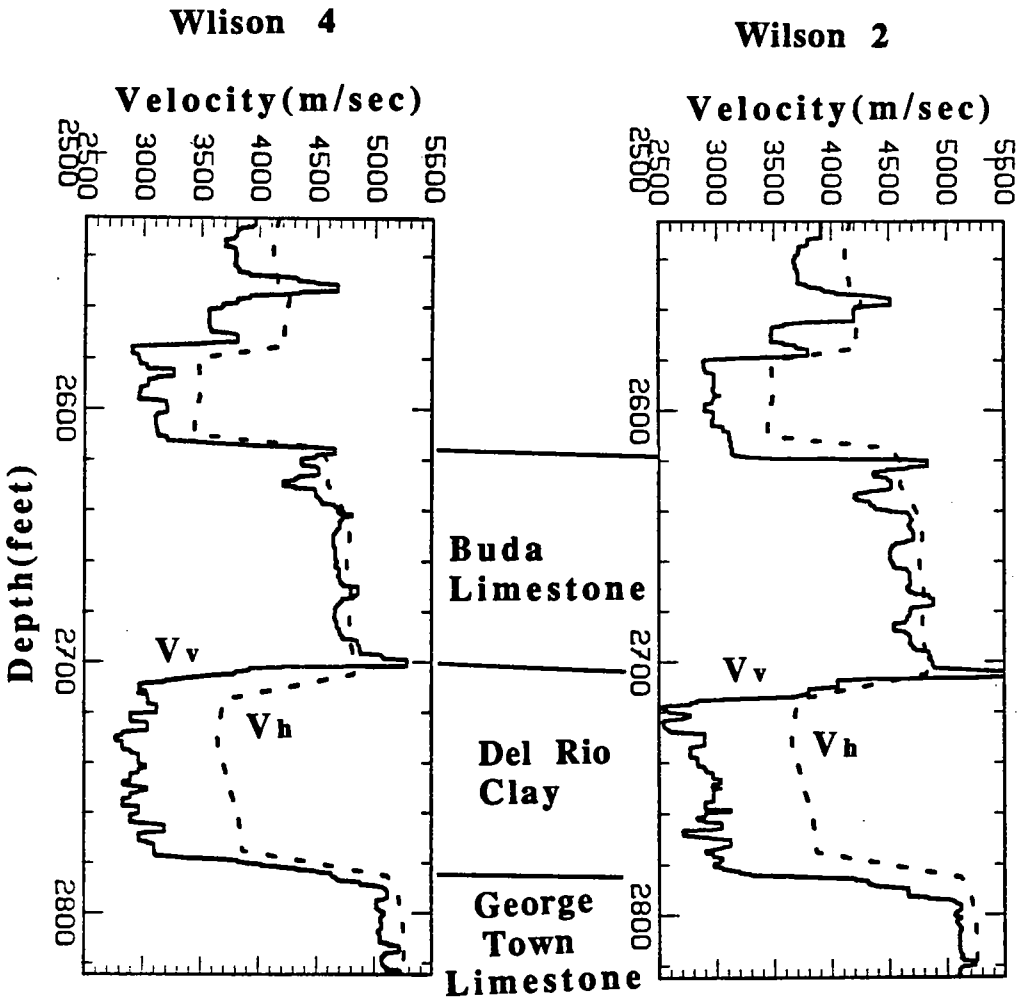

Figure 7: Comparison between the vertical and horizontal velocities. The solid and dashed lines correspond to the vertical and horizontal velocities, respectively. The clay formation shows a large discrepancy between these velocities. The surrounding limestones are almost isotropic.

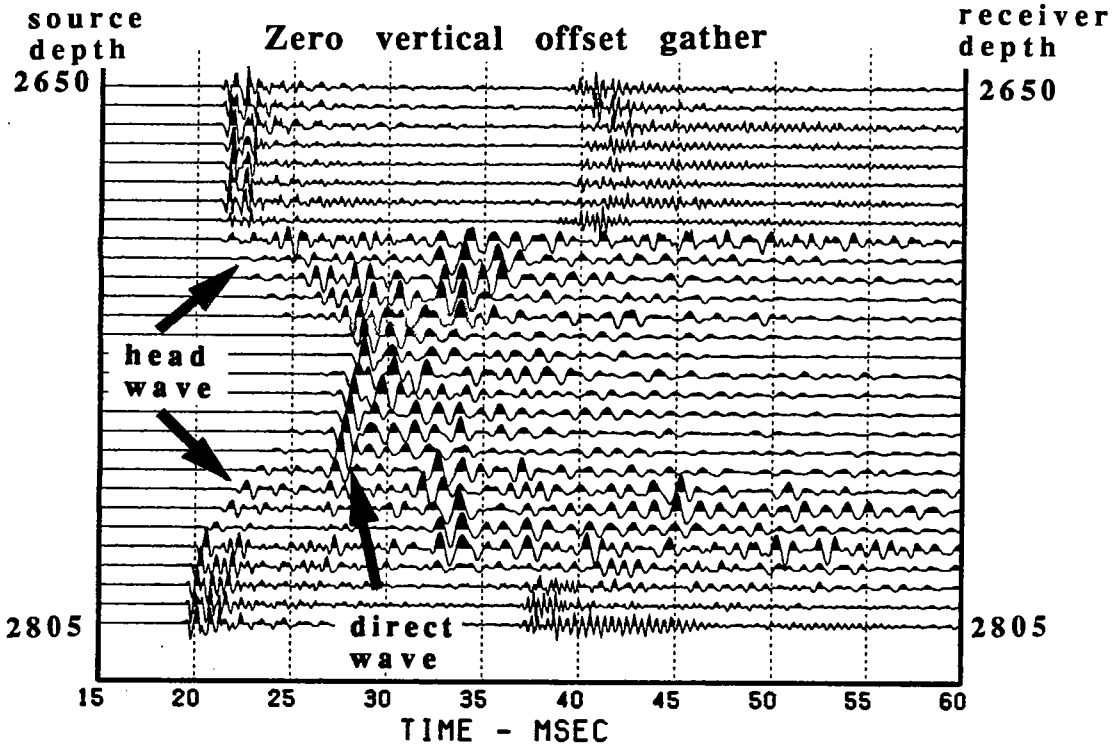

Figure 8: The zero vertical offset gather around the clay formation. Head wave from the upper and lower interfaces are easily observed.

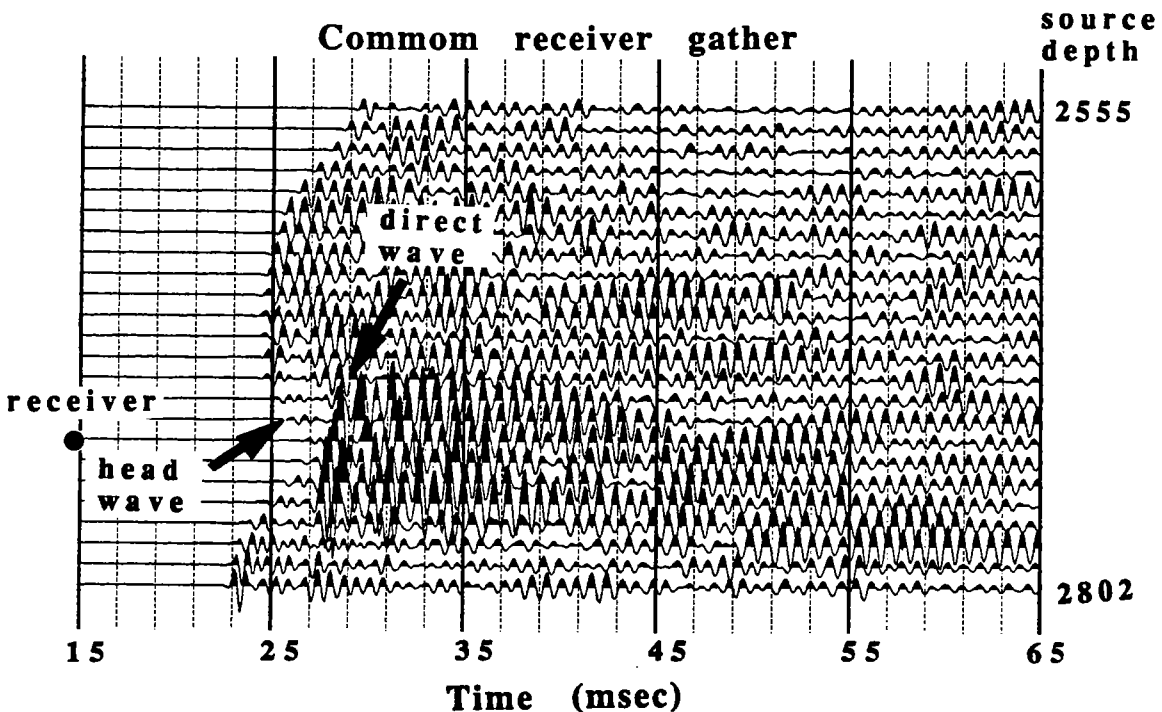

Figure 9: An example of the common receiver gathers that contain head waves from the interfaces.

THE ANALYSIS OF HEAD WAVES

The Del Rio clay formation shows strong anisotropy of about 20%. In order to verify the anisotropy, the head wave analysis presented in our previous paper was applied to the formation. The purpose of the analysis is to obtain an incident angle and a phase velocity of head waves propagating through the formation. The entire procedure consists of the following steps:

(1) Picking of travel times

Traveltimes of head waves were picked at common receiver gathers. Table 2 lists these travel times separately based on the boundaries that the corresponding head waves propagate.

(2) Determination of V_{hd}

The apparent head wave velocity V_{hd} defined as

$$\frac{1}{V_{hd}} = \sqrt{\frac{1}{V(\theta_c)^2} - \frac{1}{V_2^2}} \tag{1}$$

was determined by the least square method. V_2 is a horizontal velocity of the surrounding limestones. The traveltime of a head wave is given by the following equation

$$T = \frac{D}{V_2} + \frac{\Delta Z_s}{V_{hds}} + \frac{\Delta Z_r}{V_{hdr}} \tag{2}$$

where s and r represent a source and a receiver. θ_c is an incident phase angle, which corresponds to the critical angle of a refraction at the interface. $V(\theta_c)$ is a phase velocity of head waves propagating through the clay formation. The equation shows that the traveltimes of a head wave is a linear function of ΔZ_s and ΔZ_r. Its gradient is given by $1/V_{hds}$ and $1/V_{hdr}$. The least square method enables us to separately derive V_{hds} and V_{hdr}. This means that this method is applicable to the weakly inhomogeneous formation in lateral. The origin for ΔZ_s and ΔZ_r, which correspond to the level of the upper and lower boundaries, were determined by comparing the acoustic logging, the common zero offset gather and the common offset gathers. The results are

- Upper boundary 2700 feet
- Lower boundary 2785 feet

In fact, as shown in Figure 10, the actual travel times of head waves observed in the clay formation have a fairly linear relation with ΔZ_s and ΔZ_r.

(3) Estimation of θ_c and $V(\theta_c)$

θ_c and $V(\theta_c)$ can be calculated from the following two equations. θ_c corresponds to the angle between an interface and a wave front of head waves propagating through a low velocity formation. It should be noted that seismic rays is not perpendicular to the wave front in a transverse isotropy.

$$\frac{1}{V(\theta_c)^2} = \frac{1}{V_{hd}^2} + \frac{1}{V_2^2} \tag{3}$$

$$\theta_c = \arcsin\left(\frac{V(\theta_c)}{V_2}\right) \tag{4}$$

V_2 is simply given by the horizontally propagating P wave observed in the zero vertical offset gather.

Figure 11 shows the area covered by the head waves detected in the clay formation. The area consists of four partially overlapped zones around both wells. As shown in Figure 7, the horizontal and vertical velocity change slightly inside the clay formation. Consequently, we anticipated that these four zones have a little difference in θ_c and $V(\theta_c)$. Hence, we calculated these values independently for each zone.

Table 3 includes θ_c and $V(\theta_c)$ calculated for each zone. The result clearly indicates that they change slightly both in vertical and in lateral (see also Figure 12). There is a large discrepancy between V_h and $V(\theta_c)$. This fact simply verifies the existence of a strong anisotropy in the clay formation.

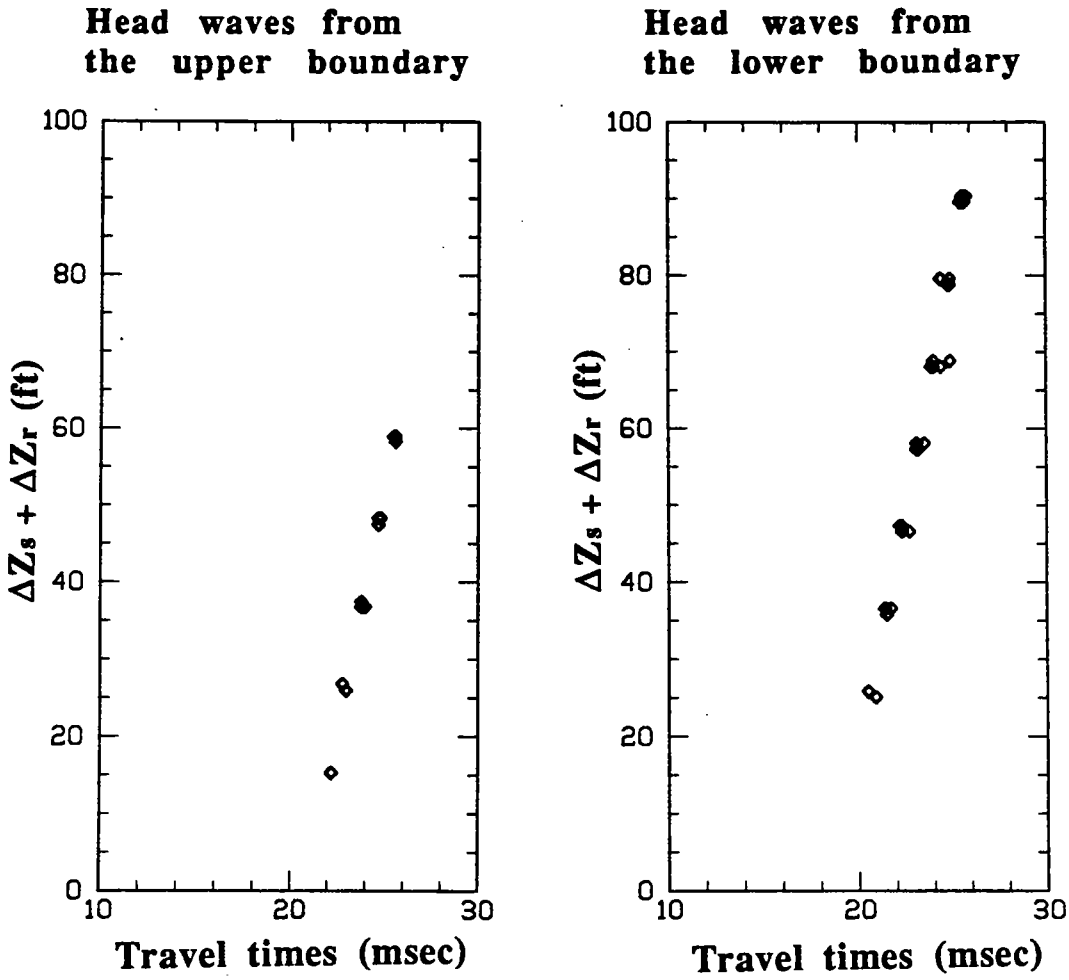

Figure 10: Relation between picked travel times and ΔZ.

Head waves from the upper boundary

Source Depth (feet)	Receiver Depth (feet)	Travel Time (msec)
2705.6	2709.6	22.2
2716.3	2709.6	23.0
2727.1	2709.6	23.8
2737.8	2709.6	24.7
2748.6	2709.6	25.6
2705.6	2721.1	22.8
2716.3	2721.1	23.8
2727.1	2721.1	24.7
2737.8	2721.1	25.5
2705.6	2731.1	24.0
2716.3	2731.1	24.7
2727.1	2731.1	25.6
2705.6	2742.6	24.8
2716.3	2742.6	25.6
2705.6	2752.6	25.6

Head waves from from the lower boundary

Source Depth (feet)	Receiver Depth (feet)	Travel Time (msec)
2770.1	2709.6	25.8
2780.8	2709.6	25.4
2759.3	2721.1	25.7
2770.1	2721.1	24.8
2780.8	2721.1	24.4
2748.6	2731.1	25.6
2759.3	2731.1	24.9
2770.1	2731.1	24.0
2780.8	2731.1	23.5
2737.8	2742.6	25.5
2748.6	2742.6	24.8
2759.3	2742.6	23.9
2770.1	2742.6	23.1
2780.8	2742.6	22.7
2727.1	2752.6	25.6
2737.8	2752.6	24.9
2748.6	2752.6	24.0
2759.3	2752.6	23.1
2770.1	2752.6	22.3
2780.8	2752.6	21.7
2716.3	2764.1	25.6
2727.1	2764.1	24.9
2737.8	2764.1	24.0
2748.6	2764.1	23.2
2759.3	2764.1	22.3
2770.1	2764.1	21.5
2780.8	2764.1	20.9
2705.6	2774.1	25.8
2716.3	2774.1	24.9
2727.1	2774.1	24.9
2737.8	2774.1	23.1
2748.6	2774.1	22.2
2759.3	2774.1	21.4
2770.1	2774.1	20.5

Table 2: Travel times of head waves picked from the common receiver gathers.

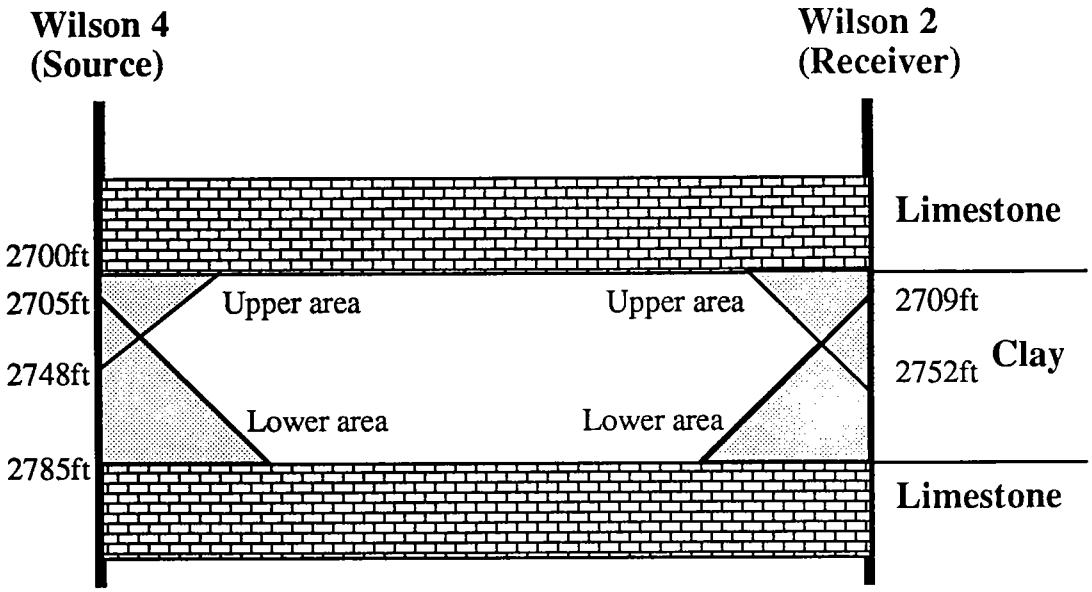

Figure 11: The areas covered by head waves. the area can be divided into partially overlapped four zones.

- # Upper area around Wilson 2
- # Lower area around Wilson 2
- # Lower area around Wilson 4
- # Lower area around Wilson 4

		V_2	θ_c	$V(\theta_c)$
Wilson 2	Upper area	4820 m/sec	37.4	2928 m/sec
	Lower area	5150 m/sec	36.4	3070 m/sec
Wilson 4	Upper area	4820 m/sec	39.0	3035 m/sec
	Lower area	5150 m/sec	37.9	3166 m/sec

Table 3: Results of the head wave analysis. Critical phase angles and velocities are derived independently for each zone.

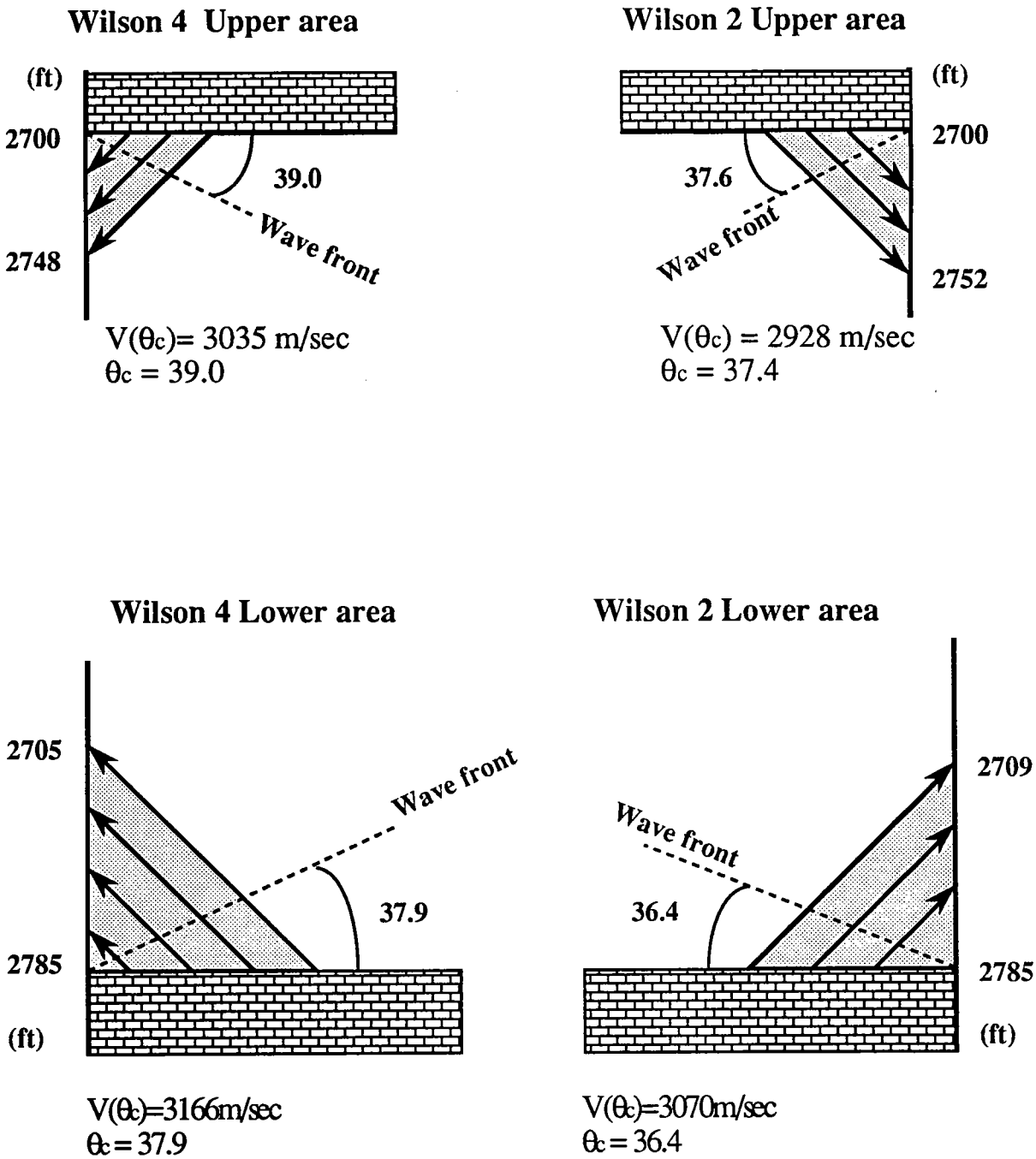

Figure 12: Results of the head wave analysis.

ESTIMATION OF ELASTIC CONSTANTS

Elastic constants and anisotropic parameters were estimated for each zone under the assumption of a transverse isotropy with a vertical symmetry axis. The Velocity of quasi-P wave $V(\theta)$ is a function of four independent elastic constants, C_{11}, C_{13}, C_{33}, and C_{44} (Thomsen, 1986).

$$\rho V^2(\theta) = \frac{1}{2}\,[C_{33}+C_{44}+(C_{11}-C_{33})\sin^2\theta+D(\theta)] \tag{5}$$

$$D(\theta) = \{(C_{33}-C_{44})^2+2[2(C_{13}+C_{44})^2-(C_{33}-C_{44})(C_{11}+C_{33}-2C_{44})]\,\sin^2\theta$$

$$+[(C_{11}+C_{33}-2C_{44})^2-4(C_{13}+C_{44})^2]\,\sin^4\theta\}^{1/2} \tag{6}$$

As discussed in the first part of this paper, this equation can be converted into the form by anisotropic parameters directly induced from the measurement of velocities.

$$V^2(\theta) = V_v^2\{\,1+\varepsilon\sin^2\theta+$$

$$\frac{1-\sigma^2}{2}\left[\sqrt{1+\frac{4\delta^*\sin^2\theta\cos^2\theta+4(1-\sigma^2+\varepsilon)\varepsilon\sin^4\theta}{(1-\sigma^2)^2}}-1\right]\} \tag{7}$$

where

- θ : Phase angle from a vertical direction
- V_v : Vertical velocity of P wave corresponding to V(0)
- V_h : Horizontal velocity of P wave corresponding to V(90)
- σ : Ratio of vertical velocities of S and P waves given by $\frac{1}{\sigma}=\frac{V_v}{V_s}$
- ε : Ratio of Vv and Vh expressed as $\varepsilon=\frac{1}{2}\left(\frac{V_h^2}{V_v^2}-1\right)$
- δ^* : Anisotropic parameters expressed as $\delta^*=\frac{1}{2C_{33}^2}[\,2(C_{13}+C_{44})^2-(C_{33}-C_{44})(C_{11}+C_{33}-2C_{44})]$

Using the above Eqns. 5, 6, and 7, the relation of δ^* and other parameters is given by the following equation:

$$\delta^* = -(1-\sigma^2+\varepsilon)\varepsilon\tan^2\theta c + \frac{(\frac{V^2(\theta_c)}{V_v^2}-1-\varepsilon\sin^2\theta_c)(\frac{V^2(\theta_c)}{V_v^2}-\sigma^2-\varepsilon\sin^2\theta_c)}{\sin^2\theta_c\cos^2\theta_c}. \quad (8)$$

V_v and V_h induced from the acoustic logging and the zero vertical offset crosswell gather immediately give the value of ε. θ_c and $V(\theta_c)$ were already derived by the head wave analysis. As for σ, we have no information because the velocity of a shear wave is still unknown. This means that δ^* cannot be mathematically determined by the given information. However, as shown in Figure 13, δ^* is not seriously affected by a shear wave velocity. As for the phase velocity induced from the results, no variation cannot be recognized (see Figure 14). In contrast, C_{13} is very sensitive to given σ (see Figure 15). These facts suggest

- Horizontal, vertical and oblique velocities of quasi-P waves enable us to successfully estimate a phase velocity as a function of its propagation angle.
- We cannot discuss C_{13} without the information about shear wave velocity. The determination of C_{13} requires an accurate velocity of the shear wave.

The clay formation is weakly inhomogeneous both in lateral and in vertical. The vertical and horizontal velocities gradually increase with depth. In addition, the acoustic logging data show a lateral variation of the vertical velocity. Consequently, different Vv and V_h are applied to each zone covered by the head waves. Those velocities are simply provided by averaging them around each zone. Hence, by tentatively setting $1/\sigma = 2.0$, anisotropic parameter δ^* and elastic constants were calculated. Table 4 include the results of the case study. The results clearly indicate that d* is much greater in the upper zone than in the lower area. This fact suggests that the anisotropic properties mainly change with depth.

Based on the results, we calculated phase and group velocities as a function of their angles. The group velocity $V_g(\phi)$ and its angle ϕ are provided by the following equations:

$$\tan\phi = \frac{V(\theta)\sin\theta + \frac{dV}{d\theta}\cos\theta}{V(\theta)\cos\theta - \frac{dV}{d\theta}\sin\theta} \tag{9}$$

$$V_g(\phi) = \sqrt{V(\theta)^2 + \left(\frac{dV}{d\theta}\right)^2}\,. \tag{10}$$

The entire results are shown in the following Figures.

- Phase velocity $V(\theta)$ (Figure 16)
- Group velocity $V_g(\phi)$ (Figure 17)
- Comparison between $V(\theta)$ and $V_g(\phi)$ (Figure 18)
- Comparison between θ and ϕ (Figure 19)
- Slowness surface (Figure 20)

The results indicate that anisotropic properties of the clay formation change with depth.

	Wilson 4		Wilson 2	
	upper area	lower area	upper zone	lower zone
Depth range (feet)	2700 - 2748	2705 - 2785	2700 - 2752	2709 - 2748
V_v (m/s)	2943	2972	2832	2861
V_h (m/s)	3691	3715	3691	3715
$V(\theta_c)$ (m/s)	3035	3166	2928	3070
θ_c	39.0	37.9	37.4	36.4
ε	0.284	0.281	0.349	0.343
δ^* **	-0.329	-0.081	-0.402	-0.099
C_{11}	2.97	3.04	3.00	3.04
C_{33}	1.91	1.94	1.76	1.80
C_{44} **	0.476	0.486	0.441	0.499
C_{13} **	0.793	1.11	0.706	1.08

Table 4: Results of the estimation of anisotropic parameters and elastic constants.
** These values assume $1/\sigma = 2.0$.

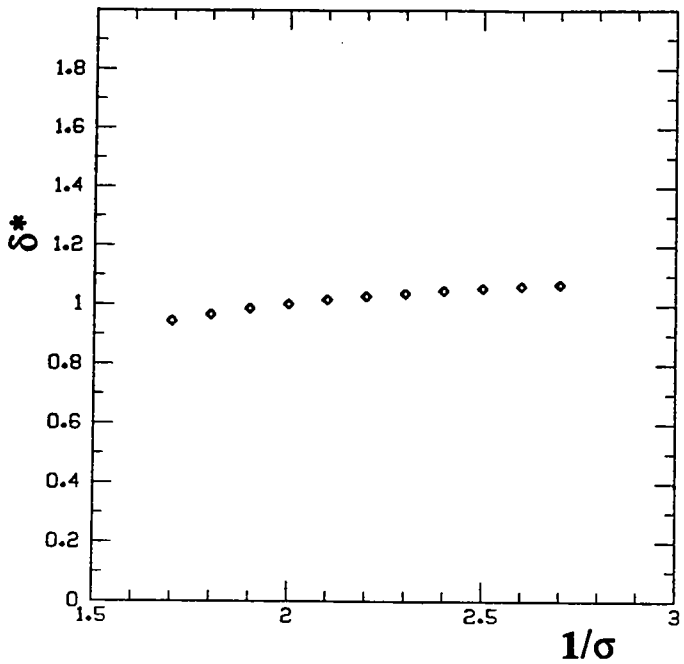

Figure 13: Relative variation of δ^* at the lower zone around Wilson 4 when s changes from 1.7 through 2.7. $\delta^*$is normalized to 1.0 when $1/\sigma = 2.0$. The actual value of $\delta^* = -0.081$.

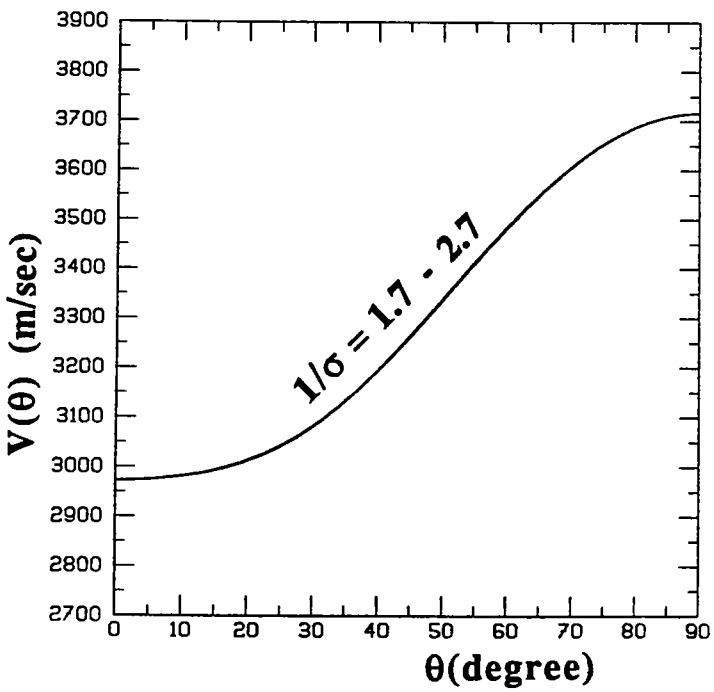

Figure 14: Response of a phase velocity V(θ) at the lower zone around Wilson4 when $1/\sigma$ changes from 1.7 through 2.7. The corresponding V(θ) is drawn as a function of θ. All curves are almost overlapping.

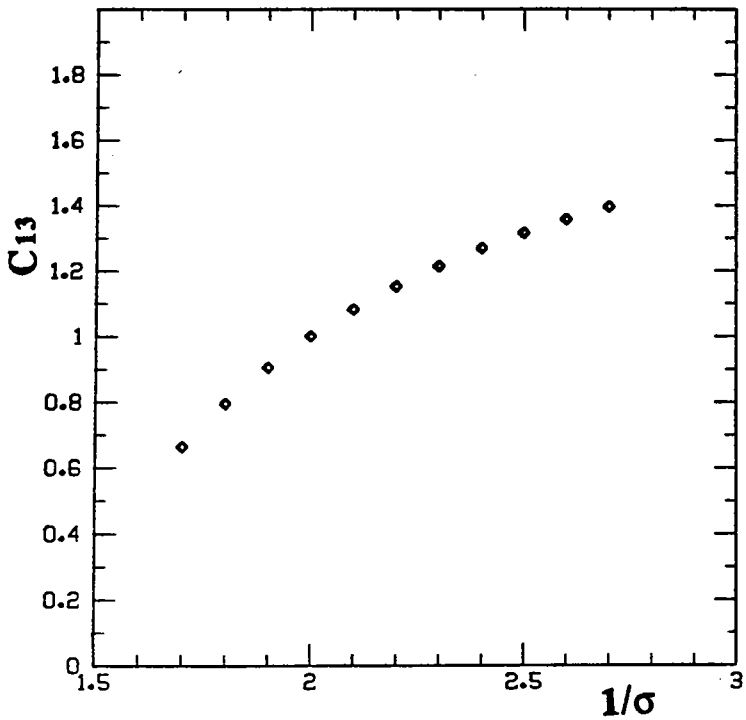

Figure 15: Relative variation of C_{13} at the lower zone around Wilson 4 when $1/\sigma$ changes from 1.7 through 2.7. C_{13} is normalized to 1.0 when $1/\sigma = 2.0$ The actual value of C_{13} is $1.11*10^{10}$ pascals.

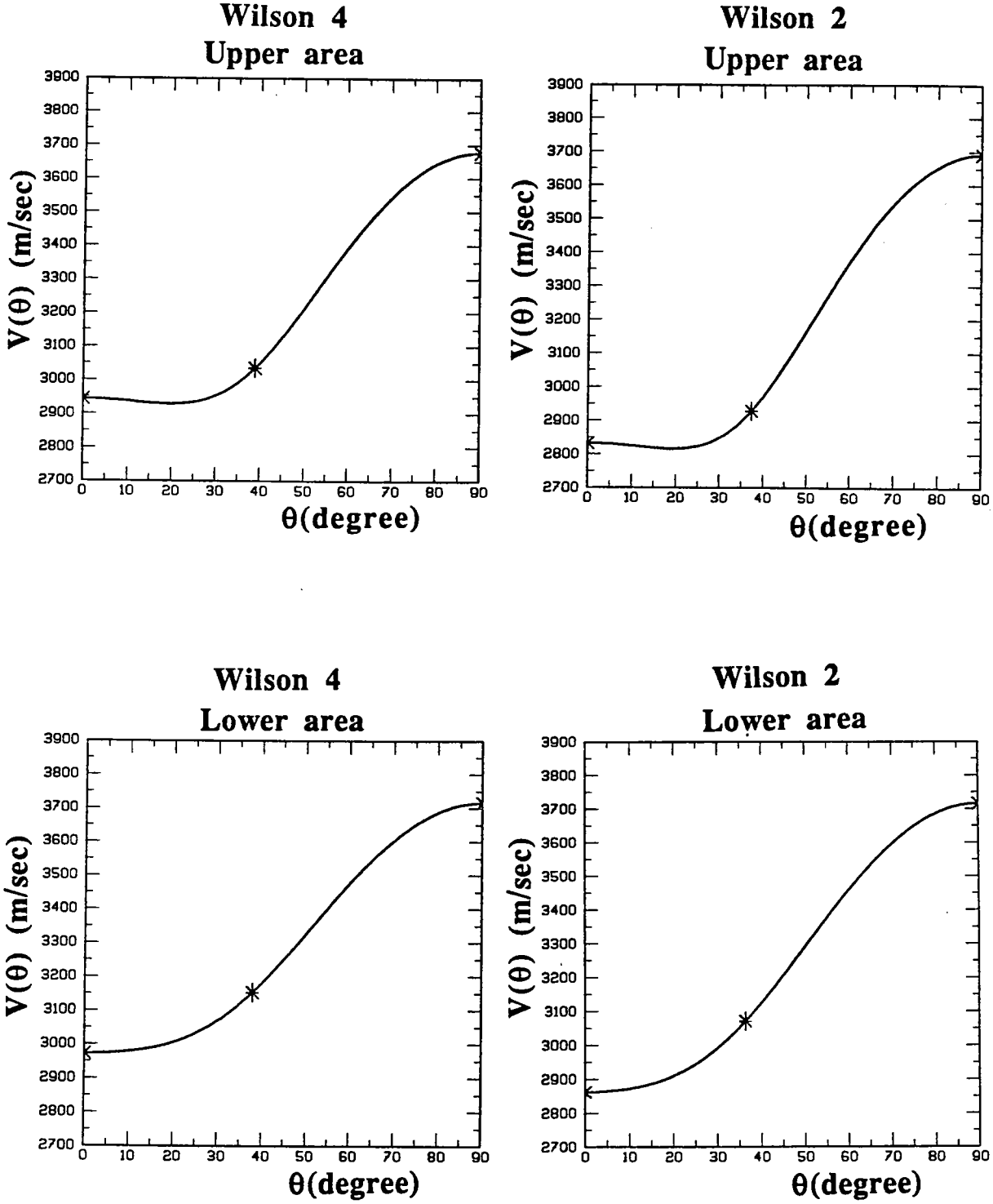

Figure 16: Relation between a phase velocity and a phase angle.
* represents θ_c and $V(\theta_c)$ derived from the head wave analysis.

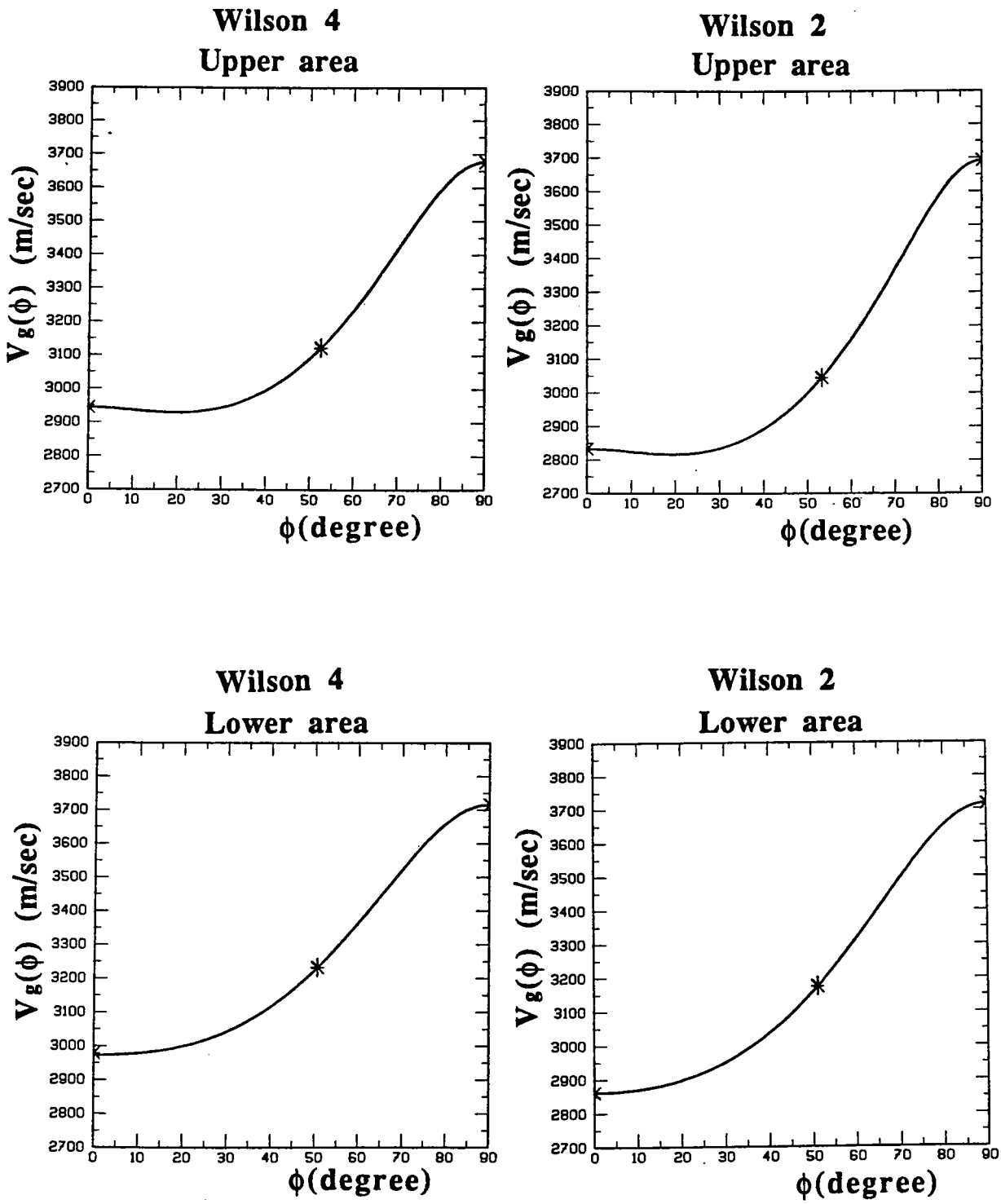

Figure 17: Relation between a group velocity and a group angle.

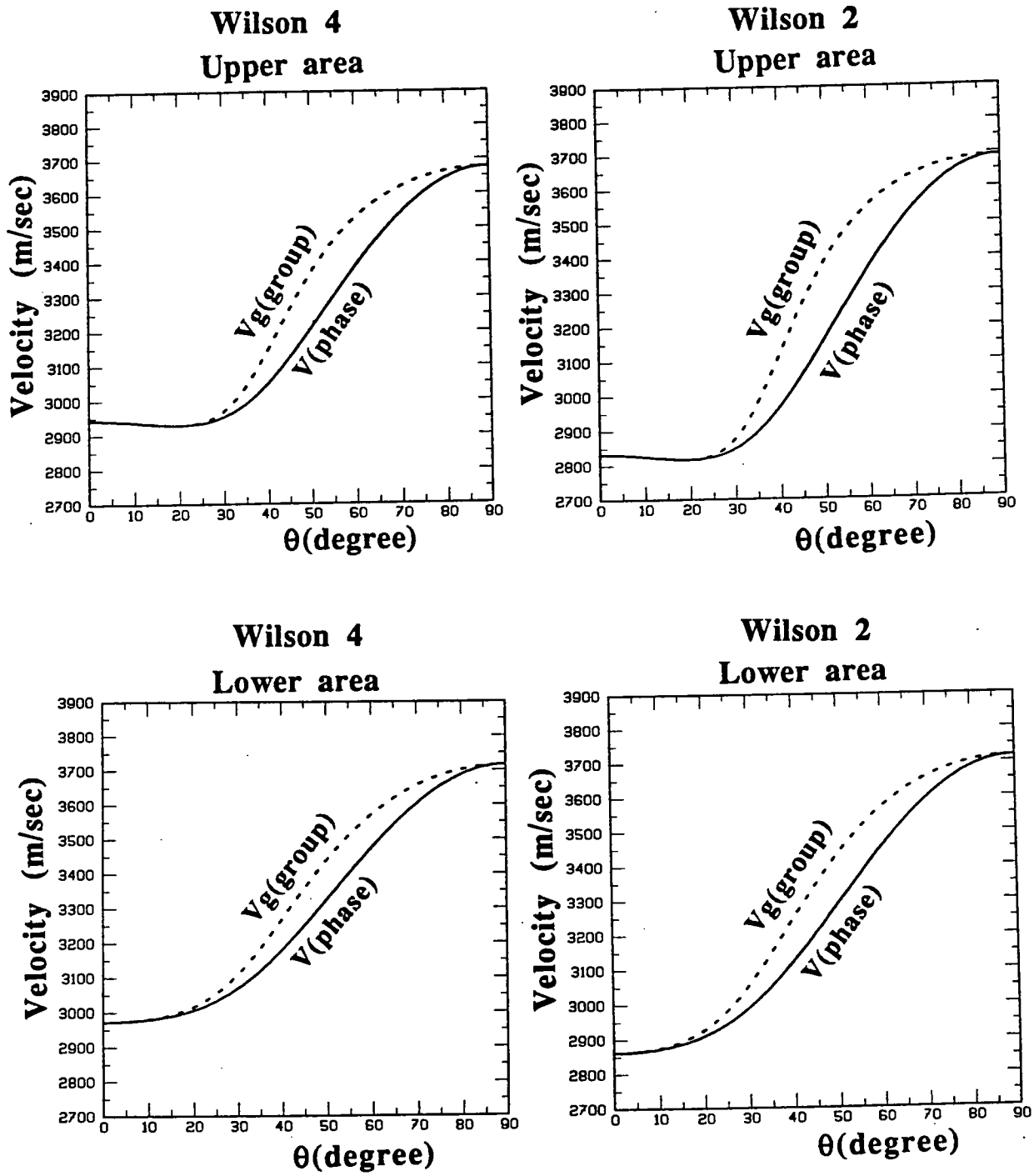

Figure 18: Comparison between the phase and group velocities. The solid and dashed lines represent $V(\theta)$ and $V_g(\phi)$ along θ.

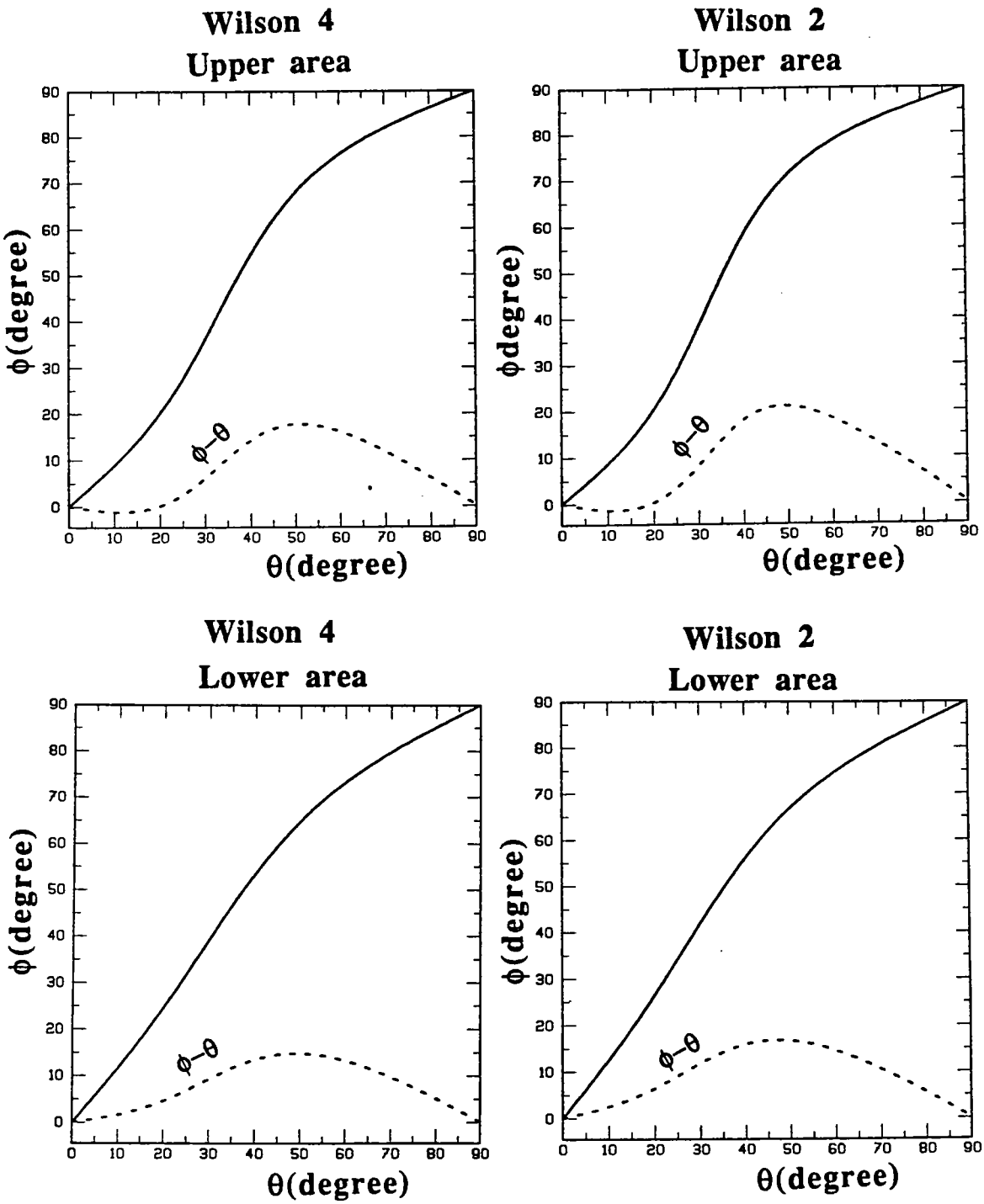

Figure 19: Comparison between θ and ϕ. The dashed line represents ϕ-θ.

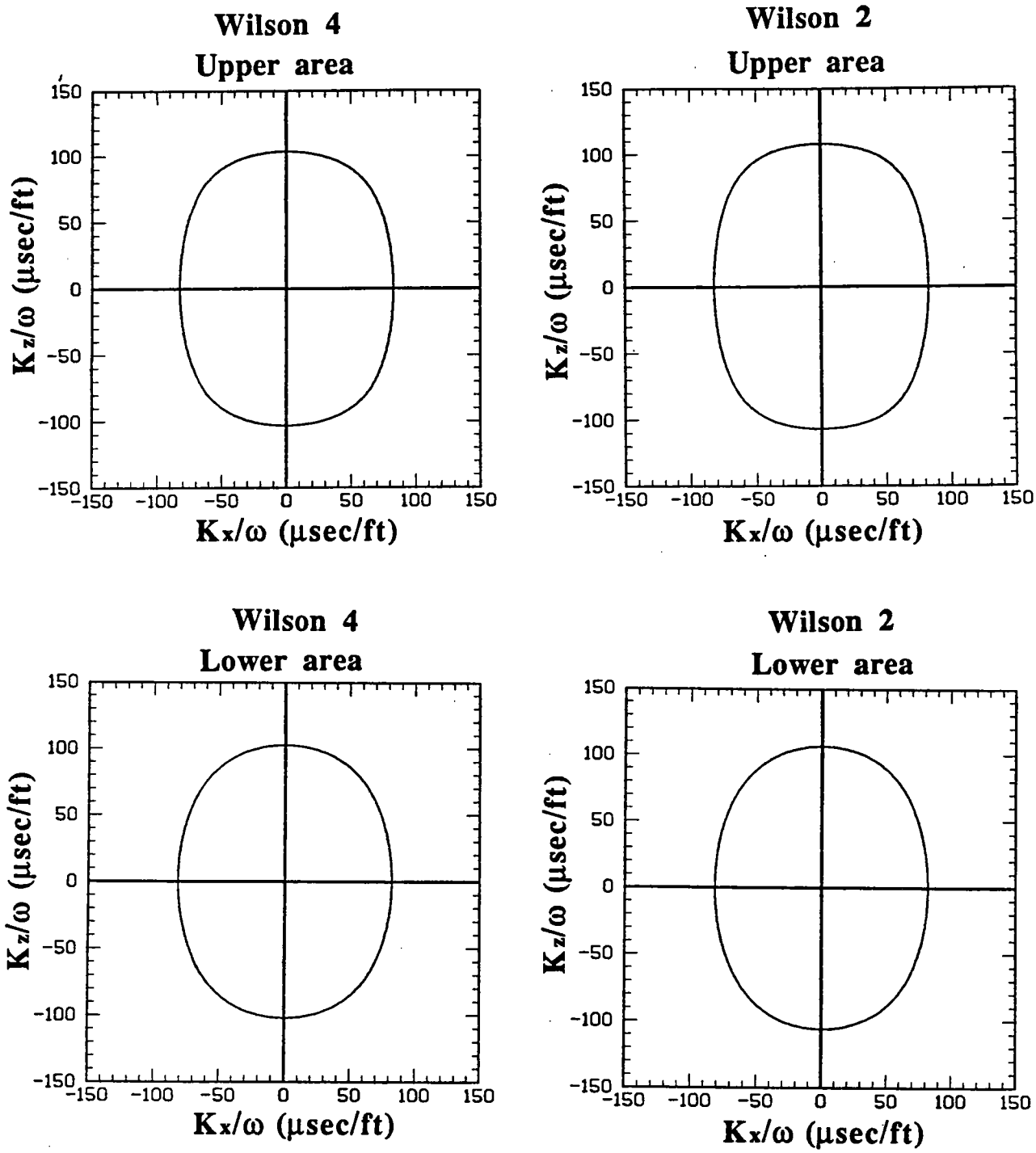

Figure 20: Slowness surface of a quasi-P wave.

CONCLUSION AND DISCUSSION

This feasibility study shows that the theory for the head wave analysis presented in the first part of this paper fairly is applicable for in-situ estimating anisotropy of sedimentary rocks. The actual analysis of using real crosswell and logging data suggests the following facts.

- We can successfully estimate the velocity of a quasi-P wave if we know the horizontal, vertical and one oblique velocity and its angle of a quasi-P wave. The head wave greatly contribute to obtaining the oblique velocity and its angle. Actually the analysis of head waves provide us with a critical phase velocity and its angle.

- The determination of C_{13} requires an accurate measurement of a shear wave velocity in addition to those velocities. Small errors for the velocity measurements cause a large error for the calculation of C_{13}.

- The spatial variation of anisotropic properties can be detectable from the behavior of phase or group velocity to its propagation angle.

The vertical variation of the anisotropic properties of the clay formation should be carefully examined. Compared to a measurement in a laboratory, the accuracy in in-situ measurements are restricted by the wave length of seismic waves and the geometry of the survey. For example, the horizontal velocity used in the analysis has no lateral resolution. For more detailed analysis, the lateral variation of such a velocity is required. In order to confirm the results and to study what causes the variation, core analysis is strongly recommended.

ACKNOWLEDGEMENT

We would like to thank BP Exploration, Inc. for providing us with the field data used in this study. The first author also thanks Japan Petroleum Exploration Co., Ltd (JAPEX) and Japan National Oil Corporation (JNOC) for financially supporting the graduate study at Stanford University.

REFERENCES

Berryman, J., 1979, Long-wave elastic anisotropy in transversely isotropic media: Geophysics, **44**, 896-917.

Harris, J., 1988, Cross-well seismic measurements in sedimentary rocks: SEG Extended Abstracts, Anahaim

Onishi, M. and Harris, J., 1991, Anisotropy from head waves in crosswell data, part 1: Paper D, this volume

Thomsen, L., 1986, Weak elastic anisotropy: Geophysics, **51**, 1954-1966.

PAPER F

ROCK PROPERTIES INTERPRETATION OF A CROSSWELL SEISMIC IMAGE

Nathalie Lucet and Gary Mavko

Stanford Rock Physics and Borehole Project
and
Seismic Tomography Project

ABSTRACT

This paper presents techniques to interpret a seismic velocity tomogram in terms of rock properties, such as porosity and clay-content. Three different approaches were used. In the first approach, we use purely "rock physics" techniques, where we apply relation between velocity and porosity obtained either from the laboratory or from the log data. In the second approach, we use geostatistical tools such as kriging or cokriging to estimate rock properties in between the wells, using both velocity information between the wells and log data at the wells. The last technique uses both our rock physics knowledge and geostatistics tools

INTRODUCTION

The essential purpose of geophysical (seismic) imaging is to detect heterogeneities in rock properties, pore fluids, and ambient conditions such as temperature and stress. Conventional seismic reflection surveys can give excellent images of velocity boundaries, since they measure reflectivity; but their spatial resolution (at typically 30-60 Hz) is often no better than several 10's to 10^2 m, and absolute velocities may be poorly constrained due to ambiguities in depth. In contrast, crosswell seismic images can achieve spatial resolution (at 1000-2000 Hz) of less than a few meters, and absolute velocities are more accurately constrained, because both traveltime and path length are well defined.

In this paper we discuss ways to exploit the superior accuracy and resolution of crosswell seismic images to infer rock properties between wells (for example, porosity and shaliness). We will discuss the use of geostatistical toolsi, specifically kriging, but we focus also on the role of rock physics—the relations between seismic and rock properties, which in geostatistics relate to the "soft" part of the problem. We emphasize the rock

physics relations for several reasons:

- At typically large interwell spacings, seismic data provide the only high resolution information about spatial heterogeneities in most of the interwell region (distances beyond the correlation range). Consequently, estimations of porosity will be dominated by the "soft" seismic data and not by the "hard" log data.
- Laboratory work suggests that the correlations between seismic and rock properties should often be better than that obtained from well logs. The usual logging problems related to depth errors, washouts and hole rugosity, environmental corrections, and acquisition through casing can cause correlations to appear misleadingly poor. Furthermore, laboratory and theoretical work have shown that better correlations can be obtained if seismic velocity is related to a combination of several rock properties.
- Log-derived "hard" estimates of porosity are interpreted indirectly from measurements such as electrical conductivity, gamma ray or neutron absorption, and sonic travel time, and may be no more direct than those inferred from "soft" crosswell seismic data.
- Some recently reported interpretations of crosswell images do not reflect current knowledge of seismic-rock properties relations, and would be improved by doing so.

We begin by describing very briefly a velocity tomogram. We then summarize some laboratory and log-derived relations between seismic and rock properties. Finally we present preliminary results of estimating porosity from the tomogram using a combination of rock physics and geostatistical techniques.

THE CROSSWELL TOMOGRAM

We use a seismic compressional wave tomogram constructed in Miocene sediments of the onshore Gulf of Mexico area (Fig. 1). This tomogram is simply a colored contour 2-D image of the estimated seismic velocities between the wells. The cross-section of interest is approximately 250 ft (76 m) wide (distance between the two boreholes) and 1140 ft (348 m) high, between depths of 2700 ft (824 m) and 3840 ft (1171 m). The region studied consists of relatively flat layers of sands, shales, and shaley sands truncated and offset by various steeply dipping faults. The original crosswell study (Harris et al, 1990) focused on the ability to image these faults which were previously mapped in the deeper Frio formation and continued upward into the region between the wells. In the tomogram, the fastest velocities correspond to low porosity shales and the lowest velocities correspond to high porosity sands.

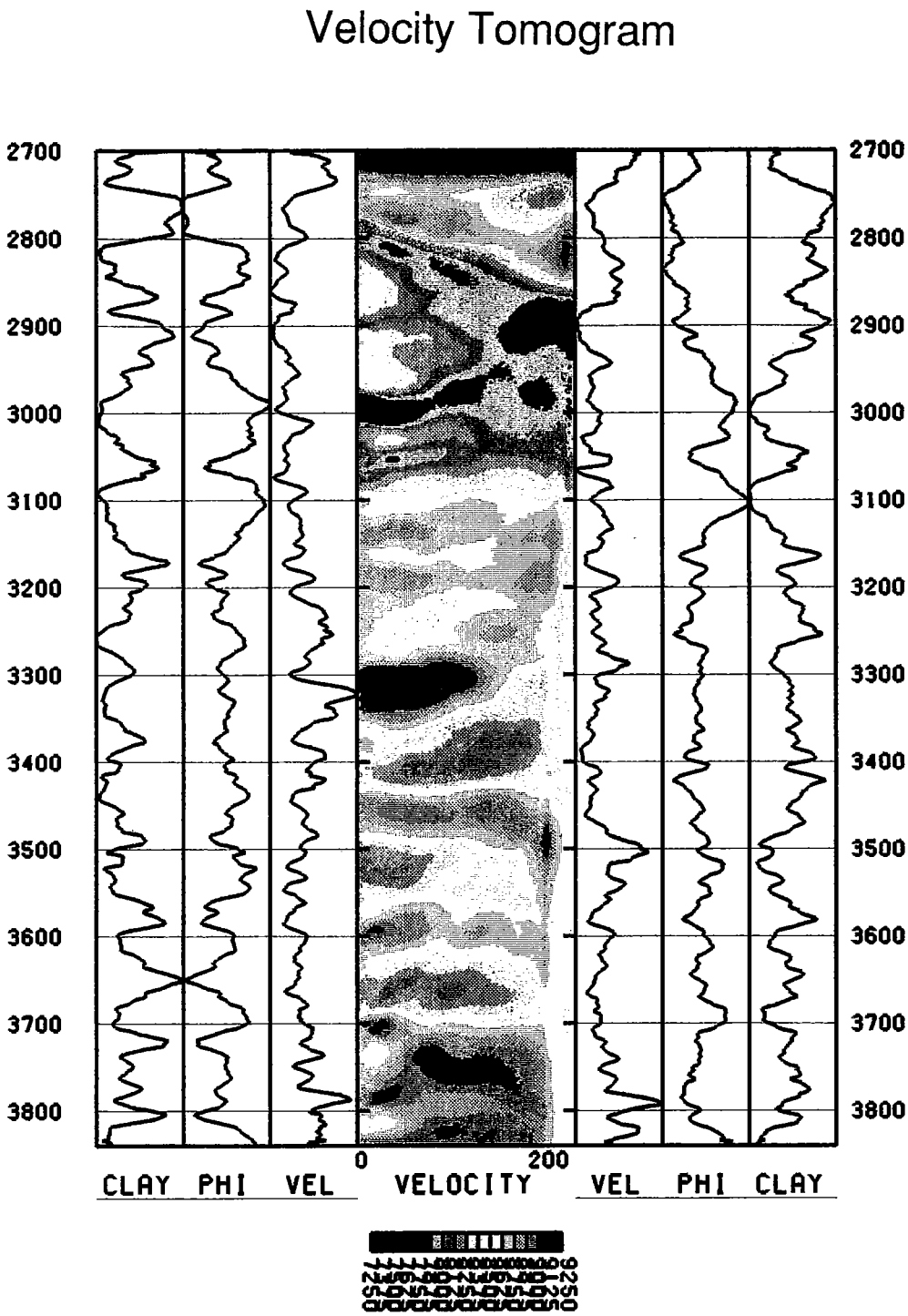

Figure 1. The crosswell tomogram of compressional wave velocities, along with well logs: porosity, clay, and velocity. (see Harris, et al. 1990).

The crosswell survey geometry is shown schematically in Fig. 2. A series of seismic source positions lies within one well and a series of receiver positions lies in the second. In this experiment there was one source tool and a string of three receivers. During the data acquisition the receivers were held stationary while the source occupied many different depths, ranging from below the receivers to above them, such that the ray paths spanned a range of angles at roughly $\pm 45^{o}$ from the horizontal. The receivers were then moved to a slightly different depth and held fixed while the source was again moved through a range of depths. When the survey is complete, the data traces can be sorted into high fold common source gathers or "fans" or common receiver "fans". A portion of a receiver fan is shown in Fig. 3.

The seismic source was a piezoelectric bender bar, which was swept over a frequency range of 400 Hz to 1600 Hz. The receivers were unclamped hydrophones. The recorded traces were cross correlated with the input sweep signal, giving the traces shown in Figure 3.

Tomography is simply the process of finding a distribution or map of velocities that can explain the many different traveltimes of the rays that redundantly sample the region between the wells at many different angles. For this survey there were more than 5000 rays. The velocity tomogram in Fig. 1 was constructed from the picked traveltimes of the direct arrivals on the recorded data. The traveltime inversion problem is nonlinear and is solved iteratively as follows:

(1) An initial velocity model is assumed, which in this case was homogeneous.
(2) Rays are traced through the velocity model to find the geometry of the ray paths between all of the source/receiver pairs and the corresponding traveltimes.
(3) The difference (residuals) between the observed and computed traveltimes is found.
(4) The velocity model is updated by distributing the residuals back along the ray path.
(5) Go to step (2).

For more details, see Harris et al.,1990.

A potentially important aspect of the tomographic imaging process, which can impact statistical analyses, is imaging anisotropy, which should not be confused with geological anisotropy or with seismic anisotropy. This imaging anisotropy is an apparent smearing of the image more in the horizontal direction than in the vertical direction. It simply means that in a crosswell environment our resolution is better in the vertical direction than in the horizontal direction, and it results from incomplete seismic ray coverage of the interwell region. Poor resolution will tend to increase the correlation range estimated from the image,

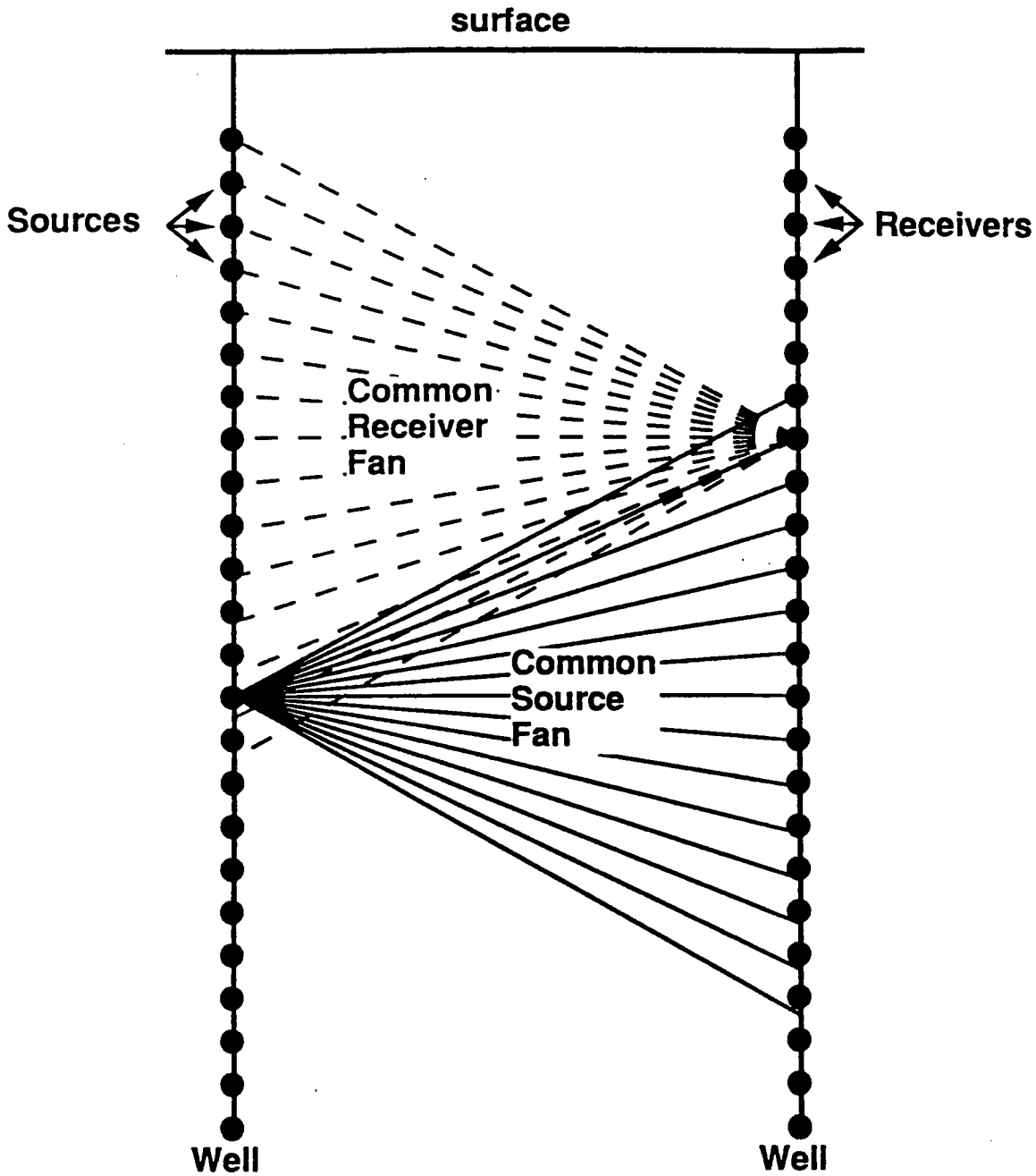

Figure 2. Typical crosswell seismic survey geometry. Sources lie in one well, receivers in the other. The solid and dashed lines show a few idealized seismic ray paths, collected here into common source and common receiver fans, respectively. In an actual inversion the rays will not be straight.

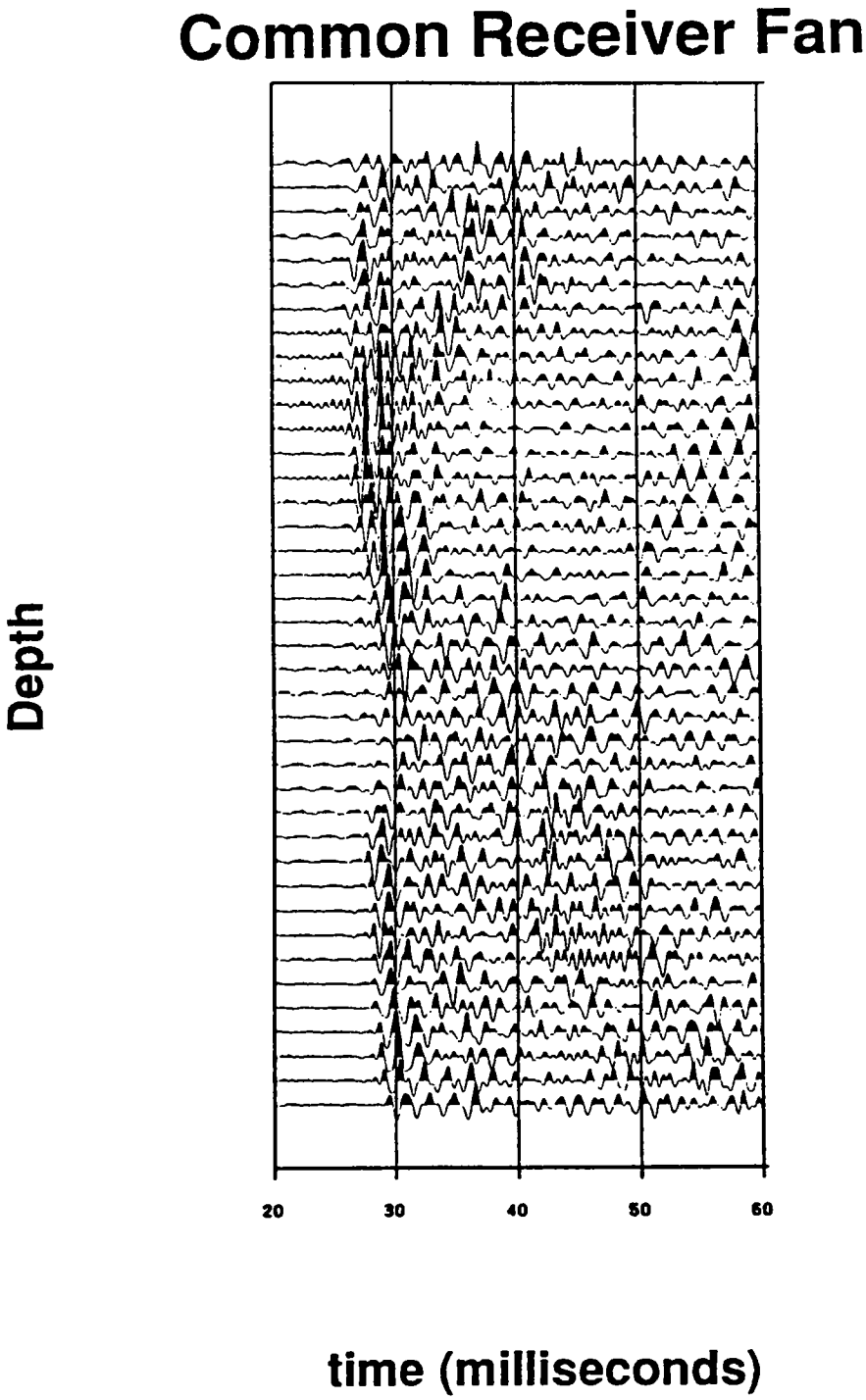

Figure 3. A portion of the traces in a common receiver fan after correlation with the sweep. Each trace is the signal recorded at the same receiver, but from a different source depth.

when the scale of resolution is comparable to or greater than the actual correlation range.

This smearing or imaging anisotropy can be difficult to detect visually, since we usually expect the geology to be more coherent horizontally than vertically. In our work, we have not done anything specifically to estimate the amount of imaging anisotropy, but it is a topic of current research.

SEISMIC-ROCK PROPERTIES RELATIONS

A critical part of the interpretation of velocity in terms of rock properties, such as porosity, is the velocity-porosity relation. We know from laboratory and theoretical work that compressional wave velocity depends on many parameters: mineralogy, porosity, cementation, pore fluid content, pressure, temperature, etc. Consequently crossplots of velocity vs. porosity almost always show large scatter. The scatter is usually not a problem of random errors in measurements, but an expression of other parameters that are not controlled. We show in this section that considerable improvement can be found by considering the coupled effect of clay. Furthermore, attempts to extract porosity from velocity data will be improved with information about clay content.

A particularly valuable data set, which we have used in our work to interpret the Gulf Coast tomogram, was collected by Han (1986) in the Stanford Rock Physics and Borehole Project. In this work Han measured the ultrasonic compressional and shear velocities, V_p and V_S, on Gulf Coast sandstones as functions of confining pressure up to 50 MPa in both gas saturated and water saturated states. Eighty sandstone samples were studied with porosity ranging from 2 to 30 percent and clay content from 0 to 50 percent. Ten samples were clean sandstones, and the remaining were shaley . We summarize some of Han's results here.

A plot of measured compressional velocity vs. porosity at high confining pressure (40 MPa) is shown in Fig. 4. The plot shows a trend of velocity decreasing with increasing porosity, but with considerable scatter. A simple linear regression was found:

$$V_p(km/s) = 5.02 - 5.63\ \phi \qquad (3)$$

where ϕ is the volume fraction of pores (porosity). The correlation coefficient is 0.8.

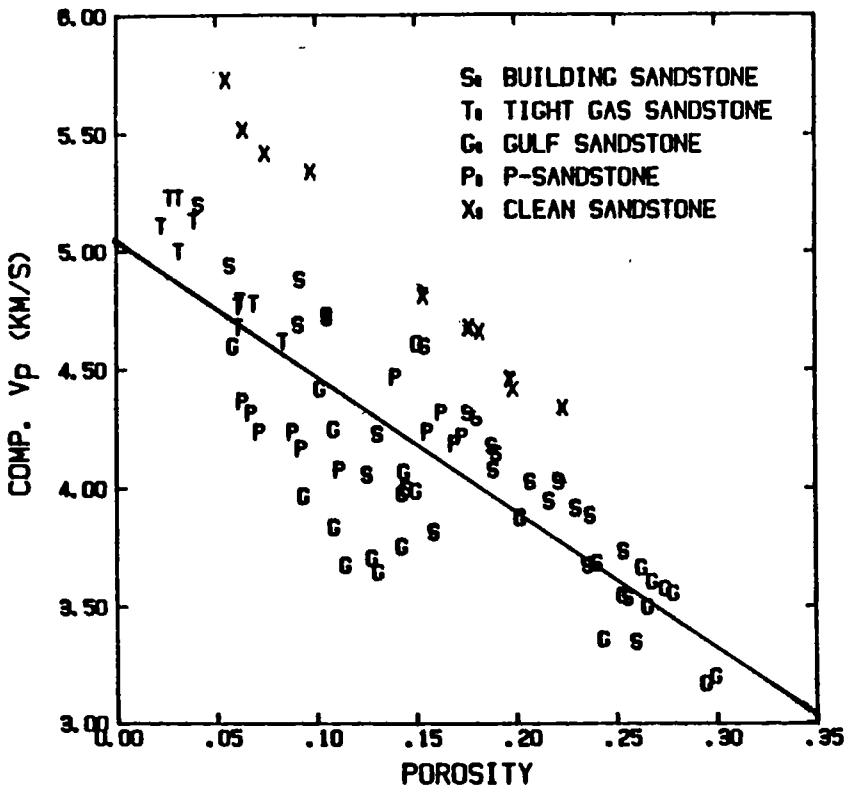

Figure 4. Laboratory measured compressional velocities vs. porosity for 80 consolidated Gulf Coast sandstone samples (Han, 1986, Chapter 2, Figure 2).

Han discovered that the scatter was related primarily to clay content, and that at a confining pressure of 40 MPa, the water saturated data can be described much better with a linear regression of the form

$$V_p\ (km/s) = 5.59 - 6.93\ \phi - 2.18\ C \qquad (4)$$

where C is the clay volume fraction. The correlation coefficient relating velocity to porosity and clay volume is improved to more than 0.9. Note that the coefficients on ϕ and C are negative indicating that both porosity and clay tend to decrease velocity. Also, the ratio of these two coefficients indicates that clay is about 1/3 as effective as porosity in reducing the velocity. The regression coefficients change slightly as a function of effective pressure (confining pressure minus pore pressure) but are fairly stable at effective pressures above 10 MPa. The linear regression is somewhat worse at lower effective pressures indicating a dependence on other parameters, such as cementation, compaction, and microcrack porosity. Fig. 5 shows a plot of the ratio predicted/measured velocity vs. porosity, using both Eqns. 3 and 4.

The study suggested that clay is the next most important parameter after porosity affecting velocity. Other variables such as mineral composition, cementation, compaction, pore geometry, grain size, and clay types show much less influence on velocity, particularly when the rock is fluid saturated. Their influence is greatest at low effective pressures, accounting for much of the observed scatter in the regressions. The influence of these secondary variables is greatly diminished at high confining pressure and with fluid saturation.

At a confining pressure of 40 MPa the velocities of water saturated *clean* sandstones (clay volume less than 1%) can be described with a linear regression which depends only on porosity:

$$V_p\ (km/s) = 6.08 - 8.06\ \phi \qquad (5)$$

with a correlation coefficient greater than 0.9.

The differences in the above relations for clean and shaley sandstones, in particular the zero clay intercept, suggest that a small amount of clay (1 or a few percent by volume), presumably placed along grain boundaries, can significantly soften the sandstone matrix.

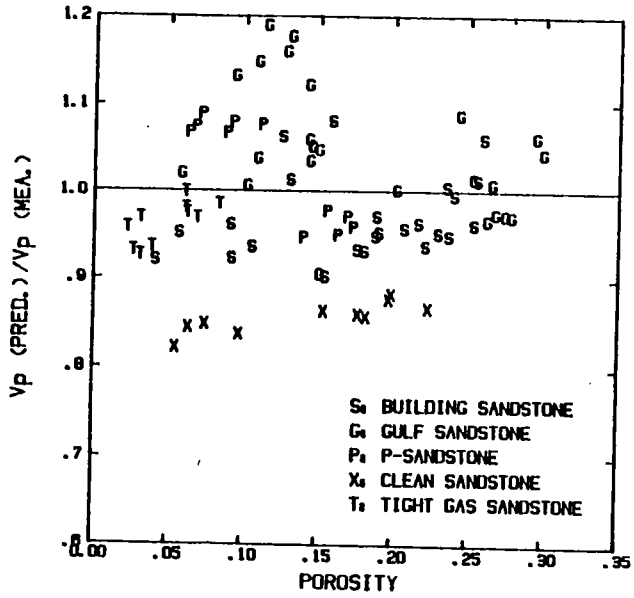

(a)

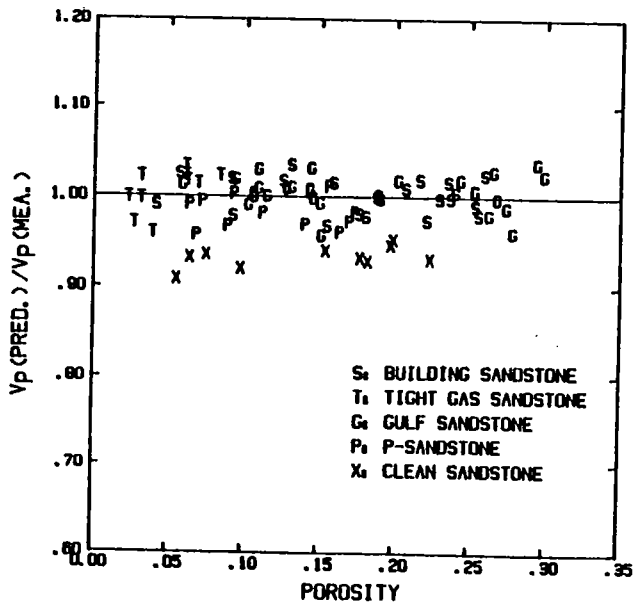

(b)

Figure 5. Compressional velocities from laboratory measurements of consolidated Gulf Coast sandstone samples (Han, 1986, Chapter 2, Figures 4 and 5).

(a) Ratio of predicted over measured velocities vs. porosity showing the apparent random distribution when clay is ignored.

(b) Ratio of predicted over measured velocities vs. porosity when clay is included.

For our purposes, the important conclusions to draw from Han's work on Gulf Coast sandstones include the following:

(1) Compressional wave velocities correlate very well ($\rho = 0.9$) with porosity in very clean (clay volume < 1%), water saturated sandstones, under moderate to high effective pressure (Eqn. 5).
(2) The correlation between velocity and porosity degrades ($\rho = 0.8$ when clay volume is ignored) for the samples with clay volume > 1%. However, the correlation is still relatively good compared to what can often be estimated from well logs.
(3) Clay volume is the next most important parameter after porosity in determining velocity. Velocity correlates well ($\rho = 0.9$) with a linear combination of porosity and clay volume.
(4) To first order, velocities do not appear to be sensitive to the location of clay particles, or to the composition of clay (Tosaya, 1982; Han, 1986).
(5) In sand-shale environments, porosity estimates can best be made from velocities if additional information about lithology or clay content is supplied, such as from wells logs.

It is of course obvious that these relations are not universal. We have studied Han's results, because both his data and the tomography data are from the Gulf Coast. Differences are to be expected when moving from one site to another, due to differences in additional parameters, such as cementation, compaction, etc. For example, we find that in more poorly consolidated Gulf Coast sands, velocities may be lower than predicted by Han's relations, and the correlations might be not quite as high. Nevertheless, in shaley sands we expect that clay volume to be a critical parameter in explaining observed velocities.

No cores were available at the site represented by the tomogram in Figure 1, so to test the applicability of the velocity-porosity-clay model we looked at well logs (for more details, see VanSchaack and Mavko, this volume). Velocity was derived from the sonic log; clay index (proportional to clay volume) was extracted from the gamma ray logs; and porosity was derived from a combination of resistivity and clay volume. All logs were carefully correlated to compensate for depth errors, and samples were extracted every 0.5 feet. For comparison with the work of Han, only values with volume fraction of shale less than 50% were used.

A linear regression with porosity alone gives

$$V_p\ (km/s) = 3.1 - 2.3\ \phi \qquad (6)$$

with a correlation coefficient of 0.46. When the clay index, C_I, is included the regression becomes

$$V_p\ (km/s\ ) = 4.3 - 4.9\ \phi - 2.3\ C_I \qquad (7)$$

with correlation coefficient 0.78 Again there is a reduction in the scatter when the clay content is included, indicating that porosity can be best estimated from velocity, if information about clay content can be supplied.

Differences in observed behavior between the laboratory and log results can be attributed to many causes such as measurements accuracy in the borehole, different measurement scales, and petrophysical differences, even though both experiments were from the Gulf Coast region. The lower velocity values at any given (ϕ, C) pair are probably due to less compaction and cementation in the field site. We believe that a large part of the scatter in the V_p-ϕ-C correlations in the field is due to the difficulty of making log measurements. We found, for example, that the caliper log indicated poor hole conditions in much of the sands, with the worst occurring with the cleanest sands. We believe that under ideal conditions—perfect depth control, good hole quality, calibrated logs, and redundant measurements—the correlation coefficient would approach that seen in the lab, or at least lie somewhere between our lab and field values.

POROSITY ESTIMATES

Our objective is to construct a porosity image between the two boreholes, using the available data through three different approaches applying (1) rock physics relations obtained in the laboratory or in the borehole, (2) geostatistical techniques, and (3) a combination of geostatistics and rock physics.

Rock Physics

In this approach we use deterministic porosity-velocity relations derived from the laboratory or the borehole to construct the porosity images from the velocity tomogram. The

simplest and the most commonly used way to relate velocity to porosity is to use the Wyllie time average equation that assumes that the traveltime in a rock is simply the sum of the travel times in the matrix and in the fluid-filled pore:

$$\frac{1}{V} = \frac{\phi}{V_{fl}} + \frac{1-\phi}{V_0}$$

Where V is the tomogram velocity, ϕ is the porosity, V_{fl} is the pore fluid velocity, and V_0 is the mineral velocity. The porosity image (Figure 6) is found by solving Wyllie's equation for porosity and substituting in the tomogram velocity pixel-by-pixel. This approach greatly overestimates the porosity because: (1) the relation does not take into account the effect of the clay and (2) Wyllie's equation is best suited for more consolidated rocks. Note also, that this one-to-one mapping creates a porosity image that looks identical to the tomogram, since it essentially rescales the color code.

A better approach is to use a velocity-porosity relation that includes the effect of clay, but this requires an estimate of the clay between the wells. Our first approach is to assume a bimodal distribution of clean sands and shaley sands. To do this the presence or absence of clay near the wells was determined from the SP logs. The corresponding velocities at the wells were then used to discriminate clean from shaley sandstones in the region between the wells. At each pixel, porosity was calculated from the velocity with the Eqn. 7, assuming a fixed clay volume of 0.05 in the clean sands and 0.15 in the shaley sands. The resulting image, shown in Fig. 7, shows much more reasonable porosities, since the velocity-porosity-clay relation determined in the wells is used. However, the estimate of clay is very crude and the image still has the appearance of a rescaled version of the velocity tomogram, because of the one-to-one mapping function that was assumed.

Geostatistical techniques

In this approach, we use purely statistical techniques: the porosity Φ and velocity V are treated as two random fields, and we make no *a priori* assumptions about their relation. Instead, we estimate their auto- and cross-correlations statistically from the data. The spatial distributions of the velocity ($v(\mathbf{x})$ from the tomogram) and porosity ($\phi(\mathbf{x})$ from the logs) are assumed to be particular realizations of the random fields $\Phi(\mathbf{x})$ and $V(\mathbf{x})$ where the vector $\mathbf{x}=(x,z)$ indicates the position of the pixel of interest.

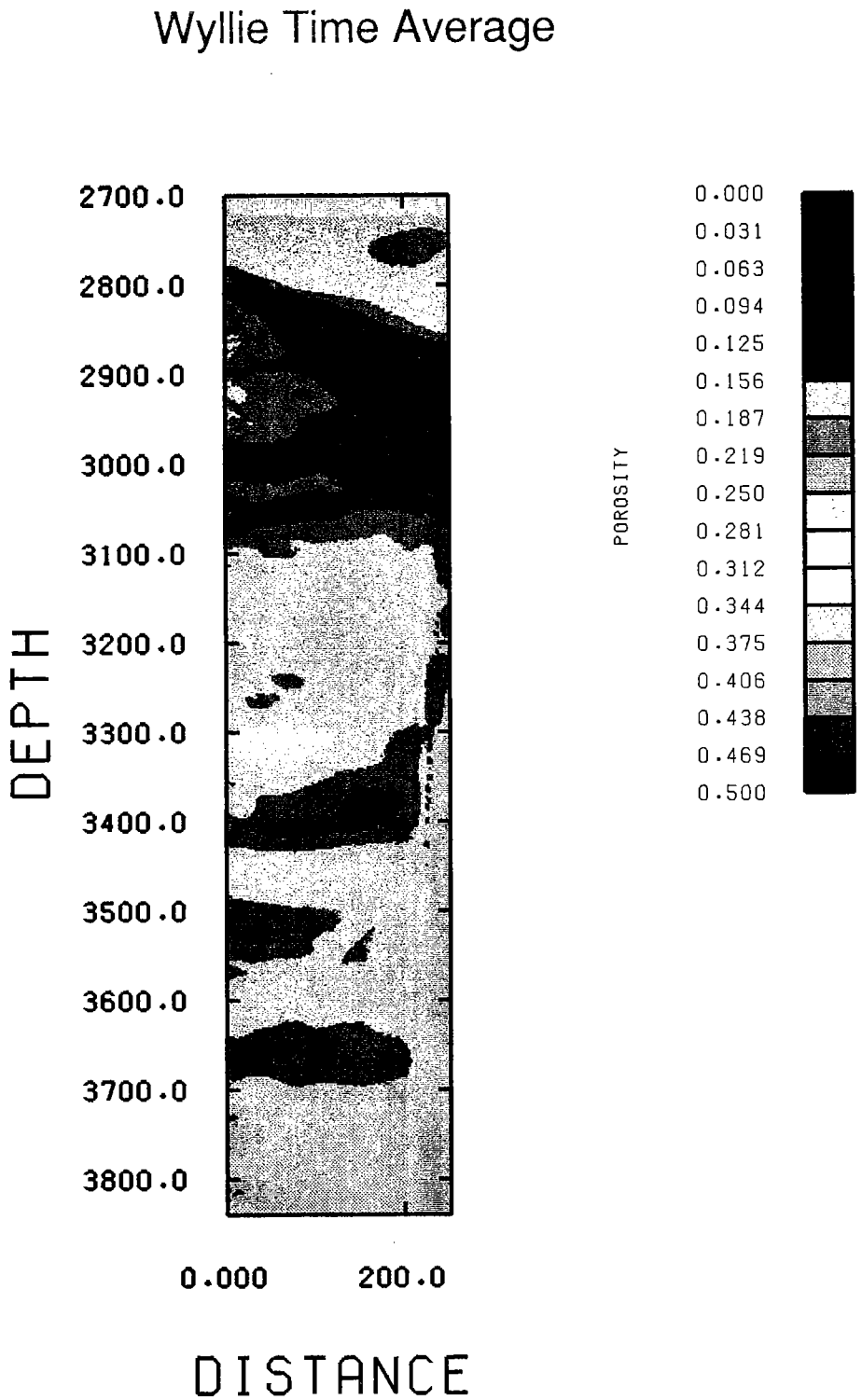

Figure 6. Porosity image estimated using Wyllie's time average equation. The method overestimates the porosity, and the image is simply a rescaled version of the velocity image.

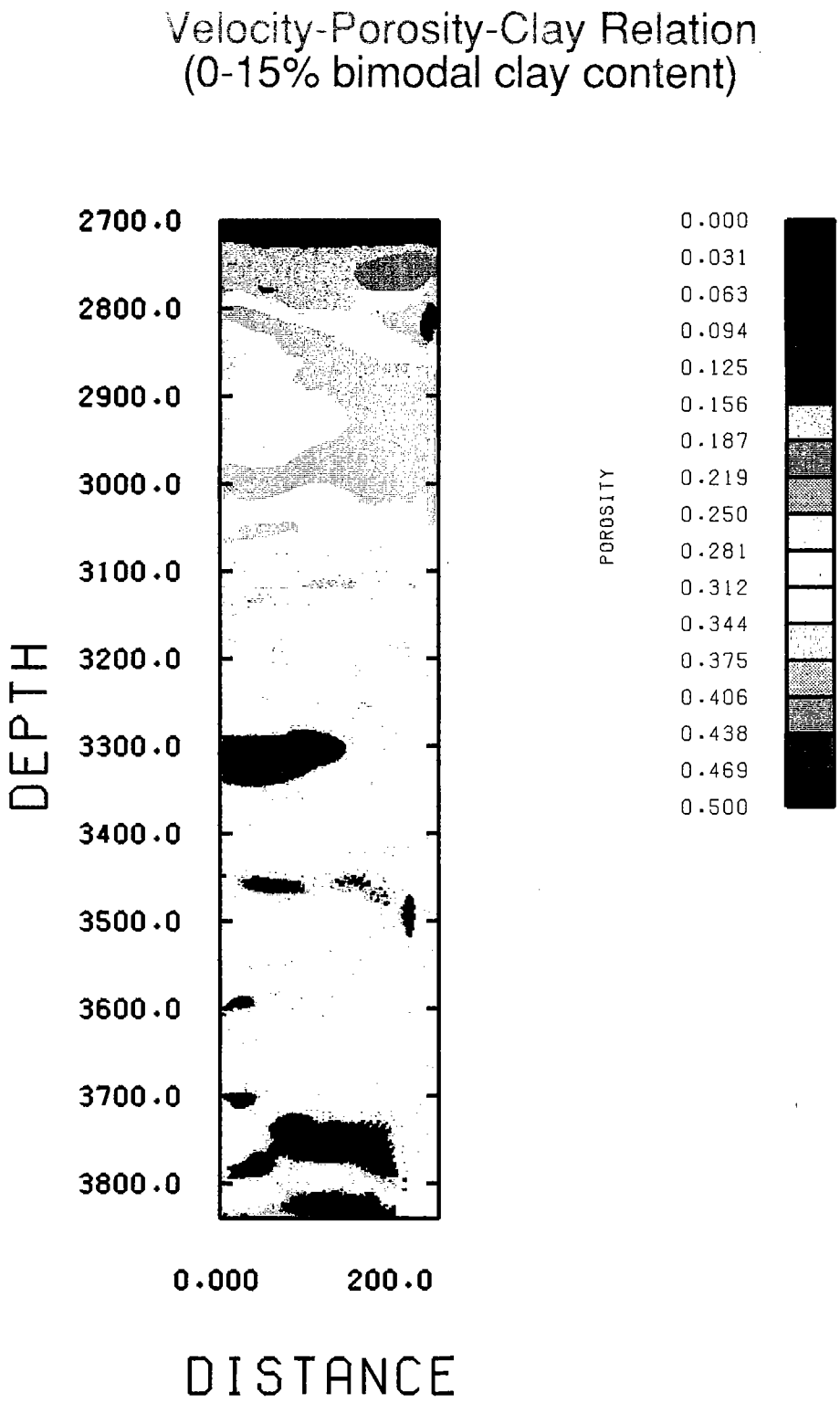

Figure 7. Porosity image estimated using the velocity-porosity-clay relation. Inputs are the velocity tomogram and a bimodal map of clay content (5% vs. 15%), which was constructed by comparing the tomogram and SP log, without any geostatistics.

Data

The available data consists of

- the distribution v(x,z) of the seismic velocity (tomogram). Velocities, that we can consider as "soft" information, are given at each pixel of a 126x570 grid, where the spacing of the grid is 2 feet.
- the distribution $\phi(x,z)$ in the two boreholes. These 2 logs were resampled to 2 feet spacing to match the tomogram grid spacing. "Hard" type information is then available at the edges of the grid for z varying between 1 and 570. On the left-hand side, x is equal to 1 whereas it varies from 113 to 126 on the right-hand side, to take into account the deviation of the well.

Correlations

The first step is to calculate the spatial autocorrelations C_{vv} and $C_{\phi\phi}$ of the velocity and porosity fields and the crosscorrelation $C_{v\phi}$ of the bivariate field. Non-ergodic correlograms computed using the GAM2M.F program of the GSLIB software are presented in Fig. 8. These correlograms were computed on both horizontal (o) and vertical (*) axes to take into account the obvious anisotropy that can be seen on the velocity tomogram, and which is related to the horizontal stratification. On Figure 8, the vertical to horizontal anisotropy appears as both an additional component of variability in the vertical direction due to stratification and a larger range in the horizontal direction (110 units, i.e., 220 ft vs. 120 ft in the vertical direction). In fact, we decided not to model the additional component of variability in the vertical direction (zonal anisotropy) because the data retained in the subsequent cokriging do not exhibit vertical coordinates differences large enough to be affected by that anisotropy.

The porosity correlogram is estimated in the vertical direction only since the porosity is available only from the logs in the vertical direction. As can be seen on Figure 8, the range is about the same as that found for the vertical velocity correlogram (about 60 units, i.e., 120 ft).

The crosscorrelogram gives a measure of the spatial interdependence between the velocity and the porosity. Negative values are related to the decreasing variations of the velocity as a function of the porosity: low (respectively high) values of velocities correspond to high (respectively low) values of porosities. As expected, the vertical

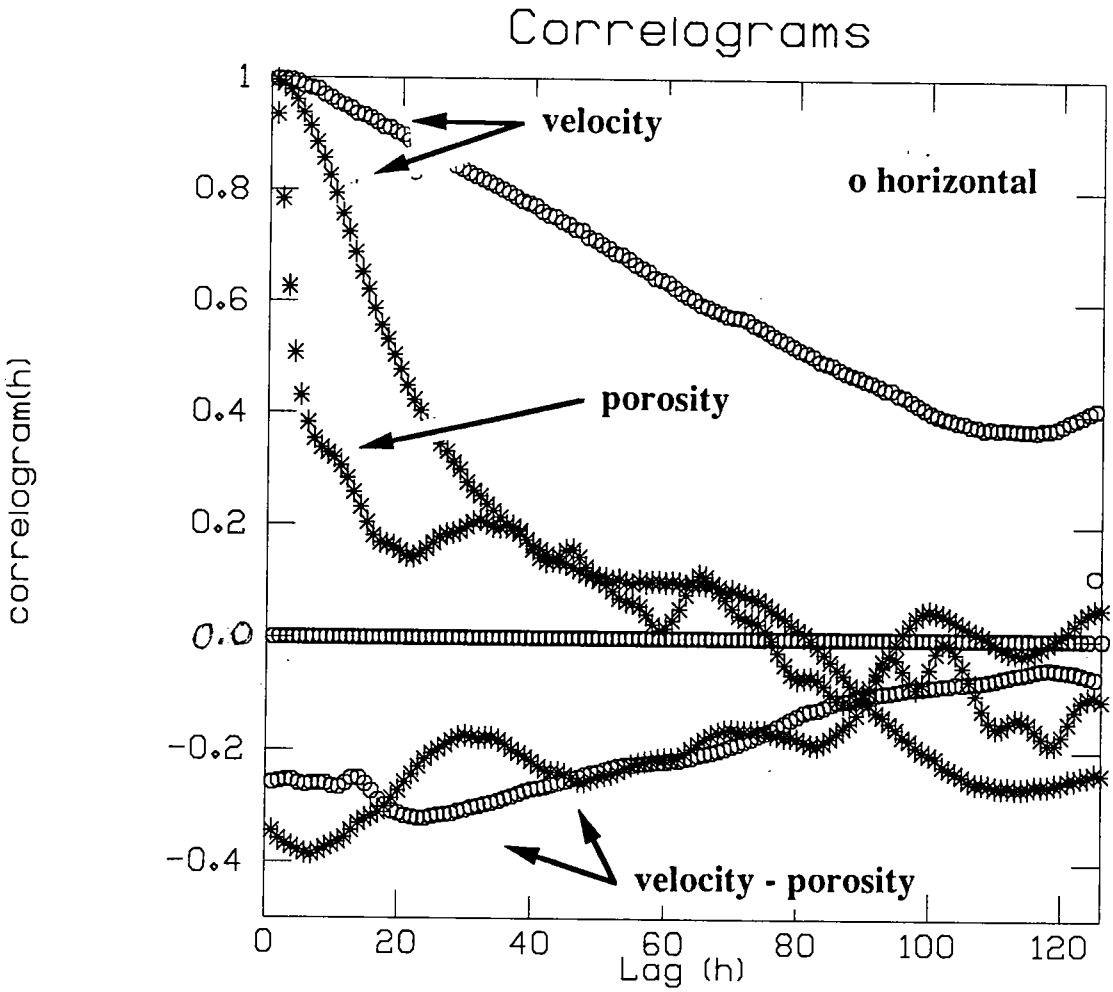

Figure 8. Correlograms and cross-correlograms of log-derived porosity and tomogram seismic velocity.

correlogram exhibits a shorter range (120 ft) than the horizontal correlogram (220 ft). It is interesting to compare the zero lag value of the crosscorrelation ($C_{v\phi}(0)$) to the crosscorrelation obtained in the laboratory from the relation between the porosities and the velocities. In the laboratory, we find $C_{v\phi}(0)= 0.8$ whereas it is equal to 0.5 from the field data. For rock physicists, this value of 0.5 is then much lower than expected. This result suggests that there are many more variables and sources of error in the field data than in the lab.and we expect that improvement of the field data quality would lead to a better correlation for use in geostatistical techniques.

Even if the shapes and range of the auto- and cross-correlograms are not quite similar, we decided in a first step to model the correlograms by spherical models.

Ordinary Kriging of Φ

Porosity was first estimated using ordinary kriging of the porosities at the wells, using the OKB2DM.F program of the GSLIB software. The resulting image in Figure 9, illustrates that the kriging is little more than an interpolation of the values at the wells. There is virtually no laterally heterogeneity in porosity, because there is no additional information supplied between the wells. This is the intuitive image that an interpreter might make by simply trying to extend the known information away from the wells.

Cokriging V-Φ

Porosity was next estimated at each pixel using the simple cokriging technique, in which we introduce the tomogram as indirect information about heterogeneities between the wells. Because of the densely sampled data, the mean m_v and m_ϕ of the distributions can be computed with a good accuracy, and an easy way to simplify the algebra is to use centered values v_c and ϕ_c defined as $v_c= v-m_v$ and $\phi_c= \phi-m_\phi$. The unbiasedness condition is then automatically fulfilled and the estimated porosity Φ_{est} can be simply estimated from a simple linear combination of the "hard" ϕ_c data at the well and "soft" velocities v_c from the tomogram:

$$\Phi_{est} = \Sigma a_i \phi_i + \Sigma b_j v_j.$$

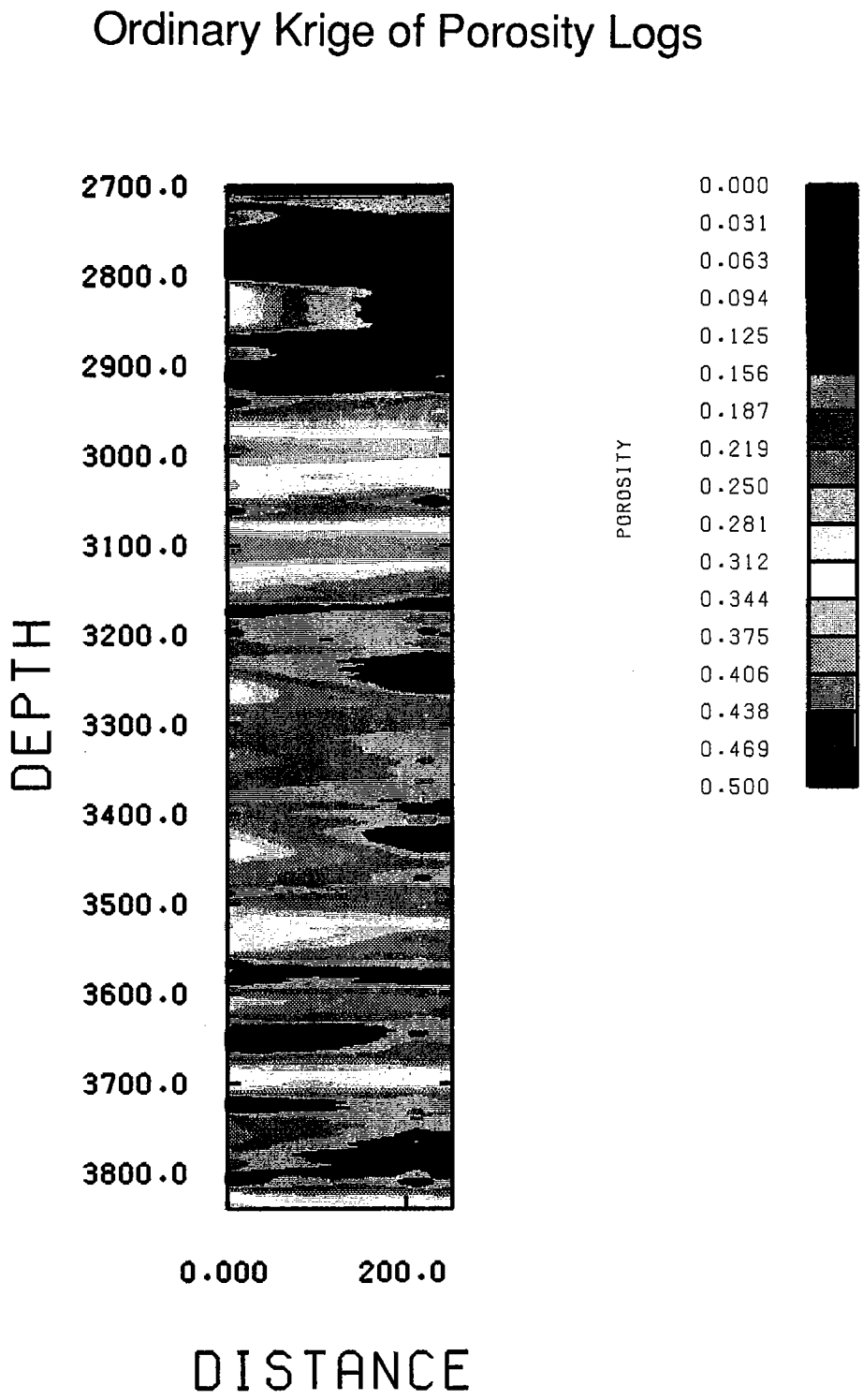

Figure 9. Porosity image estimated using ordinary kriging of the porosity logs. The image agrees with the well logs, but shows virtually no lateral heterogeneity.

The system was solved using the COKB2DM.F program of the GSLIB software, that we modified to suppress the unbiasedness condition imposed for "ordinary" cokriging. Another major modification was done in the search strategy, that was particularly long and inefficient in a case like ours where the hard data is regularly distributed in the field. This modification decreased the CPU time from 6 hours on a SUN 4 to approximately 20 minutes on the SUN 4 and 3 minutes on a DEC 5000. The image presented on Fig. 10 shows both the influence of the porosity at the well and of the velocities between the wells. Compared to the ordinary kriging, we see that many more heterogeneities appear in the interwell region. The plot also agrees with the porosities at the wells. However we have not included the effects of clay in this estimate, which we have found to be an important parameter.

Geostatistics and Rock Physics technique

In this approach we combine the laboratory rock physics relations with geostatistical tools. We have seen above that the major problem encountered when using Han's relation, or our in situ version of it, is that we do not have an estimation of the clay content between the wells, which needs to be input in the relation. To estimate this clay-content, we first estimated a clay index, proportional to clay volume, at the wells, using the gamma ray logs (See VanSchaack and Mavko, this volume). Kriging of these clay logs was then used to get a rough image of the clay content between the wells. Our velocity-porosity-clay relation, Eqn. 7, was then used at each pixel to map the velocity and clay images to porosity. The resulting porosity image is shown on Fig. 11. We now have an image that is consistent with the porosity and clay information at the wells, and which shows lateral heterogeneities between the wells due to the information from the tomogram. The tomogram influence on the porosity estimate is quantified better than before, because we have incorporated the log-derived velocity-porosity-clay relation.

CONCLUSIONS

We are in the process of developing ways of estimating subsurface porosity and shaliness, by exploiting the recent advances offered by crosswell seismic tomography and

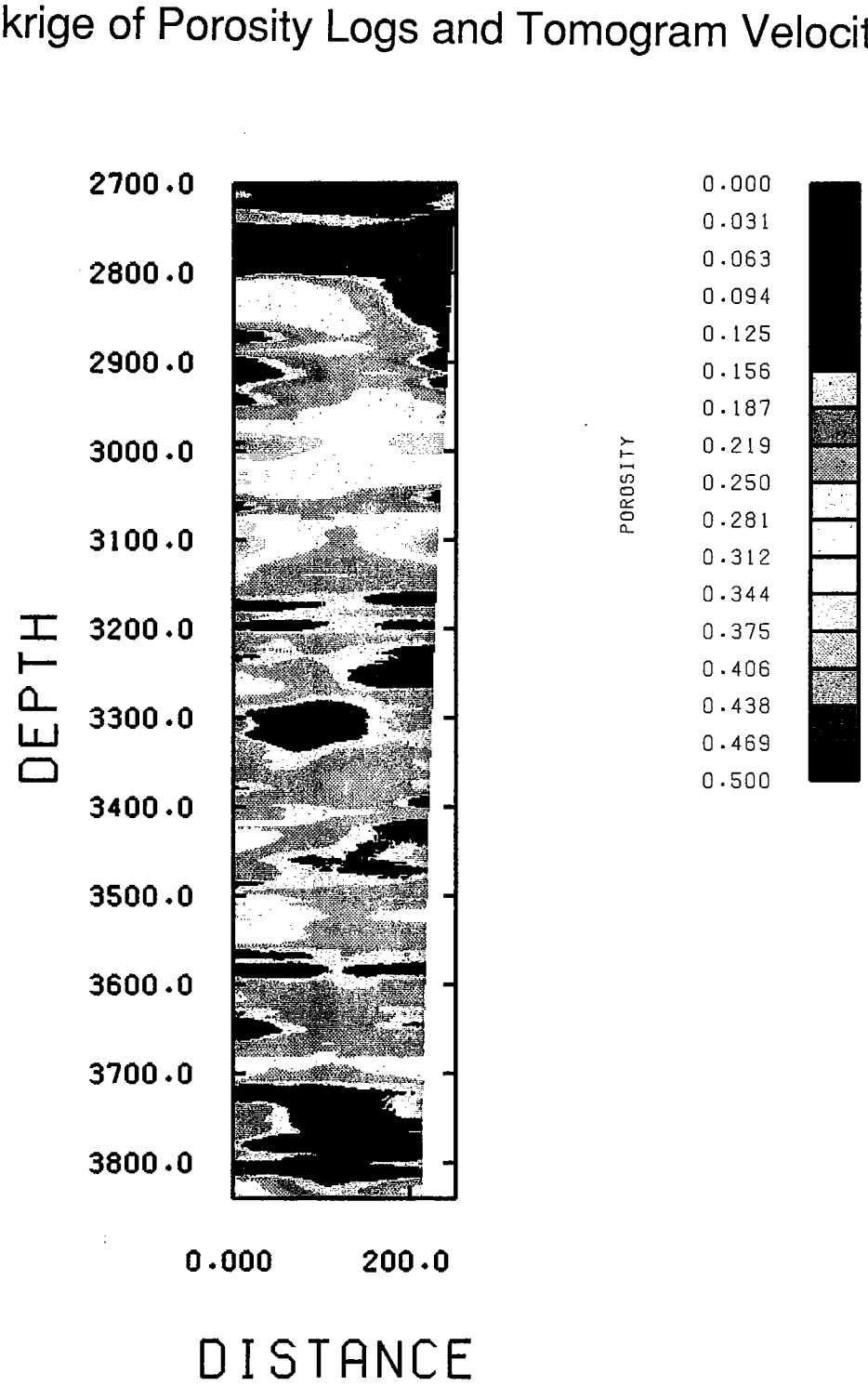

Figure 10. Porosity image estimated using cokriging. Input data the are porosity logs and tomogram velocity. Input covariances are estimated from the tomogram and porosity logs. The image now shows heterogeneities from the information in the tomogram.

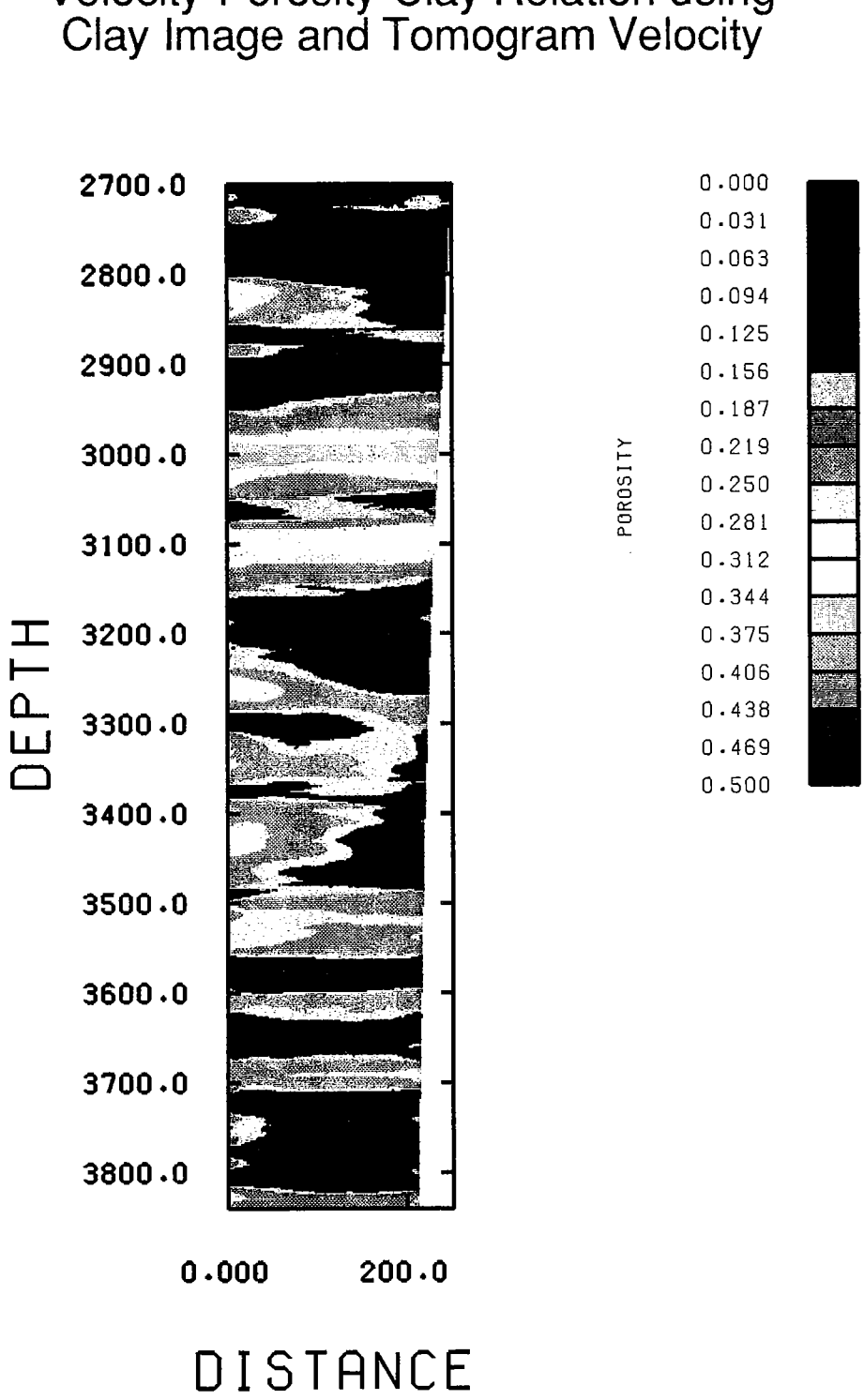

Figure 11. Porosity image estimated using a combination of rock physics and geostatistics. A clay image was estimated using kriging of the clay logs. Then the clay image and velocity tomogram were mapped to porosity using our velocity-porosity-clay relation relation.

rock physics work on velocity-rock properties relations. Crosswell seismic images provide a combination of superior resolution (on the order of a few meters) and accurate absolute velocities, that are not possible with surface seismic. Our recent laboratory and theoretical work in rock physics suggests that velocity can be related systematically to porosity within a given shaley sand environment, by accounting for clay volume fraction. Furthermore the laboratory work suggests that correlation coefficients of velocity-porosity-clay relations are probably better than indicated by well logs, due to the many difficulties and environmental factors that affect logging acquisition.

Three different approaches for estimating porosity from the seismic velocity tomograms were compared: (1) deterministic mapping from velocity to porosity using empirical rock physics relations; (2) pure geostatistical techniques (cokriging) in which no laboratory knowledge is supplied; and (3) a combination of rock physics and geostatistics. The pure rock physics approach allows us to incorporate our best knowledge of velocity-rock properties relations into the estimate; however it does not provide a flexible means of combining different kinds of data (such as well logs and tomograms) nor does it allow a precise way of quantifying the uncertainty. The purely statistical approach which incorporates only empirical relations derived from the well logs may not reflect the detailed velocity-rock physics relations that have been discovered in the lab, and it may suffer from too weak a correlation between velocity and porosity. The combined approach appears to be most flexible, allowing for ways to incorporate the widest range of data and at the same time allowing for quantitative estimates of uncertainty.

ACKNOWLEDGEMENTS

This work was supported by the Stanford Rock Physics Project, the Seismic Tomography Project, and the Gas Research Institute. The crosswell data collection and analysis were done in cooperation with Amoco Production Company. The cokriging was done using versions of the GSLIB programs from SCRF, which we modified to suit the crosswell problem. We thank Clayton Deutsch and André Journel for useful comments and suggestions.

REFERENCES

Deans, S. R., 1983, The radon transform and some of its applications: John Wiley & Sons, New York.

Deutsch, C. V., Journel, A. G., 1991, GSLIB: Geostatistical software library user's guide: SCRF internal report to be published by Oxford Press.

Han, D.-H., 1986, Effects of porosity and clay content on acoustic properties of sandstones and unconsolidated sediments: Ph.D. dissertation, Stanford University.

Harris, J., Tan, H., Lines, L., Pearson, C., Treitel, S., Mavko, G., Moos, D., Nolen-Hoeksema, R., 1990, Cross-well tomographic imaging of geological structures in Gulf Coast sediments: Proceedings of SEG 60th Annual International Meeting.

Journel, A., and Huijbregts, C., 1978, Mining Geostatistics: Academic Press, London.

Tosaya, C., 1982, Acoustical properties of clay-bearing rocks: Ph.D. dissertation, Stanford University.

PAPER G

VELOCITY-POROSITY-CLAY RELATIONS IN SHALY SANDS DERIVED FROM GULF COAST WELL LOGS

Mark Van Schaack and Gary Mavko

Seismic Tomography Project

ABSTRACT

We find that log-derived velocity-porosity relations in shaly sands are improved by including information on clay volume, similar to results previously found in the laboratory. In addition we interpret our log data to support a model where clay is present in two geometrical forms: as larger laminar units and as thin transitional units separating the clean sand units and the laminar shale units, where clay is present in varying amounts in the intrapore regions of the sand.

INTRODUCTION

Crosswell seismic tomography has been used successfully to estimate velocities between two wells (Dines and Lytle, 1979). The 2-D velocity map created using this technique has also been shown to be effective in imaging structural and stratigraphic features between wells (Harris et al., 1990). Many rock properties, such as porosity and shaliness, have been shown to have a direct effect on the velocity in rocks (Han, 1986). These relations have been seen in both the laboratory and in data collected downhole by logging. In the same way that wireline logging allows us to measure rock properties in the near vicinity of the borehole, traveltime tomography provides information which may be used to estimate rock properties away from the borehole.

Many different empirical relations have been derived from data collected in the lab. Two of the better known relationships are Archie's equation (Archie, 1942) and Wyllie's time average equation (Wyllie et al., 1958) which relate porosity to resistivity and porosity to velocity, respectively. The effectiveness of these relations has been demonstrated through their successful application in the field. Many times though, modifications to these lab derived relations have been needed for calculated information to remain consistent with what is observed. These differences most certainly reflect the different petrogenetic

histories of the rocks and the inability to simulate completely in-situ conditions in the lab measurements. In general we can expect that empirically developed relations will always prove more effective when they are derived from the same rocks we wish to describe. In this paper we will derive relationships between velocity, porosity, and shale from wireline log data. This will provide a basis from which we can use the crosswell tomogram to estimate rock properties away from the borehole. It also serves as a preliminary test of relationships derived in the lab.

Estimating rock properties between two wells using log derived relations and the crosswell velocity tomogram require a number of different issues be addressed. Some of these include the following:

- Tomogram estimated velocities must be reconciled with wireline log measured velocities. There are a number of obstacles to overcome in this area. The two velocity measurements may reflect actual differences in the rock properties such as those due to drilling induced fracturing in the near borehole region, invasion, and alterations of the clays. These alterations in the near borehole region would have a larger effect on wireline log measurements due to the greater resolution and focus of measurement of these logs in this area. The difference in the two velocities may also reflect the differences in the actual measurement technique as in the case of anisotropic beds. In this case, sonic logging tools are measuring the vertical rock velocity and crosswell tomography tends to measure the horizontal rock velocity.

- The differences in resolution between the two measurements must be defined to provide a guideline in interpreting the derived rock properties between the wells.

- Relationships developed from rock data are typically valid only for the range of lithologies from which they were derived. Attempting to apply derived relationships outside this range of lithologies will likely result in incorrect estimates of the rock properties.

- A technique of combining tomography information with the information collected at the well must be developed.

Research is currently underway to address the issue of incorporating both log and tomogram data to provide an image of rock properties between two wells (Lucet and Mavko, this volume). This paper will describe the development of a velocity, porosity,

and clay relationship from wireline log data with an emphasis on meeting the requirements of this technique under development.

LOG ANALYSIS

Log Data

A seismic compressional wave tomogram was constructed from data collected in Miocene sediments in the onshore Gulf of Mexico Area (Harris et al., 1990). Data were collected from two wells approximately 250 ft apart over a zone between the depths of 2700 ft and 3840 ft. The region surveyed consists primarily of interbedded, poorly compacted sands and shales. For future reference in this paper the two wells are referred to as W06 and W35.

Wireline logs collected in the two wells are as follows. W06: Spontaneous Potential (SP), deep induction, 16" normal, through-casing sonic (dt), through-casing gamma ray, and cement bond log. W35: SP, deep induction, spherically focused log, gamma ray, density, caliper, neutron porosity, through-casing sonic (dt), through-casing gamma ray, and cement bond log. The sonic, gamma ray, and cement bond logs were collected at approximately the same time as the crosswell tomographic survey. The remaining logs were collected in open-hole conditions following the drilling of the wells. The log sampling interval for all logs is 0.5 ft over the zone of interest.

An interpretation through the zone of interest of porosity and shaliness using logs common to both wells was desired. For this reason, the shallow resistivity log was chosen to provide a resistivity derived porosity and the gamma ray log was used to estimate bulk volume clay. For comparison purposes porosity and bulk volume shale were also computed from the density log and the compensated neutron log in W35. Unfortunately, these logs were available in only one well and both were affected by washed out, rugose hole conditions in the sand sections.

Environmental Corrections

All logs were depth correlated to the original resistivity logs run in open hole. Depth shifting and stretching were performed where appropriate. The cement bond logs showed good bonding over the region of interest which is necessary for accurate sonic velocities to be measured. Both the shallow resistivity curves, SFLU and 16" normal, fell within ranges where borehole corrections were not necessary for the resistivity of the mud used

while drilling. The density and compensated neutron logs were corrected for hole diameter. Standoff corrections needed in the sand sections were not possible due to a lack of standoff information. The compensated neutron log was calibrated for correct readings in sand.

Porosity Evaluation from Rock Resistivity

A version of Archie's equation modified for the presence of shale (Schlumberger, 1987) was used to relate the various parameters of interest:

$$\frac{1}{R_t} = \frac{\phi^m S_w^2}{a R_w (1 - V_{sh})} + \frac{V_{sh} S_w}{R_{sh}}$$

where

R_t	=	formation resistivity
ϕ	=	porosity
m	=	the cementation factor
S_w	=	water saturation
a	=	formation factor coefficient
R_w	=	formation fluid resistivity
V_{sh}	=	volume of shale
R_{sh}	=	resistivity of the shale.

By using the resistivity in the invaded zone as provided by our SFLU and 16" normal curves we can substitute R_{xo} for R_t and the resistivity of the mud filtrate, R_{mf} for R_w. The region of interest was interpreted as water wet so an invaded water saturation of 1 was used. Making these substitutions and solving for porosity yields the following relation:

$$\phi = \sqrt[m]{\frac{a R_{mf} (1 - V_{sh}) (R_{sh} - V_{sh} R_{xo})}{R_{xo} R_{sh}}}$$

Humble's formula for unconsolidated sands was used as the basis of our resistivity relationship. Humble's coefficients are m = 2.15 and a = 0.62. The resistivity of the shale was taken from log readings in a good shale zone and temperature corrected over the zone of interest. The mud filtrate resistivity was read off the wireline log and also temperature corrected over the zone of interest and used as an initial estimate for the invaded zone fluid resistivity. Due to high porosities, it was expected that the depth of invasion would be

quite shallow. For the case of $R_W < R_{XO}$ this results in the shallow resistivity tool measuring lower resistivities than would be appropriate if only mud filtrate filled the porosity within the depth of investigation of the tool. Calculated porosities were found to be higher than reasonable using the mud filtrate resistivity. In W35 the mud filtrate resistivity was adjusted until the calculated porosities in clean sand section approximated density calculated porosities in the same clean sand sections. This correction provided a basis with which we could correct the mud filtrate resistivity from W06 to approximate the average invaded zone fluid resistivity.

Shale Evaluation for Resistivity Porosity Calculation

The volume of shale was calculated from the gamma ray log using the Dresser Atlas formula (Dresser Atlas, 1979) for unconsolidated rocks:

$$V_{sh} = 0.083 [2^{(3.7 \times I_{GR})} - 1.0]$$

where

$$I_{GR} = \frac{GR_{log} - GR_{min}}{GR_{max} - GR_{min}}$$

Shale and sand index gamma ray values were read from histograms over typical zones.

Evaluation of Porosity and Vsh from NPHI - RHOB Crossplots

In a three-component system the volume of each component can be calculated from a density and neutron porosity crossplot if they all have distinctive positions in the crossplot space. The technique used is equivalent to that found in ternary diagrams used in calculating mineral percentages in rocks. This technique best describes shale and sand sequences where the shales exist in the form of laminae (Schlumberger, 1987).

The three components of the system were represented by quartz, shale, and water. Quartz properties were defined by a density of 2.65 gm/cm^3, and a neutron porosity of 0. The pore fluid, water, was defined as having a density of 1.0 gm/cm^3 and a neutron porosity of 1.0. The shale parameters were read off a crossplot of bulk density, RHOB, and compensated neutron porosity, NPHI (Figure 1 below). Shale values of 2.25 gm/cm^3 and a neutron porosity of 0.53 were used. Using these three points as the vertices of the ternary diagram, porosity (equal to volume of pore fluid), and the bulk volume of shale

were calculated. Porosity and Vsh calculated using this method will be referred to as 3pt. porosity and 3pt. Vsh.

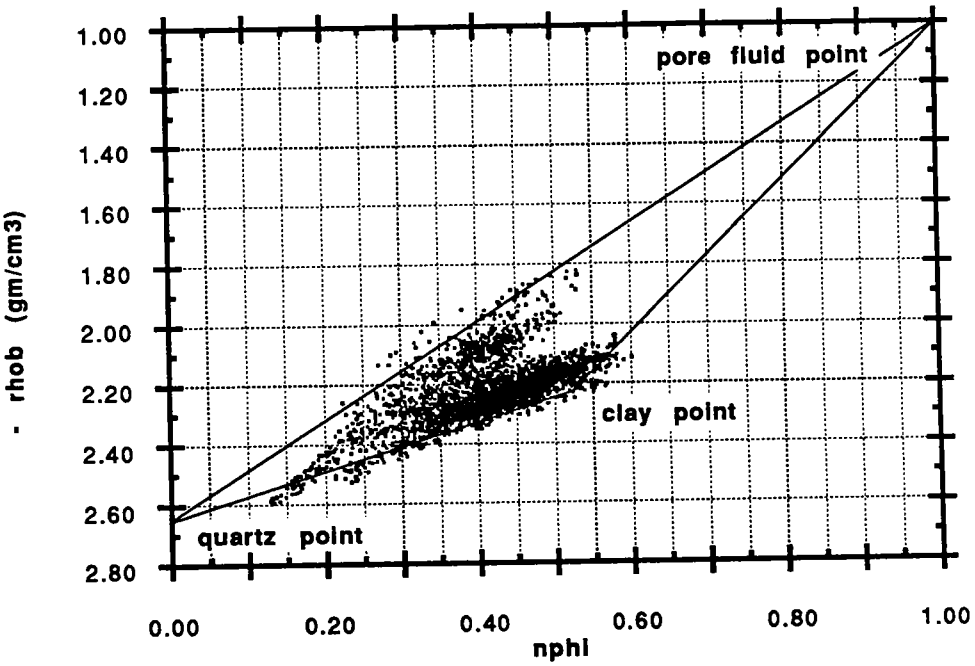

Figure 1: A crossplot of neutron porosity, NPHI vs density, RHOB over a zone of interest from 2400 to 4170 feet. Plot shows quartz, shale and water points. The scatter of points off of the sand-pore fluid line is due to poor hole conditions in the sand sections of the well.

INTERPRETATION

It has been observed that the velocity of rock is a function of a number of different parameters. These include: porosity, mineral composition, grain cement, grain contact, grain packing, pore geometry, pore fluid, confining pressure, pore fluid pressure and frequency (Han, 1986). Many of these parameters are difficult, if not impossible, to measure accurately in the lab or downhole with logging tools. For this reason an empirical approach to developing velocity-rock property relations is the most practical. Most log evaluation techniques assume velocity to be primarily a function of matrix velocity and fluid velocity and porosity. Wyllie's time average equation is a good example of this. This equation yields useful results in many cases since a number of the above described parameters remain nearly constant over the zone of interest. In cases where the rock is poorly compacted, a correction factor is employed to provide better agreement between calculated and measured values. This correction factor is best determined by comparing Wyllie calculated porosity with true porosity measured by another method.

The rocks in W35 and W06 over our zone of interest are poorly compacted with velocities ranging primarily from 2 to 3 km/s and many of the sand sections have a significant amount of clay present. It has been shown that in uncompacted shaly sands clay content can have a large effect on rock velocity (Han, 1986). Crossplots of sonic velocity vs. Vsh in W35 suggest that clay may play a role in the rock velocity especially at lower values of Vsh (Figures 2 and 3).

Although a large degree of scatter is apparent in the crossplots of Vsh and velocity for Vsh < 0.50, a trend of increasing velocity with increasing shale content is suggested in both crossplots. The importance of including a clay term in the velocity relationship is further supported by calculating a linear regression of sonic velocity vs. resistivity derived porosity for Vsh < 50% in W35. This regression yields the following relation:

$$V(\phi)\ (km/s) = 3.1 - 2.3\,\phi \quad R = .46 \text{ (refer to Figure 4)}$$

A regression of the same data using both porosity and the volume of shale yields:

$$V(\phi, Vsh)\ (km/s) = 4.3 - 4.9\,\phi - 2.1\,V_{sh} \quad R = .78 \text{ (refer to Figure 5)}$$

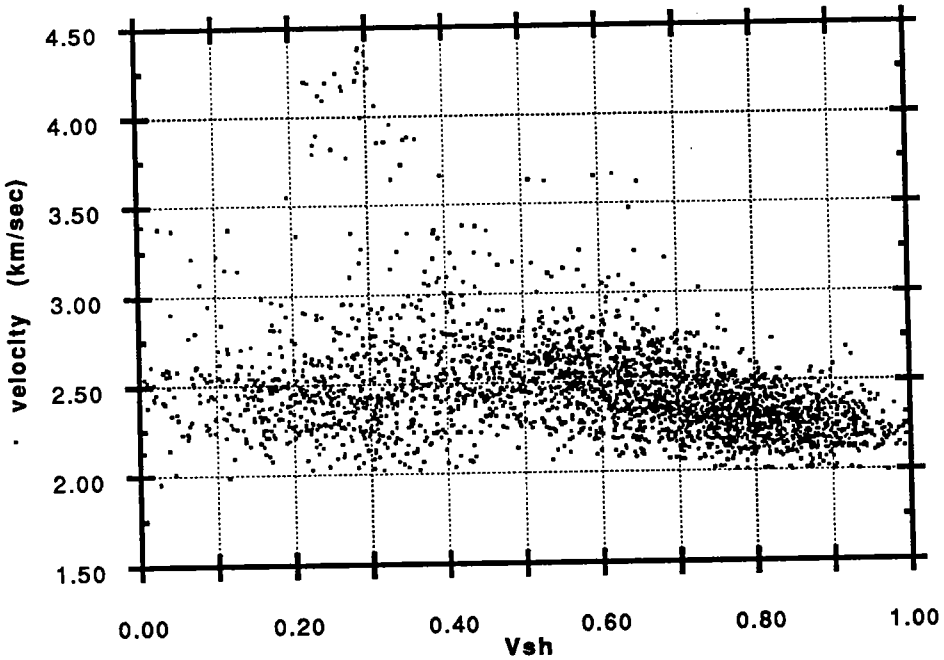

Figure 2: Plot of neutron-density calculated Vsh vs velocity.

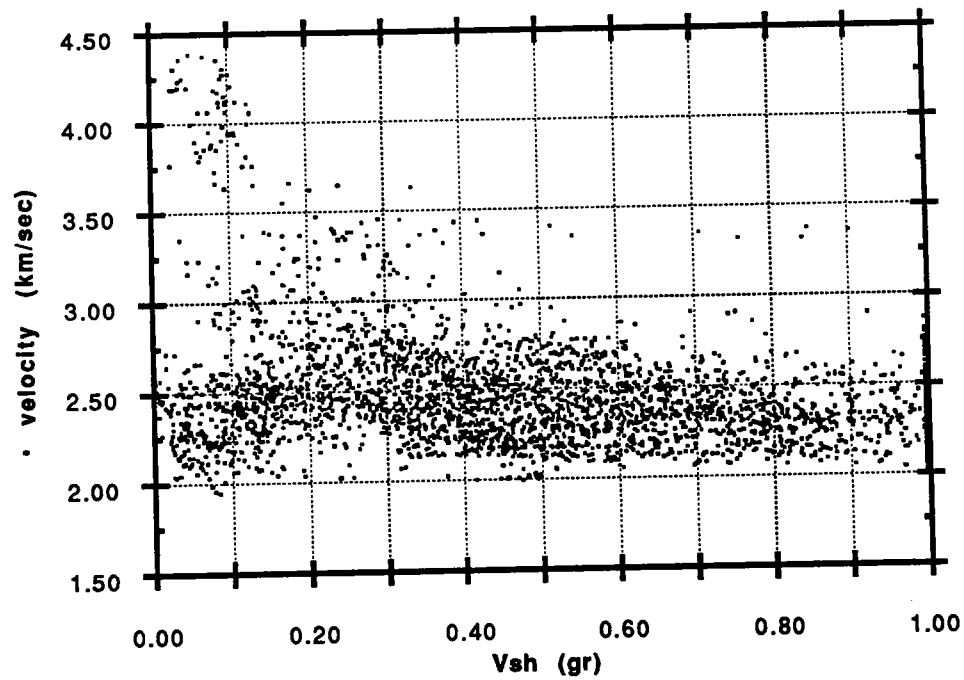

Figure 3: Plot of gamma-ray calculated Vsh vs velocity.

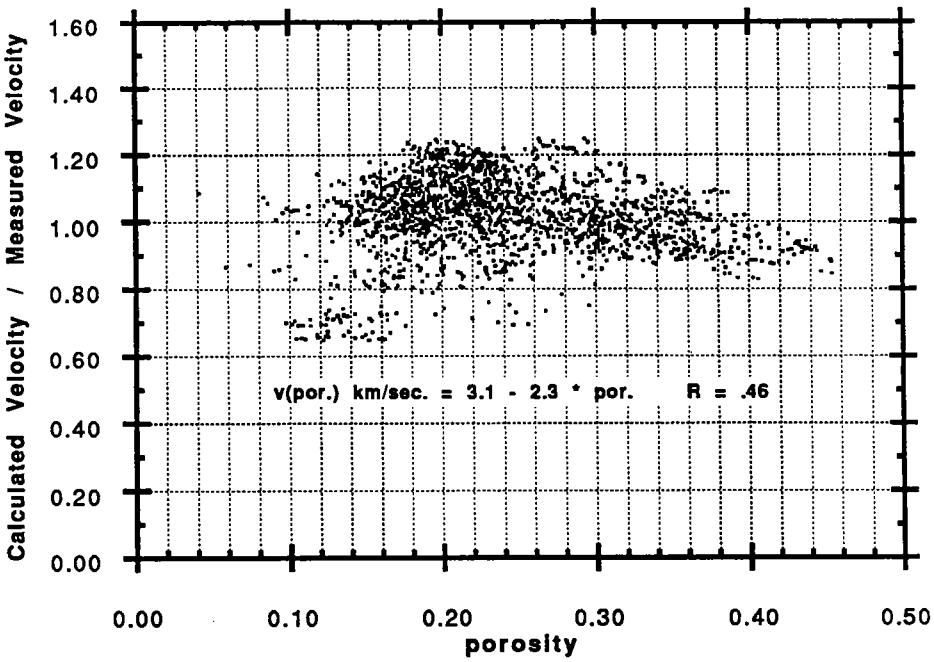

Figure 4: Ratio of calculated and measured velocity vs resistivity calculated porosity.

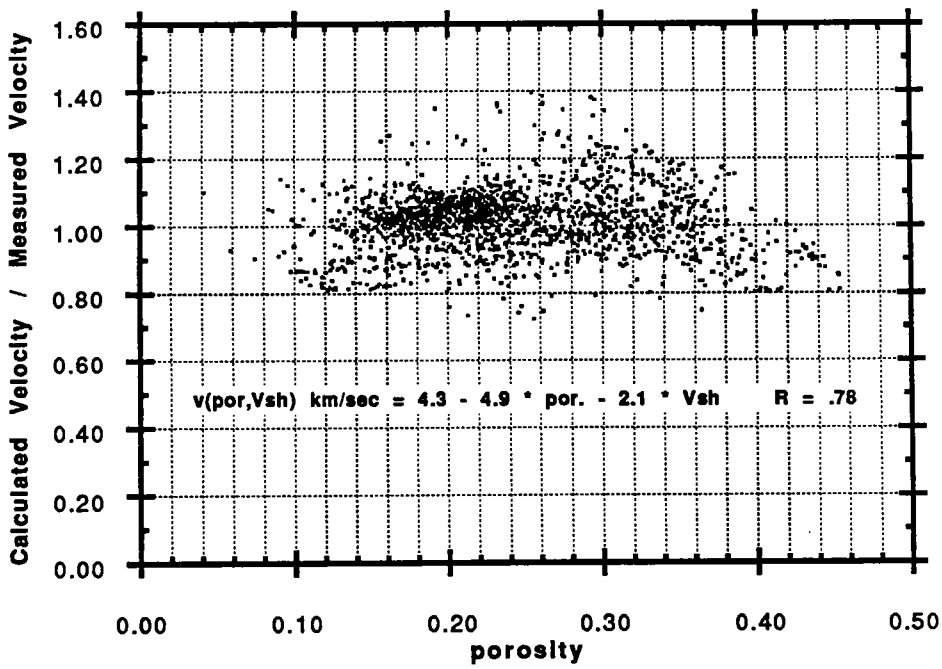

Figure 5: Ratio of calculated velocity and measured velocity vs resistivity calculated porosity. An improvement in the relation is seen from including the clay parameter.

For comparison purposes we perform the same regressions for the 3pt. porosity and Vsh data. Although this porosity and Vsh data were calculated using completely independent information with a different technique we find the calculated relations very similar:

$$V(\phi)\ (km/s) = 3.1 - 2.5\,\phi \quad R = .61 \quad \text{(refer to Figure 6)}$$

$$V(\phi, Vsh)\ (km/s) = 4.2 - 4.4\,\phi - 2.1\,V_{sh} \quad R = .78 \quad \text{(refer to Figure 7)}$$

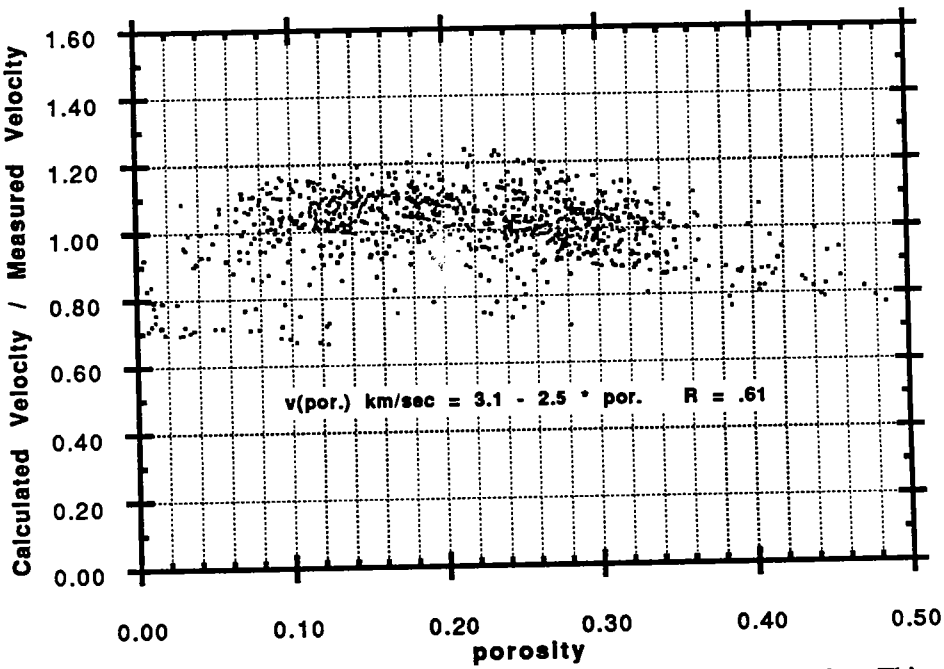

Figure 6: Ratio of calculated velocity and measured velocity vs 3pt. porosity. This plot shows a better fit of the data than that arrived at using the relationship derived from the resistivity derived porosity and Vsh calculated from the gamma-ray tool.

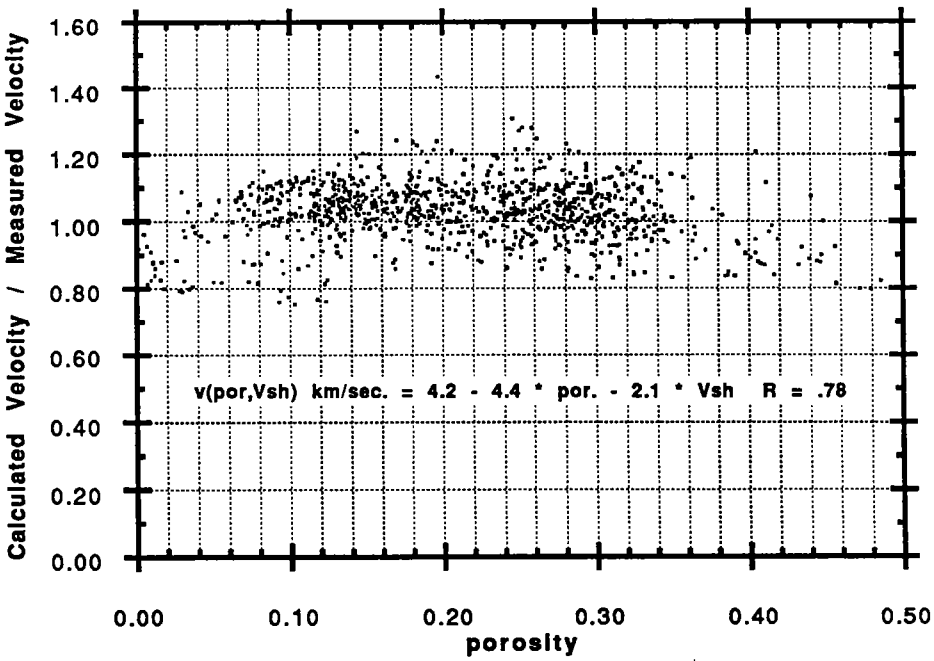

Figure 7: The ratio of calculated velocity and measured velocity vs. 3pt. porosity. Including a clay term has improved the velocity-porosity relationship.

Improvement in the correlation of coefficient is seen when the clay content is included in the regression. From our derived relation we can see that both porosity and clay act to reduce the velocity of the rock as expected. We also can observe that porosity is still a primary factor in reducing rock velocity with clay having about half the effect per unit volume. This ratio is similar to that observed by Han (1986). He found that clay had about 30% the effect of porosity on reducing rock velocity. This ratio was determined for more consolidated rocks and as expected his relation predicts higher velocities for the same porosity than we find in our two wells.

$$V(\text{porosity, Vsh}) \text{ (km/s)} = 5.59 - 6.93\,\phi - 2.18\,V_{sh} \qquad R = .98$$

This supports our belief that the development of rock parameter relations are best performed in the rocks where they will be applied.

DISCUSSION OF RESULTS AND INTERPRETATION TECHNIQUES

We have shown that, as predicted by lab work, including shaliness in our velocity-porosity relationship results in a better description of velocity with reduced scatter. Our confidence in these relationships benefits from having calculated very similar results using two different, independent techniques to calculate both porosity and Vsh. In spite of this we see that the improvement, although statistically significant, is not as dramatic as we might expect. This can be explained by several factors.

For one, both calculations of porosity incorporate several errors. In the case of the resistivity-derived porosity we have utilized a variant of Archie's equation to solve for porosity. This equation, itself only an empirical approximation, cannot with complete accuracy describe changes of porosity through resistivity measurements. Also the resistivity measurement, even with corrections, is not completely accurate. Taking these porosities with their own statistical errors and relating them with velocity will result in more scatter than if we were to compute porosity using a more direct method, such as with the density and compensated neutron information.

Density and compensated neutron logs provide us with data that is more directly related to the rock porosity and the degree of shaliness. In general these logs would be preferred for calculating porosity. Unfortunately, through our zone of interest in W35, sand sections are washed out and rugose. The logging tools taking these measurements require good contact with the borehole wall to collect good data. Fluid present between the tool and the borehole wall resulting from tool standoff is seen as porosity. Another factor relating to tool design is that the density tool incorporates a pad design which results in its measurements being less affected by poor hole. This can be seen clearly in Figure 1. Points that fall on the quartz-pore fluid line would be pushed along that line in the direction of higher porosity if both, tools were equal sensitive to rough hole. Instead, due to the compensated neutron tool's greater sensitivity to rough hole, we see the points have been pushed to the right, off the sand line. This results in a Vsh that is greater than the true value. The overestimation of Vsh can be seen by comparing the gamma ray calculated Vsh with that calculated using the RHOB-NPHI crossplot (Figures 2 and 3).

The effect of hole conditions on the density-neutron crossplots is better illustrated by comparing the crossplots of W35 data made over the interval of 2400-4170 feet with a crossplot made from log data over the interval of 5600-6100 feet (Figures 1 and 8). The hole conditions in the lower section were extremely good. This is reflected in the tighter grouping of the points except the few scattered in the lower left hand side of the plot that

are the result of a thin, low porosity sand section in this interval. Unfortunately, no velocity information was collected over this zone.

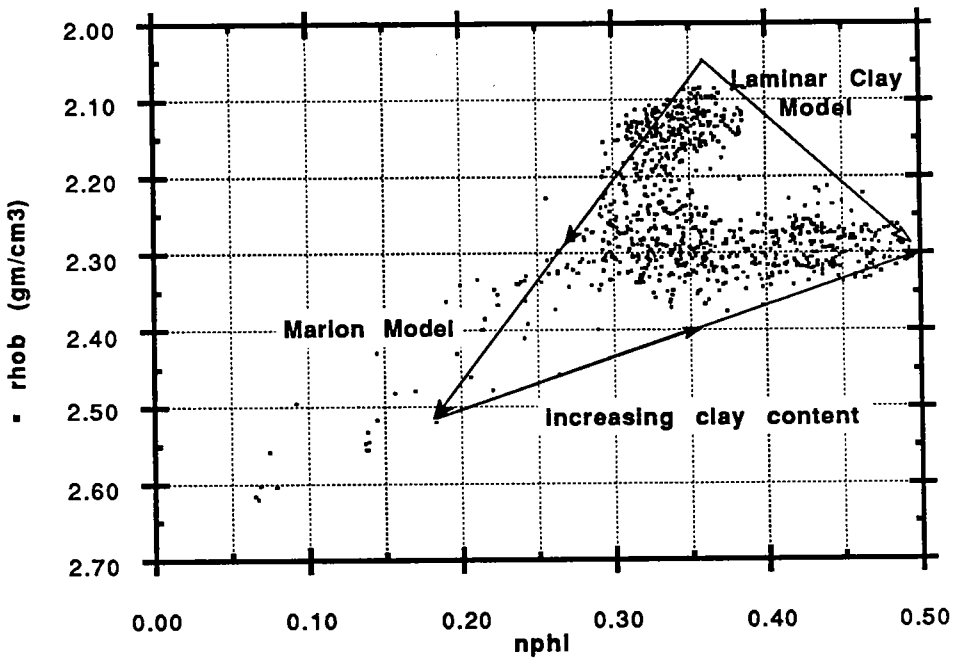

Figure 8: Crossplot of neutron porosity vs density over the interval of 5600 - 6100 feet.

The distinctive horseshoe shape of the NPHI-RHOB crossplot over the lower interval provides some clues to the manner in which the shale exists in this interval. The clean sand points, (the top half of the horseshoe) suggest that the sand in this section is a relatively uniform 32%-36% porosity. This is what we would expect of a well-sorted, mature sandstone typical of the Gulf coast sands. The 100% shale point on this crossplot is at a neutron porosity of 0.50 and a density of approximately 2.3 gm/cm3. If the shale in this interval existed only in the form of laminae and the sand was of a uniform nature (as is suggested) we would expect most points to plot along the line connecting the sand point and the shale point. This is not the case in this plot.

Clay falls into four groups based on the manner in which it is present within a rock: intrapore clay, granular clay, laminar clay, and dispersed matrix clay (Marion, 1990). The manner in which clay is present in sandstones is important for estimating properties important in the development of a production well. The primary property affected by the clay is that of permeability. Clay present in the pore space dramatically reduces permeability while clay present in thin laminae tend to affect primarily only vertical

permeabilities (Schlumberger, 1987). For this reason, any information suggested by the logs as to how the clay is present in the rocks could play an important role in the development and production of the well.

Marion (1990) proposed a model describing velocity and porosity relationships of sand-shale systems using intrapore clay as the basis by which clay is present in the system. Clay particles in this system are recognized as possessing their own micro- and macroscopic porosity. These porosities are less per unit volume than the pore fluid and greater than the sand porosity. When the clay fraction is less than the pure sand porosity, clay particles fit in the pore space and act to reduce the porosity of the system linearly with increasing clay content. When the clay fraction increases past the pure sand porosity the sand grains of the system become disconnected and the clay matrix floats the sand particles. At this point the porosity of the system begins increasing linearly with increasing clay content.

Figure 8 shows a crossplot of density vs compensated neutron porosity over the interval of 5600-6100 feet. Overlain on this plot are schematic representations of how points would fall on this plot for increasing clay content for the Marion model of intrapore clay and a model which describes all clay as existing in laminae. Both schematic representations assume a constant critical sand porosity of 36%. Pure clay is defined by its position on the NPHI-RHOB crossplot as having a density equal 2.30 gm/cm3 and a neutron porosity of about 50 porosity units (PU).

Figure 8 suggests that aspects of both Marion's model and a model of laminar clay are imaged over the interval represented by each point. The vertical resolution of both the density and neutron tools is about 6 inches. The trend of the points suggests that the change in depositional environments, from shale to sand and vice versa, is represented by a stratigraphic sequence too thin to resolve by the tools used. This would explain why no data were collected in the region of the model where the clay volume approaches the initial sand porosity (density equal 2.52 gm/cm3 and neutron porosity equal approximately 18 PU). The thin nature of the bounding zone between pure shale and clean sandstone when accompanied by these bounding regions over the 6 inch region sampled in logging would act to round off the vertice predicted by Marion.

Figure 9 provides more evidence in support of the intrapore clay model. The data plotted is from W35, 2400 to 4170 feet. We do not solve for porosity deterministically from density although we can use density as a qualitative indicator of the porosity trend. A high degree of scatter is present, particularly for low values of Vsh, but a trend of increasing density can be seen for increasing Vsh up to approximately Vsh equal 0.50.

After this point the density trend reverses and the bulk density decreases linearly for Vsh > 0.50. This is also predicted by the Marion model for intrapore clay.

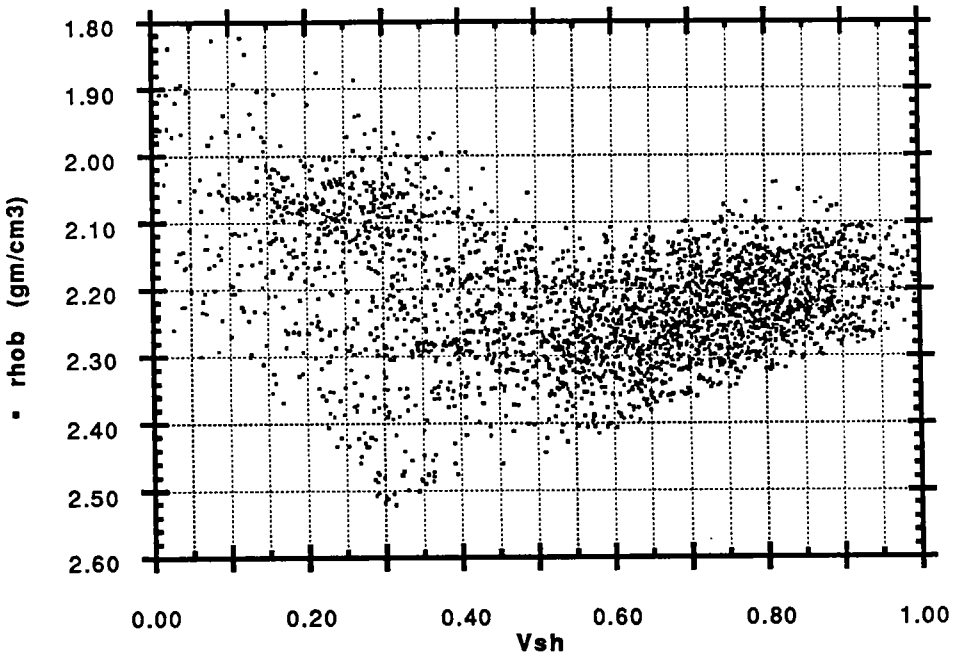

Figure 9: Density vs 3pt. Vsh over the interval of 2400 - 4170 feet. A trend of increasing density for increasing Vsh is suggested until Vsh is approximately equal .5. At this point the trend reverses for increasing shale content. These trends are predicted by a model where clay is placed geometrically intrapore.

CONCLUSIONS

We find that using information on clay volume in sandstone allows us to calculate a statistically more accurate relation of porosity to velocity in sandstones. In this particular example we did not have access to all useful log data which would allow us to test some of our interpretations of our results. Even so, we found good agreement in the velocity-porosity-clay relations calculated using independent measures of both porosity and clay content.

In addition we interpret our log data to support a model where clay is present in two geometrical forms; as larger laminar units, and as thin transitional units separating the clean sand units and the laminar shale units, where clay is present in varying amounts in the intrapore regions of the sand.

ACKNOWLEDGEMENTS

The authors would like to acknowledge the support of Amoco Production, BP Exploration, and the Gas Research Institute (GRI).

REFERENCES

Archie, G. E., 1942, The electrical resistivity log as an aid in determining some reservoir characteristics: J. Pet. Tech., **5**, No. 1.

Dines, K. A. and Lytle, R. J., 1979, Computerized geophysical tomography: Proc. IEEE, **67**, 1065-1073.

Dresser Atlas, 1979, Log interpretation charts: Houston, Dresser Industries, Inc., 107.

Han, D., 1986, Effects of porosity and clay content on acoustic properties of sandstones and unconsolidated sediments: Ph.D thesis, Stanford University.

Harris, J. M., et al., 1990, Crosswell tomographic imaging of geological structures in Gulf coast sediments: 1990 SEG Annual Convention, San Francisco.

Lucet, N., and Mavko, G., 1991, Rock properties of a crosswell seismic image: this volume.

Marion, D. P., 1990, Acoustic, mechanical, and transport properties of sediments and granular materials: Ph.D thesis, Stanford University, 44-83.

Schlumberger, 1987, Log interpretation principles / applications: Houston, Schlumberger Educational Services, 7-110.

Wyllie, M. R. J., Gregory, A. R., and Gardner, G. H. F., 1958, An experimental investigation of factors affecting elastic wave properties in porous media: Geophys., **23**, No. 3.

PAPER H

ORTHOGONAL CODED SIGNALS AS SIMULTANEOUS SOURCE SIGNATURES

Youli Quan and Jerry M. Harris
Seismic Tomography Project

ABSTRACT

Simultaneously recorded seismograms from several sources can save time and reduce the cost of data acquisition. For the purpose of separating the composite seismograms we require the simultaneous source signatures to be orthogonal. We use coding techniques to construct orthogonal signals. This work discusses three different coded signals—linear sweeps, pulse sequences and M-sequences—which may be used as simultaneous seismic source signatures. Each of these signals can also be directly used as a single source signature since each has good autocorrelation properties.

INTRODUCTION

Two main reasons support the use of coded signals as seismic source signatures. The first is the possibility of increasing the transmitted energy by exploiting the parameter of the length of transmission instead of the peak power. This is essential when the source is already operated at peak instantaneous power. The second reason is the possibility of separately processing several streams of seismic data which have been simultaneously recorded through the same seismic channel. Here we will focus on the problem of separating coded signals from simultaneous sources, though the results will be useful for analysis of single source signatures as well.

The main advantages of simultaneously recording signals from several sources are that it saves time and reduces the cost of data acquisition. More information can be obtained during the same recording period and with the same receiver. For some other situations, e.g., forward modeling for a series of sources by numerical methods, simultaneous coded sources may be expedient. For example, with finite difference method the time to calculate synthetic seismograms for multiple sources is almost the same as for a single source. Usually the procedure required to separate coded

signals is quite fast; therefore, using simultaneous coded sources in forward modeling may save computational time.

Examples of coded signal signatures are encoded sweeps, encoded pulse sequences, pseudorandom sequences, and so on. Sweeps that have been used in industry since the 1960's can be seen as frequency-coded signals. Bernhardt and Peacock (1978) defined different sweeps, such as upsweeps and downsweeps, and phase inverted upsweeps and downsweeps, as coding elements and encoded these elements based on quaternary E-Codes (Welti, 1960). Edelmann and Werner (1982) applied the E-Code sweeps to several seismic surveys of single sources; Womack et al. (1990) applied the E-Code sweeps as simultaneous source signatures to field tests. Pritchett (1991) gave another example of simultaneous recording technique using sweeps.

A coded pulse sequence provides another common source signature. Barbier (1982) developed the pulse coding technique in seismology. He pointed out the potential application of pulse coding to simultaneous sources.

Cuningham (1979) applied the maximal length sequences (M–sequences, e.g., Yarmolik, 1988) to seismology. But he discussed only the autocorrelation property of M–sequences, and used M–sequences as a single seismic source signature. We will focus on the crosscorrelation properties of M–sequences and their related sequences called Gold sequences, which are simplest and perhaps most useful simultaneous source signatures.

ORTHOGONAL SIGNALS AND WAVES

This section discusses the definition of orthogonal signals and waves, and the way to separate orthogonal waves. Consider the sum of signals

$$S_\Sigma = \sum_{j=1}^{M} S_j(t). \tag{1}$$

In principle, if the component signals $S_j(t)$ are orthogonal, they can be separated from the sum by certain well-known procedures, such as correlation. Therefore, orthogonality is a feature essential for separation.

Various definitions of orthogonality may be used. In communication theory, if two signals $S_1(t)$ and $S_2(t)$ satisfy

$$\int S_1(t)S_2(t)dt = 0, \tag{2}$$

such *signals* are said to be orthogonal. In wave propagation problems, however, we

usually define two orthogonal *waves* $W_1(t)$ and $W_2(t)$ such that crosscorrelation

$$W_1 \star W_2(\tau) = \int W_1(t) W_2(\tau + t) dt = 0, \tag{3}$$

since waves $W_1(t)$ and $W_2(t)$ may exhibit any time shift because of propagation delay.

Based on the definition of Eqn. 3, we can separate orthogonal waves. Let us consider the acoustic wave equation with two simultaneous source terms:

$$\nabla.(\frac{1}{\rho}\nabla P) - \frac{1}{\rho c^2}\frac{\partial^2 P}{\partial t^2} = S_1(t)\delta(\mathbf{r} - \mathbf{r_1}) + S_2(t)\delta(\mathbf{r} - \mathbf{r_2}). \tag{4}$$

Now suppose that a pressure seismogram $P(t)$ generated by both sources is recorded. Due to source linearity this seismogram can be interpreted as the sum of two separate seismograms each produced separately by the two sources, i.e., $P(t) = P_1(t) + P_2(t)$. Correlating $S_1(t)$ with the two sides of Eqn. 4,

$$S_1(t) \star [\nabla.(\frac{1}{\rho}\nabla P) - \frac{1}{\rho c^2}\frac{\partial^2 P}{\partial t^2}] = S_1(t) \star [S_1(t)\delta(\mathbf{r} - \mathbf{r_1}) + S_2(t)\delta(\mathbf{r} - \mathbf{r_2})]. \tag{5}$$

Note that since

$$S_1(t) \star \frac{\partial^2 P(t, \mathbf{r})}{\partial t^2} = \int S_1(\tau)\frac{\partial^2 P(t + \tau, \mathbf{r})}{\partial t^2} d\tau =$$

$$= \frac{\partial^2}{\partial t^2}\int S_1(\tau) P(t + \tau, \mathbf{r}) d\tau = \frac{\partial^2}{\partial t^2}[S_1(t) \star P(t, \mathbf{r})],$$

and

$$S_1(t) \star [\nabla.(\frac{1}{\rho}\nabla P(t, \mathbf{r}))] = \nabla.[\frac{1}{\rho}\nabla(S_1(t) \star P(t, \mathbf{r}))],$$

and noting that

$$S_1(t) \star S_2(t) = 0,$$

we can reduce Eqn. 5 to

$$\nabla.[\frac{1}{\rho}\nabla(S_1 \star P)] - \frac{1}{\rho c^2}\frac{\partial^2 (S_1 \star P)}{\partial t^2} = S_1 \star S_1\delta(\mathbf{r} - \mathbf{r_1}). \tag{6}$$

That is, we can separate the wave field P generated by S_1 and S_2 through cross-correlation. This correlation process serves as decoding.

In practice, it is difficult to find signals that strictly satisfy Eqn. 3 for any τ. Therefore, we usually only require $|W_1 \star W_2(\tau)|$ to be small enough for all τ (see examples below).

EXAMPLES OF ORTHOGONAL CODES

Amplitudes, frequencies and phases are basic parameters to describe continuous signals. For pulse sequences, pulse amplitudes and intervals are essential parameters. We can construct orthogonal signals by encoding these signal parameters, that is, following certain rules to chose appropriate amplitudes, frequencies, phases, intervals and so on. As examples, we suggest here three different orthogonal coded source signatures that correspond to frequency coding, interval coding and phase coding respectively. The next section will provide synthetic examples using these signatures.

Linear Sweeps

We can view sweeps as frequency coding signals since the basic properties of sweeps are controlled by frequency parameters. If the frequency change of a sweep is random, we call it as a random sweep; if the frequency change is linear, it is a linear sweep.

A linear sweep is defined by

$$S(t) = A\sin[2\pi(f_o + \Delta f t/2T)t], \qquad \text{for } 0 \le t < T, \tag{7}$$

where A is signal amplitude, $\Delta f = f_2 - f_1$ is bandwidth, $f_o = (f_2 + f_1)/2$ is center frequency, f_1 is beginning frequency, f_2 is ending frequency, T is signal duration, and t is time. Eqn. 7 can represent upsweeps ($A > 0$, $f_2 > f_1$) and downsweeps ($A > 0$, $f_2 < f_1$), phase-inverted upsweeps ($A < 0$, $f_2 > f_1$) and downsweeps ($A < 0$, $f_2 < f_1$). Since the frequency in Eqn. 7 changes linearly, we call it as a linear sweep.

We can use linear sweeps to construct orthogonal source signatures. A simple example is the usage of different frequency bands. If the spectra of the two sweeps $S_1(t)$ and $S_2(t)$ do not overlap, then $S_1(t) \star S_2(t) = 0$. That is, $S_1(t)$ and $S_2(t)$ are orthogonal under the definition of Eqn. 3. $S_1(t)$ and $S_2(t)$ can been viewed as two codes.

The autocorrelation of a sweep is a pulse-like wavelet. Therefore, the correlation $S_1(t) \star P(t)$ not only separates the wave field P that is generated by $S_1(t)$ and $S_2(t)$, but also produces a seismogram with high resolution. The autocorrelation function $\phi(\tau)$ of the sweep $S(t)$ is well-approximated by Cunningham (1979):

$$\phi(\tau) = (A^2/2)[T\sin(\pi\Delta f\tau)/(\pi\Delta f\tau)]\cos[2\pi(f_o + \Delta f\tau/2T)\tau], \quad \text{for } 4T\Delta f \gg 1, \tag{8}$$

where τ is the processed time. For a large Δf the factor $\sin(\pi\Delta f\tau)/(\pi\Delta f\tau)$ results in a sharp peak in the processed record at $\tau = 0$. If we keep the frequency change Δf

the same for all the sources, the envelope of the autocorrelation will look the same in the separated seismograms. We can apply the Hilbert transform to extract the envelope.

The linear sweep has extremely low correlation (or decoding) noise. Though the separated seismograms have different prevailing frequencies, they have the same envelope. After Hilbert transform, the final seismograms have the same wavelet.

Other sweep examples that have more practical significance but do not quite satisfy Eqn. 3 are E-Code sweeps (Womack et al., 1990). The E-Code is a quaternary code. If four coding elements of the E-Code satisfy the features given by Welti (1960), its autocorrelation is a single pulse; its crosscorrelation with its Mate (another E-Code) is identically zero. An E-Code and its Mate can be used as dual source signatures. Upsweeps and downsweeps, phase-inverted upsweeps and downsweeps may be used as the coding elements of the E-Code. Unfortunately, these sweep elements don't quite satisfy the features given by Welti; the correlation noise is considerably high.

Pseudorandom Pulse Sequences

A pulse sequence can also serve as source signature. Assuming the pulses are identical, we can design orthogonal pulse sequences by encoding pulse intervals.

In the case of pulse coding we still use crosscorrelation as decoding. But we cannot expect to find pulse sequences $S_1(t_i)$ and $S_2(t_i)$ which satisfy Eqn. 3 exactly. Therefore, here we will use approximate inequality relation

$$|S_1(t_i) \star S_2(t_i)| \leq 1 \tag{9}$$

to define orthogonality, where assumed pulse amplitudes are 1. Based on Eqn. 9, Barbier (1982) gave a procedure to design pseudorandom pulse sequences. Let us consider a sequence of pulses at times $t_0, t_2, ...t_n$. The pulse intervals are $T_1 = t_1 - t_0, T_2 = t_2 - t_1, ...T_n = t_n - t_{n-1}$. The correlation noise appears at times equal to each pulse interval, the sum of two successive pulse intervals, the sum of three successive pulse intervals and so on (see Figure 1).

We use computer-based trial and error methods to find intervals T_i satisfying Eqn. 9. Figure 2 shows a pulse sequence constructed by a trial and error method. Since the distribution of intervals T_i is "random", we call the sequence with intervals T_i as a pseudorandom pulse sequence.

Having obtained a pseudorandom sequence, we can divide the sequence into several short sequences orthogonal to each other. Various methods can be applied to divide

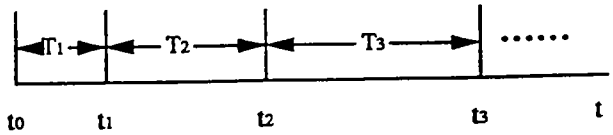

(a) A pulse sequence with intervals Ti.

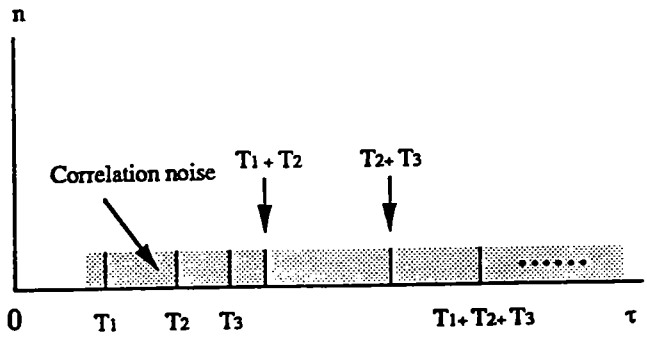

(b) The distibution of correlation noise.

Figure 1: Pulse sequence and its autocorrelation.

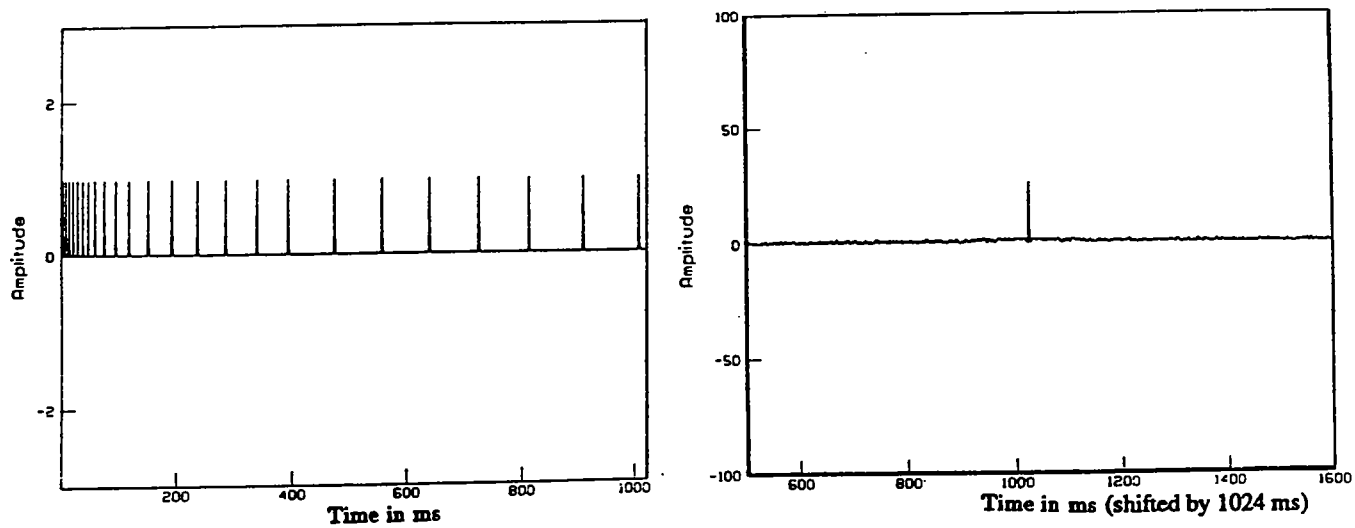

Figure 2: A pseudorandom pulse sequence (left) and its autocorrelation (right).

the long sequence, cutting it into short sequences, for instance, or picking up some pulses from the long sequence and rearranging these pulses to short sequences. The crosscorrelation property of these short sequences are tested in the next section.

The pulse coding exhibits relatively low correlation noise. Increasing the sequence length can improve the ratio of signal to noise, but it may make the sequence too long to use.

Pseudorandom Maximal Length Sequences

A pseudorandom maximal length sequence (M-sequence) of degree n is a periodic binary sequence with a period $M = 2^n - 1$. The autocorrelation function of an M-sequence is M for $\tau = 0$, and -1 for all other τ.

We can use a linear feedback shift register to generate an M-sequence. An M-sequence generator of degree n needs an n–stage register with appropriately connected feedback taps (Yarmolik, 1988).

M-sequences only serve as random codes. We also need carrier signals when we apply M-sequences to seismic sources. A sine wave $\sin(2\pi f_c t + phase)$ is a good choice. We can encode the *phase* based on an M-sequence. Corresponding to the values 0 and 1 in an M-sequence, we may set $phase = 0$ and π respectively. Figure 3 shows the cases when one binary bit corresponds to half a cycle and to a cycle, respectively. The carrier signals in Figure 3 have the same autocorrelation property as M-sequences.

When using M-sequences as orthogonal coded source signatures, we still apply correlation as decoding. Therefore, we must consider their crosscorrelation properties. The crosscorrelation properties of M-sequences and their related sequences were discussed in detail by Helleseth (1976) and Sarwate and Pursley (1980). The basic crosscorrelation properties of M-sequences are summarized in Table 1.

The number of the M-sequences of degree n is N_n. The peak value of the crosscorrelation between any pair in these N_n M-sequences is θ_c. If the crosscorrelation of two M-sequences of degree n has only three different values, -1, $-t(n)$, $t(n) - 2$, where $t(n) = 1 + 2^{[(n+2)/2]} \leq \theta_c$, we call these two sequences a preferred pair of M-sequences, which have lower crosscorrelation noise and are preferable to be used as simultaneous source signatures. The number of the preferred pairs is denoted as M_n. For a preferred pair of M-sequences of $n = 11$, the ratio of signal to noise is 31:1.

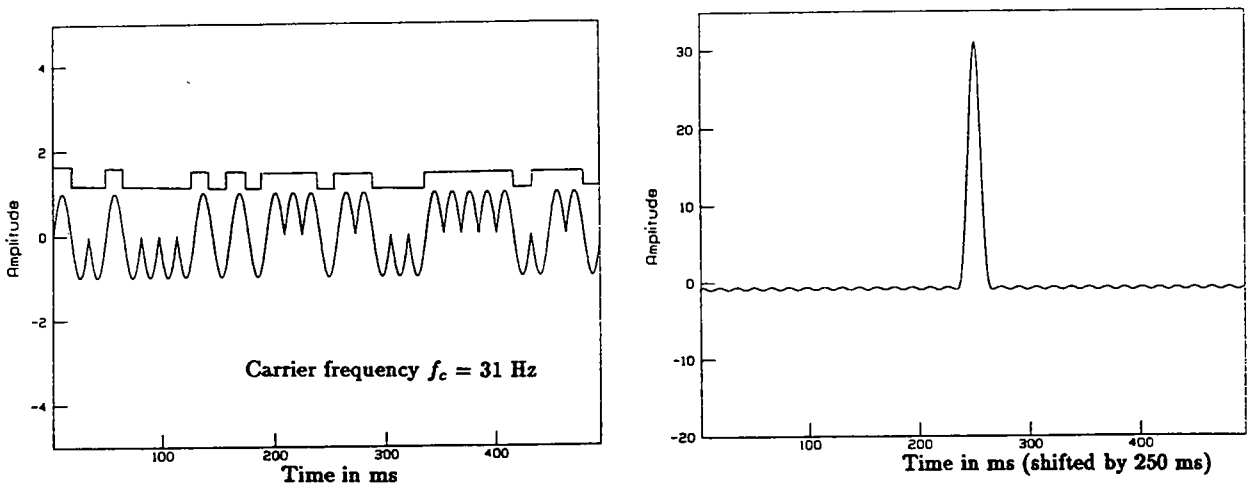

(a) One binary bit corresponds to half a cycle.

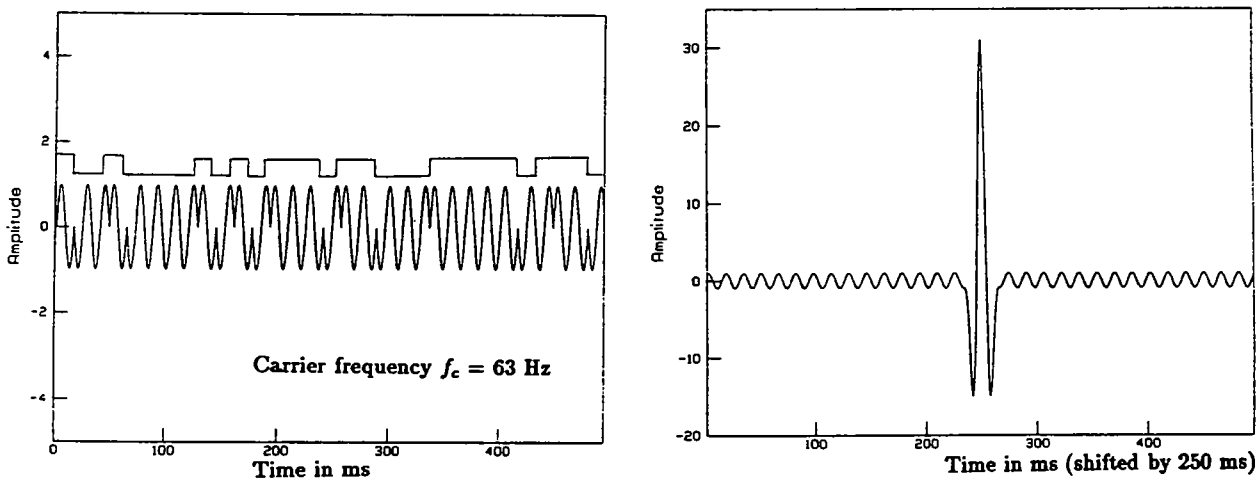

(b) One binary bit corresponds to one cycle.

Figure 3: Left: two sin-waves encoded by an M-sequence of degree n=5.
Right: the autocorrelation corresponding to the left signals.

n	$M=2^n-1$	N_n	θ_c	M_n	t(n)
3	7	2	5	2	5
4	15	2	9	0	9
5	31	6	11	3	9
6	63	6	23	2	17
7	127	18	41	6	17
8	255	16	95	0	33
9	511	48	113	2	33
10	1023	60	383	3	65
11	2047	176	287	4	65

Table 1: Crosscorrelation properties of M-sequences. M is the sequence length, N_n is the number of M-sequnences of degree n, θc is the maximum value of crosscorrelation, M_n is the number of preferred pairs and t(n) is the maximum value of crosscorrelation of preferred pairs.

If we need more than N_n simultaneous sources, we can use so-called Gold sequences (Gold, 1967). A set of Gold sequences of degree n consists of $2^n + 1$ sequences with $\theta_a = \theta_c = t(n)$, where θ_a is the peak value of autocorrelation noise. Table 1 shows that $2^n + 1 \gg N_n$. A set of Gold sequences can be directly constructed by binary adding of two appropriately selected M-sequences.

SYNTHETIC SEISMOGRAMS

This section provides three examples that test the orthogonality of the coded signals above, We calculate composite seismograms by travel time delay that simulates waves from different sources. Figure 4 is the model used for these three examples.

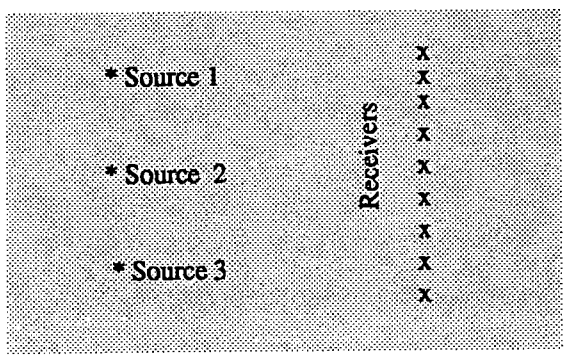

Figure 4: A model in cross-well geometry.

Figure 5 is an example for linear sweeps. We use three linear sweeps with the same absolute bandwidth but different starting and ending frequencies as multiple source signatures. Figure 4 shows that the decoding (correlation) noise is very low, and the envelopes of the correlated signals have the same shape.

Figure 6 is an example for pulse sequences. Each of the short pulse sequences used as multiple sources consists of 10 pulses, which are picked from the long sequence shown in Figure 2. Since each sequence consists of only 10 pulses, the ratio of signal to noise (S/N) is low; if we only use the first arrivals, it is acceptable. We can improve the S/N by increasing the pulse length.

Figure 7 is an example for M-sequences. We use three M-sequences each with the length of $M = 2^9 - 1 = 511$ as multiple source signatures. Figure 6 shows that the S/N is relatively high. If the M-sequence and the pulse sequence have the same length in time, the S/N for M-sequences is higher than that for pulse sequences because of the denser pulses in M-sequences.

CONCLUSIONS

It is possible to use coded signals as simultaneous source signatures. Linear sweeps, pulse sequences and M-sequences are typical examples of these coded signals. Among them, sweeps have least correlation noise, but their frequence band may be too wide for some practical applications. Carefully designed pulse sequences may have very low correlation noise, but the sequence may be too long. M-sequences and Gold sequences seem to be the most powerful. Since the frequency band does not increase when the number of the sequences increases, the number of M-sequences and Gold sequences that can be used as simultaneous source signatures is large, and easy to generate.

ACKNOWLEDGEMENTS

The authors would like to thank the Gas Research Institute for support of this work.

REFERENCES

Barbier, M. G., 1982, Pulse coding in seismology: IHRDC.

Bernhardt, T. and Peacock, J. H., 1978, Encoding techniques for the vibroseis system: Geophysical Prospecting, **26** 184-193.

Cunningham, A. B., 1979, Some alternate vibrator signals: Geophysics, **44**, 1901-

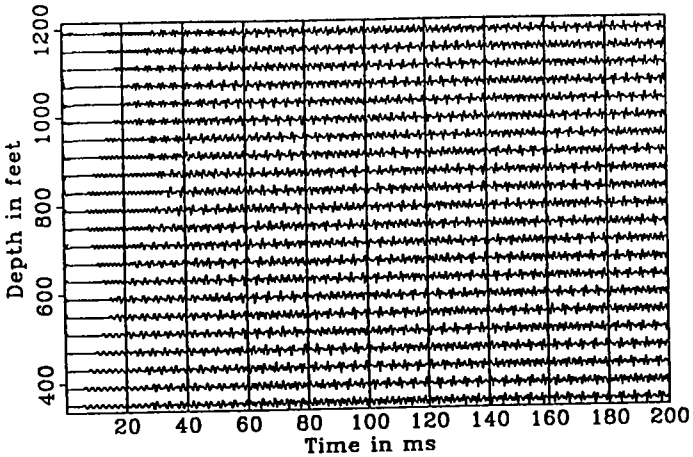

(a) Composite seismograms.

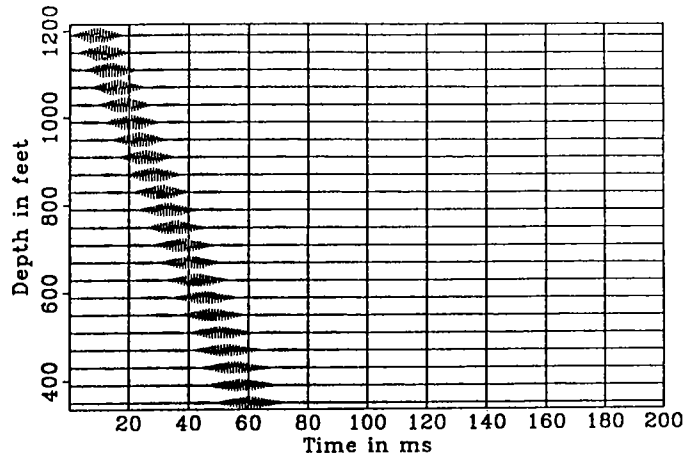

(b) Separated seismograms corresponding to $S_1(t) \star S_1(t)$.

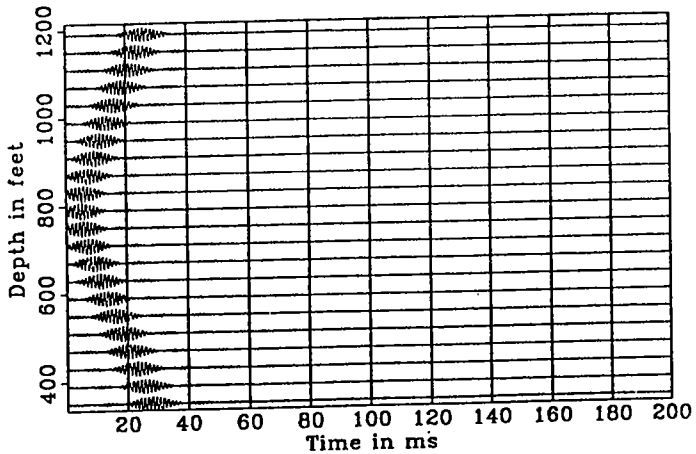

(c) Separated seismograms corresponding to $S_2(t) \star S_2(t)$.

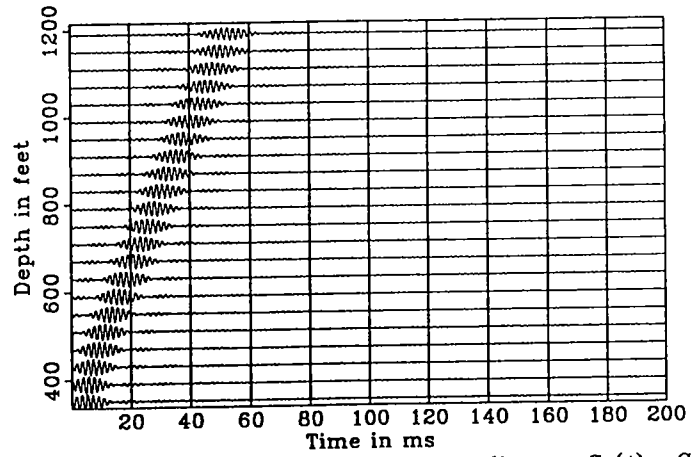

(d) Separated seismograms corresponding to $S_3(t) \star S_3(t)$.

Figure 5: Composite seismograms generated by sweeps $S_1(t) = sin[2\pi(400 + 95t/T)t]$, $S_2(t) = sin[2\pi(300 + 95t/T)t]$ and $S_3(t) = sin[2\pi(200 + 95t/T)t]$ (upper left), and separated seismograms corresponding to sources $S_1(t) \star S_1(t)$, $S_2(t) \star S_2(t)$ and $S_3(t) \star S_3(t)$ respectively(right), where '$\star$' represents correlation.

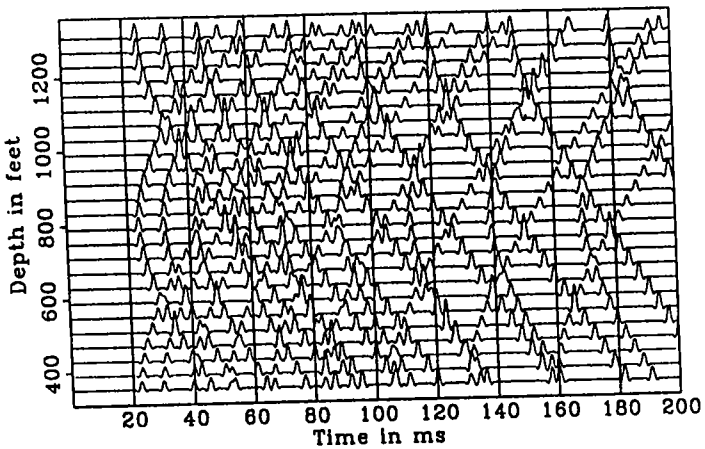

(a) Composite seismograms.

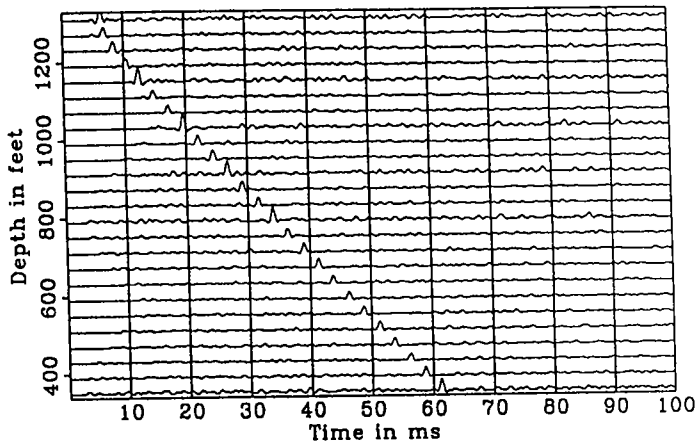

(b) Separated seismograms corresponding to $P_1(t) \star P_1(t)$.

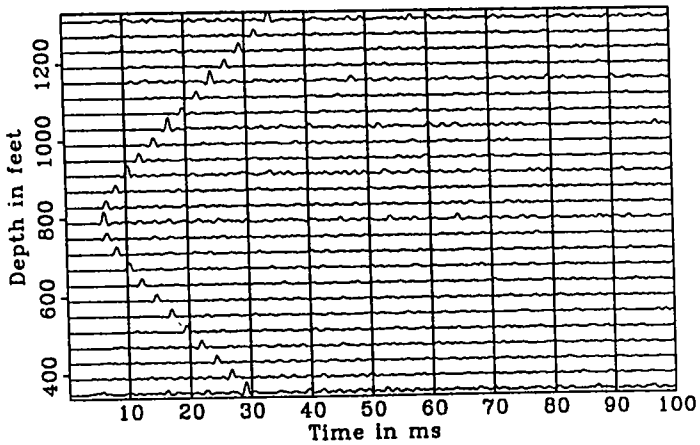

(c) Separated seismograms corresponding to $P_2(t) \star P_2(t)$.

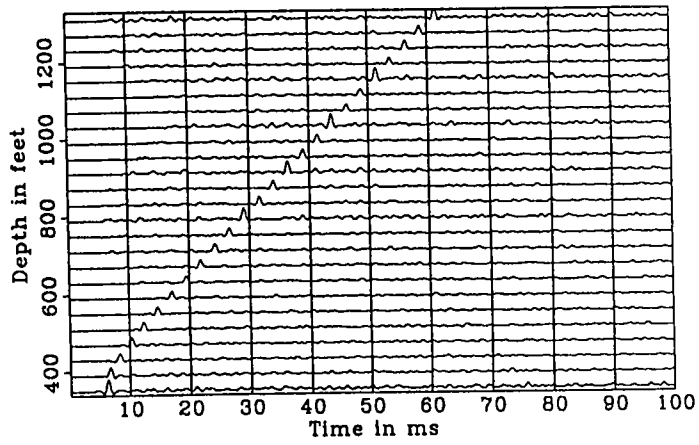

(d) Separated seismograms corresponding to $P_3(t) \star P_3(t)$.

Figure 6: Composite seismograms generated by pulse sequences $P_1(t)$, $P_2(t)$ and $P_3(t)$ (upper left), and separated seismograms corresponding to $P_1(t) \star P_1(t)$, $P_2(t) \star P_2(t)$ and $P_3(t) \star P_3(t)$ respectively.

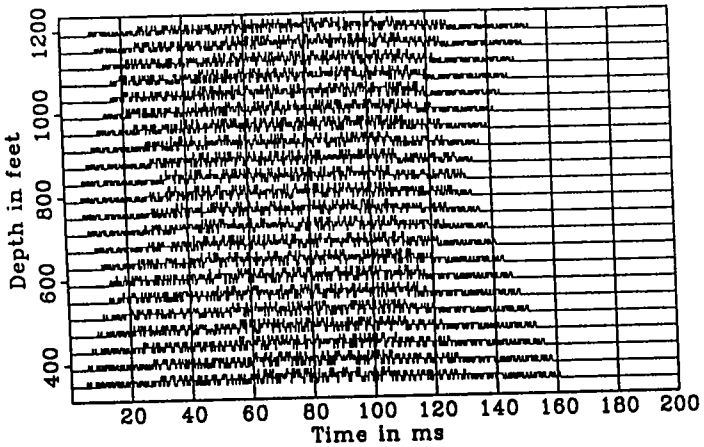

(a) Composite seismograms.

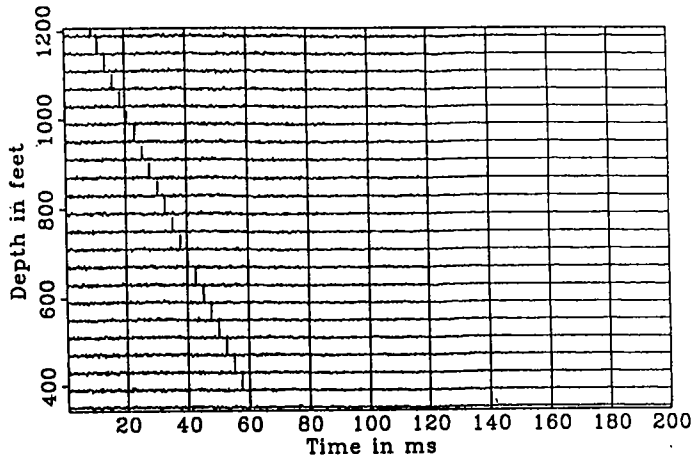

(b) Separated seismograms corresponding to $M_1(t) \star M_1(t)$.

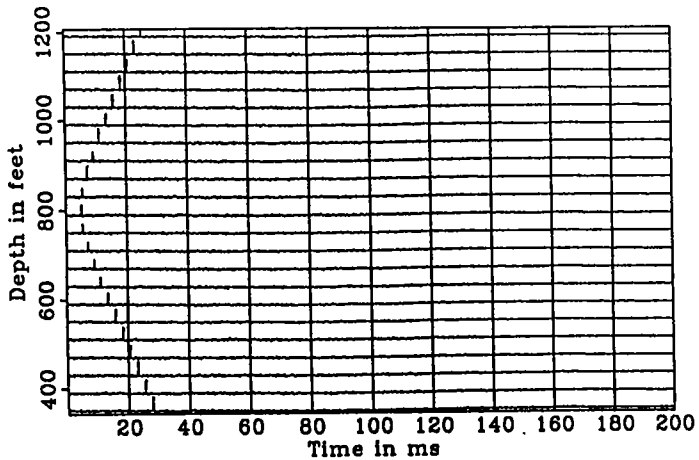

(c) Separated seismograms corresponding to $M_2(t) \star M_2(t)$.

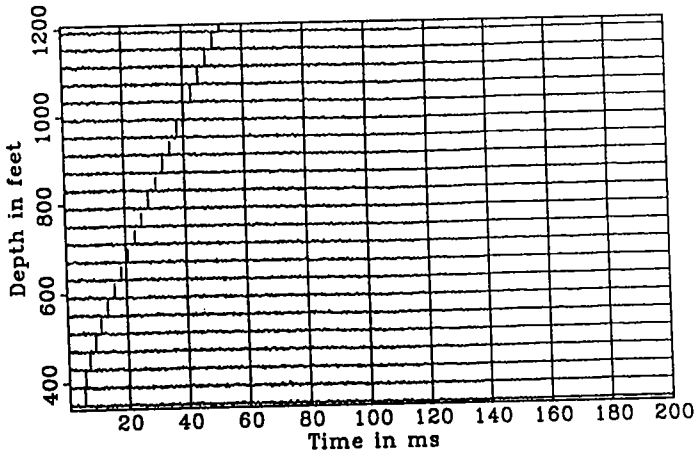

(d) Separated seismograms corresponding to $M_3(t) \star M_3(t)$.

Figure 7: Composite seismograms generated by M-sequences $M_1(t)$, $M_2(t)$ and $M_3(t)$ (upper left), and separated seismograms corresponding to $M_1(t) \star M_1(t)$, $M_2(t) \star M_2(t)$ and $M_3(t) \star M_3(t)$ respectively.

1921.

Edelmann, H. and Werner, H., 1982, The encoded sweep technique for vibroseis: Geophysics, **47**, 809-818.

Gold, R., 1967, Optimal binary sequences for spread spectrum multiplexing: IEEE Trans. Inform. Theory, **IT-13**, 619-621.

Helleseth, T., 1976, Some results about the cross-correlation function between two maximal linear sequences: Discrete Math., **16**, 209-232.

Pritchett, W., 1991, An example of simultaneous recording where necessary signal separation is easily achieved: Geophysics, **56**, 9-17.

Sarwate, D. and Pursley, M., 1980, Crosscorrelation properties of pseudorandom and related sequences: Proceedings of the IEEE, **68**, 593-619.

Welti, G., 1960, Quaternary codes for pulsed radar: Inst. Radio Eng. Trans. Inf. Theory, **6**, 400-408.

Womack, J., Cruz, J., Rigdon, H. and Hoover, G. 1990, Encoding techniques for multiple source point seismic data acquisition : Geophysics, **55**, 1389-1396.

Yarmolik, V., 1988, Generation and application of pseudorandom sequences for random testing: Wiley.

PAPER I

SIMULTANEOUS ITERATIVE TRANSFORM TOMOGRAPHY
(Generalized String Inversion)

Jerry M. Harris
Seismic Tomography Project

ABSTRACT

I present the theoretical basis for a new method of traveltime inversion based on a semi-continuous representation of the slowness field. The inversion can be called a pseudo-transform method of reconstruction. I use an iterative solver to invert the pseudo-transform, thus the name iterative transform tomography. When discretized and numerically implemented, iterative transform tomography resembles a finely gridded series-expansion method of reconstruction such as ART or SIRT. Iterative transform tomography captures many of the benefits of both transform inversion methods and finite series-expansion methods. It is demonstrated to be a fast, robust, and flexible method for traveltime tomography. This paper presents the reconstruction theory and the description of a special case known as string tomography.

INTRODUCTION

In a recent review paper (Lewitt, 1983) on reconstruction algorithms, transform reconstruction methods were characterized as having three main steps:

1. formulate a mathematical model in which the known and unknown are functions whose arguments come from a continuum of real numbers;
2. derive an inversion formula for the unknown continuous function;
3. adapt the inversion formula to discrete and noisy data.

In contrast, in series-expansion algorithms (Censor, 1983) the mathematical model is discretized at the beginning with a finite set of unknowns (basis functions) representing the image. Moreover, the most popular choice of basis function is the orthogonal pixel of

constant slowness; therefore, the unknowns are the actual image values in homogeneous regions, thus inseparably mixing inversion and display. This choice of parameterization of the image provides a clear mathematical and physical understanding of the inversion model but can yield unsightly sharp boundaries in the reconstruction. Furthermore, the approximation of smoothly varying images is expensive in the sense that a large number of these pixels may be necessary to obtain an adequate representation. A "high resolution" result demands many model parameters, thus burdening tomography with inversion of a large and sparse projection matrix. In practice, resolution (the number of pixels N) is traded off against the expense of inversion.

It's readily seen that transform methods clearly separate inversion (step 2) from image discretization (step 3). Although the series-expansion approach is not restricted to orthogonal pixels, when used as often is the case, such orthogonal pixels combine two conflicting objectives - parameterization for inversion purposes and discretization for display purposes. Transform methods are very popular in the medical world due primarily to their speed, accuracy of reconstruction, and the conformance of the data to the requirements of the computer algorithms. Series-expansion methods are far more popular in geophysics, especially for crosswell tomography, primarily because of their flexibility in handling curved ray paths and their adaptability to noisy data taken from limited apertures. Despite these obvious advantages of series-expansion or algebraic methods in geophysics, transform (or pseudo-transform) methods may have powerful complementary benefits.

In this paper, I describe an inversion method which exploits the merits of both transform and series-expansion methods. The inversion algorithm, called iterative transform tomography, is performed by a pseudo-transform method which is adapted to curved ray paths and irregularly sampled acquired from limited-view geophysical apertures. The method is developed specifically for crosswell seismic traveltime tomography applications but is applicable to other geophysical inversion problems as well. The paper is divided into two major sections. Mathematical models for reconstruction are formulated in the first section; this includes a sub-section on the discrete model and series expansion reconstruction and a sub-section on the semi-continuous models and the new pseudo-transform reconstruction. In the second section, the theory is developed into a geophysical algorithm with two dimensional ray tracing for applications to crosswell seismic tomography.

THEORY AND FORMULATION

Let S(x, z) represent the 2D continuous slowness field (inverse velocity). The problem is to estimate S(x, z) from a finite set of observed traveltimes $\{t_i\}$, $1 \le i \le M$. Two models are required to pose the inversion problem: (1) a mathematical model which captures albeit approximately the physical process of generating the observed traveltimes; and (2) a measurement model which describes the physical process of seismic wave propagation in heterogeneous media, i.e., the slowness field, which produced the observed traveltimes.

Mathematical model

A projection through S(x, z) about a line connecting the source and receiver points is defined to be the traveltime function $\tau(r, s)$. The traveltime is a continuous function of the pair-variables (r, s), where "r" and "s" denote the receiver and source position, respectively. Mathematically, the values of $\tau(r, s)$ are assumed to be given by a two dimensional surface integral through the slowness field, where the support of this integral is the beam path denoted by B(S; r, s; x, z). The beam path depends on the slowness field and represents the area of the slowness field influencing the traveltime observed by the source-receiver pair (Michelena and Harris, 1991). Mathematically, the continuous beam equation is

$$\tau(r, s) = \int_{\Omega} B(S; r, s; x, z) S(x, z)\, dxdz. \tag{1}$$

An equivalent model for discrete traveltimes is

$$\tau_i = \int_{\Omega} B_i(S; x, z)\, S(x, z)\, dxdz, \qquad 1 \le i \le M \tag{2}$$

where subscript "i" denotes the ith source-receiver pair. For convenience, I will sometimes use the notation $\tau_i = B_i S$ instead of Eqn. (2) to describe a traveltime value calculated for the ith source-receiver pair. For mathematical purposes that will be discussed in detail in the following sections, it is necessary to assume that the slowness field has finite support, i.e., $S(x, z) = 0$, if (x,z) is outside the region Ω, and square integrable, i.e., $\int_{\Omega}[S(x, z)]^2\, dxdz$ exists. If S(x, z) has these properties then S(x, z) will be called an image. Eqn. (1) and Eqn. (2) define the "mathematical model." Clearly, it is not the only choice possible and as will be discussed below this beam equation is often replaced with the "ray" equation. A

test of validity is the ability of the mathematical model to adequately describe the observations.

Measurement model

The measurement system which produced the observed traveltime "t_i" is completely unaware of our mathematical model. For purposes of description only, I assume that a finite set of functionals, $F_1, F_2, \ldots F_M$, exists; each assigns to any real world slowness image a real number $t_i = F_i S$ equaling the observed traveltime t_i for $1 \le i \le M$. Just as Eqn. (1) is called the mathematical model, the finite sequence $F_1, F_2, \ldots F_M$ is called the "measurement model." If the calculated traveltime τ_i approximately equals the measured traveltime t_i, then the mathematical model adequately describes the physical process for purposes of inversion. In practice, however, due to measurement error and physical effects not captured by Eqn. (1), the calculated traveltimes will only approximately equal the measured traveltimes. Further, for sake of the development of the inversion theory, I must explicitly assume that the functional F_i describing the measurement is linear and continuous. That is, $F_i(S_1 + S_2) = F_iS_1 + F_iS_2$ and if $S_1(x, z) \approx S_2(x, z)$ for all (x, z), then $F_iS_1 \approx F_iS_2$. The importance of these assumptions is discussed in the following section.

In the next sub-section, I will introduce two alternative reconstruction models. The *discrete model* describes the slowness field with a finite set of numbers, e.g., pixel values, spline coefficients, etc. The discrete model is common to series-expansion reconstructive algorithms. The *semi-continuous model* describes the slowness field as a continuous function of position estimated from discrete data, thus the name. The semi-continuous model is the basis for the subject of this paper - iterative transform reconstructive algorithms.

Discrete Series-Expansion Reconstruction

Suppose S(x, z) is an image parameterized by the vector $a_1, a_2, \ldots a_N$, and observed traveltimes $\{t_i\}$ are known for $1 \le i \le M$. Find the constants $\{a_i\}$. This is a *discrete series-expansion reconstruction problem.* Parameterizing the slowness field by a discrete set of values first requires definition of a set of basis functions $\{\varphi_j(x, z)\}$, $1 \le j \le N$ whose linear combination give an adequate approximation, e.g., $\widehat{S}(x, z) \approx S(x, z)$, to the true slowness. I am free to choose the basis functions to suit convenience or other criteria. In effect, each basis function $\varphi_j(x, z)$ is itself an image according the definition given above, i.e, compact support and square integrable. For example, a common choice is the orthogonal set of

constant pixel functions: $\varphi_j(x, z) = 1$ inside a small rectangular region called a pixel and $\varphi_j(x, z) = 0$ outside. Thus for any image constructed with this model, there exist real numbers $a_1, a_2, \ldots a_N$ such that

$$S(x, z) \approx \hat{S}(x, z) \equiv \sum_{j=1}^{N} a_j \varphi_j(x, z) \tag{3}$$

The a_j's in Eqn. (3) form a finite set which parameterize the slowness, i.e., a series-expansion. Linearity of the measurement model leads to an equation relating the measured traveltimes for this approximate image to the constants describing the slowness, that is

$$F_i\hat{S}(x, z) = \sum_{j=1}^{N} a_j F_i \varphi_j \qquad 1 \le i \le M. \tag{4}$$

Hence, for purposes of the series-expansion reconstruction, the finite set of numbers $F_i\varphi_j$ over which the sum in Eqn. (4) is taken may describe the measurement model sufficiently. In practice, however, because the exact nature of F_i is not known, one is forced to replace $F_i\varphi_j$ with an estimate W_{ij} computed say from the mathematical model Eqn. (1):

$$F_i\varphi_j \approx W_{ij} = \int_{\Omega} B_i(S; x, z)\, \varphi_j(x, z)\, dxdz, \tag{5}$$

where B_i is the beam operator defined by Eqn. (2). The value W_{ij} is "calculated" for ith source-receiver pair and the jth basis image $\varphi_j(x, z)$, whereas $F_i\varphi_j$ is "measured" through $\varphi_j(x, z)$. When $\varphi_j(x, z)$ is the orthogonal pixel of constant unit slowness, W_{ij} is simply the area of the ith beam intersecting the jth pixel. Substituting (5) into (4) gives

$$\hat{t}_i = \sum_{j=1}^{N} W_{ij}\, a_j \qquad 1 \le i \le M. \tag{6}$$

where $\hat{t}_i$ is the measured traveltime in the approximate image $\hat{S}(x, z)$. Eqn. (6) nearly achieves the intermediate goal of discrete inversion, that is, to find a set of relationships between the observed traveltimes $\{t_i\}$ to the coefficients $\{a_j\}$. Unfortunately the left side of (6) is not exactly the known traveltimes but can be approximated by such, i.e., $\hat{t}_i \approx t_i$.

Combining all our approximations to this point yields the matrix system to be solved for the unknown constants:

$$\mathbf{t} = \mathbf{W}\mathbf{a} + \mathbf{e}, \tag{7}$$

where **t** is the (Mx1) column vector of observed traveltimes, **W** is the (MxN) projection matrix whose elements are defined in Eqn. (5), **a** is the (Nx1) column vector of unknown coefficients which parameterize the slowness field, and **e** is the vector of errors due to the many approximations such as the inaccuracies in measurements $\hat{t}_i \approx t_i$, the approximate nature of the series expansion $\hat{S} \approx S$, and the approximation for the projection matrix $W_{ij} \approx F_i\varphi_j$. The derivation leading to Eqn. (7) clearly identifies these approximations.

A rich literature exists on the subject of solving Eqn. (7) for the constants $\{a_j\}$. See Censor (183). While I will not address the general aspect of the problem here, I present here the solution based on well-known algebraic reconstruction techniques:

$$a_j^{(i+1)} = a_j^{(i)} + \frac{t_i - \tau_i}{\sum_{k=1}^{K} W_{ik}^2} W_{ij} \qquad \text{D-ART} \tag{8}$$

$$a_j^{(k+1)} = a_j^{(k)} + \frac{1}{M} \sum_{i=1}^{M} \frac{t_i - \tau_i}{\sum_{k=1}^{K} W_{ik}^2} W_{ij} \qquad \text{D-SIRT} \tag{9}$$

Eqns. (8) and (9) iteratively yield the coefficients discretely parameterizing the slowness image. In ART, the coefficients are updated sequentially with each projections. In SIRT, the coefficients are updated once for a set of projections whose number is denoted here by L. I refer to these as discrete (D) algebraic techniques. i.e., D-ART and D-SIRT. For more details, see Haykin (1985). In geophysics, especially for cross-well tomography, the most popular choice of basis function is the orthogonal pixel of constant slowness, i.e., $\varphi_j(x, z) = 1$ if (x, z) is inside the jth pixel and $\varphi_j(x, z) = 0$ otherwise; therefore a_j represents the actual slowness in that pixel. This choice of basis functions provides a clear mathematical and physical understanding of the inversion model but can yield unsightly sharp boundaries in the reconstructed image. Furthermore, the approximation of smoothly varying images is expensive in the sense that a large number of these pixels may be necessary to obtain an adequate representation. A "high resolution" result demands many model parameters, thus burdening the inversion procedure with a large and sparse

projection matrix **W**. In practice, resolution (the number of pixels N) is traded off against the expense of inversion. Although the series-expansion approach is not restricted to just orthogonal pixels, when used as often is the case, such orthogonal pixels combine two conflicting objectives - parameterization for inversion purposes and discretization for display purposes. In the next sub-section, I will introduce a method for avoiding this conflict.

Semi-Continuous Reconstruction

First, a statement of the *"continuous"* reconstruction problem: Suppose S(x, z) is an image and traveltimes t(r, s) are known for continuous values of source and receiver locations, find an estimate of S(x, z). This is a statement of the *continuous reconstruction problem*, that is, S(x, z) is not pixelated into a fixed number of unknowns as in the discrete reconstruction described above. Instead, a continuous estimate of S(x, z) is sought. More often than not, transform methods are used for reconstruction problems of this type. Though well-posed in general, this continuous formulation is unrealistic for geophysical applications. First, it assumes that the traveltimes are known for continuous source and receiver positions. And, second, it ignores the limited aperture effects which severely restrict the number and location of sources and receivers. Whereas the problem of limited aperture is not the subject of this paper and will not be addressed, the handling of discrete data is essential, thus demanding the semi-continuous model described below.

A more realistic reconstruction model uses discrete data but still seeks to form a continuous estimate of S(x, z), thus defining the the *"semi-continuous"* problem: Suppose S(x, z) is an image and discrete traveltimes t_i are known for $1 \le i \le M$, find an estimate of the continuous image S(x, z) satisfying all observed traveltimes. Combining discrete observations $\{t_i\}$with a continuous model for S(x, z) leads to the semi-continuous model. In contrast , the discrete model given by Eqn. (7) combines both discrete data with a discrete slowness representation and the continuous model combines continuous data with a continuous slowness representation.

A solution method known for the semi-continuous reconstruction problem is described in Appendix A, where an iterative solution similar to conventional ART or SIRT is presented. The solution can be summarized in two equations, from (A-3) and (A-5), which iteratively give an estimate for the continuous slowness:

$$\hat{S}^{(i+1)}(x, z) = \hat{S}^{(i)}(x, z) + \frac{t_i - \tau_i}{A_i} B_i(x, z) \qquad \text{SC-ART} \qquad (10)$$

$$\hat{S}^{(k+1)}(x, z) = \hat{S}^{(k)}(x, z) + \frac{1}{M_B} \sum_{i=1}^{M} \frac{t_i - \tau_i}{A_i} B_i(x, z) \qquad \text{SC-SIRT} \qquad (11)$$

where in Eqn. (11), M_B is the number of beams touching the image point (x,z). Eqns. (10) and (11) describe iterative semi-continuous (SC) ART and SIRT. Unlike their counterparts (Eqns. (8) and (9)), however, these versions define solutions for the continuous slowness field itself not the coefficients of a discrete paramerization model, e.g, $\{a_j\}$. The constant $A_i = \int_\Omega B_i(x, z)\, dxdz$, where $B_i(x, z)$ functionally describes the beam path itself, i.e., $B_i = 1$ on the ith beam path, $B_i = 0$ otherwise. Either of these equations resemble transform reconstruction methods more than series expansion methods: they estimate the slowness as a continuous function of space. Indeed, solutions of this type have been called iterative transform reconstructions (Hermann and Lent, 1974). I refer to Eqn. (11) as Simultaneous Iterative Transform Tomography.

The differences between the semi-continuous reconstructions and the discrete reconstruction become blurred when the SC-model is discretized for numerical solution or when the pixel size in the D-model is shrunk to zero. At that point, both become finely gridded iterative solutions. A numerical algorithm implementing the SC-SIRT for cross-well tomography is presented in the next section.

CROSSWELL SEISMIC TOMOGRAPHY

The formulations summarized above are generally useful in their stated form for linear inversion problems, where the beam path is known and inversion is performed to obtain the slowness field. Seismic applications are often highly nonlinear in that the beam path depends on the slowness and both are unknown. That is, the variations in slowness are large enough that refraction is significant thus rendering the beam path as well as the slowness unknown. This dependence is easily seen in Eqns. (1) and (2) where the beam path is shown to depend explicitly on S. The usual and well known procedure of addressing this nonlinearity is to linearize Eqn. (1) by assuming that the slowness can be decomposed into a known component $S_o(x, z)$ and an unknown perturbation $\delta S(x, z)$, i.e.,

$$S(x, z) = S_o(x, z) + \delta S(x, z). \qquad (12)$$

Fermat's principle is then invoked in order to produce

$$\delta\tau(r, s) = \int_{\Omega} B(S_o; r, s; x, z)\delta S(x, z)\, dxdz\,, \tag{13}$$

where $\delta\tau = \tau - \tau_o$ is the difference between the total traveltime in the unknown slowness model S and the traveltime τ_o for the known slowness model S_o. The beam path for all traveltime calculations is found for the known (background) slowness field. For inversion purposes, Eqns. (12) and (13) define a linear mathematical model between the slowness perturbation and the traveltime perturbation. This model relies on Fermat's principle to argue explicitly that the traveltime computed in the slowness field S is not too different from the traveltime calculated in slowness field S_o provided δS is small. Inversion is actually performed for for the perturbation, usually within an iterative numerical scheme of assuming S_o, calculating residual traveltimes, solving for δS, then updating the slowness as S_o for input to the next iteration. In most practical situations, convergence of the scheme is measured by the smallness of the traveltime perturbation $\delta\tau$ and/or the smallness of changes in the slowness.

String Tomography

A special case of the iterative transform method is the string algorithm, designed here for seismic tomography. The string algorithm uses conventional ray tracing rather than more general beam tracing. For geophysical applications, SIRT methods appear to be more robust than ART with respect to noise such as picking errors and limited view. For this reason, only the SC-SIRT algorithm of Eqn. (16) has been implemented to date; that is, model updates are performed for all projections (traveltimes) at once. The general string algorithm, schematically illustrated in Figure 1, features unlinked ray tracing and interpolation of the measured traveltime data.

The ray equation replaces the beam equation Eqn. (1):

$$\tau_i = \int_{L_i} S_o(x, z)\, dl, \qquad 1 \le i \le M \tag{15a}$$

Or,

$$\tau_i = \int_{\Omega} S_o(x, z)\, \phi_i(x, z)\, dxdz, \qquad 1 \le i \le M \tag{15b}$$

where $\phi_i(x, z)$ defines the ray path in two dimensions, i.e., $\phi_i = 1$ on the ray path and $\phi_i = 0$ otherwise. A simple numerical scheme solving the eikonal equation is used to find $\phi_i(x, z)$.

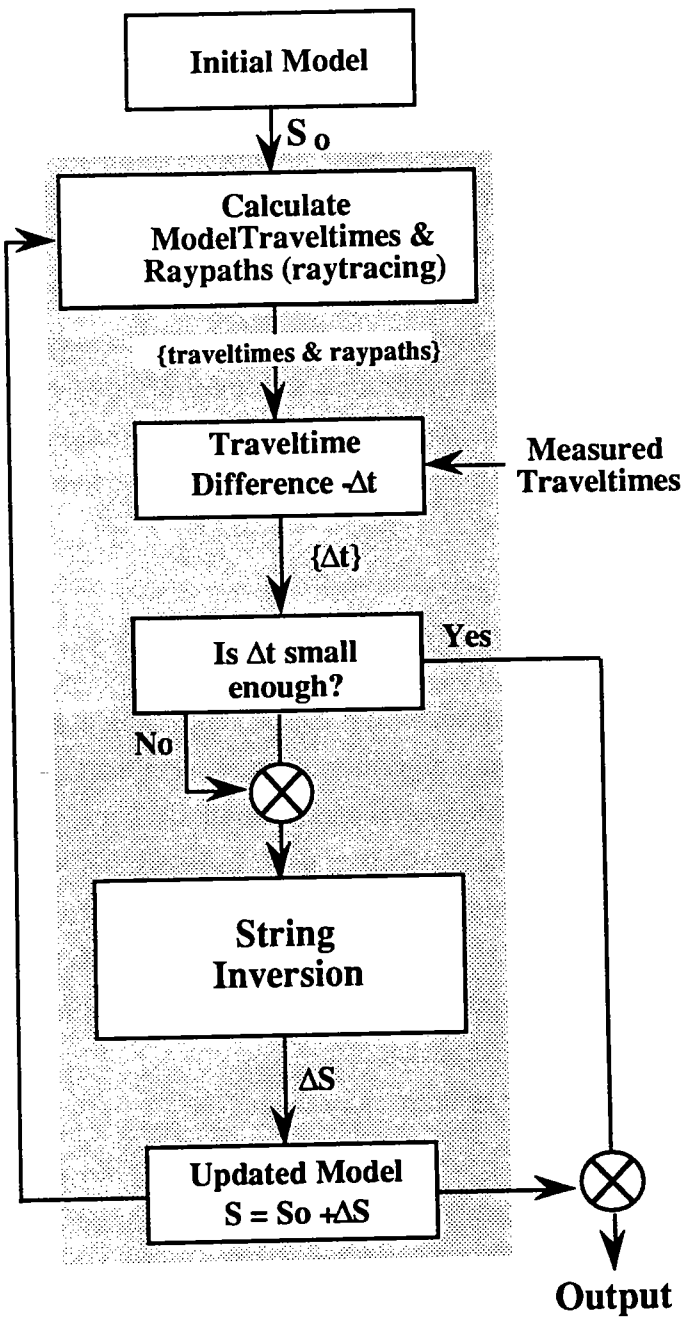

Figure 1. Schematic outline of the string inversion algorithm

The numerical scheme is a standard Runge-Kutta integration (McMechan, et, al 1987). but is specially implemented to run on a scalar workstation. Rays are not linked between source and receiver; instead, a common-source gather of traveltimes is computed by launching a sequence of rays from the source toward the receiver borehole. At the receiver well, a set of pseudo-receivers intercept these rays thus generating synthetic traveltimes at numerous points along the receiver wellbore. These synthetic traveltimes are then compared to the measured traveltimes to produce the SC-SIRT correction $\delta\hat{S}$ to the background model:

$$\delta\hat{S}^{(k+1)}(x, z) = \frac{1}{M_\phi} \sum_{i=1}^{M} \frac{t_i - \tau_i}{R_i} \phi_i(x, z), \tag{16}$$

where R_i , τ_i ,and ϕ_i , are the effective length, traveltime, and path function, respectively, of the ith ray in the kth model and M_ϕ is the number of rays touching the image point at (x,z). While Eqn. (16) expresses only one correction per ray trace iteration, it is possible to perform several iterations thus refining the estimate for $\delta\hat{S}$ between ray tracings.

Recall that rays are not linked between the sources and receivers. Therefore, in order to compare the synthetic with the measured traveltimes, the measured values must be estimated at the pseudo-receiver locations. To accomplish this, a numerical wavefront is fit to the actual measured traveltimes as a function of depth and a "measured" traveltime is estimated for each of the synthetic pseudo-receivers. This procedure relies on the fact that the measured traveltimes are adequately sampled to reconstruct the wavefront; otherwise, important structure of S(x, z) manifested in the traveltime wavefront would be missed. In general the number of rays launched in the simulated gather is about 2 times greater than the actual number of measured traveltimes and the traveltime data used in Eqn. (16) are replaced by data generated from the interpolation equation

$$t_m = \sum_{i=m-2}^{m+2} \mathbf{I}_{i-m}\, t_i \tag{17}$$

where $\mathbf{I}_{i-m}$ is an interpolation operator applied to the measured data t_i, and t_m are the interpolated traveltimes. Aside from simplifying the ray tracing algorithm, the pseudo-receivers play a very important role in interpolating the image in a manner consistent with the model S_o. For all practical purposes, this method of traveltime interpolation creates a

semi-continuous dataset thus satisfying the requirement of the semi-continuous reconstruction theory.

The next step is to add the background model S_o to the estimate $\delta\hat{S}(x, z)$ and discretize the result:

$$\hat{S}(i\Delta r_x, j\Delta r_y) = S_o(i\Delta r_x, j\Delta r_y) + \frac{1}{2M_\phi} \sum_{m=1}^{2M} \frac{t_m - \tau_m}{R_m} \phi_m(i\Delta r_x, j\Delta r_y) \tag{18}$$

In effect, Eqn. (18) is the implementation of Lewitt's step (3) described in the Introduction. However, the image produced by Eqn. (18) is irregularly sampled on a grid determined by the ray coordinates. In practice, ϕ_i is regularly sampled along the ray path $(i\Delta r_x, j\Delta r_z)$ not a Cartesian grid. So, the final step in the overall tomography process is to regularize Eqn. (18) for display on an equi-spaced Cartesian grid:

$$\hat{S}(i\Delta x, j\Delta z) = \sum_{m=i-L}^{i+L} \sum_{n=j-L}^{j+L} B(m-i,n-j)\, \hat{S}(m\Delta r_x, n\Delta r_z) \tag{19}$$

The sample intervals $(\Delta x, \Delta z)$ and $(\Delta r_x, \Delta r_z)$ should be kept as small as practical in order to maintain consistent approximations for the semi-continuous model. Eqns. (18) and (19) complete the theoretical development of the iterative transform tomography algorithm.

ACKNOWLEDGEMENTS

The author thanks the Gas Research Institute for its financial support of the crosswell tomography project and the David and Lucille Packard Foundation for its Research Fellowship awarded the author.

REFERENCES

Censor, Y. 1983, Finite series-expansion reconstruction methods, Proc. IEEE, Vol. 71, No. 3, pp. 409-419.

Haykin, S., 1985, Array Signal processing, Prentice-Hall, Inc. Englewood Cliffs, New Jersey, Chapter 6.

Herman and Lent, 1976, Iterative reconstruction algorithms, Comput. Biol. Med. Vol. 6, pp. 273-294.

Lewitt, R. M., 1983, Reconstruction methods, Proc. IEEE, Vol. 71, No. 3, pp. 390-408.

McMechan, G. A., Harris, J. M., and Anderson, L., 1987, Cross- well tomography for strongly variable media with application to scale model data, Bulletin of the Seismological Society of America, Vol. 77, No. 6, pp. 1945-1960.

Michelena, R, and Harris, J. M., 1991, Tomographic traveltime inversion using natural pixels, Geophysics, Vol. 56, No. 5, May 1991, pp. 635-644.

Appendix A - Iterative Transform Inversion

Following Herman and Lent [], I will first derive a inversion formula which can be used to reconstruct S(x, z) from discrete traveltime data. This inversion is similar to algebraic reconstruction techniques, so I'll proceed with a similar derivation.

Iterative reconstruction algorithms such as ART and SIRT are well established. However, unlike conventional ART and SIRT which are based on discrete representation of the slowness as represented by (3), I seek here a continuous representation for the slowness image. There are many excellent treatments of the ART and SIRT algorithms based Kaczmarz's "method of projections", so I will not repeat those details here but will describe the geometrical interpretation of my reconstruction which differs for the semi-continuous model. The derivations rely on a Hilbert space representation as follows: The set of all continuous images $\{S_i\}$, each being defined in the sub-section on mathematical models, forms a vector space in which the inner product of any two images say $S_1(x, z)$ and $S_2(x, z)$ can be defined by

$$\langle S_1 \cdot S_2 \rangle = \iint_P S_1(x, z)\, S_2(x, z)\, dxdz \qquad \text{(A-1)}$$

where "P" is the entire two-dimensional Cartesian x-z plane. It is well known that with this inner product the set of all equivalent classes of images forms a Hilbert space, which I'll denote by **H**. The aim of the continuous reconstruction is to find an image, say one image $\hat{S}(x, z)$, which satisfies all M traveltimes $\{t_i\}$, $1 \le i \le M$.

Now, if one assumes that $\hat{S}(x, z)$ is a member of **H**, then the set of all images which satisfy the single traveltime t_i also forms a closed subspace of **H** that I'll denote by $\mathbf{N_i}$, $1 \le i \le M$. If the image which satisfies all M traveltimes is denoted by $\mathbf{N_0}$, then clearly $\mathbf{N_0}$ is the intersection of the M closed subspaces. See Figure A-1. Evidently, $\mathbf{N_0}$ itself is a subspace of **H** and may have more than element (i.e., image). In this case, it is important to establish some additional optimally criteria. Herman and Lent [1976] point out that the minimum-norm solution to which the method of projections converges is the image in $\mathbf{N_0}$ which minimizes

$$\langle \hat{S} \cdot \hat{S} \rangle = \iint_P [\hat{S}(x, z)]^2\, dxdz. \qquad \text{(A-2)}$$

Finally, the notion of orthogonal projections on a closed linear variety is required to complete the development. Solomon[] has shown that the orthogonal projection denoted by $S^{(k+1)}(x, z)$ of the image $S^{(k)}(x,z)$ onto the closed linear variety N_i is given by

$$\widehat{S}^{(i+1)}(x, z) = \widehat{S}^{(i)}(x, z) + \frac{t_i - \tau_i}{A_i} B_i(x, z) \tag{A-3}$$

where t_i is the observed traveltime, τ_i is the calculated traveltime in the image model $\widehat{S}^{(k)}(x, z)$, $B_i(x, z)$ is the ray path, and $A_i = \int_\Omega B_i(x, z)\, dxdz$ is the characteristic of the beam path, i.e, the path integral given by Eqn. (2) with a unity slowness field everywhere. The new image $\widehat{S}^{(k+1)}(x, z)$ is continuously defined for the variables (x, z) at every point within the support of the ith beam path. Moreover, the sequence of images $\widehat{S}^{(0)}$, $\widehat{S}^{(1)}$, $\widehat{S}^{(2)}$, ... converges to the minimum norm element of $\mathbf{N_0}$. This says that if S(x, z) is the unique image which among all images to satisfy the traveltimes which minimizes (A-2), then

$$\lim_{k \to \infty} \iint_P [\widehat{S}^{(k)}(x,z) - S(x, z)]^2\, dxdz \longrightarrow 0\,, \tag{A-4}$$

See Figure A-1 for a geometric interpretation of this convergence for M = 2.

The similarity of Eqn. (A-3) to conventional discrete ART is of little surprise. This iterative solution might be called semi-continuous or SC-ART. Unlike conventional ART, the iterations for SC-ART produce the slowness image directly not the model coefficients parameterizing the slowness. In this sense, Eqn. (A-3) is a transform method. The method avoids discretization of the slowness field at the beginning as conventional algebraic methods do. For practical use, Eqn. (A-3) must be discretized just as any other transform inversion. Inversion according to Eqn. (A-3) is referred to as iterative transform tomography. Algorithms implementing iterative transform tomography deal with one equation at a time and their convergence is assured (Herman and Lent, 1976). It is possible, however, to alter the algorithms for a small subset of the equations or all equations simultaneously, e.g., a semi-continuous SC-SIRT method which is discussed in a later section.

$$\widehat{S}^{(k+1)}(x, z) = \widehat{S}^{(k)}(x, z) + \frac{1}{M_B} \sum_{i=1}^{M} \frac{t_i - \tau_i}{A_i} B_i(x, z), \tag{A-5}$$

where M_B is the number of beams touching the image point at (x,z).

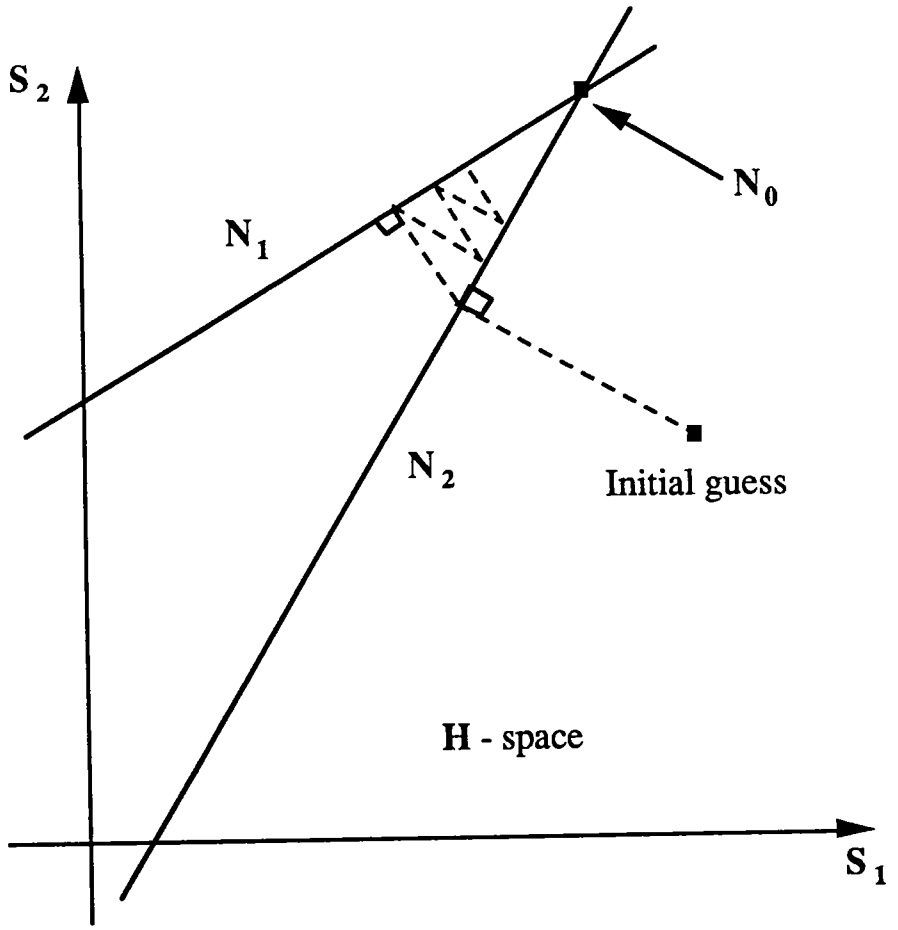

Figure A-1. Geometric interpretation of Hilbert space convergence of SC-ART algorithm for simple case of M = 2. N_1 and N_2 are closed linear varieties in the Hilbert space of possible images satisfying traveltimes t_1 and t_2, respectively. N_0 is the closed linear variety of images satisfying both t_1 and t_2.

PAPER J

STATISTICS FROM STRINGS

Nicholas Smalley and Jerry M. Harris
Seismic Tomography Project

ABSTRACT

The computation and interpretation of higher order statistics for the imaging region in tomographic traveltime inversion is presented in this paper. Tomographic String Inversion allows for easy computation of several orders of statistics in the imaging process. These statistics can be used to make interpretations about the values which go into calculating the mean or first order statistic, and can be used to improve the convergence of the string inversion as well as the convergence slowness value.

INTRODUCTION

In traveltime tomography, the objective is to obtain as much information from the traveltime data as possible. Usually the slowness value that is assigned to individual square regions or pixels is a mean or optimum value that results from inversion of the matrix equation

$$\mathbf{A}\,\mathbf{s} = \mathbf{t}, \tag{1}$$

where **s** is the slowness vector consisting of all the square pixels, A is the projection matrix, and **t** is the traveltime vector consisting of all the raypath traveltimes. The raypaths that intersect each pixel affect the mean or optimum value of that pixel by varying degrees. Knowing the degree to which each raypath or traveltime affects the result might yield additional information about the region.

Statistically, many different distributions of numbers can yield the same mean or optimum value. Higher order statistics of the distribution, such as standard deviation, skewness, and kurtosis constrain the possible interpretation of the distribution. Knowing how each of the traveltimes contributes to the mean value can give us a distribution of

possible slownesses for each pixel. It is hoped that higher order statistics can give us some additional information about the region.

STRING TOMOGRAPHY

A recent paper (Harris 1990) in traveltime tomography allows for a direct method of statistical analysis of slowness values. Tomographic string inversion separates traveltime tomography into separate steps of inversion and imaging.

Inversion

The inversion process uses the raypaths as basis functions for the slowness field reconstruction. It is the assignment of slowness residuals to each individual raypath that allows for direct statistical analysis. The slowness residual for each raypath is determined by

$$\delta S = \frac{\Delta t}{L}, \tag{2}$$

where $\Delta t = t_{calculated} - t_{measured}$, L is the length of the raypath through the input (background) model, $t_{calculated}$ is the calculated traveltime through the input model, and $t_{measured}$ is the measured traveltime between the source and the receiver. By writing the definition of Δt as

$$\Delta t = \int_L \Delta S(r) dl , \tag{3}$$

where ΔS is the error of the slowness estimate in the input model, we see the residual slowness of the raypath is the average of the slowness error of the input model along the raypath

$$\delta S = \frac{1}{L} \int_L \Delta S(r) dl . \tag{4}$$

Imaging Statistics

The imaging process is now carried out separately from the inversion. Post inversion imaging areas will be refered to as bins. Each bin will have a number of raypaths intersecting it (Figure 1). Each of the residual slowness values represents a possible residual slowness value for that bin. The residual slownesses for each bin form the set of numbers to be used for statistical analysis. The statistics assigned to each bin come from raypaths which sample many other bins. Therefore the statistics contain information about the region of coverage, not just the imaging bin. Nevertheless, the set of statistics will have a localized weighting; regions close to and including the bin of measurement will have a stronger effect on the statistics than other bins. This is due to the greater sampling of bins near and including the bin of measurement (Figure 1).

FOUR ORDERS OF STATISTICS

The distribution of numbers or residual slownesses can be quantified in terms of four orders of statistics. These statistics are the mean (first order) , standard deviation (second order), skewness (third order), and kurtosis (fourth order). The mathematical definitions of each of these statistics are given in table 1. The mean and the standard deviation describe a set of numbers or residual slownesses that have a normal distribution (Figure 2). The skewness and kurtosis are quantities that describe deviations from a normal distribution.

The Mean

The mean value of a bin is calculated by the average of the slowness residuals corresponding to the raypaths which intersect the bin

$$\Delta S_c = \frac{1}{N} \sum_{i=1}^{N} \delta S_i , \tag{5a}$$

where

$$\delta S_i = \frac{1}{L_i} \int_{L_i} \Delta S(r) dl , \tag{5b}$$

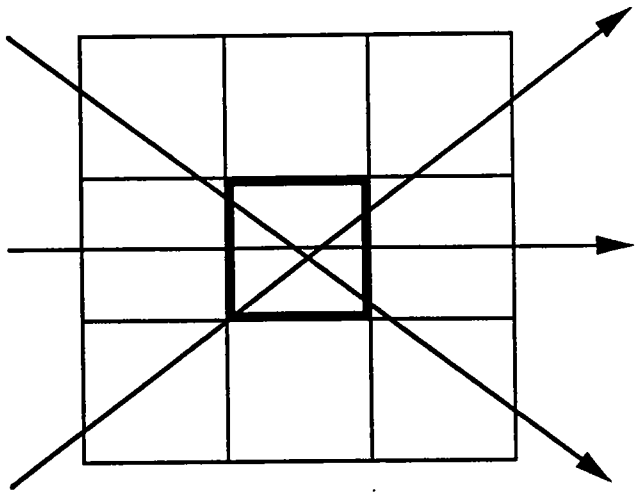

Figure 1. Raypaths intersecting a post inversion imaging area; a bin (solid box). The residual slownesses of the intersecting raypaths constitute the distribution of numbers for statisical analysis. The intersecting raypaths also contain information about other bins (lighter boxes).

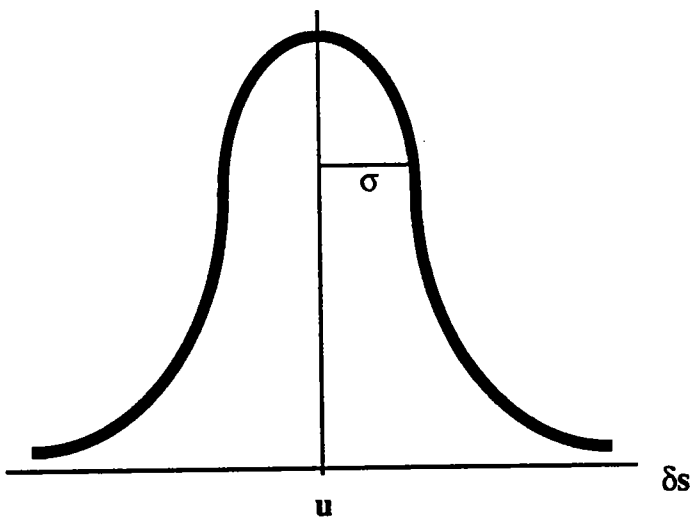

Figure 2. A normal distribution of data points. This type of distribution can be fully described by its mean, **u** , and its standard deviation, σ.

ORDER OF STATISTIC	MATHEMATICAL DEFINITION
FIRST ORDER (MEAN)	$S1 = \frac{1}{N}\sum_{I=1}^{N} S_I$
SECOND ORDER (STD. DEVIATION)	$S2 = \left[\frac{\sum_{I=1}^{N}(S_I - S1)^2}{N}\right]^{\frac{1}{2}}$
THIRD ORDER (SKEWNESS)	$S3 = \frac{\sum_{I=1}^{N}(S_I - S1)^3}{N \cdot S2^3}$
FOURTH ORDER (KURTOSIS)	$S4 = \frac{\sum_{I=1}^{N}(S_I - S1)^4}{N \cdot S2^4}$

Table 1. Four orders of statistics for a distribution of numbers.

N is the number of raypaths that intersect the bin, and L_i is the length of the i th raypath. The calculated mean serves as the approximation to the true residual slowness

$$\Delta S_e \cong \Delta S . \tag{6}$$

This estimate is added to the input slowness, S_o, to obtain an estimate for the slowness S,

$$S = S_o + \Delta S_e . \tag{7}$$

By adding S_o to each raypath residual slowness, statistics can be calculated for absolute slowness.

The Standard Deviation

The calculated standard deviation of a bin is a measure of the average deviation of the raypath slowness residuals that intersect the bin from the average raypath slowness residual. Since each slowness residual represents an average of the input slowness estimate error, ΔS , the standard deviation is an estimate of how ΔS varies throughout the region of coverage. Therefore the standard deviation is an estimate of the heterogeneity of the region of coverage relative to the input model; heterogeneity of ΔS.

The heterogeneity of ΔS in the region can give an indication of the error in the approximation of ΔS; $| \Delta S_e - \Delta S |$. A large source of error in traveltime inversion comes from the nature of the cross-well traveltime measurement. The slowness estimates for local regions (bins) are made from non-localized measurements. How greatly the non-localized measurements differ from each other can influence the accuracy of the estimate of ΔS.

Therefore the standard deviation might give an indication of the slowness estimate error; $| \Delta S_e - \Delta S |$. The logic sequence is

STANDARD DEVIATION => HETEROGENEITY ABOUT ΔS,

HETEROGENEITY ABOUT ΔS => ERROR IN ESTIMATE OF ΔS,

STANDARD DEVIATION => ERROR IN ESTIMATE OF ΔS,

where => symbolizes "implies".

Skewness

The skewness is a measure of the asymmetry of the distribution of slownesses for a bin (Figure 3). There are many geologic situations where a large number of raypaths intersecting a bin have many slownesses concentrated near one value, and a few slownesses with considerably smaller or larger values (Figure 4). These extreme values often will not carry useful information about the bin we are trying to image, yet these values can greatly influence the mean slowness value. Certain magnitudes of skewness might indicate the median instead of the mean should be used to estimate the slowness for a bin, since the median will not be affected by these extreme values.

Kurtosis

The kurtosis is a measure of the modality or bimodality of a distribution of slownesses for a bin (Figure 5) (Chissom 1970). It can tell us if the distribution is concentrated more closely around one or two different values of residual slowness. Geologically these two situations are distinct (Figure 6). This quantity can tell us about the homogeneity of the region of raypath coverage for a bin (Figure 1). An estimated slowness for a bin is more likely to be accurate if the slowness values of the intersecting raypaths are concentrated around one slowness value as opposed to two slowness values.

INVERTING FOR THE FOUR ORDERS OF STATISTICS

Synthetic measured traveltimes were computed from a model with a background slowness of 117.65 usec/ft (velocity = 8500 ft/sec), with four higher velocity layers in between (Figure 7). The first iteration of the string inversion used a constant slowness model of 117.65 usec/ft as the input model. The result of the first iteration is the first order statistic added to the input model, and is shown with the second, third, and fourth order statistics in figures 8a,b,c, and d respectively.

The inversion result shows resolution of the layers, with slowness errors within the layers. This is due to the limitations of the transmission measurement. Areas near the middle of the layers, particularly the thicker layers, are more accurate. The error between the inversion and the true model is shown in figure 9. When compared to the standard deviation in figure 10, we see a very small error in the slowness estimate for bins with standard deviations between 0 and 1. For higher standard deviations we see a gradual increase in error with increasing standard deviation. Overall the second order statistic

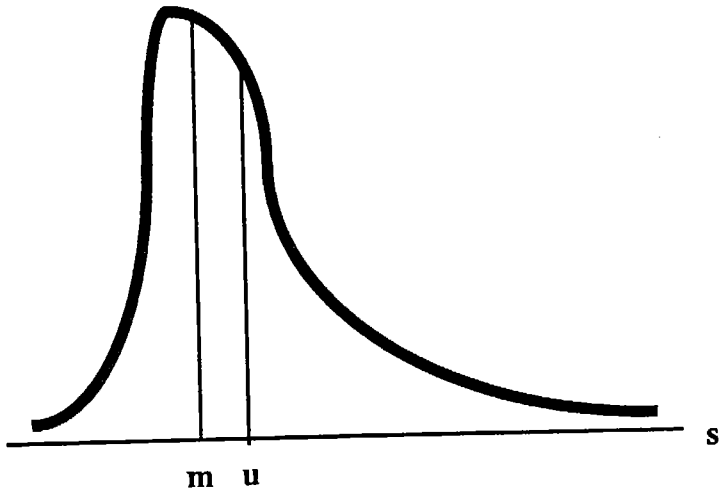

Figure 3. A skewed distribution of data points. This type of distribution is often better described by its median, **m**, rather than the mean. The mean , **u**, is strongly influenced by the few extreme values, while the median remains the same.

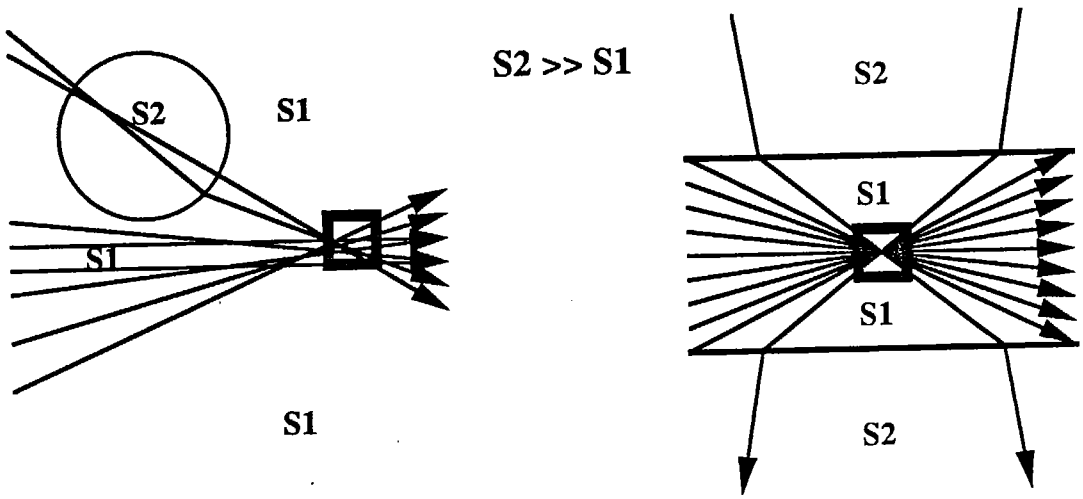

Figure 4. Two geologic situations that can yield high values of skewness for the imaging bin (dark box). Both will have values clustered around one value, with a few extreme values. The imaging bin on the left will have a negative skewness value, due to a few smaller values in the distribution. The imaging bin on the right will have a positive skewness value, due to a few larger values in the distribution. In both cases the median of the distribution will give a more accurate estimate of the slowness than the mean.

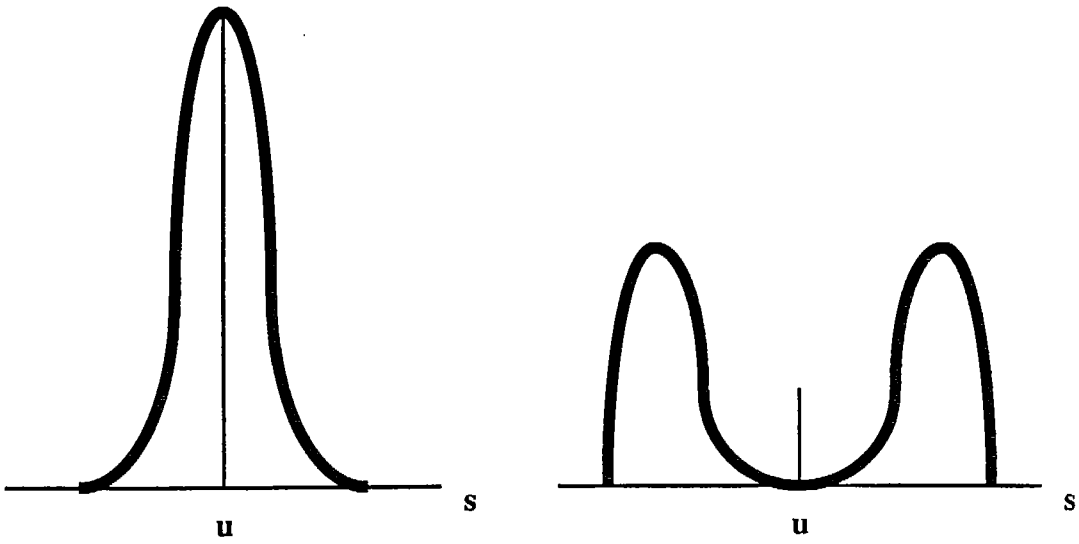

Figure 5. Two extreme values of kurtosis. The right graph is a unimodal distribution; representing a high value of kurtosis. The second graph is a bimodal distribution; representing a low value of kurtosis.

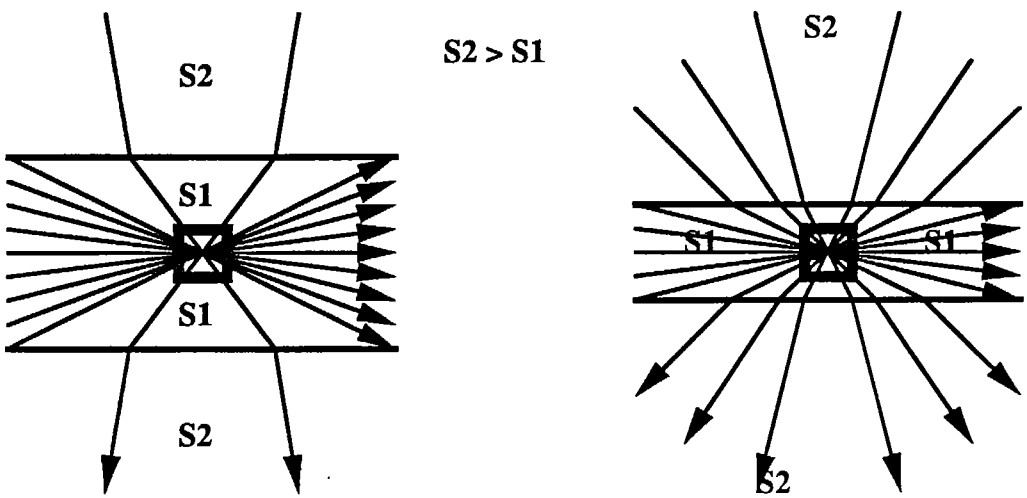

Figure 6. Two geologic situations that result in a large contrast in kurtosis values. The figure on the left has raypaths with a high concentration of slownesses at one value (unimodal), therefore having a large value of kurtosis. The figure on the right will have raypath slownesses clustered around both S1 and S2 (bimodal), therefore having a low value of kurtosis.

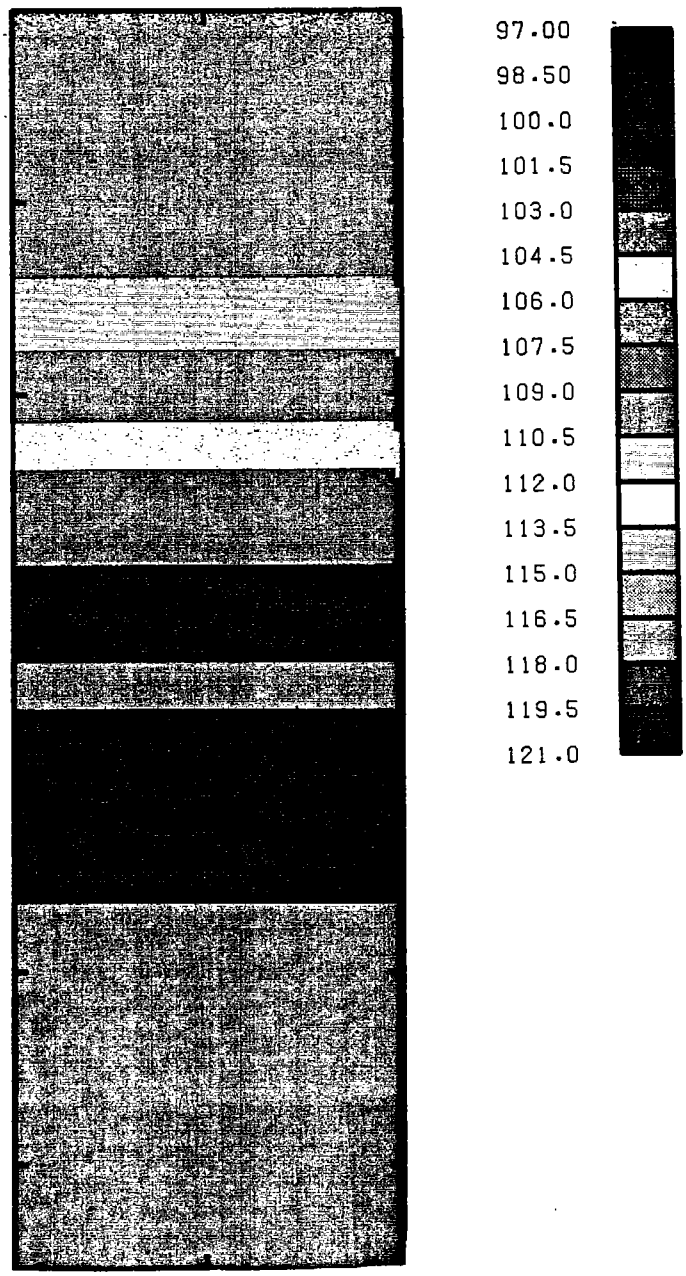

Figure 7. Slowness model used to generate synthetic measured traveltimes. Units are usec / ft.

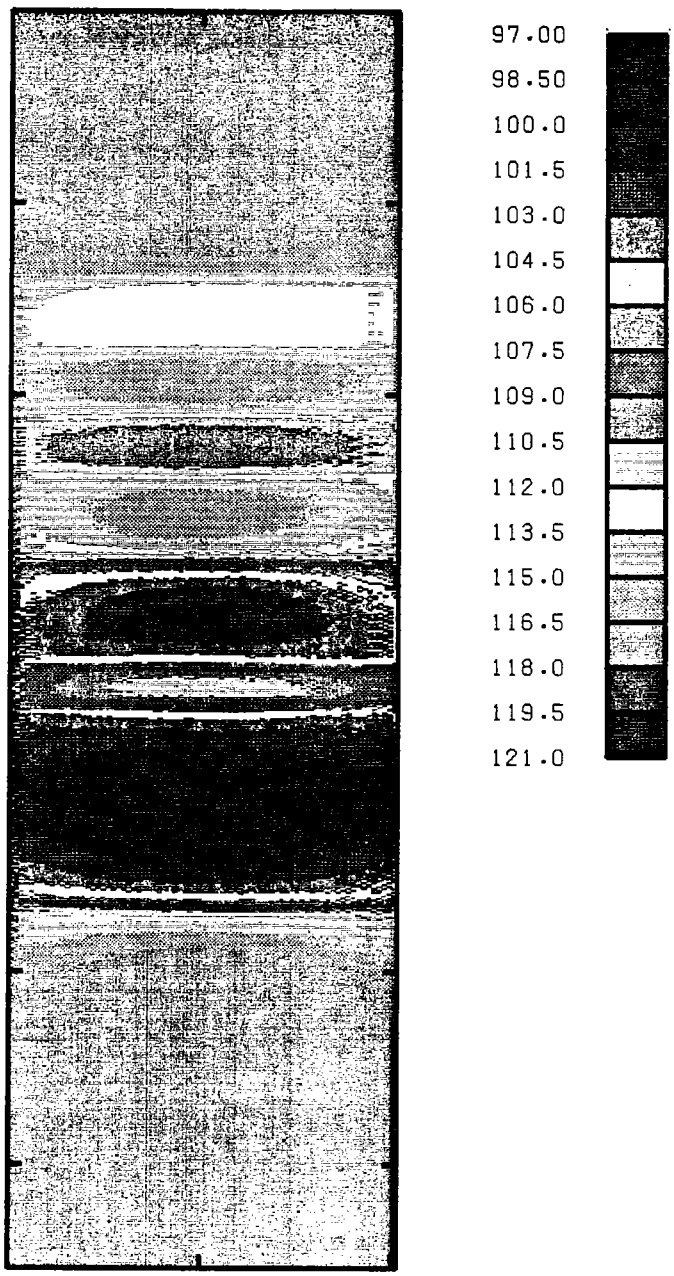

Figure 8a. Result of first iteration of string inversion. First order statistic plus input model. Units are usec / ft.

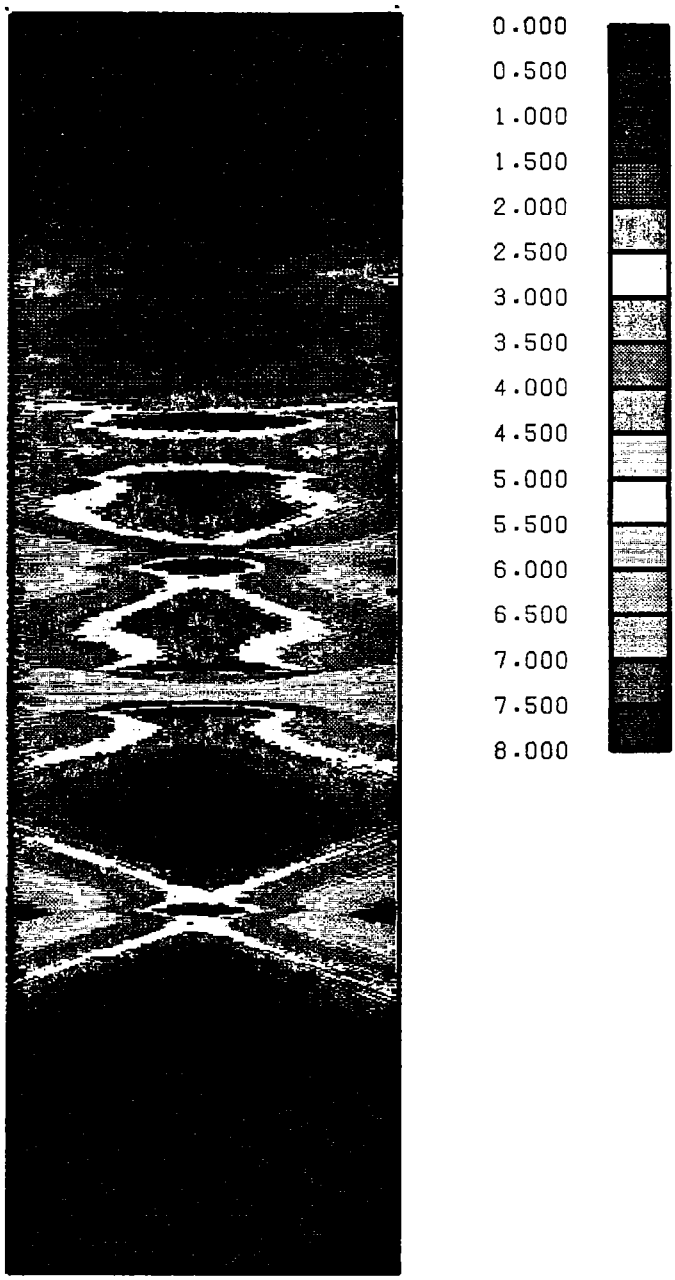

Figure 8b. Second order statistic. Units are usec / ft.

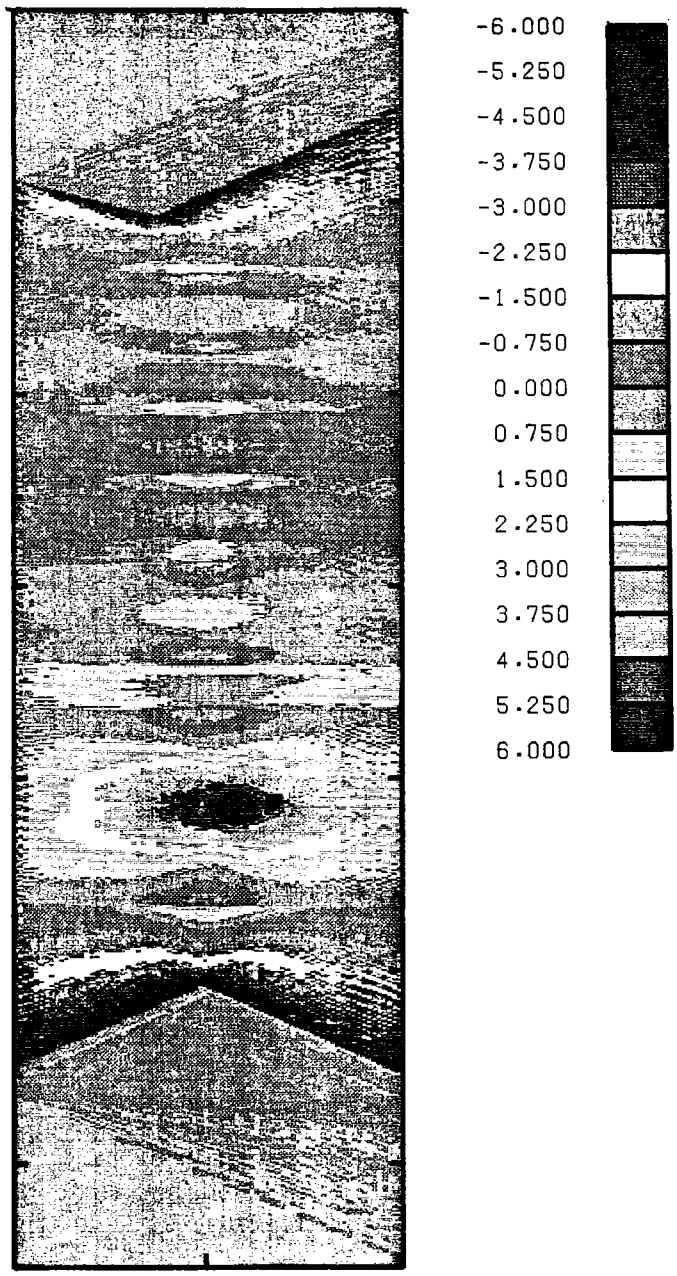

Figure 8c. Third order statistic.

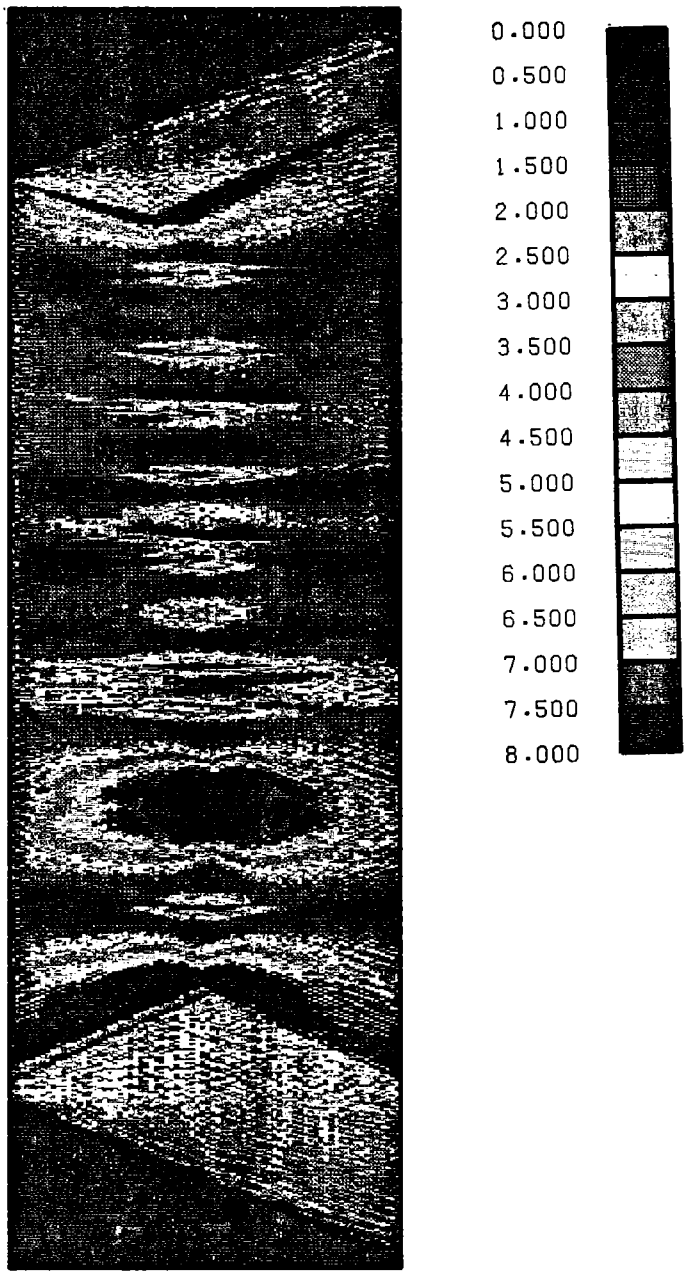

Figure 8d. Fourth order statistic.

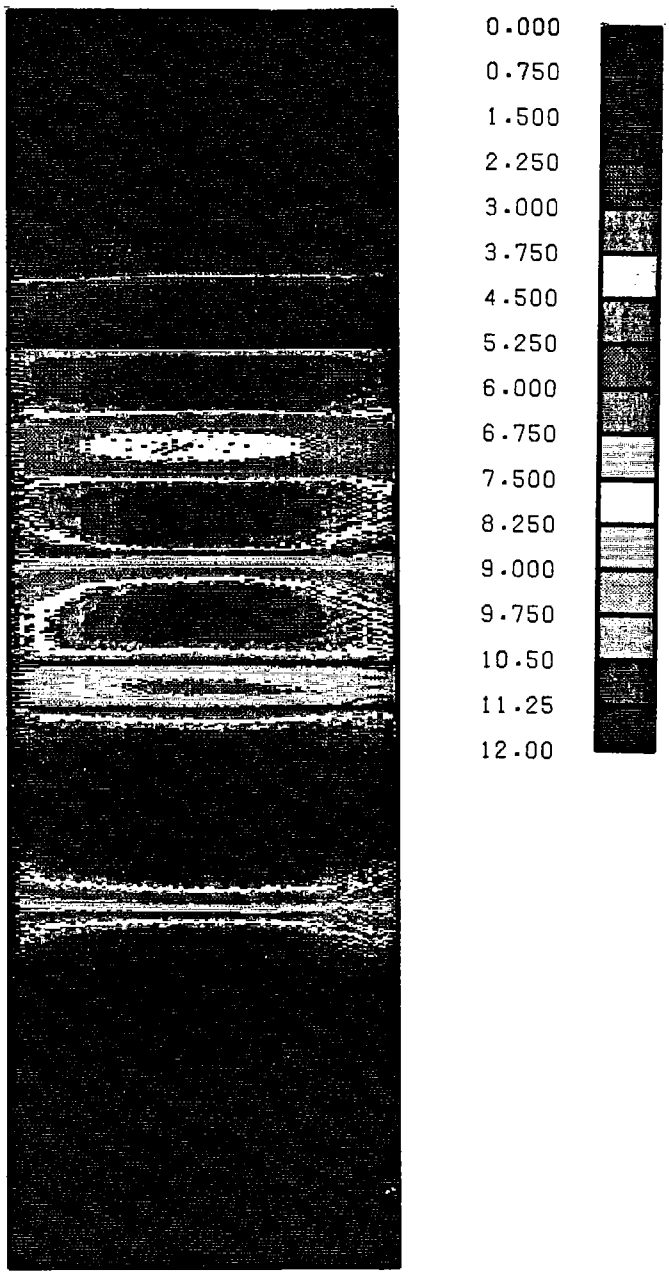

Figure 9. Error in slowness estimate after first iteration. Units are usec / ft.

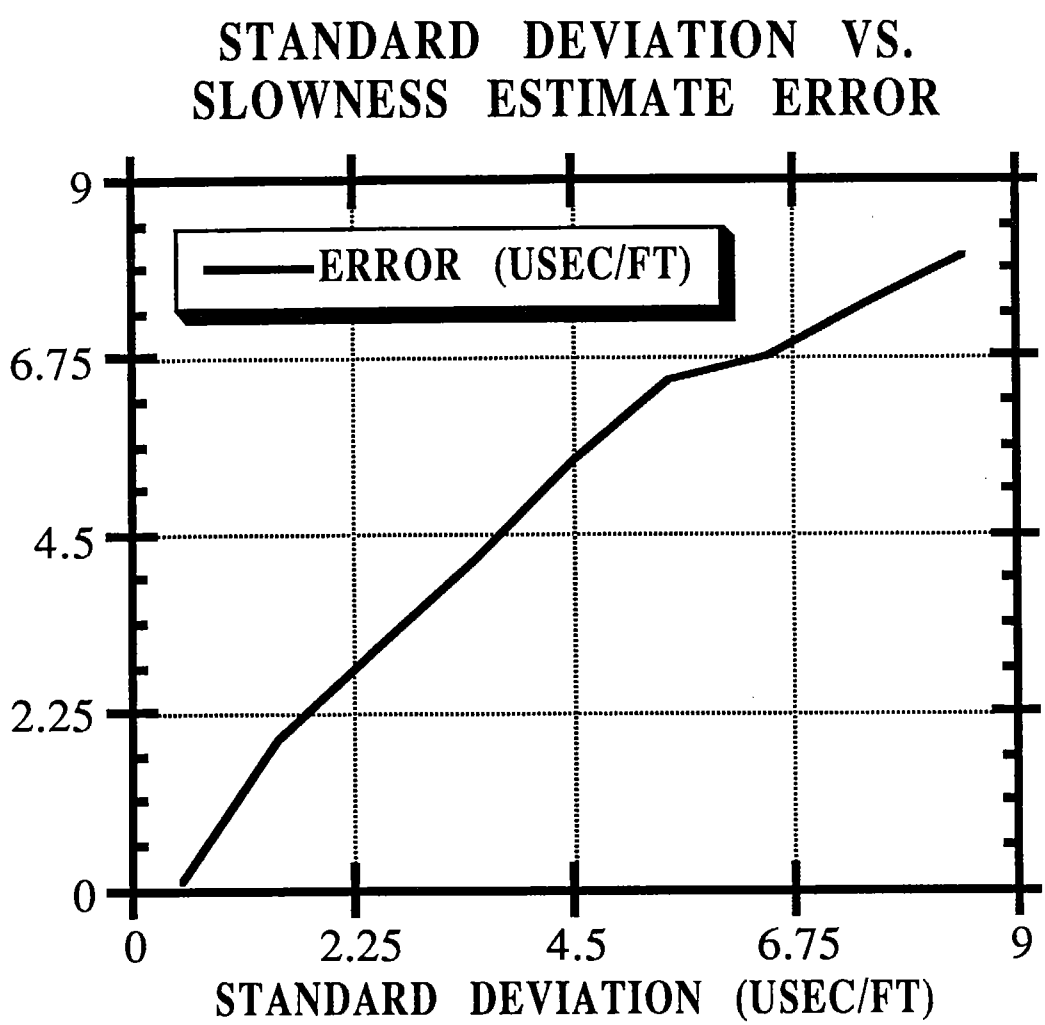

Figure 10. Standard deviation versus error. The error was calculated by averaging the errors of standard deviations within intervals of 1 usec / ft.

shows a good correlation with the error except near the middle of layer boundaries.

The third order statistic shows contrasts within layers and on the edges of boundaries. The low slowness (high velocity) layers show an increase in positive skewness towards the center. The high slowness layers (low velocity layers resulting from the input of high velocity layers in a lower velocity background) show an increase in negative skewness toward the middle. The low slowness layers will have raypaths or strings that sample areas outside the layer with higher slownesses. These raypath slownesses will be larger than the raypath slownesses that only intersect the layer of constant low slowness. This results in positive skewness with many values concentrated below the mean value and a few larger values. The opposite is true for high slowness layers resulting in negative skewness. This results in sign reversals of the skewness at the boundaries of some of the layers.

The fourth order statistic also shows transitional behavior at the boundaries and within layers. Within thin layers the kurtosis values decrease toward the middle. The thicker layers show an increase in kurtosis towards the middle. The middle of thinner layers will have raypath slownesses that are concentrated around the surrounding medium slowness and the layer slownesses (two values). The middle of thicker layers will have raypath slownesses concentrated around the layer slowness (one value). Due to the symmetry of the raypaths at the middle of layer boundaries, there will be many raypath slownesses clustered around one value. Therefore bins at these locations also have high kurtosis values.

STRING INVERSION USING THE STANDARD DEVIATION

Previously it was stated the magnitude of the standard deviation might be an indicator of the error in the slowness estimate. This would suggest the standard deviation might be used to improve subsequent iterations of the inversion. The original string inversion algorithm calculates the slowness residual from equation (2), and backprojects this correction evenly along the raypath. This can have the effect of backprojecting residual slownesses into bins that already have the correct or nearly the correct slowness value. A new algorithm was written that uses a weighted residual slowness along the raypath. The weight is a function of the standard deviation of the bins along the raypath. The average

slowness residual for the raypath was calculated using equation (2), and then was weighted as a function of the bin along the raypath using the formula,

$$\delta S_{ij} = \frac{\sigma_j^p}{\sigma_i^p} \delta S_i , \tag{8a}$$

where σ_j^p is the standard deviation to the p th power of the j th bin, σ_i^p is the average standard deviation to the p th power along the i th raypath,

$$\sigma_i^p = \frac{1}{L_i} \int_{L_i} \sigma^p (r) dl , \tag{8b}$$

δS_i is the residual slowness for the i th raypath, and δs_{ij} is the backprojected slowness as a function of the raypath and bin. The new backprojection formula has the benefits of

1) backprojecing less residual into bins with small standard deviations.

2) backprojecting more residual into bins with large standard deviations.

3) honoring the traveltime residual.

The power p in equations (8a), (8b) depends on the relationship between the standard deviation and the error in the slowness estimate. There is no exact theoretical expression for this relationship. The relationship between standard deviation and error can change as the number of iterations increases. If p is chosen to equal 1, this would backproject the slowness by assuming the standard deviation was linearly related to the error. Since standard deviation has the linear units of slowness, and is written as a linear error or deviation to the mean slowness residual, p is chosen to equal 1 for the second iteration. Continuing to use this assumed linear relationship in subsequent iterations can cause poor results in certain regions. This is due to two problems:

1) There are bins after the first iteration that have a low standard deviation but a relatively high error.

2) As the number of iterations increases, the residuals of the strings converge to certain values, often very small values. Therefore the standard deviations will become smaller. This will be true for some bins even though the errors might be approaching values that do not correlate with the small standard deviations.

Certain types of symmetry of the true inversion region relative to the input model can yield bins which have small standard deviations, but relatively large errors. All of the residual slownesses of raypaths that intersect a bin might have similar values, however the mean of these values might be quite different from the true error of the input model, ΔS . This is due to the limitations of the transmission measurement; the calculation of localized information based upon non-localized measurements. As the number of iterations increases, we are still limited by the type of measurement. This can be illustrated by equation (4)

$$\delta S = \frac{1}{L} \int_L \Delta S(r) dl .$$

As δS converges, the values of ΔS may or may not converge to the same value, since δS is an average of $\Delta S(r)$ along the raypath. Therefore as the number of iterations increase, there is the potential for an increasing number of bins to have standard deviations that are not representative of the slowness estimate error. Thus, for some bins the implication that the magnitude of the standard deviation is related to the magnitude of the slowness estimate error is violated.

Therefore by keeping p equal to one in the subsequent iterations, some bins with relatively large errors will not be corrected. This would suggest backprojecting the slowness residuals more uniformly along the raypath for subsequent iterations. If we set

$$p = \frac{1}{n-1}, \tag{9}$$

where n is the iteration number, the slowness residuals will be backprojected more uniformly along the raypath as the number of iterations increases. The average absolute

error in slowness, computed by

$$\text{AVEERR} = \frac{1}{M} \sum_{j=1}^{M} \left| S_T - S_E \right|_j , \qquad (10)$$

where $| S_T - S_E |_j$ is the magnitude of difference between the true slowness and the estimated slowness for the j th bin, and M is the total number of bins, versus iteration number is shown for p=0 (original string algorithm - uniform backprojection), p = 1, and p = 1 / n -1 in figure 11, and tabulated in table 2. The slowness estimate errors for each inversion path after 5, 9, and 18 iterations are shown in figures 12a,b,and c. The p = 1 / n -1 path showed improved convergence in the slowness estimate, and an improved convergence value. For example, the 12 th iteration of the p = 1 / n -1 path has a lower average error than the 18 th iteration of the p = 0 path. The convergence value for the p = 1 / n -1 path value is a 2.3% improvement in the error over the original strings algorithm. The convergence value was defined at the iteration before subsequent iterations stopped showing any improvement. The convergence value occured at iteration 18 for both the original string algorithm and the p = 1 / n -1 path. Figure 11 and table 2 also show for the first 6 iterations the p = 1 path provides improvement over the p = 0 path, but has a larger error for subsequent iterations.

CONCLUSION

The usefulness of string inversion theory has been demonstrated in the easy calculation of higher order statistics for the inversion region. It has shown that each of the four orders of statistics can provide us with certain information about the region of interest. It was also shown that the standard deviation can be used to provide a better convergence of the string algorithm and an improved convergence value. More research needs to be done using the third and fourth order statistics to obtain information about the inhomogeneity of the medium and improving the inversion. More research needs to be done on the relationship between the standard deviation and the slowness estimate error.

ACKNOWLEDGEMENTS

The authors would like to thank The Gas Research Institute for supporting this work. The first author would like to thank the entire STP group for helpful comments and suggestions.

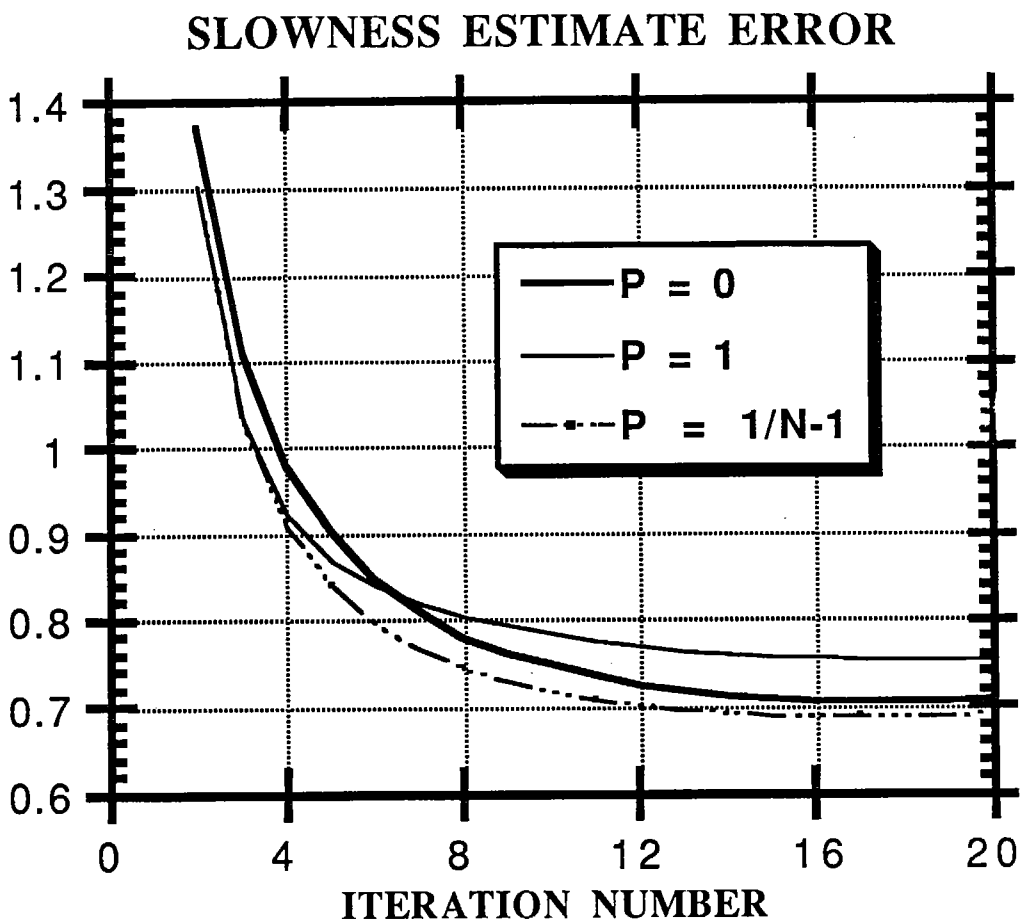

Figure 11. Average slowness estimate error for three paths of inversion. Units are usec / ft.

SLOWNESS ESTIMATE ERROR

ITERATION NUMBER (n)	P = 0 (USEC / FT)	P = 1 (USEC / FT)	P = 1 / n - 1 (USEC / FT)
2	1.3727	1.3030	1.3030
4	0.97961	0.92322	0.91013
6	0.84815	0.84021	0.79643
8	0.78089	0.80531	0.74503
10	0.74747	0.78520	0.71755
12	0.72489	0.76951	0.70239
14	0.71237	0.76052	0.69416
16	0.70651	0.75703	0.68993
18	0.70541	0.75599	0.68864
20	0.70735	0.75392	0.69197

Table 2. Average slowness estimate error for three paths of inversion. Units are usec / ft.

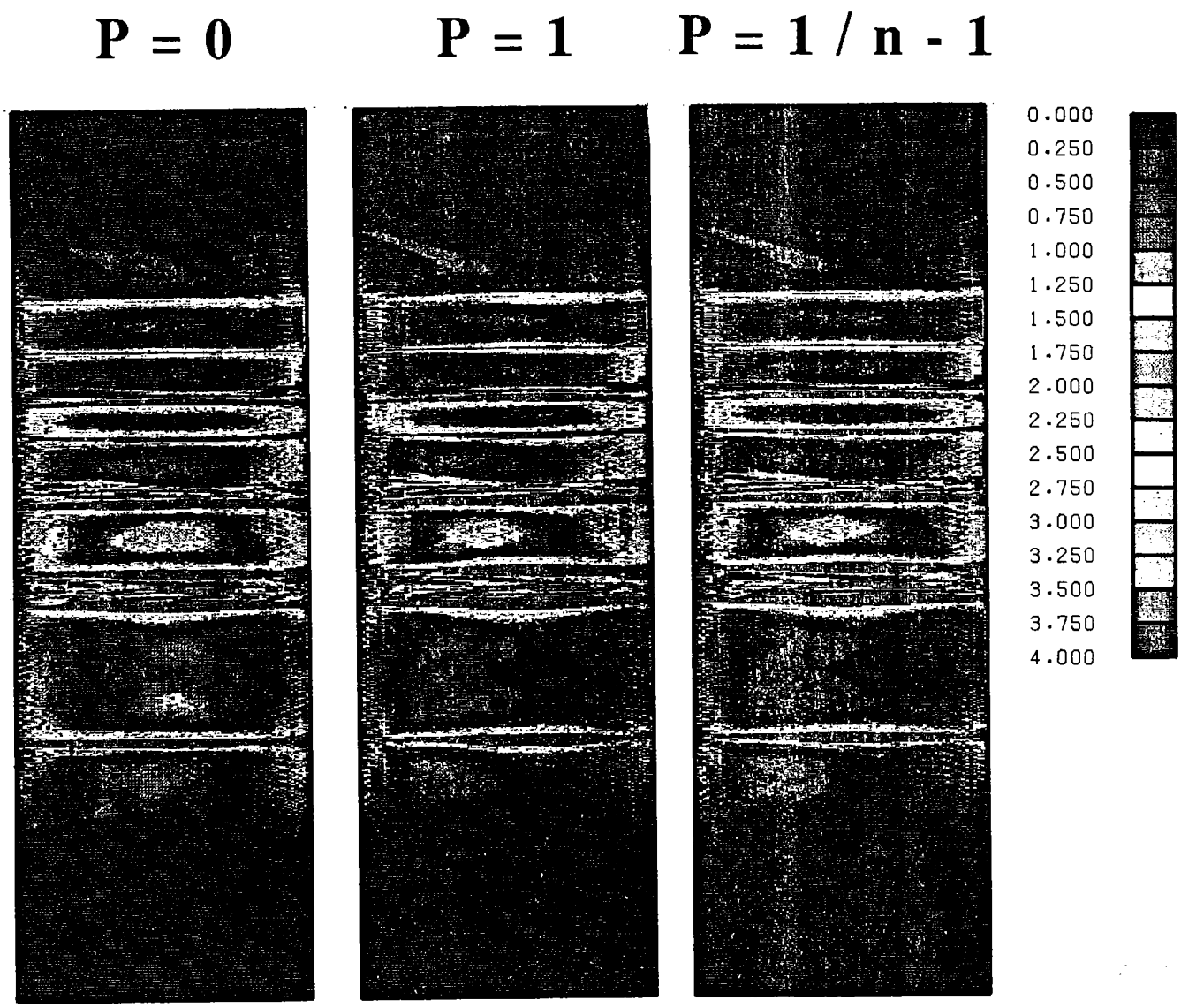

Figure 12a. Slowness estimate error after 5 iterations. Units are usec / ft.

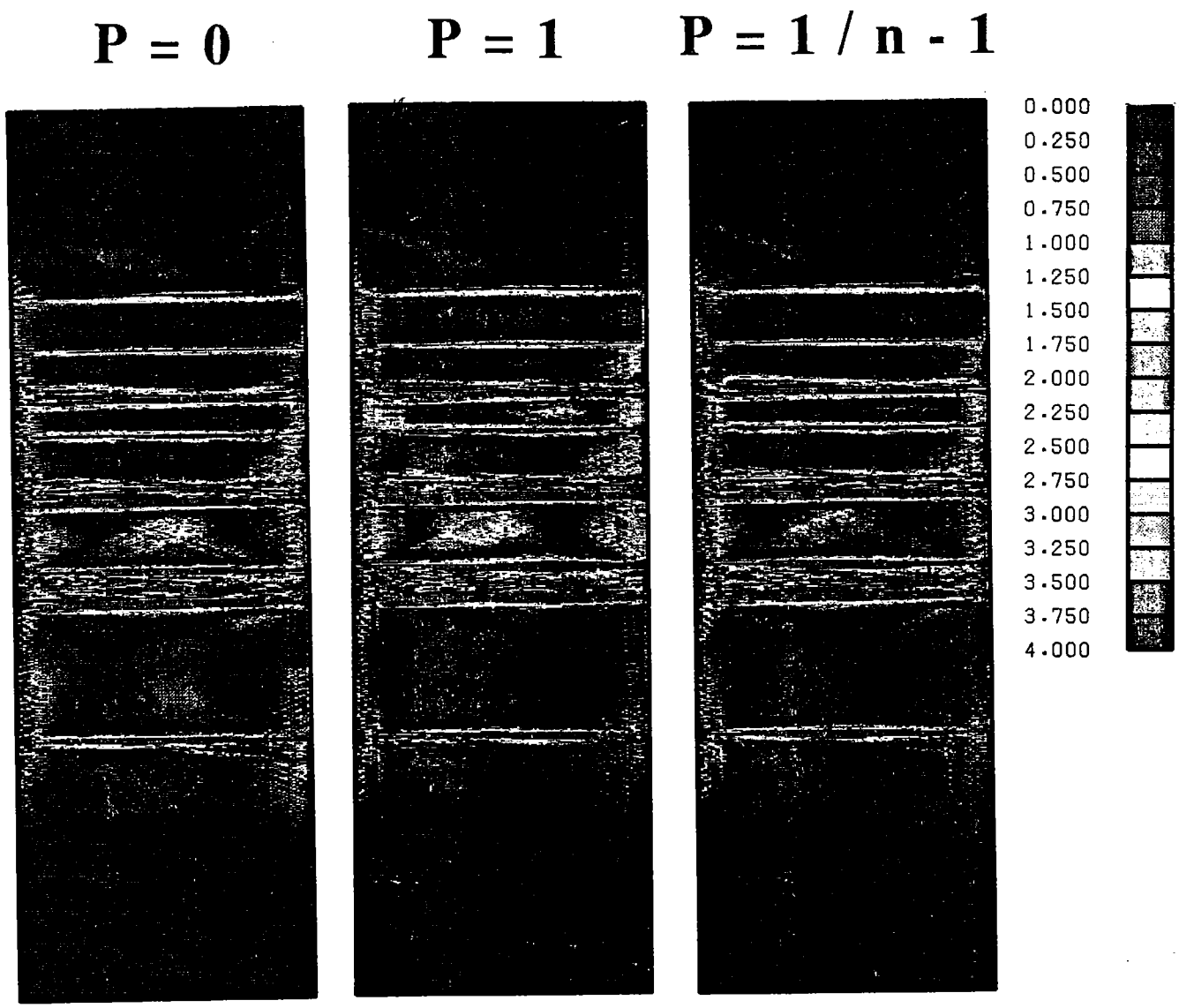

Figure 12b. Slowness estimate error after 9 iterations. Units are usec / ft.

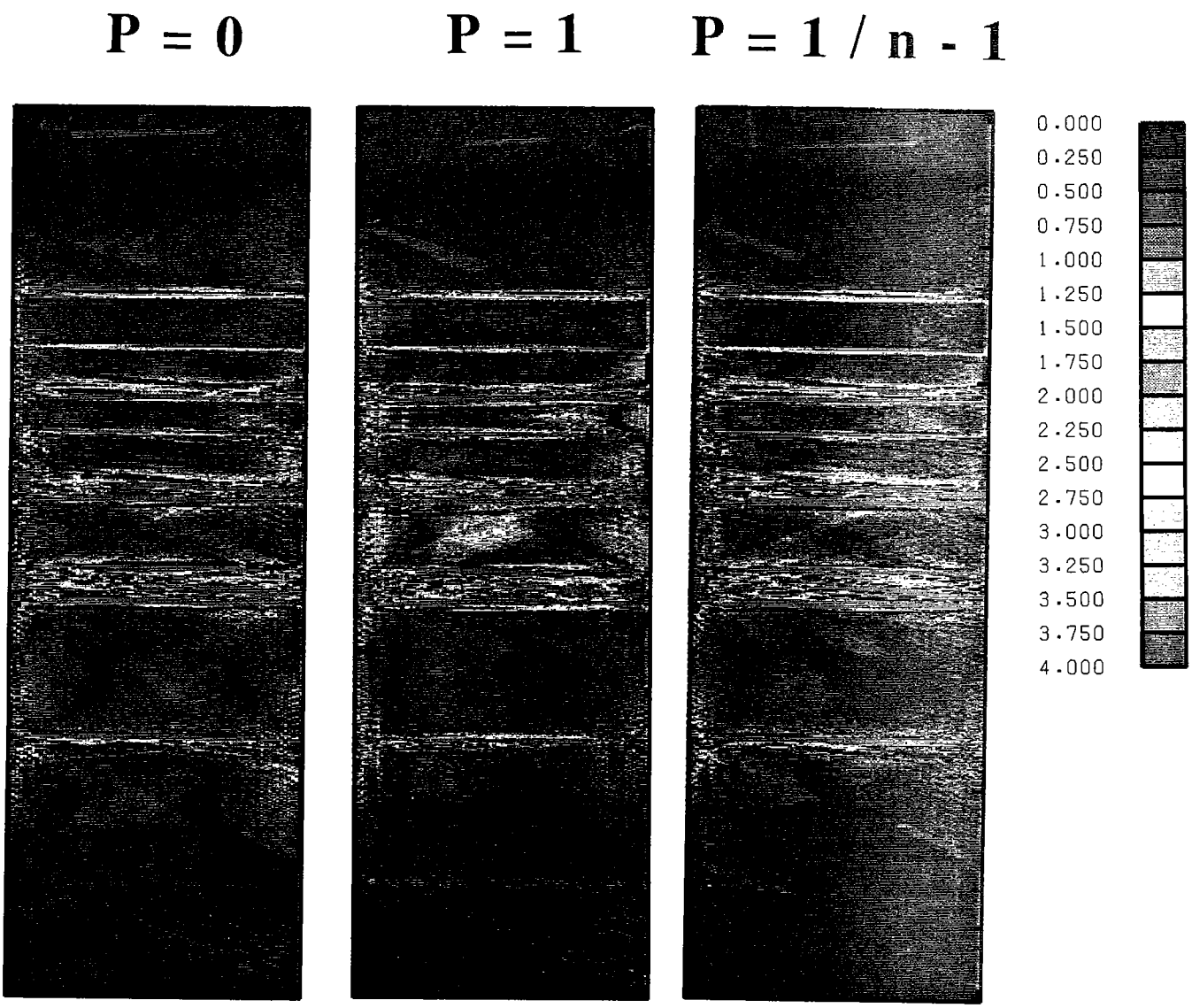

Figure 12c. Slowness estimate error after 18 iterations. Units are usec / ft.

REFERENCES

Bjerhammar, A., 1973, Theory of Generalized Matrix Inverses, Elsevier Scientific Publishing Company.

Chissom, B. S., Oct. 1970 Interpretation of the Kurtosis Statistic, The American Statistician, **24**, pp. 19-22.

Harris, J.M., Lazaratos, S., Michelena, R., 1990, Tomographic String Inversion, STP volume 1, paper B.

Sachs, L., 1984, Applied Statistics, Second Edition, Springer-Verlag.

PAPER K

TRACE INTERPOLATION IN THE F-X DOMAIN

Luis L. Canales
Seismic Tomography Project

ABSTRACT

In this paper we present a method for trace interpolation in the f-x domain. The method relies on the fact that linear events in t-x are predictable in f-x. For the complex Wiener prediction we use an extension of the Burg technique, which allows us to forego the usual assumption that the data is zero at places where it is unavailable, in this case not only the end but also the unknown values in the middle. This approach for interpolation should be very useful in the crosswell geometry, because as previously shown in the surface seismics data, the prediction permits the data to have a few jumps. Other methods will smear those jumps that are critical for traveltime tomography.

INTRODUCTION

Prediction in the f-x domain is a very successful method for removing random noise from seismic data (Canales, 1984). In that domain, linear events are perfectly predictable with a Wiener prediction filter. The prediction is made at each frequency, after a Fourier transform in time. The complex form of the prediction is needed, since the transformed data is complex.

Once you have the proper prediction filter, it can be used to interpolate missing data, as long as there are not very large gaps. The main problem is to estimate the autocorrelation function from incomplete data.

Here we will use an extension of the Burg technique that handles the missing data in the same well known way as it handles the missing end points.

F-X PREDICTION

The method assumes that the traces are composed of delayed impulses as shown in the next figure:

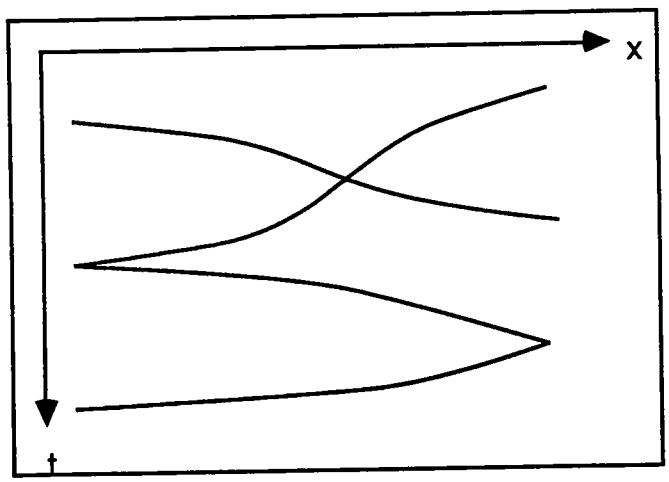

The events are defined by:

T-X Domain

$$u(t,x) = \sum_k a_k \, \delta(t - g_k(x))$$

F-X Domain

$$u(\omega,x) = \sum_k a_k \, e^{-i\omega \, g_k(x)}$$

where: a_k represent the strength of the impulses

and: $g_k(x)$ are delay functions that define the shape of the events.

After assuming the events are linear and allowing the events to have an arbitrary wavelet, the frequency domain form of the model is (Canales, 1984) :

$$u(\omega,x) = \sum_k v_k(\omega) \, e^{-i\omega \, \beta_k \, x}$$

This suggests that the model is composed of purely sinusoidal complex functions, and thus is perfectly predictable with a complex Wiener filter (Canales, 1984).

It turns out that some small amount of curvature is handled correctly, since such a curved event can be represented with a combination of a few linear ones.

THE BURG TECHNIQUE

The needed statistical information is contained in the prediction filter, the autocorrelation, the power spectrum and the reflection coefficients. Once you know one function, you can estimate the other ones. The standard technique starts with an estimate of the autocorrelation function.

The Burg technique estimates the reflection coefficients directly from the data, without explicitly obtaining the autocorrelation, (Burg,1975). The technique is particularly good for short time series because of its treatment of the end effects (Claerbout, 1972).

We will use the complex form of the Burg algorithm, but for simplicity we here start with the Burg algorithm for real data. Its extension to complex data is very simple (Claerbout, 1976).

Start with :

$$f_0(z) = b_0(z) = x(z)$$

Update as:

$$f_{n+1}(z) = f_n(z) - c_{n+1}\, z^{n+1}\, b_n(z)$$

$$b_{n+1}(z) = b_n(z) - c_{n+1}\, z^{-n-1}\, f_n(z)$$

Where $f_n(z)$ is the z-transform of the forward prediction error (using a filter of order n) and $b_n(z)$ is the backward prediction error one and $x(z)$ is the data. Note that z is the delay operator so that the relation indicates shifting before adding.

Burg's formula for the (n+1)-th reflection coefficient c_{n+1} is:

$$c_{n+1} = \frac{2 * \mathbf{f_n} \cdot \mathbf{b_n}}{\mathbf{f_n} \cdot \mathbf{f_n} + \mathbf{b_n} \cdot \mathbf{b_n}}$$

Where $\mathbf{f_n}$ is the vector representation of the forward prediction error and $\mathbf{b_n}$ is the backward prediction error. The c_n are of magnitude less than one as required by the minimum-phase assumption.

The scalar c_{n+1} is the solution to the following Least Squares Problem (Claerbout,1976).

$$\begin{bmatrix} f_{n+1} \\ b_{n+1} \end{bmatrix} = \begin{bmatrix} f_n \\ b_n \end{bmatrix} - \begin{bmatrix} b_n \\ f_n \end{bmatrix} c_{n+1}$$

The updating and the computation of the reflection coefficients use the Burg treatment of the end effects. That is, at each iteration we eliminate the end points from the calculation.

The previous one least squares problem with one unknown parameter relates pairs data from the forward and backward prediction errors. The Burg technique simply eliminates the pairs at the end where the data is missing. We can do this and still have an acceptable value for the reflection coefficient, since its bounding depends entirely on the Schwartz inequality for vectors.

INTERPOLATION WITH THE BURG TECHNIQUE

It is very natural to use the Burg technique in the f-x prediction method, because during the calculation of the reflection coefficients we always update the prediction error. This error is subtracted from the original data to give the predicted signal.

Another advantage is that the Burg technique is good for short time series, because it is not necessary to assume zero values at the ends. In the f-x prediction case it means we do not have to assume zero traces at the ends.

For the interpolation case it is even more important, since we can extend the treatment of the end effects to missing data. We simply eliminate pairs that have a missing data point, not only at the ends but also in the middle.

One important fact is that for the missing data at the end, once a data point is eliminated it is never used in subsequent lags. On the other hand, a data point in the middle may pair with a missing data point at one lag and with a known point at another lag. In on case the data point will not be used and in the other case it will be.

RESULTS

In figure 1 we show a synthetic section. It has continuous events with some curvature and a large amount of added random noise. Traces 19, 20, 22, 23, 45, 46 and 47 have been zeroed (counting from the right).

Figure 2 shows the section from figure 1, after f-x Prediction. The missing traces have been predicted with the one-step ahead prediction filter. Note that in general a great deal of random noise has been attenuated, this is the standard benefit of f-x prediction.

Figure 3 show the section after using the new treatment of missing data. The only difference in the method is the estimation of the reflection coefficients since the prediction is done in exactly the same way. Note that the amplitudes in figure 2 are biased towards zero. This is of course because the estimation assumed those traces to be zero for the standard f-x Prediction. On the other hand the new treatment of missing data has predicted the missing traces correctly.

Note that the results are different from linear interpolation between traces. The noise has not been interpolated.

CONCLUSIONS

We have presented a method for interpolation of missing traces based on f-x prediction via the Burg technique. By extending the Burg treatment of the end effects for missing data, we estimate the reflection coefficients and thus the prediction filter without assuming zeroes for the missing data.

The technique predicts traces that satisfy a very simple interpretational model, and it can handle events with some curvature.

The method is very valuable in two aspects. First it improves the standard random noise attenuation when traces are missing and secondly it provides us with the interpolated traces.

For larger gaps, an average from forward and backward prediction should be used, as the prediction deteriorates with prediction distance.

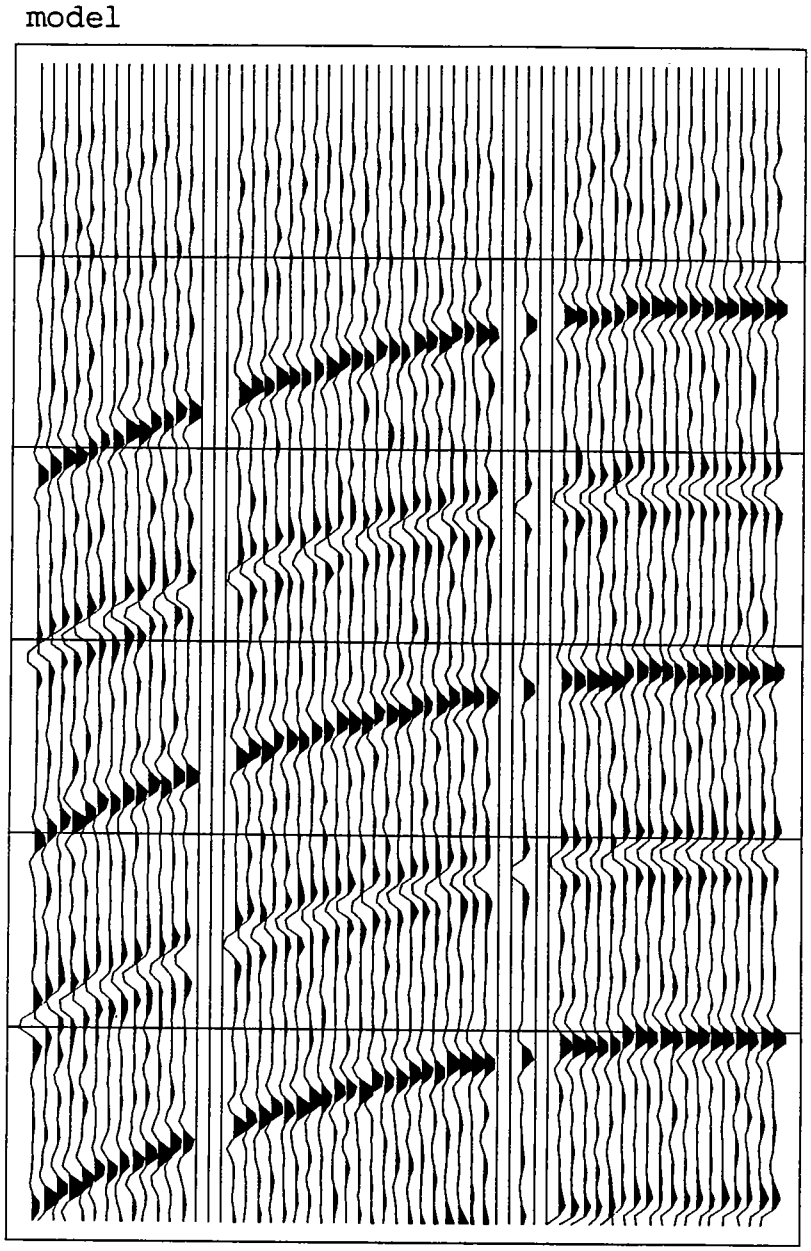

Figure 1
Synthetic input model.

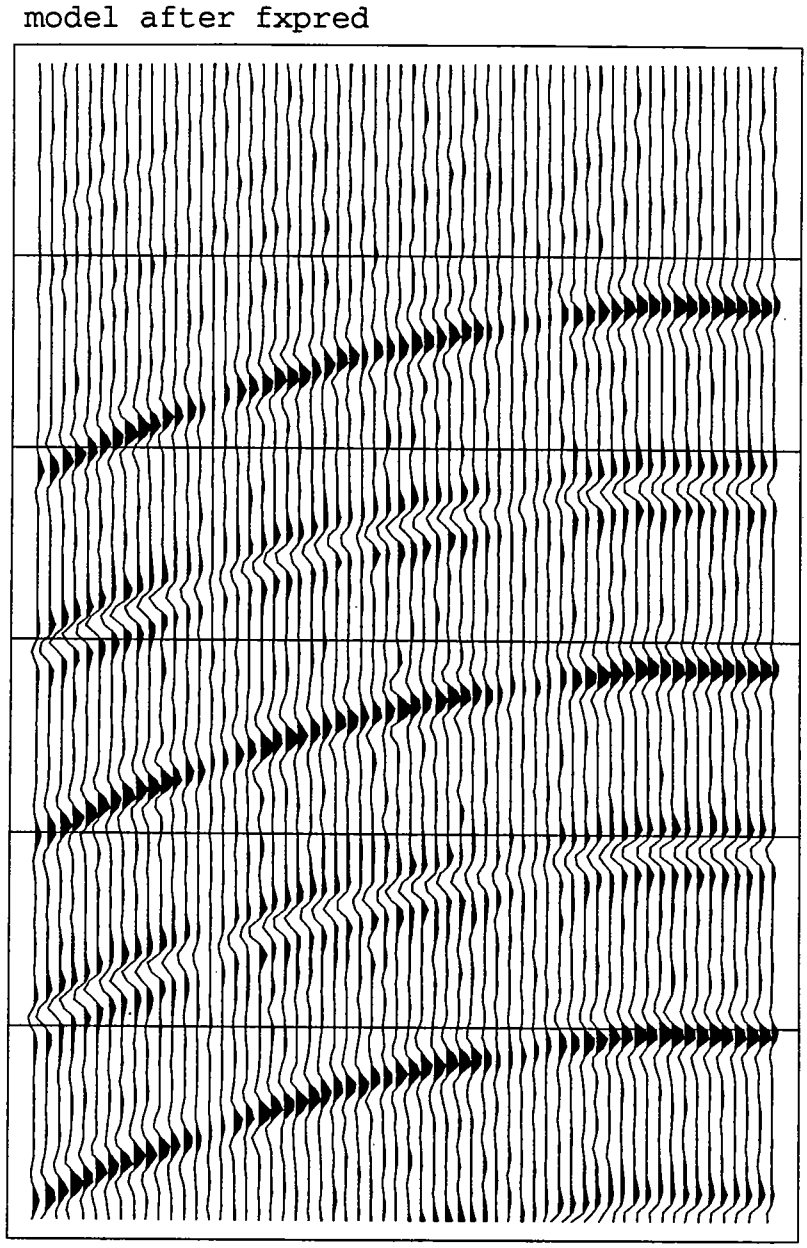

Figure 2
Model after Standard f-x Prediction.

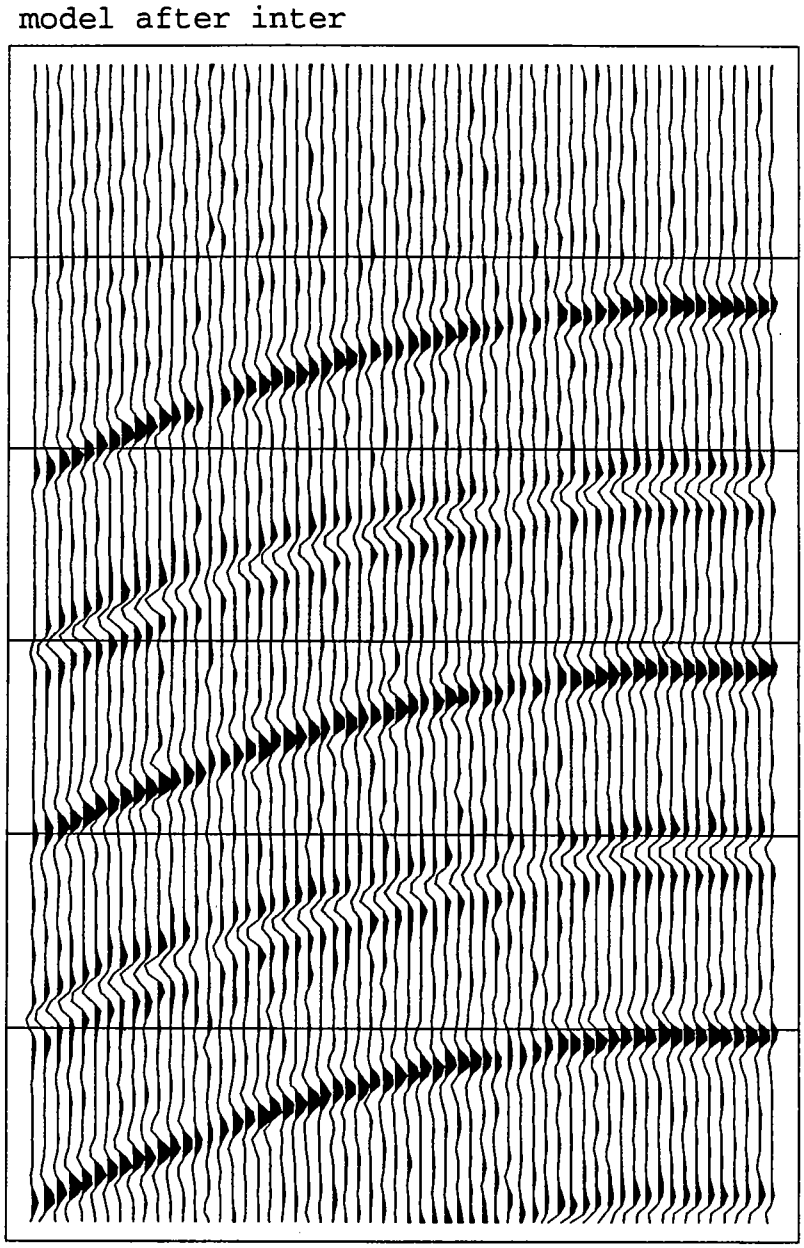

Figure 3
Model after f-x Prediction with the new method

AKNOWLEDGEMENTS

The autor gratefully acknowledges the Gas Research Institute for its support of the Stanford Tomography Project.

REFERENCES

Burg, J. P., 1975, Maximum Entropy Spectral Analysis: Ph. D. Thesis, Stanford University.

Canales L. L., 1984, Random Noise Reduction , Extended Abstracts SEG meeting Atlanta.

Claerbout J. F. 1976, Fundamentals of Geophysical Data Processing, McGraw-Hill, New York.

PAPER L

XPICK - X WINDOW INTERACTIVE TRAVEL TIME PICKER FOR CROSSWELL SEISMIC DATA

Caroline Lambert
Seismic Tomography Project

ABSTRACT

The xpick program allows the user to quickly pick crosswell seismic data in a window environment. The use of X windows makes the program network transparent and easily portable. Data is read in from TIMS segy files, and the picked travel times are written out in TIMS pick format, which can then be read into subsequent TIMS programs or can be converted to ASCII format. Within the program the user can select from several picking modes, and can view the data in a variety of sorts.

INTRODUCTION

xpick is an interactive travel time pick program written specifically for crosswell seismic data. The program is written as an X window application, which allows it to be executed across a computer network, and should be easily portable to any system that runs X. Whole data sets or sub-cubes of data sets can be read into the program. The ability to switch easily between different sorts, such as common source, common receiver, or common offset, makes the program also useful as a tool for viewing data quickly on the screen.

XPICK PROGRAM

Data

xpick reads crosswell seismic data stored in TIMS segy files. Any subset of sources, receivers or time samples can be chosen to be read in. As the data is read in it is converted from floating point (32 bit) to short integers (16 bit). There is no loss of resolution in doing

this since the data is used only for display purposes, but the conversion allows better utilization of run-time computer memory. After the data has been picked, the travel times are written out to a file in TIMS pick format. This file can be read back into the program if the picks need to be reviewed or modified. Once in TIMS pick format, the picks can be read into other TIMS programs, such as the string inversion program or the pick plotting program, or can be converted to ASCII format.

Display

After the data is read in, a window is brought up and the first common source gather displayed. A sample display is shown in fig. 1. The traces are drawn horizontally and are registered by depth (in a common offset gather the source depth is used). The depth of the source and receiver for any trace can be found by placing the cursor over the trace - the depths are automatically displayed in the main window panel and automatically updated as the cursor is moved. The time sample under the cursor, the source and receiver numbers, and any picked travel time for the current horizon are also shown in the panel.

Unless overridden by command line arguments, default values are used for display parameters. If the display parameters, such as depth axis scaling, time axis scaling or trace amplitude scaling, are not suitable, they can be changed by selecting the DISPLAY button and entering a new value into a pop-up window. At any time the original parameters can be restored. Alternatively, a selection of the data can be magnified by choosing the ZOOM button and outlining the portion of data to be magnified using mouse buttons. If the gather being viewed cannot fit into the window with the specified scaling parameters, the window can be scrolled to view the hidden portion.

Picks are displayed by default in red. In some situations red can be difficult to see, so the user can select another color from the "colors" menu. If more than one horizon is picked, the different horizons are displayed in different colors.

Sorting

Initially, the data is displayed as a common source gather. A pull-down menu allows the user to quickly switch back and forth between different data sorts. The sorts that are currently implemented are common source, common receiver and common offset. This is extremely useful in travel time picking; when running into difficulties deciding where to pick a travel time, it is often very illuminating to switch to another sort to see how the picks match up.

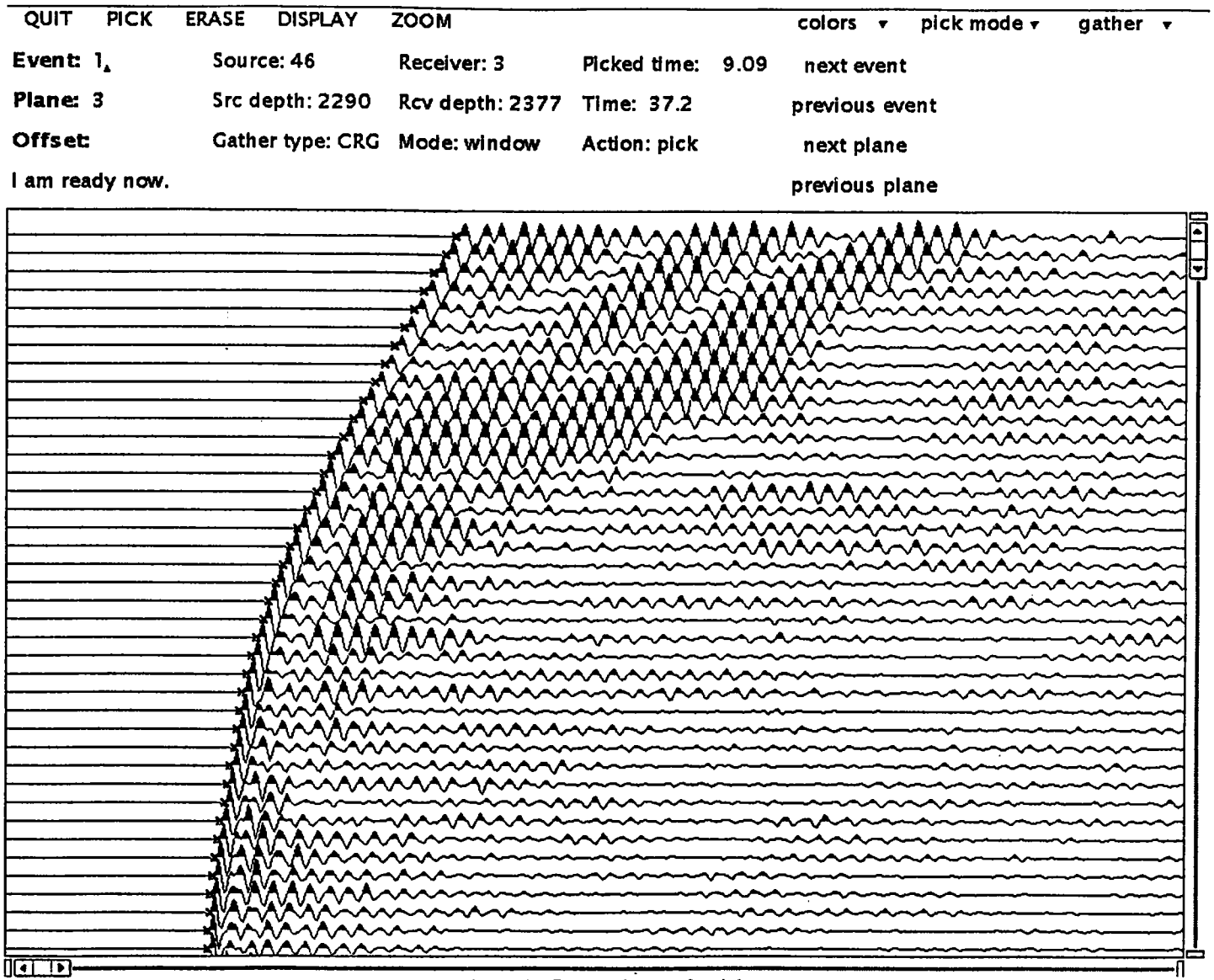

Figure 1: Screen dump of xpick program

After selecting the common source or common receiver gather option, the first gather in that particular sort is displayed. The data can then be stepped through one plane at a time by selecting the "next plane" or "previous plane" buttons, or the user can enter the number of a plane to be viewed into the main window panel. When the common offset gather is chosen, the first gather displayed is the gather with 0.0 unit depth offset. A new offset can be selected by entering the number into the appropriate place in the main window panel.

Picking

Picking can be done in one of several modes, manual, automatic, window or first break.

In "manual" mode, the selected event is chosen with the mouse individually for each trace. If a change needs to be made, the trace can be picked again and the original pick is erased.

In "automatic" mode the user makes a pick on a beginning trace. The program finds the peak or trough on the trace nearest to where the mouse button is and draws the pick there. Whether a peak or trough is chosen depends on whether "maximum" or "minimum" has been chosen under the "pick mode" menu. Then an ending trace is selected in the same manner, and the program performs a correlation on successive traces between the selected ones. If the correlation makes erroneous picks, they can be corrected in manual mode, or a range of picks can be erased by switching to ERASE mode, selecting a range of traces to be erased, going back to PICK mode, and attempting the automatic pick again.

In "window" mode the user outlines a horizon of interest by drawing lines with the mouse on either side of the horizon. The program then interpolates the data within this window using splines, and selects either the maximum or minimum value within the window as the pick value. With the interpolation this results in a more accurate pick than the initial sampling interval allows. While in "window" mode, only lines can be selected to be erased. Once a segment of a line is erased, the picks within the corresponding window are also erased.

Portability

xpick was written using the XView user-interface toolkit, version 2.0. This toolkit follows the OPEN LOOK (TM) Graphical User Interface, and consequently has the OPEN LOOK 'look and feel'. XView is publicly available software from MIT, and has been ported to many systems. The only requirement for XView is that the window manager should be ICCCM-compliant (for example, olwm or mwm).

xpick also uses the netCDF library for data storage. netCDF is publicly available from UCAR (University Corporation for Atmospheric Research), and is used here to enhance portability between different computer systems.

(OPEN LOOK is a trademark of AT&T, the X Window System is a trademark of MIT, XView is a trademark of Sun Microsystems, Inc., netCDF is a trademark of UCAR).

Acknowledgements

This work was supported by the Gas Research Institute. The author also acknowledges the assistance of Steve Cole (SEP) in setting up XView, and Jerry Harris for his constructive comments.

PAPER M

COMPUTATIONAL SPEEDUP OF THE STRING ALGORITHM

Luis L. Canales
Seismic Tomography Project

ABSTRACT

The string algorithm has been speeded up 4 fold. The program was analyzed with the UNIX profiler and found to spent 93% of the time in the ray tracer, which is based in the Runge-Kutta method. Inside the ray tracer, the interpolation to obtain the velocity at the required point used 77% of the time.

A fine mesh grid was incorporated in the algorithm to avoid the interpolation. With the fine grid, instead of interpolating to obtain the velocities, we just look for the grid point nearest the required location. This fine grid is normally output by the String inversion, so subsequent iterations do not require additional effort to produce it.

The grid is very fine, compared with the ray coverage and it is very important to smooth the velocity grid between iterations. Fortunately smoothing is very inexpensive as compared to ray tracing.

INTRODUCTION

The String algorithm basically works by generating a fan of rays from a source position. The number of rays is large enough so that there is good sampling of the velocity values in the grid. A ray normally passes between two receivers, whose measured arrival times are interpolated to give an estimate of the time at the ray. The time residual is then back projected to give corrections for the velocity at the grid points touched by the ray.

It turned out after using the UNIX profiler that the program spent most of the time (93%) in the ray tracing part of the algorithm. Further analysis showed that the interpolation needed to compute the velocity at the locations needed by the algorithm used 77% of the time. This is because the rays do not necessarily travel along grid points, especially when using a coarse velocity grid.

A fine grid was introduced so that instead of interpolation we just do a simple look-up to return the velocity value of the nearest neighbor. This essentially reduces the amount of computation to one fourth of the original time. In order to use the nearest neighbor we have to make sure that the velocities are smooth, but smoothing is very inexpensive as compared with ray tracing.

SMOOTHING

Smoothing is done in the velocity grid. A very satisfactory way to smooth the data is to use the Hanning smoother. This has the virtue that the smoothing function does not have impulsive derivatives. Impulsive derivatives of high order can seriously affect the effectivity of the Runge-Kutta method for solution of differential equations, so normally the velocity grid needs to be smooth.

The Hanning function consists of a three point weighted running average with weights (.24, .56, .24), centered in the middle point. The amount of smoothing depends on how many times the filter is passed trough the data. Normally two to four times in the z-direction and four to sixteen times in the x-direction.

Even though we are using a fine grid for the velocities, the ray coverage is still very coarse. It turns out that the amount of smoothing needed to account for the ray coverage coarseness is more than enough to smooth the velocity grid, so we do not lose any efficiency on account of the smoothing.

RESULTS

We tried the modification on some synthetic data. Figure 1 shows the velocity perturbation produced by the iteration. The coarseness of the ray coverage can be seen. Normally before plotting and before a new iteration the velocity field have to be smoothed. Figure 2 shows the velocity field after smoothing. There was smoothing before and after computing the perturbation.

To validate the change on the algorithm, we run an iteration with the old algorithm, it is shown in figure 3, after smoothing. The smoothing was equivalent to that of figure 2. As you can see there is hardly any difference between the two velocity fields, showing that indeed we did not lose anything in the speedup.

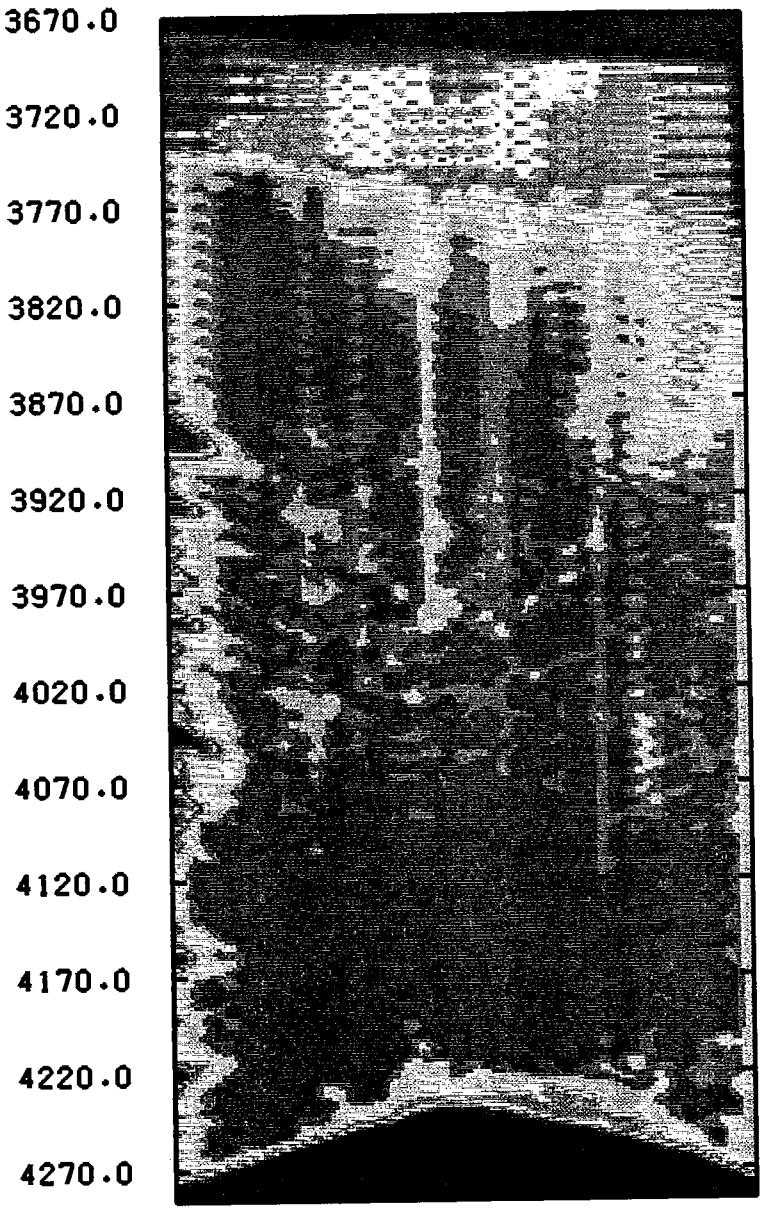

Figure 1
String iteration with fine grid, no interpolation without smoothing

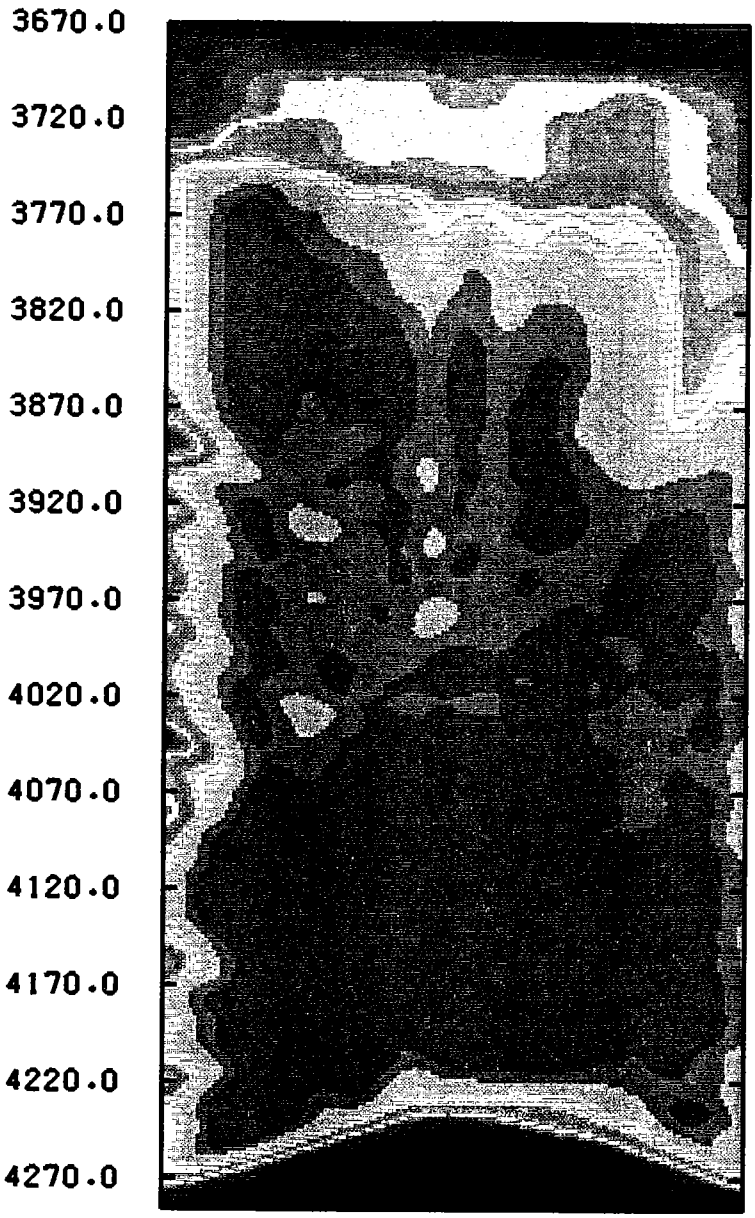

Figure 2
String iteration with fine grid and no interpolation after smoothing

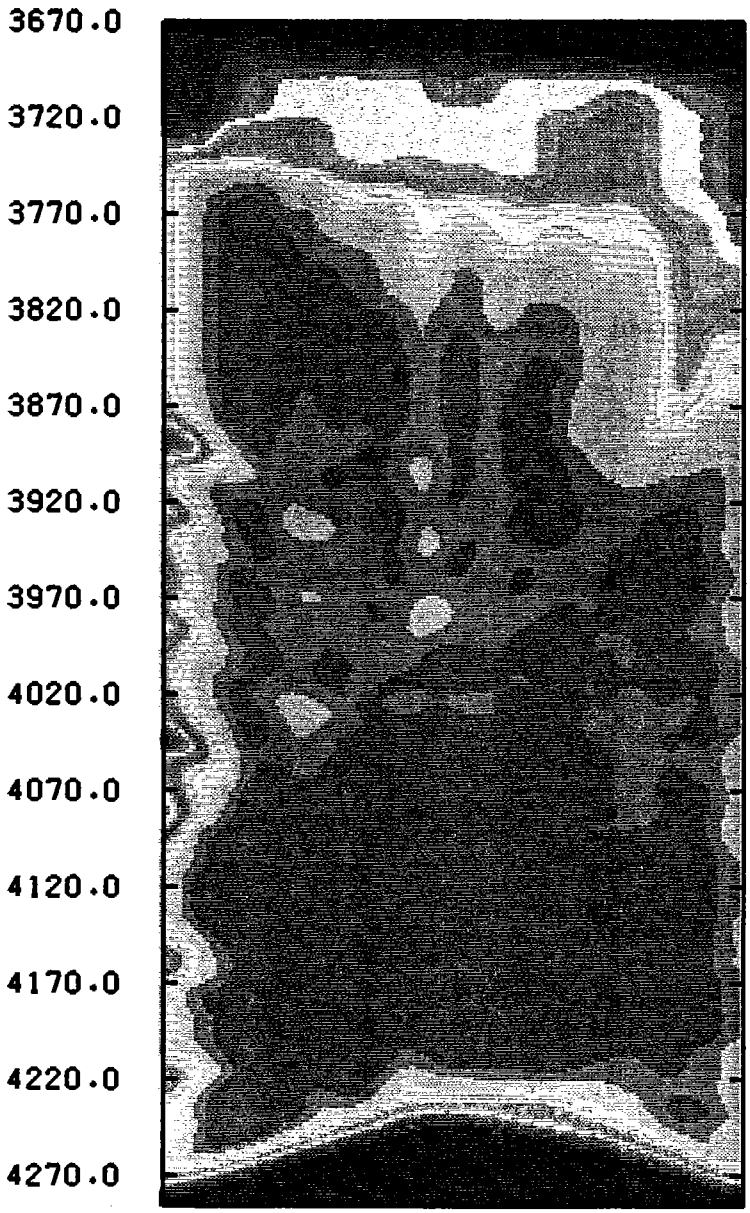

Figure 3
String iteration with coarse grid and interpolation after smoothing

CONCLUSIONS

We have shown that by using a fine velocity grid we can eliminate the grid interpolation needed by the ray tracing part of the string algorithm. Instead of interpolating we just look for the nearest neighbor, thus speeding the algorithm four times. A grid giving about 10 points per wavelength has been very satisfactory.

To avoid inaccuracies we need to smooth the velocity field between iterations, but it turns out that the smoothing needed by the coarseness of the ray coverage is enough, so we do not really lose any computational efficiency in doing this step.

ACKNOWLEDGEMENTS

The author gratefully acknowledges the Gas Research Institute for its support of the Stanford Tomography Project.

Paper N

HIGH RESOLUTION DATA ACQUISITION SYSTEM UPDATE

Jerry M. Harris
Seismic Tomography Project

SUMMARY

Last year I reported the development of a new data acquisition system for recording high frequency cross-well seismic data. The system includes a downhole source and hydrophone array operating in the band of 200-4000 Hz, and two fully equipped logging trucks for crosswell operations. The source was built by Southwest Research Institute and the hydrophone array by Century Geophysical Corporation. The logging trucks are being reconditioned and will be ready for field operations by the end of summer. Over the past year, four cross-well surveys (at Gulf Coast and West Texas sites) and a deep hole transmission test (Gronigen, N. Holland) were successfully run with STP's new high resolution cross-well data acquisition system. This short paper reviews the general system, describes recent additions to the hardware, and provides a brief summary of planned future improvements.

SYSTEM DESCRIPTION

A schematic description of the source system is given in Figure 1. The original source has two active ceramic elements, symmetrically balanced between two high power step-up transformers. These elements are wired to be driven either in phase or 180 degrees out to create a single extended monopole or a vertical dipole source. The new source unit has three active ceramic elements configured into a three-element adjacent array for purposes of beam-steering. Each element is independently driven as illustrated in Figure 1. When beam steering is not desired, the elements may be operated as three independent sources to speed data acquisition. Source signatures are generated by three 12-bit D-to-A phase-coherent waveform generators. Arbitrary programmable waveforms including sweeps, pulses, and pulse sequences can be generated.

The source is powered by a three-channel 24 kVA linear power amplifier built to STP's specs by Instruments, Inc. This power is delivered via a 7-conductor armored wireline designed at STP and built by the Rochester Corporation. The cable maintains the standard 7-conductor configuration but utilizes larger low resistance conductors and special insulation for more efficient power transfer to the source. Downhole step-up transformers at the source are optimized for the three-element and special cable operation.

A block diagram of the receiver system is shown in Figure 2. The system consists of a 9-element hydrophone array. Two Compu-Log computers (one in the source truck and one in the receiver truck) provide joint control and monitoring of the receiver system and to a limited degree the source as well. The system operator has complete software control over system configuration, including selection of the source signature, receiver sampling rates, analog and digital gains, stacking depth, and filter settings. The computers also monitor sonde depth and provide display of user selected recorded data traces. Data are recorded to hard disk and written to tape in SEGY format.

The receiving system uses OAS deep ocean hydrophones as detectors. Each hydrophone is housed in a slotted stainless steel enclosure interconnected with 7-conductor logging cable and has a dedicated DSP for 16-bit downhole digitization. Shots may be stacked downhole to recorded lengths of 16,000 samples at a sample rates down to 50 υSec. Current filter settings include a 250 and 350 Hz lo-cut and 2000 Hz and 4000 Hz hi-cut. Data are telemetered to the surface at a maximum rate of 38,400 baud. Increased data rate options are scheduled for upgrade following this years' acquisition season. A more detailed block diagram of the Compu-log system is given in Figure 3.

The receiver sondes and interconnect cableheads have been successfully tested to temperatures of 125 Centigrade and pressures to 5000 psi. Each receiver sonde is 2 1/2 inches in diameter and about 4.5 feet long each.

PLANNED HARDWARE UPGRADES

There are several changes to the overall system either complete or in progress. These are (1) the addition of the third source transducer element and 3-channel driver for testing source beam steering; (2) the addition of two wireline trucks - one with a special high power source cable; (3) the addition of an analog channel to the receiving array; (4) the addition of a gamma ray logging tool; (5) and, reconfiguration of the source and receiver for operation in the same borehole. A much needed three-axis detector is not yet available.

A special analog receiving channel is being installed on the Compu-Log downhole digital system. This channel is to be used for in-filed monitoring and quality control.

Also, new lo-cut and high-cut filter cards are available and will be added on an as-needed basis.

Schlumberger Well Services has donated two tandem-axle logging trucks to STP. These trucks are being reconditioned and retro-fitted with measuring heads, etc and made ready for field operations. The source truck will have 11,000 feet of high power 7-conductor cable (0.569") installed. The receiver truck will have 17,000 feet of 7-conductor cable (0.46").

A gamma ray logging tool will be added to the system as an aid for depth control and tie to other wireline logs. Initially, the gamma logging will not be fully integrated onto the crosswell system but must run separately. We expect to upgrade this to a fully integrated system next year.

The source and receiver array are being reconfigured for operation in the same borehole as a seismic logging or single-well reflection profiling system. This appears not to be too difficult because the receiver system uses only four conductors and the source only two out the 7-conductor cable. One identifiable need is for source-receiver tube wave isolation.

Finally, we are planning to install one of STP's DEC 5000 workstations in the logging trucks during field operations. This system will run all the tomography software and possibly ProMax (if a license can be obtained). Options include a high resolution plotter and a 1/2" tape drive.

ACKNOWLEDGEMENTS

The author thanks the Gas Research Institute and the David and Lucille Packard Foundation for their financial support of the Seismic Tomography Project. Also, thanks to Schlumberger Well Services for the donation of two logging trucks.

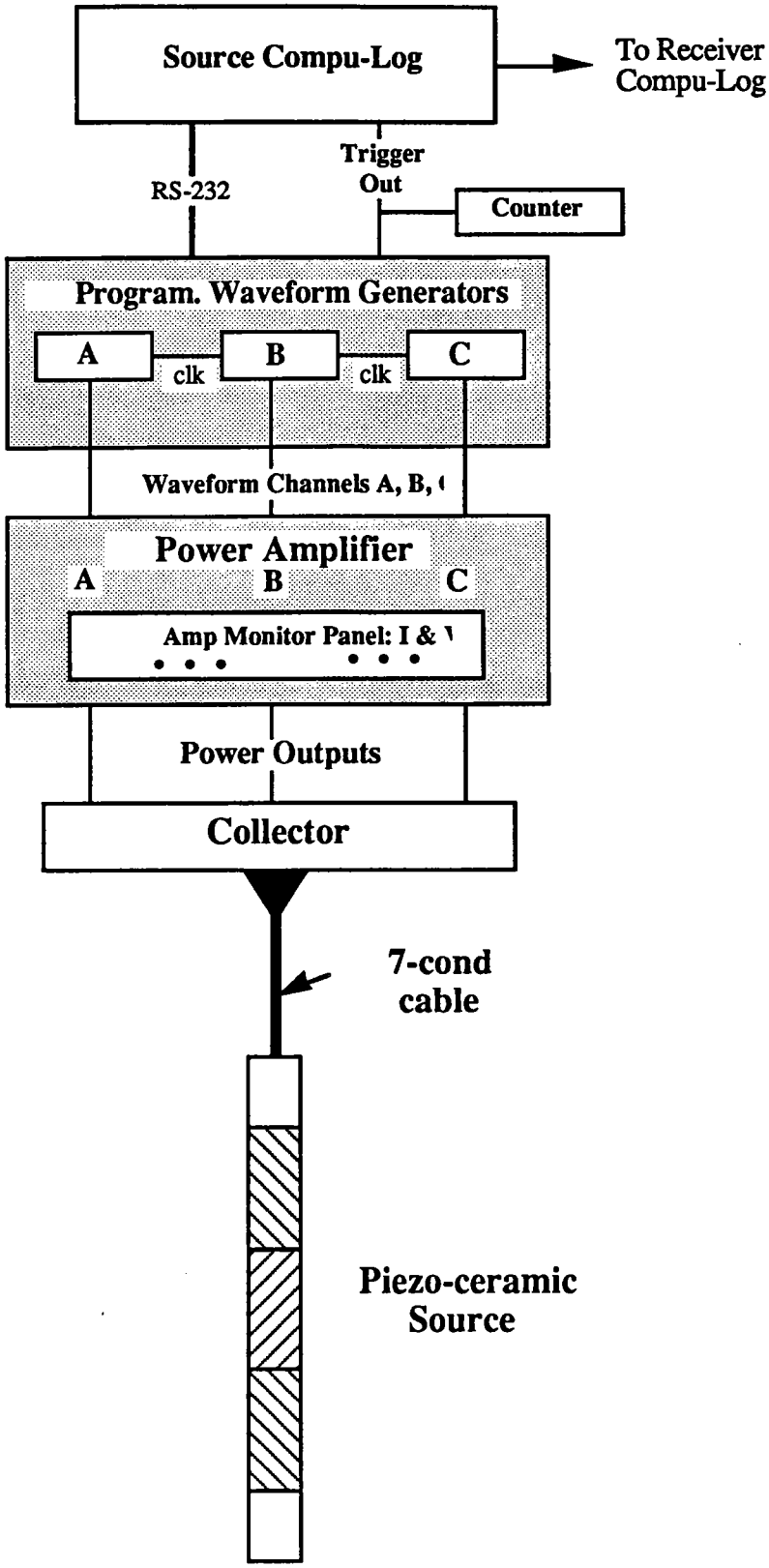

Figure 1. Piezo-ceramic downhole source and driver system.

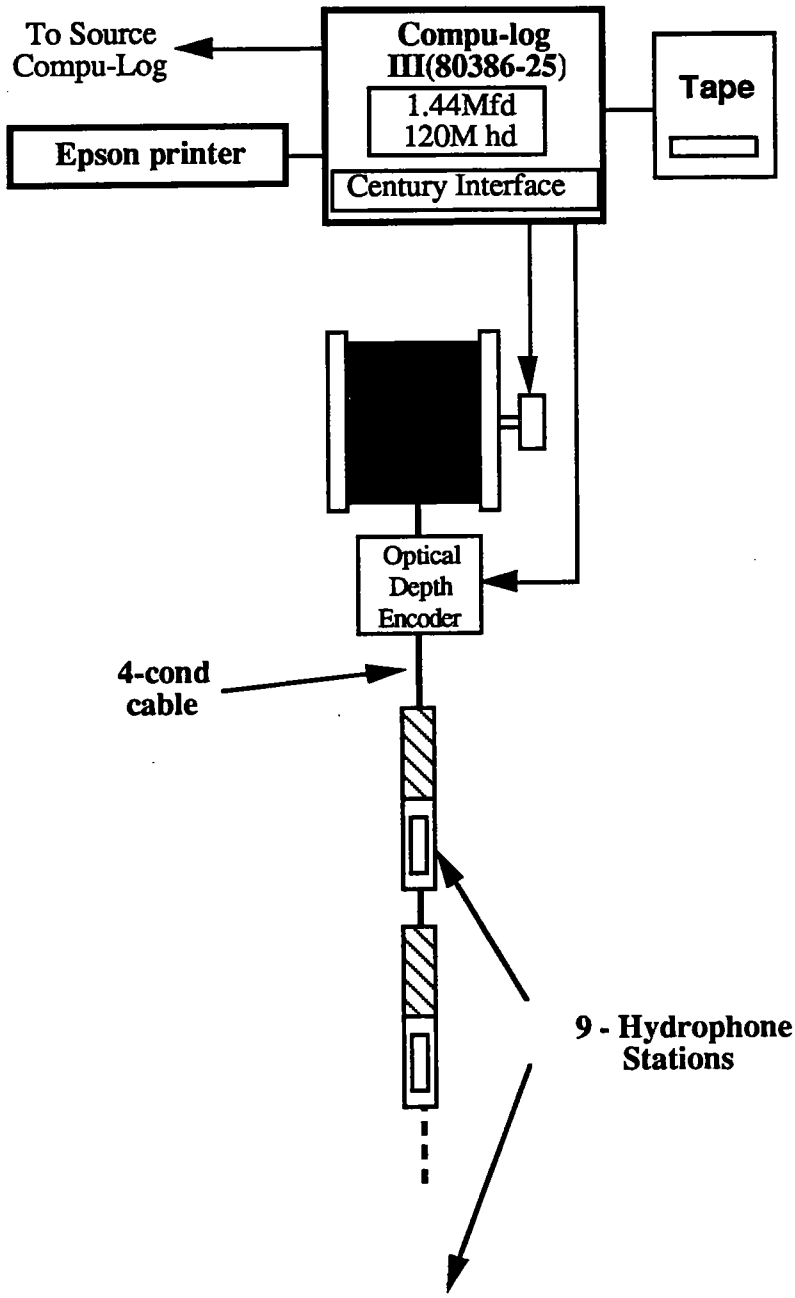

Figure 2. Nine-element hydrophone array system.

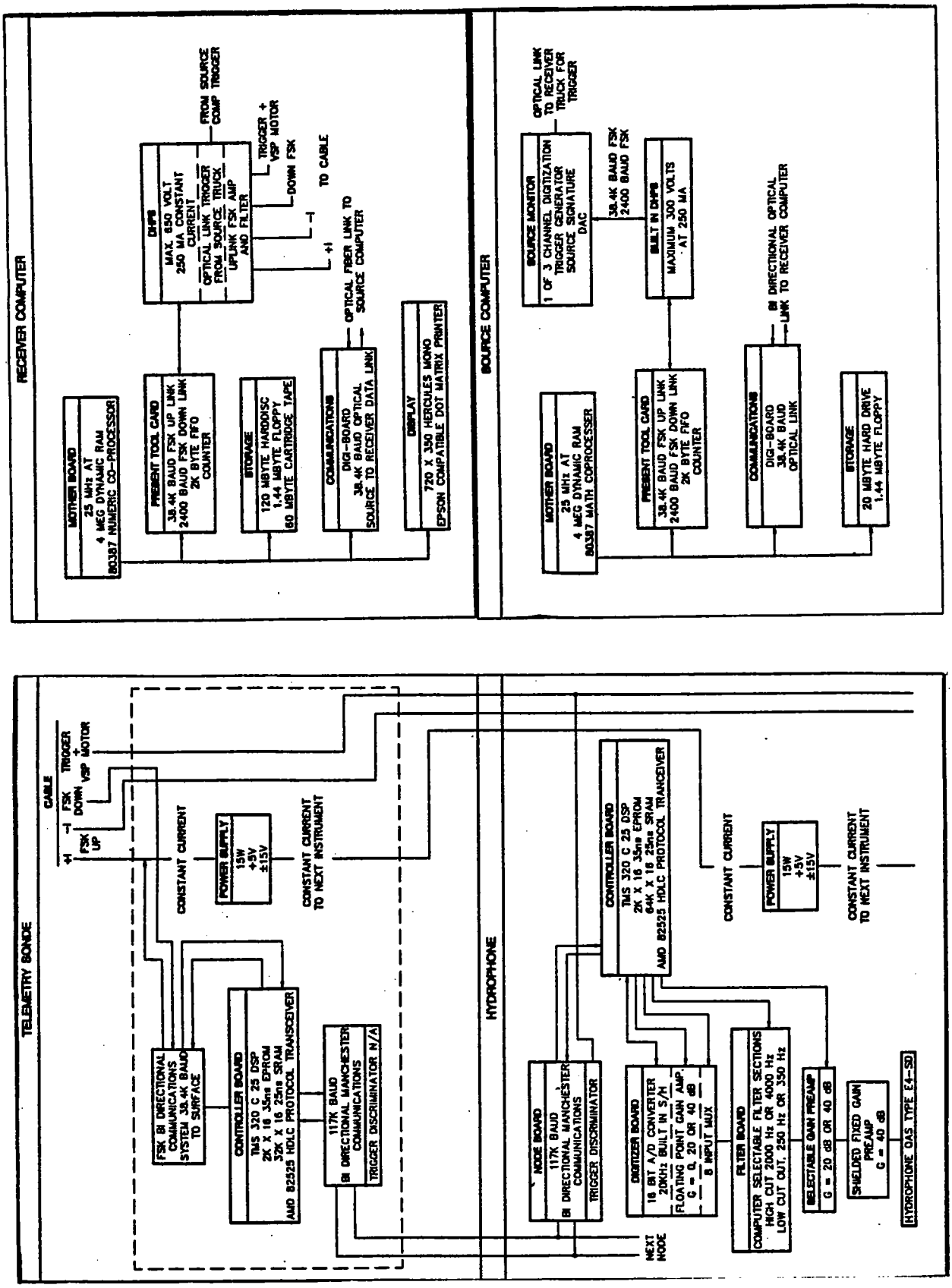

Figure 3. Detailed block diagram of the Compu-log receiving system.

STP DIRECTORY

Name:	Phone:	Electronic-Mail (@pangea.stanford.edu)
Faculty:		
Jerry M. Harris	(415) 723-0496	harris
Gary Mavko	(415) 723-9580	gary
Research Associates:		
Luis Canales	(415) 723-3463	canales
Richard Nolen-Hoeksema	(415) 723-0092	richard
Post Doc:		
Nathalie Lucet	(415) 723-0166	lucet
Jamie Rector	(415) 723-9410	rector
Graduate Students:		
Spyros Lazaratos	(415) 723-4469	spyros
Reinaldo Michelena	(415) 723-4469	reinaldo
Masazumi Onishi	(415) 723-9410	masazumi
Youli Quan	(415) 723-9410	quan
Nicholas Smalley	(415) 723-9410	smalley
Mark Van Schaack	(415) 723-9410	vschaack
Tomography staff:		
Patricia Davillier	(415) 723-1099	patd
Caroline Lambert	(415) 723-9410	caroline
Tomography lab:	(415) 723-9410	
Geophysics Department FAX:	(415) 723-7344	
Stanford University FAX:	(415) 723-0010	
Stanford University Telex:	348402 STANFORD STNU	

RESEARCH PERSONNEL

Luis Canales - received his BS in civil engineering at the University of Mexico in 1970. He received his MS (1973) and Phd (1975) in geophysics at Stanford. He worked at CICESE (Center for Graduate Studies and Scientific Research of Ensenada Mexico) as a professor of geophysics and head of the computer center. He worked at Mobil Oil Co. as a research geophysicist in Dallas. Additionally, he spent eight years in England with Digicon Geophysical Inc. where he was the director of special projects. Luis invented the method for random noise reduction know as LUNA, FXPrediction or FXDeconvolution. He is a member of SEG, EAEG, SSA, AGU. His interests are exploration geophysics, time series analysis, and digital signal processing.

Jerry M. Harris received the Ph.D. degree (1980) in engineering from the California Institute of Technology. From 1974 to 1977, he was with the Communications Satellite Corporation working as an experimentalist on millimeter wave scattering and attenuation for satellite communications. After receiving the Ph.D. degree, he joined Exxon Production Research Company where he worked on adaptive signal processing and scattering of seismic waves. In 1984, he joined the Standard Oil Company to lead development of the seismic tomography project. Dr. Harris joined the faculty at Stanford University in 1988 as Associate Professor of Geophysics. His current research interests include experimental methods in seismology and electromagnetics for imaging and measurement of in-situ rock properties, cross-well tomography, and general topics involving wave physics and signal processing.

Caroline Lambert - received her BS from the University of Alberta, Canada, in 1980, in Geology and Geophysics. She received a MS in Geophysics from California Institute of Technology in 1982. After receiving her master's degree, she worked for a three years for Geometrics, located in Sunnyvale, as a geophysicist working on aeromagnetics. She then came to Stanford to work on an MS in Computer Science, specializing in graphics and image processing, which she completed in 1990. Caroline started working for the STP group in 1989 as a student, and continued as a staff member after graduation. She is mainly responsible for the continued development of the TIMS software package, and systems administration.

Spyros Lazaratos -received his diploma from the National Technical University of Athens, Greece, in 1985 and a MS from Princeton University in 1987, both in electrical engineering. He has been a graduate student at Stanford since 1987 and plans to complete his PhD. in geophysics in the spring of 1992. His current research interests include borehole seismic imaging, tomography and signal processing. He is a member of SEG and IEEE.

Gary Mavko - received his PhD in geophysics from Stanford in 1977. He then joined the Tectonophysics branch of USGS in Menlo Park where he worked in areas of rock physics and earthquake fault mechanics. In 1984 Gary joined Entropic Geophysical Inc., in its first months as a start-up reflection seismic processing company. Gary developed may of Entropic's algorithms and software for reflection and refraction analysis, and eventually became their Vice President of research and development. He returned to Stanford in February, 1989 as an acting associate professor in geophysics, and has been working on modeling and analysis of the acoustic properties of rocks, cross-well seismic imaging and interpretation, and techniques of seismic reflection processing.

Reinaldo Michelena - received his B.S. in Physics in 1984 from Universidad Simon Bolivar, Venezuela. From 1985 to 1988, he worked as a research geophysicist for Intevep, S.A. He received his M.S. in Geophysics from Stanford University in 1990 and is currently working toward a PhD in geophysics under a Intevep, S.A. scholarship. He is a member of SEG.

Richard C. Nolen-Hoeksema - received his B.A. with majors in physics and geology from Hope College and his PhD in geophysics from Yale University. After post-doctoral research at Yale, he worked in the Exploration Research Department at Cities Service Oil & Gas Corporation and in the Reservoir Engineering Division at Chevron Oil Field Research Company. His research interests are in rock physics, rock mechanics, and their application to subsurface characterization and engineering. He has been a Research Associate in Geophysics at Stanford University since 1988.

Masazumi Onishi - received his BS from the University of Tokyo, Japan, in 1978, in Geophysics. From 1978 to 1989 he worked for Japan Petroleum Exploration Co., Ltd. (Japex) and Japex Geoscience Institute Inc., mainly as a research geophysicist on three dimensional reflection seismology. He started his graduate study at Stanford University in September 1089 and has received his MS in Geophysics in June 1991. He will return to Japan and work at Japex in Tokyo.

Youli Quan - received his BS in 1982 from the University of Science and Technology of China, MS in 1986 from the Institute of Geophysics, Chinese Academy of Sciences, and is presently a PhD student at Stanford University with the Stanford Tomography Project (STP). He worked for the Institute of Geophysics, Chinese Academy of Sciences from 1986 to 1989.

James Rector - received his BA in mathematics in 1981 from University of Wisconsin. He then joined Shell Oil in Houston, Texas where he worked as a geophysicist in the rocky mountain division. In 1983 Jamie returned to Stanford and received his MS in geophysics in 1984. Upon graduation he joined Tomex Corporation in Mountain View, California, and in 1986, while continuing his work at Tomex he joined the SRB program at Stanford as a PhD candidate, completing his PhD in 1990. He is currently working with the STP project on aspects of full waveform analysis.

Nicholas Smalley - received his BS in Geophysics from Texas A&M in 1989. He is currently working towards a PhD in Geophysics. His research interests are statistical and non - linear traveltime inversion. He is a member of SEG

Mark Van Schaack - received his BS in geophysical engineering from the Colorado School of Mines in 1985. He joined Schlumberger Wireline Services in 1985 and spent his next four years working in Syria, Egypt and Sudan as a Field Engineer. In 1989, Mark went to work as a Research Associate for University of California, Santa Barbara's Institute for Crustal Studies. His work at ICS included the processing of several surface seismic lines shot in the Southeastern Sierra Nevadas. He has been a graduate student at Stanford since 1990 and is currently working toward his PhD in geophysics.

STP 1991 SPONSORS

Amoco Production Company
P.O. Box 3385
Tulsa, OK 74102

BP Exploration
5151 San Felipe
Houston, Tx 77210

Chevron Oil Field Research Co.
P.O. Box 446
La Habra, CA 90633-0446

Conoco, Inc.
1000 South Avenue
Ponca City, OK 74603

Exxon Production Research Co.
P.O. Box 2189
Houston, Tx 77252

Gas Research Institute
8600 Bryn Mawr Avenue
Chicago, IL 60631

Japex Geosciences Institute, Inc.
Akasaka Twin Tower East Wing
3rd Floor, 2-17-22 Akasaka Minato-Ku
Tokyo 107, Japan

Noranda Technology Centre
240 boulevard Hymus
Pointe-Claire, Que.
Canada H9R1G5

Oryx Energy Company
Technology Center
18325 Waterview Parkway
Dallas, Tx 75252

Phillips Petroleum Co.
5706 Plaza Office Bldg
Bartlesville, OK 74004

Texaco Exploration & Production
P.O. Box 770070
Dallas, Tx 77215

Unocal Science & Technology
P.O. Box 76
Brea, CA 92621